THERMALLY - SPRAYED COATINGS FOR CORROSION PROTECTION OF STEEL OPERATING IN SEAWATER ENVIRONMENTS

by

BERENIKA ANNA SYREK – GERSTENKORN

A thesis submitted to the University of Birmingham for the degree of

DOCTOR OF PHILOSOPHY

SCHOOL OF

METALLURGY AND MATERIALS

UNIVERSITY OF BIRMINGHAM

JUNE 2021

ABSTRACT

The corrosion behaviour of thermally-sprayed sacrificial coatings was investigated under different operating conditions which simulated those of an offshore structure in active service. Electrochemical measurements, combined with several characterisation techniques, such as SEM, EDX and Raman spectroscopy were used to assess the performance of the coatings during exposures to various conditions of simulated full and alternating seawater immersion, splash zone conditions and atmospheric corrosion conditions. The effect of temperature and graphene-containing sealants were also studied under artificial seawater immersion on aluminium-coated steel samples containing defects.

The results of immersion tests of thermally sprayed aluminium (TSA) coatings with defects revealed significantly worse performance of the coatings exposed to cold temperatures (4°C) compared with other temperatures tested. A significant amount of rust was observed in the defect region and required polarisation (-0.8 V vs Ag/AgCl) was not provided by the TSA. This was related to low solubility of aluminium and decreased precipitation of calcareous deposits. The application of graphene - containing sealants on TSA coatings turned out to be effective in decreasing the contact between the electrolyte and the steel substrate at warm temperatures (25°C) under full immersion conditions. However, the addition of the sealants was found to be detrimental to the performance of TSA coatings operating at cold temperatures (4°C) under full immersion conditions as well as warm temperatures (25°C) under alternating immersion conditions.

The results of atmospheric corrosion tests showed that cathodic and anodic regions were not easily distinguishable on TSA coatings. Droplets did not spread, and

sulphur-containing corrosion products were detected after the test. This highlights the importance of using seawater, and not NaCl solutions, as a corrosive medium simulating marine environment.

Dedicated to my family and friends.

“Nothing in life is to be feared, it is only to be understood. Now is the time to understand more, so that we may fear less.” – Maria Skłodowska - Curie

ACKNOWLEDGMENTS

Firstly, and most importantly, I would like to express my sincere gratitude to my supervisors: **Professor Alison Davenport** and **Dr Shiladitya Paul**, for their guidance, valuable comments, great help and dedicated time.

I am also extremely thankful to my friends who I met at Birmingham University: **Sarah Glanville**, **William (George) Rowley**, **Steven Street**, **Angus Cook** and **Flaviu Gostin**. Thank you for all you help and support!

I also wish to thank my friends from TWI, especially from the cake office. My PhD would not have been so enjoyable without your presence and baking skills. I would like to take this opportunity to especially thank **Rosa Griñon Echaniz**, not only for her incredible help with the SEM, but also for always being there for me. Moreover, a big thank you to **Nikos Marinos** for being an amazing friend who helped me stay sane during this long journey.

I also would like to thank my **Polish** and **Yorkshire family (the Coopers)** for their continued support and encouragement.

Last but not least, I would like to thank my better half **Pedro Santos** for his mental support, patience, love and morning coffees which helped me to survive the difficult writing up period during the lockdowns.

This project was made possible by the sponsorship and support of Lloyd's Register Foundation, a charitable foundation helping to protect life and property by supporting engineering-related education, public engagement and the application of research. The work was enabled through, and undertaken at, the National Structural Integrity Research Centre (NSIRC), a postgraduate engineering facility for industry-led research into structural integrity established and managed by TWI through a network of both national and international Universities. I gratefully acknowledge financial support from the Centre for Doctoral Training in Innovative Metal Processing (IMPaCT) funded by the UK Engineering and Physical Sciences Research Council (EPSRC), grant reference EP/L016206/1.

Table of contents

CHAPTER 1 INTRODUCTION 1

1.1 AIM OF THE PROJECT 3

CHAPTER 2 LITERATURE REVIEW 5

2.1 CORROSION OF STEEL 5

2.1.1 Effect of temperature 5

2.2 CORROSION OF ALUMINIUM 8

2.2.1 Introduction 8

2.2.2 Corrosion in seawater 11

2.2.2.1 Pitting corrosion 12

2.2.2.2 Effect of temperature 13

2.2.2.2.1. Pitting potential 13

2.2.2.2.2. Corrosion potential 14

2.2.2.2.3. Galvanic potential when coupled to steel 14

2.2.2.2.4. Corrosion rate 16

2.2.3 Atmospheric corrosion 17

2.3 SACRIFICIAL COATINGS 18

2.4 THERMAL SPRAYING 20

2.4.1 Electric Arc Spraying 20

2.4.2 Wire Flame Spraying 21

2.5 LABORATORY TESTS 21

2.5.1 Effect of the Spraying Method and its Parameters 21

2.5.2 Effect of Coating Thickness 22

2.5.3 Effect of Coating Composition 23

2.5.4 Effect of Sealing 28

2.5.4.1 Graphene-reinforced epoxy 31

2.5.5 Effect of Temperature 32

2.5.5.1 Calcareous deposits 33

2.5.6 Effect of Oxygen 36

2.6 LONG-TERM FIELD STUDIES 37

2.7 LABORATORY CORROSION TESTING METHODS 40

2.8 IN-SERVICE PERFORMANCE OF AL COATINGS 41

2.9 SUMMARY 43

CHAPTER 3 METHODOLOGY 45

3.1 MATERIALS 45

3.2 EXPERIMENTAL PROCEDURE 46

3.2.1 Full immersion experiments 46

3.2.1.1 Samples preparation 46

3.2.1.2 Experimental methods 49

3.2.2 Experiments under droplets 52

3.2.2.1 Silver wire experiments 52

3.2.2.2 Luggin probe experiments 53

3.2.2.3 Calibration of Ag wire electrode vs Ag/AgCl electrode 54

3.2.2.3 Atmospheric corrosion tests 54

3.2.3 Characterisation of corrosion products 57

3.2.4 Roughness measurements 58

CHAPTER 4 ELECTROCHEMICAL BEHAVIOUR OF ALUMINIUM AND STEEL IN SIMULATED SEAWATER ENVIRONMENTS 59

4.1 INTRODUCTION 59

4.2 RESULTS AND DISCUSSION 60

4.2.1 Effect of temperature on corrosion of steel in artificial seawater 60

4.2.2 Effect of temperature on aluminium in artificial seawater 66

4.2.2.1 Long exposures 66

4.2.2.2 Shorter exposures 68

4.2.2.3 Long and short exposures - comparison 76

4.2.3 Performance of aluminium as a sacrificial anode 78

4.3 CONCLUSIONS 81

CHAPTER 5 PERFORMANCE OF THERMALLY SPRAYED COATINGS UNDER SUBMERGED CONDITIONS 82

5.1 INTRODUCTION 82

5.2 RESULTS AND DISCUSSION 83

5.2.1 The effect of alloy coating composition and substrate. 83

5.2.2 The effect of temperature and damage 87

5.2.2.1 Undamaged TSA coatings 87

5.2.2.2 Damaged TSA coatings 89

5.2.3 The effect of sealing 105

5.2.3.1 Samples without defects 25℃ – full immersion 105

5.2.3.2 Samples with defects at 25℃ – full immersion 110

5.2.3.1 Samples with defects at 4°C – full immersion 127

5.2.3.2 Samples with defects at 25°C - alternating immersion 139

5.3 CONCLUSIONS 143

CHAPTER 6 PERFORMANCE OF THERMALLY SPRAYED COATINGS UNDER SPLASH ZONE AND ATMOSPHERIC CONDITIONS. 145

6.1 INTRODUCTION 145

6.2 ELECTROCHEMISTRY UNDER DROPLETS 146

6.2.1 Effect of the droplet volume 146

6.2.2 Effect of RH 147

6.2.3 Comparison between splash zone and full immersion conditions 150

6.2.3.1 Preliminary measurements under droplets 150

6.2.3.2 Performance of coated and uncoated steel samples 152

6.3 ATMOSPHERIC CORROSION EXPERIMENTS 155

6.3.1 Solid aluminium *155*

6.3.2 TSA *160*

6.4 CONCLUSIONS 164

CHAPTER 7 GENERAL DISCUSSION, CONCLUSIONS AND FUTURE WORK 165

7.1 GENERAL DISCUSSION 165

7.1.1 Temperature *165*

7.1.2 Time *166*

7.1.3 Seawater vs NaCl for testing TSA *167*

7.1.4 Exposure type *168*

7.1.5 Summary *168*

7.2 GENERAL CONCLUSIONS 169

7.3 RECOMMENDATIONS FOR FUTURE WORK 171

REFERENCES 173

APPENDICES 184

APPENDIX 1 184

Acronyms and symbols

AA	Aluminium alloys
ASW	Artificial seawater
CP	Cathodic protection
CRA	Corrosion-resistant alloys
DC	Direct current
DCLS	Direct classical least square
D	Diffusion coefficient
DI	Deionised
E	Potential
E_{corr}	Corrosion potential
E_{pit}	Pitting potential
E_{rp}	Repassivation potential
EA	Electric arc
EDX	Energy-dispersive X-ray spectroscopy
EIS	Electrochemical impedance spectroscopy
F	Faraday´s constant
FEM	Finite element method
FS	Flame spraying
GNP	Graphene nanoplatelets
GPS	Geometric product specification
i	Current density
i_{corr}	Corrosion current density
i_{O2lim}	Diffusion limited current density
i_{pass}	Passive current density
IM	Intermetallic particles
IMS	Industrial methylated spirit
LPR	Linear polarisation resistance
OCP	Open circuit potential
PCA	Principal component analysis
PEO	Plasma electrolytic oxidation
RH	Relative humidity
Rp	Polarisation resistance
SEM	Scanning electron microscope
STS	Stainless steel
TLP	Tension leg platform
TS	Thermally-sprayed
TSA	Thermally sprayed aluminium
TSZ	Thermally sprayed zinc
XPS	X-ray photoelectron spectroscopy
XRD	X-ray diffraction
δ	Diffusion layer thickness
ΔC	Concentration difference

Chapter 1 Introduction

Clean energy sources, such as offshore wind power, are being promoted as a consequence of efforts aimed at minimisation of the environmental footprint often attributed to the global warming. In 2017 over 6% of the UK's electricity demand was covered by the offshore wind farms, which reduced the UK's CO_2 emission by 8.6 million tonnes [1]. It is expected that development of offshore wind turbines will accelerate even further, and larger and more distant offshore wind turbines will be built [2]. Currently, most offshore wind turbines are based on monopile foundation made of a steel pipe [3]. Rolled and welded carbon steel plate is used due to its high strength and weldability, combined with relatively low cost. However, it is prone to corrosion in seawater environments and therefore, corrosion mitigation methods must be applied.

The most common corrosion mitigation methods for the protection of offshore structures that are made of steel (usually mild or low-alloyed [4]) involve the application of cathodic protection and/or protective coatings, depending on the conditions to which the structure is subjected. The types of exposure for these materials can be divided into four main zones: atmospheric, splash/tidal, submerged, and buried (Figure 1-1). Parts of an offshore structure that are constantly immersed in seawater (submerged zone) are usually protected by the application of cathodic protection, while parts that are only exposed to the marine atmosphere (atmospheric zone) are usually protected by organic coatings. In the splash/tidal zone however, the corrosion of steel is usually controlled by robust coatings and allowance of steel corrosion (in the splash zone) as well as cathodic protection (for parts located below mean water level) [5] . This is the

most severe and the most challenging area for corrosion protection due to alternating wetting and drying conditions, easy access to oxygen, atmospheric pollutants, UV radiation, and erosive actions combined with frequent contact with floating objects such as debris, boats or ice.

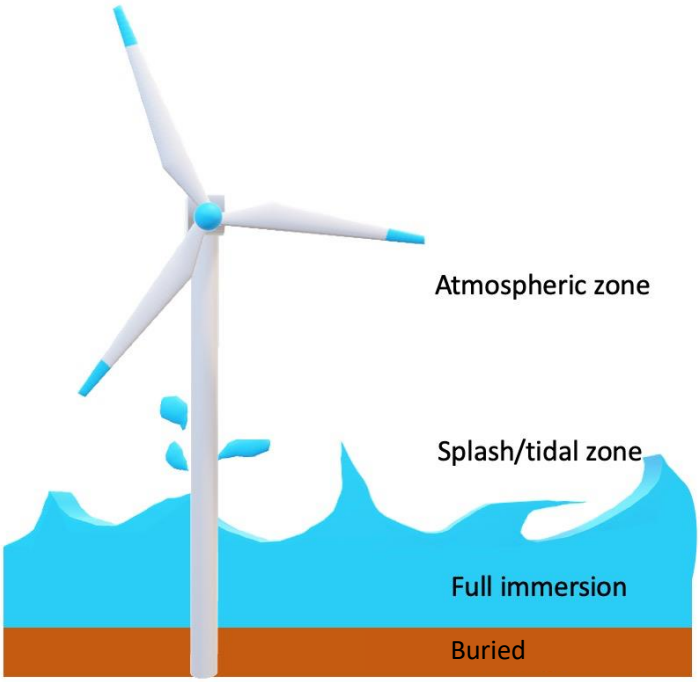

Figure 1-1 Schematic showing operating zones of an offshore structure.

One of the corrosion mitigation methods, increasingly used in the offshore sector, is application of sacrificial coatings, such as: thermally sprayed aluminium (TSA) coatings. TSA offers long-term, maintenance-free protection to steel, working as a barrier to the corrosive environment when intact, and acting as an evenly distributed anode which sacrificially dissolves giving full protection to steel when damaged. Furthermore, high resistance to mechanical damage, large operating temperature range, and low corrosion rate makes it an excellent corrosion mitigation coating for offshore applications.

The most common application method for TSA coatings prepared for corrosion protection of steel is an electric arc spraying process. This technique allows not only the application of the coating by an automatic system in the factory, but also manually on-site (for example to repair a damage in the coating). In both cases, immediately before spraying, the substrate must be thoroughly prepared by grit blasting. This ensures an appropriate level of cleanliness and roughness of the substrate which is essential for the bond to be developed between the coating and the substrate.

Despite well-documented performance history of TSA, gaps in knowledge still remain. To date the performance of the coatings at low temperatures has not been widely explored. The majority of the testing has been conducted at either room or elevated temperature, for example: [6–12]. Understanding the mechanisms controlling the performance of the TSA coatings in colder seawater is of a paramount importance, as many of offshore structures are exposed to cold environments such as the North Sea or the Baltic Sea. Moreover, the influence of operating conditions on the corrosion protection properties provided by TSA coatings has not been fully understood yet. As the offshore structures are exposed to different conditions in different operating zones, the corrosion performance of TSA might vary.

1.1 Aim of the project

The aim of the project is to address the areas that have not been fully understood or addressed yet, namely:

1. Performance of damaged TSA coatings in seawater at different temperatures.
2. Suitability of using TSA coatings in splash and atmospheric zones.

3. Performance of TSA coatings sealed with graphene-containing epoxies and paints. The work is completed by systematic studies of electrochemical behaviour of steel and aluminium at different temperatures.

Chapter 2 Literature review

This chapter is an extended version of the following paper:

Syrek-Gerstenkorn, Berenika, Paul Shiladitya, and Davenport Alison J: "Sacrificial thermally sprayed aluminium coatings for marine environments: A review." Coatings 10.3 (2020): 267.

2.1 Corrosion of Steel

The dominant anodic reaction for corrosion of steel follows Equation 2-1:

$$\mathbf{Fe \rightarrow Fe^{2+} + 2e^{-}} \qquad \text{Equation 2-1}$$

Two types of cathodic reactions occur in neutral to basic solutions (seawater pH ~ 8): oxygen reduction:

$$\mathbf{O_2 + 2H_2O + 4e^{-} \rightarrow 4OH^{-}} \qquad \text{Equation 2-2}$$

and hydrogen evolution:

$$\mathbf{2H_2O + 2e^{-} \rightarrow H_2 + 2OH^{-}} \qquad \text{Equation 2-3}$$

2.1.1 Effect of temperature

It has been observed that temperature affects the corrosion of steel in aqueous environments. It has been reported by several authors (e.g. [13–15]) that the corrosion rate of steel placed in an open vessel increases with increasing temperature up to 80°C (Figure 2-1).

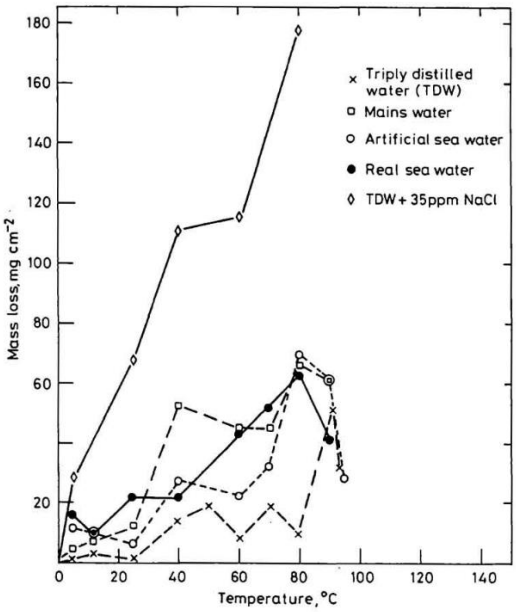

Figure 2-1 Effect of temperature on corrosion rate of mild steel after the 50-day immersion in various air-saturated waters. Taken from [16]***.***

This is related to the increasing diffusivity of oxygen in water with temperature (Figure 2-2 (a)). However, at the same time, the concentration of oxygen decreases with the increasing temperature (Figure 2-2 (b)), and above 80°C, there is very little oxygen dissolved in the solution. Therefore, the corrosion rate starts to decrease. Increasing diffusivity and decreasing concentration of oxygen with temperature is associated with the increasing energy of molecules. Higher energy results in higher velocity and hence faster diffusion. It also makes it easier for the oxygen molecules to overcome the attractive potential that keeps them in the solution.

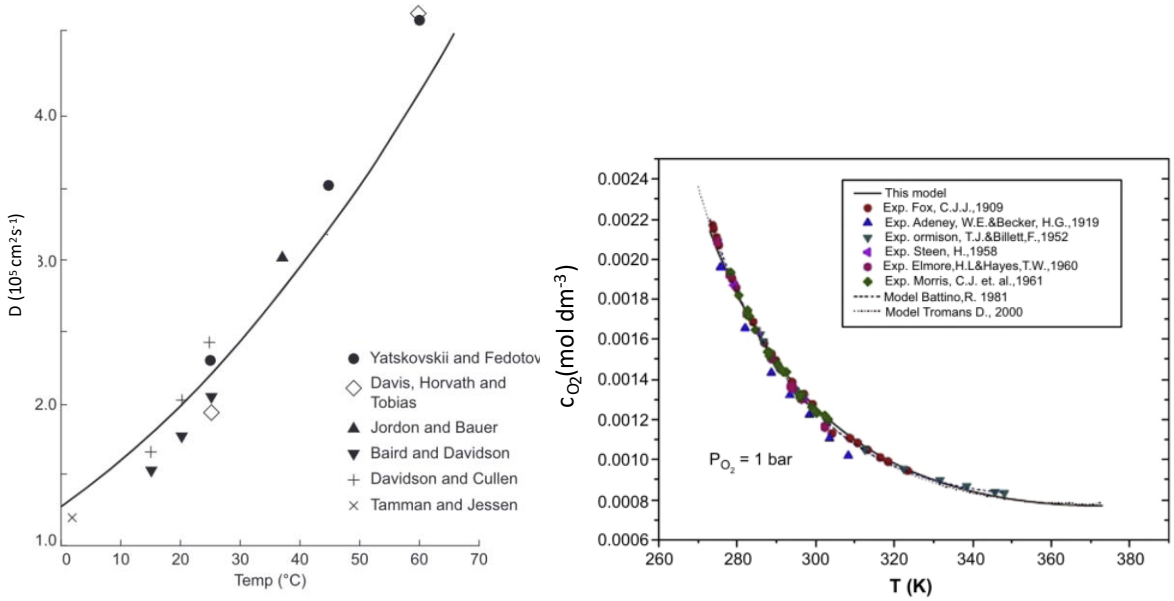

Figure 2-2 Diffusion coefficients (a) and solubility (b) of oxygen in water as a function of temperature. Taken from [17]***.***

Moreover, it has been noticed that not only the cathodic activity, but also anodic activity is affected by the temperature change. This can be seen from Figure 2-3 showing polarisation curves performed on X65 steel in 3.5% NaCl at different temperatures (between 20 and 95°C) [15]. From the data, it is evident that both anodic and cathodic reactions are enhanced at higher temperatures.

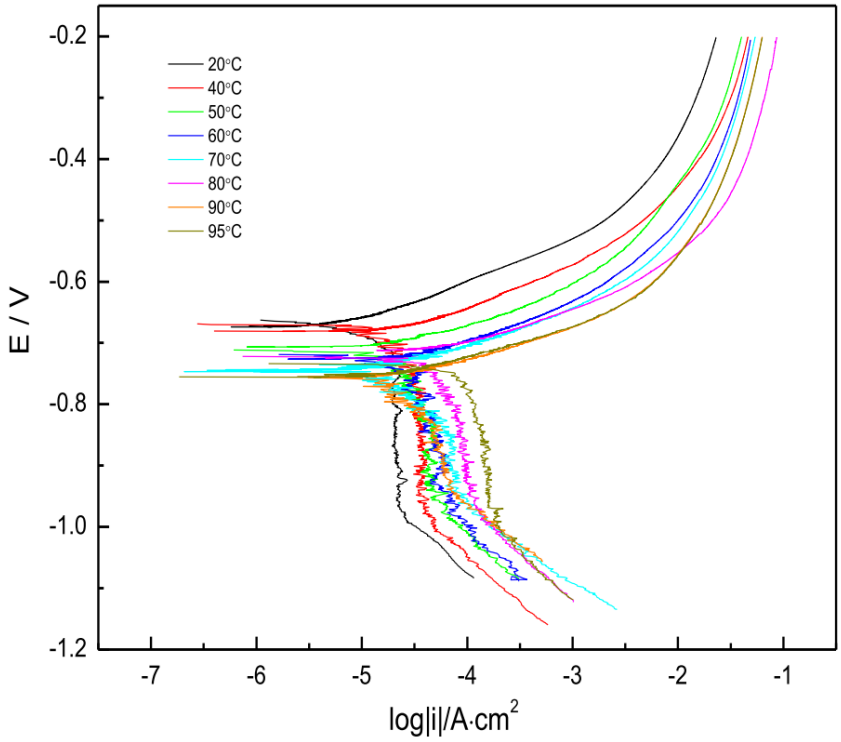

Figure 2-3 Potentiodynamic polarisation curves of X65 steel in 3.5% NaCl at different temperatures. Taken from [15]***.***

Less attention has been given to the corrosion performance of steel in colder seawater, however it has been reported that the rust deposits formed in cold (0°C) 3.5% NaCl solution (on EH40 steel) are loose and porous while at warm temperature (25°C) are uniform and compact [18].

2.2 Corrosion of Aluminium

2.2.1 Introduction

In a wet, aerated environment aluminium undergoes simultaneous reactions: anodic

$$\mathbf{Al \rightarrow Al^{3+} + 3e^{-}}$$ Equation 2-4

$$\mathbf{2Al + 3H_2O \rightarrow Al_2O_3 + 6H^{+} + 6e^{-}}$$ Equation 2-5

and cathodic. The two main cathodic reactions involved in corrosion of aluminium are: reduction of oxygen dissolved in the solution:

- in neutral or alkaline solutions: Equation 2-2.
- in acidic solutions:

$$O_2 + 4H^+ + 4e^- \rightarrow 2H_2O \qquad \text{Equation 2-6}$$

and reduction of water, leading to evolution of hydrogen:

- in neutral or alkaline solutions: Equation 2-3
- in acidic solutions:

$$2H^+ + 2e^- \rightarrow H_2\,. \qquad \text{Equation 2-7}$$

Pure aluminium is known to have good corrosion resistance properties in neutral environments due to its passive nature [19]. A passive oxide film, which forms on the surface of aluminium according to Equation 2-2 works as an electrical insulator [20,21]. It prevents the movement of electrons (produced during anodic dissolution of the metal) from the metal to the oxide/solution interface, which results in the inhibition of cathodic reactions. However, it has been determined (based on thermodynamic considerations) that the protective passive film is stable only in a certain pH range – which varies with temperature. This can be seen in the pH – potential diagrams in Figure 2-4, also known as the Pourbaix Diagrams. The pH range where Al dissolution is minimum is shown in green.

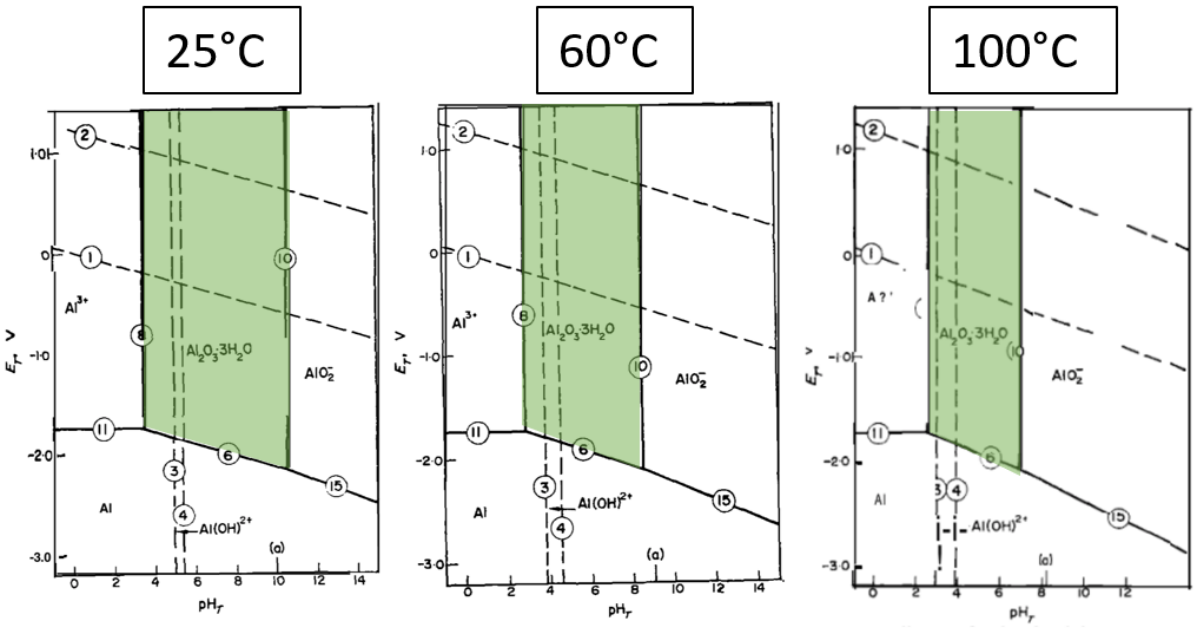

Figure 2-4 Potential - pH diagrams of aluminium – water systems at different temperatures. Taken from [22]***.***

The protective passive film consists of two layers. The first very thin (2 - 4nm) alumina (Al_2O_3) layer forms immediately after polishing the surface of the metal. It is very compact and amorphous. Upon contact with water, the air-formed layer dissolves and a hydrated oxide film forms [23,24]. The nature of the oxide film formation on aluminium was a subject of several investigations, for example: [23–25]. It has been observed that at first, the initial film consists of pseudoboehmite layer, which transforms over time into boehmite and bayerite. Moreover, it has been noticed that the time needed to nucleate and grow the bayerite layer reduces with decreasing temperature [23]. At high temperatures (above 90°C), only boehmite forms.

It has been also reported that the solubility of aluminium hydroxide films depends on the pH and temperature of the solution. This can be seen from the theoretical solubility diagrams of amorphous $Al(OH)_3$ plotted for two temperatures: 4 and 25°C (Figure 2-5).

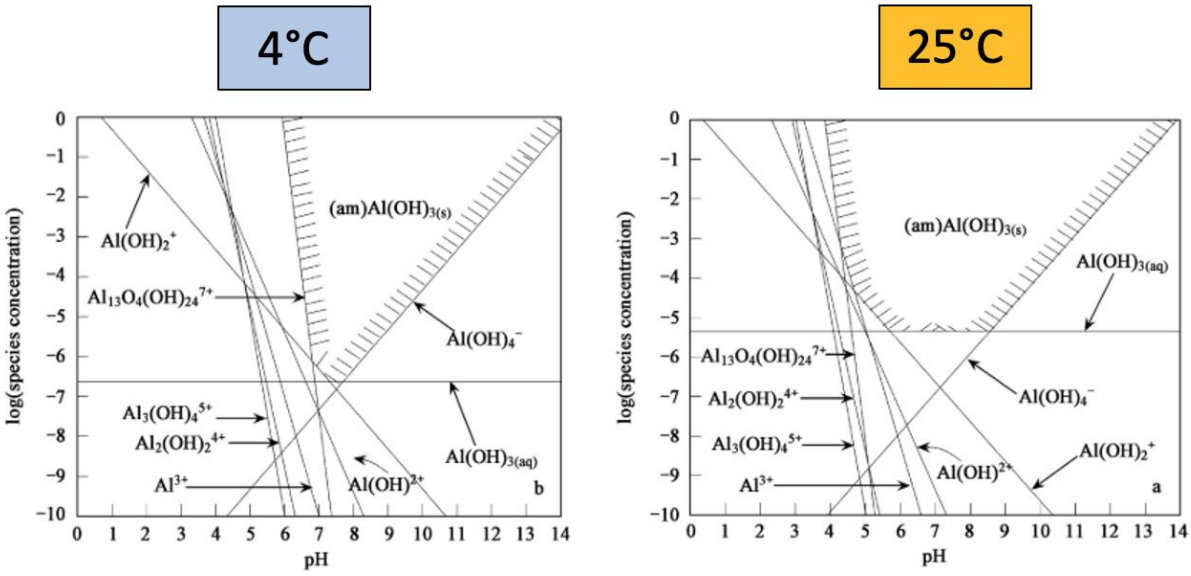

Figure 2-5 Solubility diagrams of $Al(OH)_3$. Taken from [26]***.***

Moreover, it has been reported that the protectiveness of the oxide film depends also on the purity of an alloy. Generally, corrosion resistance increases as the level of impurities decreases. The most common impurities in pure aluminium are iron and silicon [27], which form intermetallic particles (IM) such as: $FeAl_3$ or α-AlFeSi, which are cathodic sites for reduction of oxygen [28]. It has been observed that iron-rich intermetallic particles are detrimental for corrosion resistant properties of aluminium in two ways. Firstly, they enhance cathodic reactions, as they are usually covered with thinner and conducting oxide films. Secondly, they act a nucleation sites for pitting corrosion [29].

2.2.2 Corrosion in seawater

General corrosion of aluminium in seawater is quite low due to its passive nature. However, in the presence of aggressive anions present in seawater, particularly chloride (Cl^-), aluminium undergoes breakdown of its passive layer leading to a local dissolution called pitting corrosion [19,30–32].

2.2.2.1 Pitting corrosion

Pitting corrosion is associated with the local acidification in small cavities caused by chloride ions and hydrolysis of metal cations. The aggressive acidic environment and depletion of oxygen lead to the local anodic dissolution of the metal inside the pit, and the shift of the cathodic reaction outside the cavity (as shown in Figure 2-6), where oxygen is available.

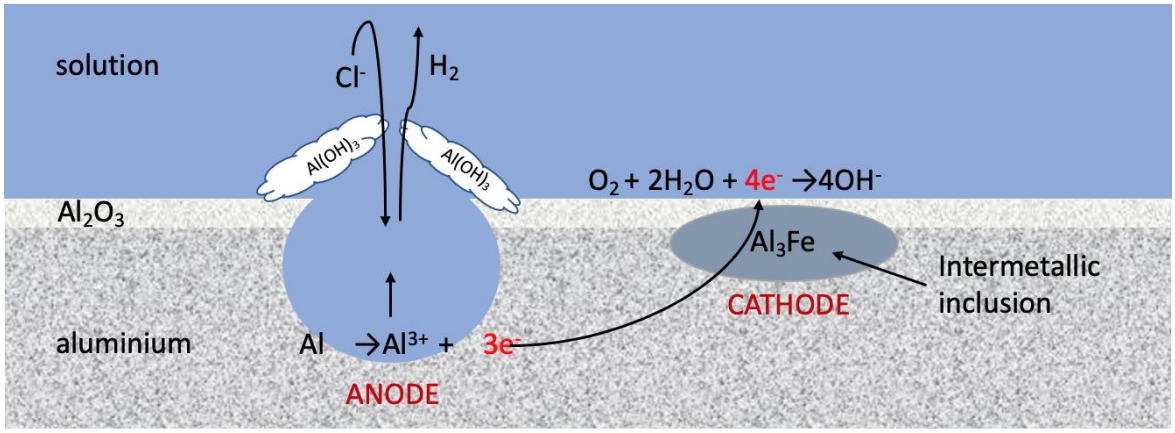

Figure 2-6 Mechanism of pitting corrosion.

The most common electrochemical approach to study corrosion resistance of metals susceptible to pitting is potentiodynamic polarisation. This method allows determination of important parameters, such as corrosion current density (i_{corr}), passive current density (i_{pass}), corrosion potential (E_{corr}), pitting potential (E_{pit}) and repassivation potential (E_{rp}). A typical anodic polarisation curve of a passive metal is shown in Figure 2-7. In this technique the material under investigation is electrochemically polarised from the cathodic region toward the anodic region by sweeping the potential while the corresponding current density is recorded.

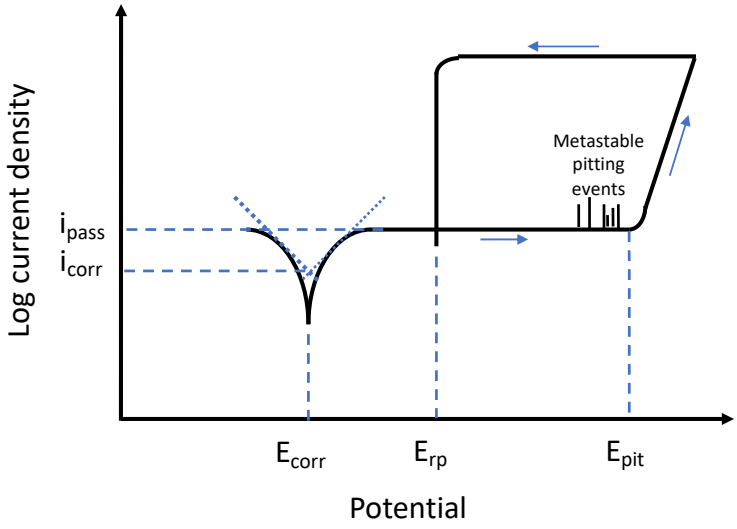

Figure 2-7 A typical potentiodynamic polarisation curve showing the anodic region.

2.2.2.2 Effect of temperature

Even though the effect of temperature on corrosion of aluminium in aqueous environment is complex, little research effort has been directed into this subject, especially to temperatures below 20°C. However, it is known that temperature influences rates of chemical reactions, solubility and diffusivity of gasses as well as precipitation of corrosion deposits. These factors, in turn, alter important corrosion parameters, such as pitting potential, corrosion potential and corrosion rate.

2.2.2.2.1. Pitting potential

It has been shown that pitting potential of aluminium in chloride containing aqueous solutions decreases with increasing temperature [33–35] This has been related to decreasing activation overpotential for the anodic dissolution reaction within a propagating pit [33] and stronger chemisorption of Cl^- ions on the aluminium's surface [34]. Furthermore, it has been reported that above 30-40°C, the influence of temperature on the pitting potential becomes more pronounced. This has been

correlated with the passive film structure forming on the metal upon the immersion in water [33]. It has been suggested that below 40°C, only bayerite forms, whereas at higher temperatures, pseudo-boehmite can be found underneath the bayerite [33].

2.2.2.2.2. Corrosion potential

Studies performed on aluminium immersed in seawater showed that the corrosion potential of this metal decreases with increasing temperature [34,36,37]. This has been attributed to changes in CO_2 system with temperature. Rowland and Dexter [38], who conducted experiments on alloy 5052 and 99.99% aluminium explained the ennoblement of the corrosion potential with decreasing temperature by increased cathodic activity due to the formation of H_2CO_4 (which works as a cathodic depolarizer). They also suggested incorporation of CO_3^{2-} into the oxide film at warm temperature (25°C).

2.2.2.2.3. Galvanic potential when coupled to steel

The suitability of aluminium to provide a sacrificial protection to steel operating in seawater depends on its ability to lower the corrosion potential of steel into the "protection potential region" – which is considered to be between -0.8 V to -1.1 V (vs Ag/AgCl ref electrode) [39]. Studies performed on Al-Fe galvanic couples in 100 ppm NaCl revealed that temperature has a strong influence on the polarity behaviour of the couple. It was shown that at 20°C, aluminium is the anodic element of the Al-Fe couple, however at high temperatures (50, 75 and 90°C), polarity reversal occurs after some time. This is due to large change of the potential of aluminium with temperature. No studies at low temperatures (below 20°C) and salinities corresponding to seawater environment have been found in the literature.

However, the DNVGL-RP-B401 recommended practice (regarding cathodic protection design) [39] advises higher design current density for cathodic protection of steel exposed to cold seawater. This can be seen in Table 2-1. The higher current density demand at colder temperatures is associated with increased seawater resistivity (Figure 2-8).

Table 2-1 Recommended mean design current densities (A/m^2) for seawater exposed bare metal surfaces, as a function of temperature. Taken from [39]***.***

	Temperature range			
Depth	<7ºC	7-12 ºC	12-20 ºC	>20 ºC
0-30 m	0.120	0.100	0.080	0.070

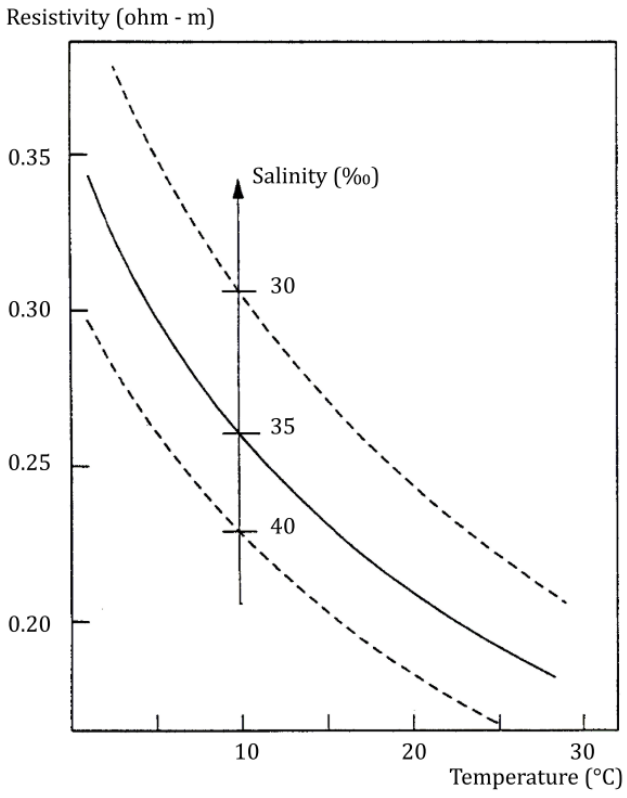

Figure 2-8 Resistivity of seawater as a function of temperature for salinity 30 to 40 ‰. Taken from [39]***.***

2.2.2.2.4. Corrosion rate

It has been observed that, similarly to steel, the corrosion rate of aluminium immersed in open container filled with water increases with temperature until 80°C. Above this temperature the corrosion rate starts to slow down [36,40,41]. However, it has been shown that the corrosion rate of aluminium alloys (of 2024-T3, 6061-T6 and 7075-T6) changes with the immersion time and after longer exposures (30 days) lower corrosion rates were reported at high temperatures (60-80°C) than at low temperatures (20-40°C). This has been attributed to the formation of a protective surface film at high temperatures [42]. Moreover, very interesting findings were revealed from the 5-year field study on corrosion of 5086 aluminium [43]. It was reported that corrosion rate of this alloy is low except at temperatures around 10°C and 23°C, as shown in Figure 2-9. The authors speculated that the 23°C peak could be related to changes in corrosion products, but the reason for the high corrosion rate at 10°C was not provided and remains unknown.

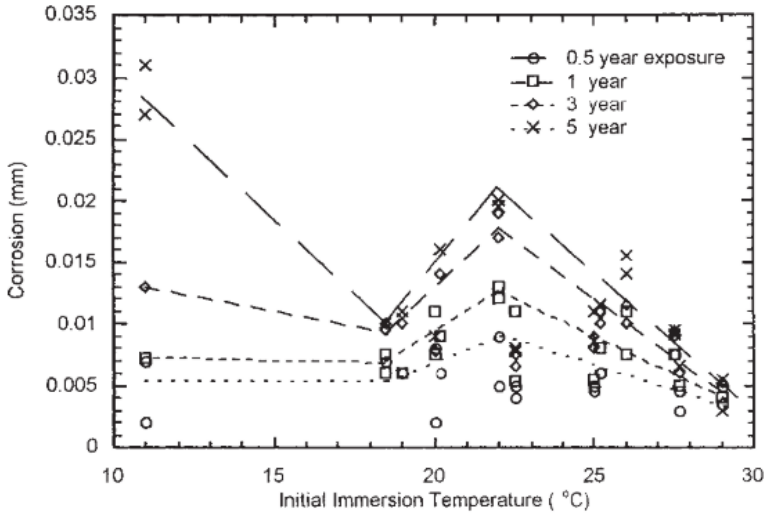

Figure 2-9 Severity of corrosion of 5086 aluminium alloy as a function of initial immersion temperature of natural seawater and exposure time. Taken from [43]***.***

2.2.3 Atmospheric corrosion

Atmospheric corrosion develops under a thin layer of electrolyte or under droplets, therefore the mechanism of this type of corrosion is significantly different from the one under constant immersion conditions. Firstly, during atmospheric exposure, corrosion develops under confined volume of the solution, with an easy access to oxygen. Secondly, atmospheric pollutant deposited on the metals' surface form corrosive salts, especially during alternating wet/dry cycles when the concentration of salts increases as water evaporates.

There are several factors influencing atmospheric corrosion of aluminium. Firstly, ionic (mainly SO_2 and Cl^-) as well as solid (for example dust) contaminations were found to be detrimental for corrosion performance of this metal. Secondly, it was observed that in unpolluted air, there is a certain threshold value for relative humidity (RH) of 70% under which, corrosion does not develop, due to insufficient moisture level.

Droplet spreading is a common phenomenon observed in atmospheric corrosion of metals. It has been observed on zinc [44–47], copper [48–50] steel [46,51] and aluminium [52,53]. It occurs due to the formation of cathodic areas near the edge of the droplet, where the thickness of the water layer is smallest and thus oxygen diffusion is easiest. Alkaline conditions, resulting from the cathodic reactions, lead to dissolution of the passive film and a change in the interfacial energy. This creates a pH gradient within the droplet, leading to a change in interfacial energy between the metal and the electrolyte, resulting in the droplet spreading [48].

Different methods were used to study atmospheric corrosion of aluminium and its alloys, such as: field exposure tests [54,55], salt spray tests [56], droplet tests at constant RH [57] and constant dew point corrosion tests [58,59]. Results of these

studies revealed that aluminium demonstrates high resistance to atmospheric corrosion and its average corrosion rate is less than 1 µm/year [59].

Different techniques were utilised to identify corrosion products formed on aluminium surface, for example x-ray diffraction (XRD) and Raman spectroscopy. Some examples of corrosion products found on aluminium are shown in Table 2-2.

Table 2-2 Corrosion products found on corroded aluminium. Taken from [60]

Type	Substance	Formula
Oxides and hydroxides	Aluminium oxide	γ-Al_2 O_3
	Akdalaite	Al_2O_3 ·¼H_2O
	Boehmite	γ-AlOOH
	Gibbsite	$Al(OH)_3$
	Bayerite	$Al(OH)_3$
	Tucanite	Al(OH)3 ·½H_2O
Sulphates	Aluminium sulphate hydrate	Al_x $(SO4)_y$ ·$(H_2O)_z$
	Aluminium sulphate	$Al_2(SO_4)_3$ ·4H_2O
	Aluminium sulphate	$Al_2(SO_4)_3$ ·5H_2 O
	Aluminium sulphate	$Al_2(SO_4)_3$ ·16H_2O
	Jurbanite	$Al(SO_4)(OH)$·5H_2O
	Aluminite	$Al_2(SO_4)(OH)_4$·7H_2O
	-	$Al_3(SO_4)_2(OH)_5$·9H_2O
	Mendozite	$NaAl(SO_4)_2$ ·11H_2 O
Chlorides	Aluminium chloride	$AlCl_3$
	Cadwaladerite	$AlCl(OH)_2$·4H_2O
	Lesukite	$Al_2Cl(OH)_5$ ·2H_2O
Carbonates	Dawsonite	$NaAlCO_3$ $(OH)_2$

2.3 Sacrificial Coatings

Metallic coatings (which are more active than steel) such as Al, Zn, and their alloys (Figure 2-10), supply cathodic protection to the substrate by working as a sacrificial anode. When Al (or Zn) and steel are coupled together and exposed to seawater, a galvanic couple is established between those two metals, and electrons flow from the coating (anode) towards the substrate (cathode), which is accompanied by the dissolution of the coating, as schematically shown in Figure 2-11. When steel is

cathodically protected, calcareous matter deposits on its surface (due to local pH changes explained in Section 2.5.5.1), which decrease the cathodic protection (CP) demand.

Although Al coatings show good resistance to mechanical damage, they can be subjected to damage during transportantion and assembly of the offshore structure. Therefore, the sacrificial nature of the coatings is of paramount importance.

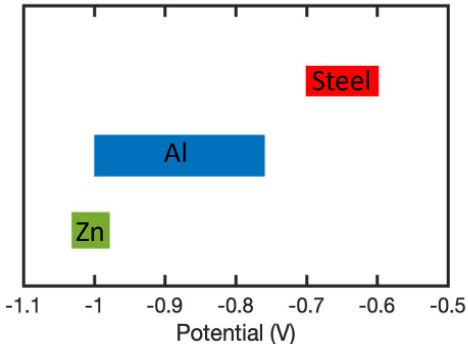

Figure 2-10 Galvanic series in seawater showing corrosion potential of steel, Al, Zn and their alloys. All values are against saturated calomel electrode (SCE).

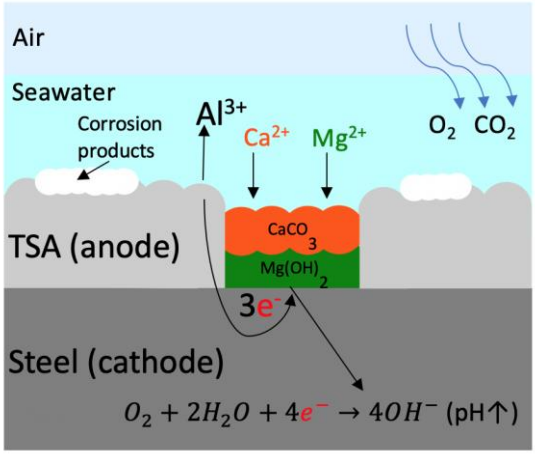

Figure 2-11 Sacrificial protection mechanisms provided by Al coatings.

There are two key factors that determine the performance of sacrificial coatings: low self-corrosion rate and current output enabling the polarisation of the steel in the protective regime, usually considered to be between −0.8 and −1.1 V

(Ag/AgCl/seawater) [39]. Values more negative than −1.1 V are generally not recommended to avoid excessive hydrogen generation.

There are many advantages of sacrificial metallic coatings:

- Barrier properties combined with cathodic protection.
- Newly applied coatings can be handled immediately (i.e., no drying time) [61].
- Spraying and repair can be performed on-site.
- More economical over the lifetime than organic coatings (total life cycle cost).

2.4 Thermal spraying

Though there are several thermal spray processes that can be used for the preparation of coatings, only two of them are commonly used for the deposition of sacrificial metallic coatings, namely electric arc and flame spray. Both involve propelling molten or semi-molten metal particles towards the substrate by a stream of air, thus creating a layer-by-layer deposition, until the required thickness of the coating is achieved. In contrast to other techniques, the two spraying processes indicated above can be performed on-site and are economical.

2.4.1 Electric Arc Spraying

This technique, also known as twin wire arc or wire arc spray, is based on melting the tips of two metallic wires with an electric arc, which is established between them through the application of direct current (DC). Molten particles are then accelerated and propelled towards the substrate via an air stream. More information about the process can be found elsewhere: [62–64]. A cross-section of a typical arc-sprayed aluminium coating on steel is shown in Figure 2-12.

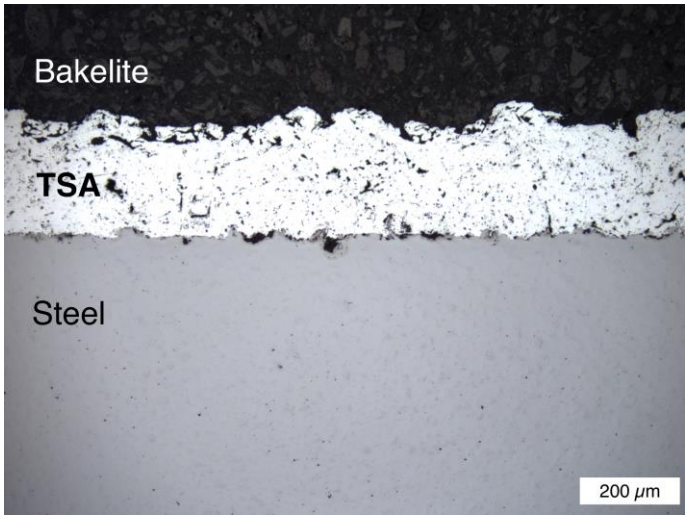

Figure 2-12 Cross-section of arc-sprayed Al coating on steel.

2.4.2 Wire Flame Spraying

In this technique, a metallic wire is melted by a flame, and the molten particles are accelerated towards the workpiece by pressurised air. More details can be found elsewhere: [65,66].

2.5 Laboratory Tests

Corrosion protection that is provided by thermally-sprayed aluminium coatings has been a subject of many investigations during the past three decades. Attempts have been made to understand the mechanisms and parameters that influence the performance of the coatings by using different methods. The most notable findings are reviewed below.

2.5.1 Effect of the Spraying Method and its Parameters

A comparison between TSA coatings that are deposited by using electric arc (EA) and flame spraying (FS) was conducted by several researchers. Rodriguez et al. [67] observed differences in the oxide layers of coatings that were deposited by using arc and flame spraying through the use X-ray photoelectron spectroscopy (XPS). They

also detected the different corrosion products that were formed on those coatings after a 4000-hour saline mist test: bayerite in the FS process and boehmite in the coating that was deposited by EA. Gartland and Eggen [68] concluded, based on their lab and field tests on TSA that was prepared by using both methods, that the spraying method had little influence on the performance of the coating, but the arc-sprayed coatings exhibited better adhesion (arc-sprayed Al: 9.0 ± 1 MPa, flame-sprayed Al: 3.5 ± 0.34 MPa). A higher adhesion of arc-sprayed coatings was also reported by others [69,70]. Moreover, coatings that are prepared by flame spraying tend to exhibit a higher level of porosity in comparison to the ones that are prepared by arc-spraying [64]. Porosity is an inevitable characteristic feature of thermally-sprayed coatings, but its level can be altered by selecting appropriate feedstock material, application method, and spraying parameters. To obtain a less porous coating, oxyfuel flame spraying and small diameter wire (1.6 and 2.3 mm), or low current (100–200 A) arc spraying should be used [64]. It has also been estimated that arc-spraying is more economical [64].

2.5.2 Effect of Coating Thickness

The effect of TSA coating thickness on corrosion performance was studied by Han et al. [6] using electrochemical methods. They used stainless steel STS 304 steel substrates. Several experiments were performed, and their data were presented in the paper. However, based on the presented results, meaningful conclusions could not be drawn.

The results of the mechanical testing of arc-sprayed Al coatings (222–397 µm) on mild steel showed that the adhesion strength of the coatings increased with the coating thickness [71]. However, even the 222 µm coating showed a very good adhesion strength of 10.74 MPa. The minimal required adhesion strength of TS aluminium

coatings varies across different standards from 4.5 to 10.3 MPa, as shown in Table 2-3.

However, laboratory tests that were performed by Thomason et al. [72] on flame - sprayed Al coatings revealed that a high coating thickness (~400–450 μm) may lead to the development of blisters, especially in an aggressive splash zone environment. It was suggested that residual stresses are higher in thick coatings. A similar correlation between the coating thickness and the tendency to develop blisters was also reported in a 19-year study conducted by the American Welding Society [73]. In order to provide a sufficient level of protection for the whole service life of a structure, the coating must not be too thin. The corrosion rates of TSA in saltwater environments that have been reported in the literature (Table 2-4) - although estimated by using different experimental methods, exposure periods and temperatures - suggest that the dissolution of the coating in seawater is probably less than 20 μm per year. This indicates a minimum coating thickness of 200 μm for 10 years exposure. The AWS C.2 18–93 standard recommends thickness between 200 and 350 μm for seawater immersion.

Table 2-3 Adhesion strength specifications for thermally-sprayed aluminium coatings in key standards.

Standard	Min. adhesion strength [MPa]
ISO 2063	4.5
SSPC-CS 23.00/AWS C2.23M/NACE No. 12	6.89
NORSOK M-501	9
AWS C2.18-93	10.3

2.5.3 Effect of Coating Composition

The most commonly used alloys for the preparation of thermally-sprayed Al coatings for the corrosion protection of steel are Al 1050 (99.5% Al) and Al–5%Mg, as can be

seen from Table 2-4. ISO 2063-1 and NORSOK M-501 also recommend those alloys. The required compositions of relevant wires provided in AWS C2.25 and ISO 14919 are shown in Table 2-5.

Table 2-4 Corrosion rates of Al-coatings in simulated seawater environments.

Coating consumable	Spraying method	Substrate	Electrolyte	Temperature [°C]	Duration	Method	Corrosion Rate [µm/year]	Ref.
Al 99.5%	Electric arc	22%Cr Duplex stainless steel	Artificial seawater	18 ± 2 80 ± 2	25 days	Linear polarisation resistance (LPR)	5–8 6–7	[7]
Al 99.5%	Electric arc	glass	Artificial seawater	25 50 100	22 days	LPR	0.2–1.5	[74]
Al 99.6% AlMg5%	Electric arc and flame	Steel	Natural seawater	6.5–11	11 months	LPR Polarisation curves	~3.3 (Al arc) ~2.4 (AlMg arc) 2.0–2.7 (Al flame) ~3.2 (AlMg flame)	[68]
Al 99.5%	Electric arc	Carbon Steel	Natural Seawater	10 ± 2	30 days	Polarisation resistance Polarisation curves	20	[75]
Al 99.0%	Electric arc	Mild steel	3.5% NaCl	Room	44 days	Tafel Electrochemical impedance spectroscopy (EIS)	Not given	[76]
AlMg5%	Electric arc	Carbon steel	Natural seawater	20 50 70 90 (internal temp)	280 days 280 days 60 days 280 days	Polarisation curves LPR	~1.0 ~2.2 ~4.0 ~4.8	[76]
Al 1100	Electric arc	Carbon steel	Natural seawater	10 50 70	(1)230 days (2)250 days	LPR (1) Polarisation curves (2)	7 and 5 6 and 5 16 and 8	[77]
Al 99.7%	Electric arc	Stainless steel (SS)	Natural seawater	Room	24 hours	Polarisation curves	Not given	[6]
Al 99.5%	Electric arc	Carbon steel	Artificial seawater	25 ± 1	32 days	LPR	Not given	[9]
Al 99.5%	Electric arc	Carbon steel	Artificial seawater	26 ± 1	90 days	LPR	<20	[10]
Al 99.99%	Electric arc	Mild steel	3.5% NaCl	26–28	264 h	Polarisation curves EIS	Not given	[11]

Al Al–Al_2O_3	Electric arc and Plasma spray	SS 316L	Artificial seawater	30	30 days	Polarisation curves EIS	Not given	[78]
Commercially available Al powder	Cold spray	Mild steel	3.5% NaCl	Room temperature	96 h	Polarisation curves EIS	Not given	[79]
Al–Al_2O_3	Cold spray	Mild carbon steel	0.01%NaCl 0.1%NaCl 1%NaCl	80	21 days	Mass change	~0.04 ~0.05 ~0.06	[80]
Al 99.5%	Electric arc	Carbon steel	Artificial seawater	5 ~101.5	50 days	LPR	5–7	[81]
Al 99.5%	Electric arc	SS404L	3.5% NaCl	Ambient temperature	0 h 500 h 1000 h	Tafel analysis	17.1 0.1 0.2	[82]

Table 2-5 Composition of wire feedstock reported in relevant codes and standards.

	Element (wt%)											
	UNS	**Common Name**	**Al**	**Cr**	**Cu**	**Fe**	**Mn**	**Si**	**Ti**	**Zn**	**Mg**	**Other**
AWS C2.25	A91100	Al (1100)	99.00 min	-	0.05–0.20	0.95 (Fe and Si)	0.05	0.95 (Fe and Si)	-	0.10	-	-
	A91350	Al (1350)	99.50 min	0.01	0.05	0.40	0.01	0.10	0.02 (V+Ti)	-		GaB (0.03-0.05)
	A95356	Al–5Mg	Rem.	0.05–0.20	0.10	0.40	0.05–0.20	0.25	0.06–0.20	0.10	4.5–5.5	
	A71001	Al MMC	88 min	-	-	-	-	-	-	-		Al_2O_3 (8–12)
ISO 14919	Not provided	Al 99.5	99.5 min	-	≤0.02	≤0.40	≤0.02	≤0.25	≤0.02	≤0.07		≤0.03
		Al–5Mg	Rem.	0.05–0.2	≤0.10	≤0.40	0.05–0.20	≤0.30	0.06–0.20	≤0.10	4.5–5.6	≤0.15

Pure aluminium shows excellent corrosion resistance due to its passive nature. When exposed to an oxidising environment (e.g. air and water), a continuous and uniform natural oxide film (Al_2O_3) develops on the metal's surface, which works as an electrical insulator. It prevents the movement of electrons (produced during the anodic dissolution of the metal) from the metal to the oxide/solution interface, which results in the inhibition of cathodic reactions.

Mg, when added in small amounts, improves the mechanical properties of solid Al, but it does not decrease its corrosion performance. However, alloys containing 3% Mg or more are susceptible to the precipitation of intermetallic particles (Al_3Mg_2) at the grain boundaries when exposed to elevated temperatures for a longer period of time [83]. Those particles are anodic in relation to the Al matrix and corrode preferentially, leading to intergranular corrosion and stress corrosion cracking [83]. In the case of thermally-sprayed Al, Morakul et al. [84], who tested Al–2%Mg and Al–5%Mg in 3.5% NaCl at 25°C, reported a lower corrosion resistance and a shorter fatigue life of the coating with a higher Mg concentration. Park and Kim [85] observed higher corrosion potentials of Al-Mg coatings (Al–3%Mg and Al–5%Mg) than that of pure Al coating in natural seawater at room temperature. At elevated temperatures, thermally-sprayed Al–5%Mg coatings with and without external CP were tested by Wilson et al. [86], who observed coating degradation (thickness reduction) at higher temperatures. They suggested chemical dissolution as a possible degradation mechanism. Moreover, one of the samples that was exposed to 90°C (internal temperature of the pipe) exhibited blistering.

In 2017, Quale et al. [75] tested a thermally-sprayed sacrificial coating comprised of Al, Zn and In, based on the assumption that the addition of Zn and In to aluminium

prevents its passivation. The results of the tests revealed that the open circuit potential (OCP) of the freely corroding Al–Zn–In coating reached -1000 mV (Ag/AgCl) after 60 days in natural seawater and was 65 mV more negative than the Al (99.5%) coating. The difference was even more pronounced after 235 days when the coatings were coupled to carbon steel in a 10:1 ratio and the Al–Zn–In coating reached −972 mV, whereas the Al coating stabilised at −803 mV. It was concluded that the Al–Zn–In coating provides better protection than a conventional TSA coating due to its better CP efficiency. Moreover, the Al–Zn–In coating can be used in conjunction with conventional anodes with minimal current drain. It was also noticed that thermal spraying leads to a reduction of Zn content in the deposited coating.

In 2019, Adamiak et al. [87] tested arc-sprayed Al coatings with and without NiAl-buffered sub-coating on armour-grade steel. They observed that the use of the sub-coating increases adhesion and improves erosion wear resistance of the Al layer.

2.5.4 Effect of Sealing

As shown by Lee et al. [11], corrosion products that form on Al-coated steel enhance the barrier properties of the coating by blocking the pores and cracks inside the coating. However, during the initial immersion, when corrosion deposits are not yet present, the dissolution of the Al coating can be relatively high. Moreover, if the coated structure is stored in a humid environment before being placed in service, rust staining may occur [61].

To prolong the lifetime of TSA coatings and prevent the development of discoloured areas, suitable sealant systems can be applied. Sealants are designed to penetrate and fill the surface-connected porosity, suppressing the diffusion of corrosive molecules from the environment through the coating.

Organic sealants are comprised of epoxies, phenolics, furans, polymethacrylates, silicones, polyesters, polyurethanes, and polyvinyl esters. For TSA, aluminium-filled vinyl and silicone have been used [88]. In accordance with the NORSOK M-501 standard [89], for low-temperature operations (below 120 °C), two-component epoxy should be used, whereas for high-temperature applications (above 120 °C), aluminium silicone should be used. Information on organic materials that are compatible with TSA is provided in ISO 1244-5. ISO 2063 and AWS C2.23 mention that the thickness of sealants should not exceed 40 μm. López-Ortega et al. [4,90] conducted a series of experiments in which arc-sprayed aluminium with an organic topcoat (epoxydic paint [91]) on high strength low alloy steel R4 grade was studied. Based on weathering aging tests in different climatic cabinets, as well as immersion tests and tribocorrosion tests in artificial seawater, it was concluded that this duplex system exhibits good corrosion and tribocorrosion properties. The same group [91] also studied a functionalised topcoat system containing 25% wt of SiO_2 and a 1.5 wt% Cu_2O (to obtain superhydrophobicity and antibacterial characteristics) on a TSA coating that was modified by plasma electrolytic oxidation (PEO). The use of PEO on TSA was previously reported to be a promising technique for improved corrosion and wear resistance [92,93]. The effect of an epoxy sealant applied on an arc-sprayed Al coating by using a cathode electrophoresis method was investigated by Pang et al. [94] and compared with sealing by using boiling water. After immersion in 3.5% NaCl at 40°C for seven days, it was observed that the thickness of epoxy-sealed TSA was unchanged but the thickness of the TSA that was sealed by using boiling water decreased from 100 to 40 μm.

Other inorganic sealing methods that have been investigated to enhance the behaviour of thermally-sprayed coatings have involved the thermal diffusion of Zn [95], the use of phosphate-containing salts that chemically react with Al [96], calcium nitrate [97], hydrothermal treatment in boiling deionised (DI) water [98], and the sol–gel method [99]. The use of glass powders to seal porosity in an arc-sprayed aluminium coating was also investigated [100].

The reduced porosity level of an arc-sprayed aluminium coating was also achieved by Wenming et al., who used a CO_2 laser to re-melt the coating [101]. They also noticed that the re-melting of the coating changed the way the coating adhered to the substrate from mechanical to metallurgical bonding.

Though the use of sealants can significantly improve the performance of TSA, it should be noted that there have been some examples where sealed coatings developed blisters (Hutton tension leg platform [102]) or failed prematurely (Heidrun platform [72]). The degradation mechanisms of painted TSA was studied first by Knudsen [103] and later by Sumon et al. [104]. Knudsen attributed the accelerated degradation of TSA to the development of an acidic environment underneath the paint. His work focused on the scenarios where TSA/organic system was either in electrical contact with bare steel or contained a defect. Sumon et al. tested several organic coatings on TSA (with and without a scribe) and bare steel by using salt spray exposure. They observed organic coating delamination on TSA-coated samples, not only on scribed samples but also on intact ones due to the diffusion of water and chloride ions through the epoxy layer. The proposed organic coating disbonding mechanisms included the development of voluminous corrosion products lifting the organic layer, anodic undermining, and cathodic disbonding.

2.5.4.1 Graphene-reinforced epoxy

Graphene is a single layer of carbon atoms. It has attracted a lot of attention in the scientific community due to its extraordinary mechanical, optical, electronic and chemical properties. It has been reported that the addition of graphene nanoplatelets (GNP) into a polymer coating can improve its anticorrosion properties by enhancing the barrier properties of the polymer [105]. Due to its large surface area and impermeability to almost all molecules and gases, the presence of GNP creates a tortuous diffusion pathway for corrosive species. This is schematically shown in Figure 2-13.

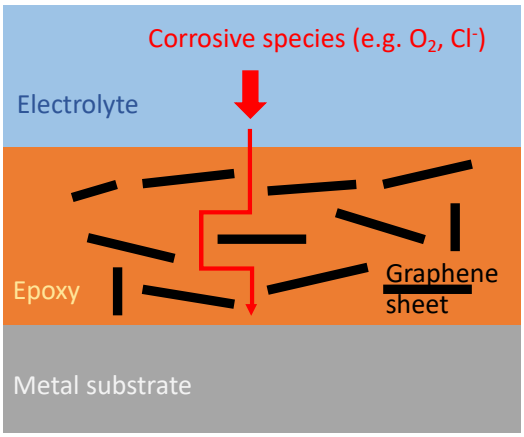

Figure 2-13 Schematic representation of the role of graphene sheets dispersed in epoxy coatings for corrosion protection of metals.

It has been also observed that the addition of GNP can improve mechanical properties of the epoxy coating [106]. However, it was also reported that in order to obtain the improved properties of the epoxy/graphene composite, only a small amount of the platelets should be added to the epoxy matrix [105,107,108]. For example, Wei et al. reported the best dispersion of graphene in the epoxy matrix with graphene concentration of 0.3 wt% [106]. Higher loading led to nonuniform dispersion within the epoxy matrix and agglomerates formation. The agglomeration of the graphene

platelets at higher graphene loadings is caused by the large surface area producing stronger van der Waals forces (electrostatic forces that attract molecules to one another) and π- π interactions (interactions between aromatic rings) [109].

It has also been observed that the addition of graphene changes the wettability of the epoxy coating. It can be seen from the data generated by Abakah et al. [110] (Figure 2-14) that the addition of different graphene nanoparticles led to the increased contact angles indicating hydrophobic properties of the different graphene nanoparticles.

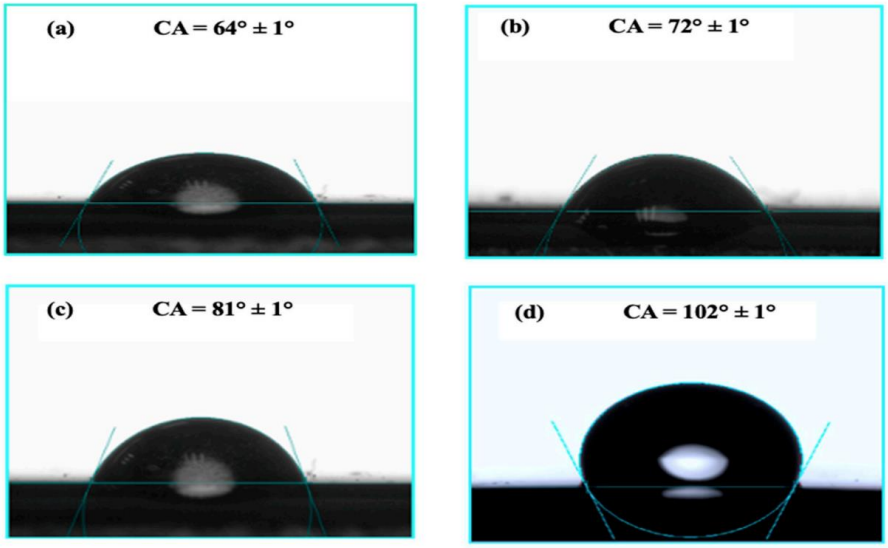

Figure 2-14 Surface contact angles of (a) neat epoxy, (b) epoxy loaded with X50 graphene nanoparticles, (c) epoxy loaded with M15 graphene nanoparticles and (d) epoxy loaded with C750 graphene nanoparticles. Taken from [110].

2.5.5 Effect of Temperature

It has been shown that the corrosion rate of TSA increases with temperature and that the initial corrosion rate decreases with the immersion time [8,86]. This may be due to corrosion product formation. Moreover, it has been reported that temperature influences precipitation of different corrosion products on the coating. Ce and Paul reported formation of $Al(OH)_3$ at 30°C and κ-Al_2O_3 at 60°C [111]. They also observed a difference in local pH evolution near the TSA coating during corrosion in seawater.

The pH increased with time at 60°C (to the value between 7 and 8.5), whereas the opposite behaviour occurred at 30°C (decreased to pH 4.76).

Tests that were performed by Dexter [37] on aluminium metal in seawater revealed an ennoblement of the potential with temperature decrease. A similar trend should be expected for sprayed aluminium. If the potential of a coating is less negative at lower temperatures, its ability to provide cathodic protection (when coating gets damaged) is probably lower, too. However, information about the performance of TSA in cold seawater is scarce.

2.5.5.1 Calcareous deposits

As mentioned in previous sections, when an aluminium coating gets damaged and the steel is in direct contact with an electrolyte, a galvanic couple is established between the coating and the substrate due to the potential difference between those two metals. Since Al exhibits more active potential than steel in seawater, it undergoes dissolution in accordance with Equation 2-4.

Electrons that are produced during the above reaction are consumed at the steel (cathode) according to Equation 2-2 and Equation 2-3. The production of OH^- ions during cathodic reactions causes an increase in the pH of the solution in the vicinity of the cathode, which triggers the precipitation of calcareous matter: $CaCO_3$ and $Mg(OH)_2$, in accordance with the following equations:

$$\mathbf{Mg^{2+} + 2OH^- \rightleftharpoons Mg(OH)_2} \qquad \text{Equation 2-8}$$

$$\mathbf{Ca^{2+} + CO_3^{2-} \rightleftharpoons CaCO_3} \qquad \text{Equation 2-9}$$

The effect of temperature on the formation of calcareous deposits under constant cathodic polarisation provided by the potentiostat has been studied by several authors. It has been shown that the formation rate of Ca-rich deposits on cathodically polarised

steel decreases with decreasing temperature [112–114]. This has been attributed to the increased solubility and lower kinetic parameter of $CaCO_3$ in cold seawater [112,113]. Moreover, it has been observed that at low temperatures (<10°C) the predominant $CaCO_3$ phase is calcite, whereas at higher temperatures aragonite dominates. The difference has been attributed to the inhibitive properties of Mg^{2+} ions, which inhibit both nucleation and growth of calcite but only nucleation of aragonite. Moreover, it has been observed that deposits formed at low temperatures (< 10°C) provide little protection towards the steel substrate and they are Mg rich [115,116]. This has been related to the higher interface pH at a given potential at low temperature [116] and lower solubility of $Mg(OH)_2$ at low temperatures [115], as can be seen from Figure 2-15.

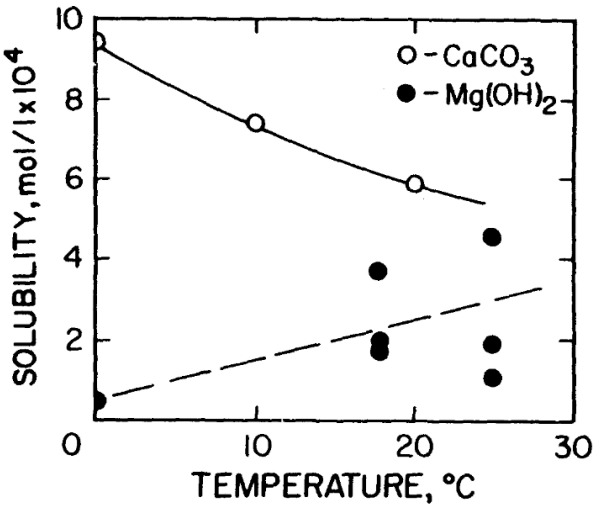

Figure 2-15 Solubility limit of $Mg(OH)_2$ and $CaCO_3$ in water as a function of temperature. Figure taken from [115]***.***

Furthermore, it has been also noticed that the stability of the calcareous deposits changes with temperature. Lin and Dexter [116] measured the evolution of the current density during potentiostatic polarisation of steel in seawater and observed its increase

when the temperature of the solution was decreased from 25 to 3°C. This can be seen from Figure 2-16. The authors suggested the dissolution of $CaCO_3$ at 3°C.

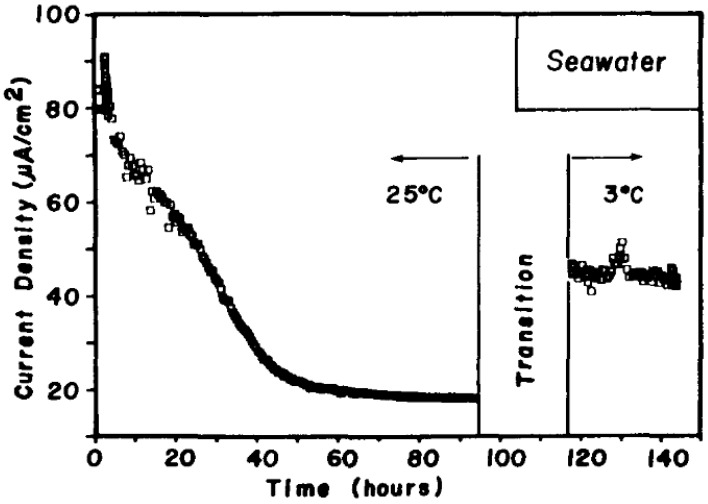

Figure 2-16 Evolution of the current density during potentiostatic polarisation of steel to - 0.906 V_{SCE} during immersion in seawater. The temperature of seawater was initially 25℃ and then was changed to 3℃. Figure taken from [116]**.**

However, it has been also shown, that the effect of temperature on the precipitation rate and composition of the calcareous layer depends also on the applied potential. Barchiche et al. [117] reported a faster precipitation rate of deposits at 30°C than at 20 and 10°C when -1 V (vs SCE) was applied. Furthermore, they only detected aragonite at those temperatures and the applied potential. Under more cathodic polarisation (- 1.2 V (vs SCE)), however, the effect of temperature was not apparent and both brucite and aragonite were identified.

Studies performed on calcareous matter formed under cathodic protection provided by TSA coatings at various seawater temperatures (5, 26, 30, 60°C) revealed the presence of double-layered deposits consisting of an Mg-rich inner layer and a Ca-rich outer layer [10,81,111,118]. However, it has been observed that in boiling seawater $CaCO_3$ does not precipitate [119]. The development of calcareous layers on exposed steel is important in the context of the cathodic protection provided by TSA coatings

because the deposits impede oxygen diffusion to the steel surface and reduce the rate of dissolution of aluminium. Even though the formation of calcareous deposits is relatively well understood under constant applied potential conditions, it should be highlighted that the potential of aluminium changes with the immersion time. It is also sensitive to temperature. Therefore, more research is needed to understand the influence of temperature on the formation of calcareous layers in damaged TSA coatings.

2.5.6 Effect of Oxygen

Eighteen-day lab-based experiments [118] that were conducted in aerated and deaerated artificial seawater at 25 °C on TSA with 3% holiday showed that under deaerated conditions, the corrosion rate of TSA coatings is lower and calcareous deposits that are formed consist mainly of brucite ($Mg(OH)_2$).

The effect of oxygen on the galvanic corrosion of aluminium–steel couple in an NaCl solution was studied by Pryor and Keir [120]. They noticed that at pH lower than 4 and higher than 10, the galvanic current flow and mass change of Al were independent of the dissolved oxygen concentration, which was attributed to the main cathodic reaction being the reduction of water leading to the evolution of the hydrogen gas. Within the 4–10 pH range, however, dissolved oxygen had a strong effect on the galvanic corrosion. The saturation of the solution with oxygen resulted in an increase in galvanic current, whereas deaeration caused a decrease of the current to nearly zero.

2.6 Long-Term Field Studies

TSA coatings have proven to be an effective corrosion mitigation control for steel during several long-term field studies that were performed in the past three decades. The most notable ones are summarised in the Table 2-6.

Table 2-6 Long-term field tests involving testing of thermally-sprayed aluminium (TSA) coatings.

Name/ organisation	Exposure time	Exposure type	Coating material	Coating thickness	Spraying method	Sealed	Holiday/artificial defect	Findings	Ref.
BISRA	12 years	Atmospheric (rural, coastal industrial) Seawater immersion	Zn, Al, Cd, Pb, Sb	3–4 mils	Thermal Spraying (type not specified), electroplating, and hot dipping.	No	No	Life of the coating roughly proportional to the coating thickness regardless of the application process.	[121] [122]
LaQue Centre	12 years extended to 34 years	Atmospheric (marine and industrial)	Powders of various compositions of Zn, Al, Zn and Al Zn and Al and Mg Mn, Al and Mg	0.08–0.2mm	Powder flame spraying	No	No	Al-based coatings performed better than Zn-based ones in industrial atmospheres but worse in marine atmospheres after 12 years exposure. There were more resistant coatings with high Al content than Zn after longer (34 years) exposure in marine atmosphere.	[121] [123]
AWS	19 years	Atmospheric and immersion	Zn, Al	80–460 µm	Wire flame spraying	Wash primer, clear vinyl, Al-pigmented vinyl, Chlorinated rubber	No	80–150 um TSA coatings with and without sealing protect steel in seawater and in atmosphere. The coating that gave the best performance was a thin TSA. It exhibited the lowest level of pitting and blistering.	[73]
JACC	18 years	Atmospheric, immersion	Zn, Al, Zn–Al	175 ± 25 µm (flame and arc-sprayed coating) 400 ± 25 µm only for Al (arc-sprayed)	Wire flame and electric arc spraying	Epoxy	No	TSA not effective in splash zone when there is a damage in the coating.	[121]
PATINA project	3.5 years	Atmospheric	Al, Zn, Zn–Al	150 µm	Flame spraying (type not specified)	No	Yes	TSA only effective in atmosphere with high chloride content.	[124]
the Corrosion Advice Bureau of BISRA	10 years	Atmospheric, immersion	Al, Zn, Zn and Al	50,100,150 µm	Wire and powder spraying (exact method not specified)	Variety of paints and topcoats	Yes	Painted TSA can provide 10 years life without maintenance under atmospheric exposures. When damaged, rusting of the substrate occurs under all conditions.	[125]

								Unpainted Zn coatings failed under immersion conditions, whereas unpainted Al coatings provided protection.	
US Army, Buzzard's Bay	20 years	Atmospheric, splash, tidal, immersion in natural seawater	Various organic and metallic coatings	150 µm (TSA without sealant) 80-90 µm sealed	Wire flame spraying	Wash coati primer and Al vinyl	Yes	TSA with sealant was the best performing coating among 24 systems tested Unsealed Al coating failed in atmospheric and splash zones (red rust present).	[126] [102]
US Army, La Costa Island	21 years, results reported after 10 years	Atmospheric, splash, tidal, immersion in natural seawater	Various organic and metallic coatings	150 µm	Wire flame spraying	Vinyl topcoat	Yes	The most severe corrosion in the splash zone.	[126]–[127]

2.7 Laboratory corrosion testing methods

In order to predict the long-term performance of anti-corrosive coatings, long-term field testing is the most reliable approach; however, these are expensive and require long-term access to marine test sites. Short laboratory testing can give some indication and insight into the mechanisms that dictate the protectiveness of the system. The most common lab-based testing methods involve salt spray tests and electrochemical measurements, such as monitoring of the open circuit potential (OCP) and electrochemical impedance spectroscopy (EIS), during immersion tests. In order to estimate the rate of corrosion of the coatings, several methods have been employed by different researchers, such as linear polarisation resistance (LPR), polarisation curves, and mass change, as shown in Table 2-4.

Unfortunately, all of the above methods have some limitations. For example, the LPR method is not applicable when a non-conductive sealant or paint is used. Moreover, this technique should be used when the system undergoes general corrosion, whereas Al is known to suffer from localised corrosion in aqueous solutions containing Cl^- ions. Additionally, it should be mentioned that if the samples contain defects, the use of polarisation curves is not accurate, because anodic and cathodic polarization curves reflect reactions that occur on both metals simultaneously. Therefore, the Tafel slopes (which are needed to calculate corrosion rates) that are obtained from those curves are not accurate.

EIS is a powerful technique that is especially useful for studying coatings. However, the selection of appropriate equivalent electrical circuit that explains the mechanism occurring in the system can be very difficult, especially in case of porous coatings,

such as TSA. Nonetheless, some researchers have done EIS modelling to understand the corrosion behaviour of sacrificial coatings [12,78,79,128–131].

The common industrial practice of the monitoring of corrosion based on salt spray testing and visual examination has its limitations, particularly for long-term prediction of performance.

The estimation of corrosion rates based on the mass change of the samples is not applicable to thermally-sprayed coatings due to their porous nature. Corrosion products form on the coating, fill the pores, and are not possible to remove. Therefore, the mass of the corroded samples is changed due to both the dissolution of the coating and the corrosion products that get trapped inside it.

2.8 In-Service performance of Al coatings

One of the earliest applications of TSA coatings for the corrosion protection of an offshore structure was the Hutton tension leg platform (TLP) which was installed in 1984 in the North Sea [132] TSA was applied on risers and tethers and flare boom. The risers were connected to the TLP hull (protected by an impressed current CP) and a subsea template (connected to sacrificial anodes). In 1986 one of the tethers was removed for inspection, and one of the risers was removed in the following year. The inspections revealed the presence of blisters on the coating that was applied on tethers (with vinyl sealer), and no signs of the degradation of the coating were observed on the risers (with silicone sealer). Apart from the blisters, TSA was in very good condition even after 12 years in service [72]. The possible reasons for the development of the blisters were related to the vinyl sealer, which either reacted with TSA or did not penetrate the coating.

In the Norwegian offshore sectors, TSA (mainly Al–5%Mg) has been used for the protection of several offshore structures (e.g., Shell Draugen field, Sleipner riser platform, Troll Gas, Heidrun field, Heimdal platform). By 1997, approximately 400,000 m^2 of steel was protected using TSA coatings. The most common areas that were protected by the TSA coatings include flare booms, crane booms, pipes, under cellar decks, vessels under thermal insulation, and burner booms [133]. An excellent performance of TSA with aluminium silicone paint on the Heimdal platform was reported after 10 years in service. However, a premature degradation of TSA was observed on the Sleipner platform (after seven years in service) as well as on Jotun B. In both cases, TSA coatings were applied as duplex systems consisting of sprayed aluminium and a thick overcoat [134]. A similar problem occurred on a gas platform near East Timor in Australia, where TSA failed after one year in service [135].

Another example where TSA did not provide adequate protection was the Heindrun TLP installed in 1995 in the Norwegian North Sea. After less than four years in service, a serious damage of the TSA coating (supported by CP from sacrificial anodes) with silicone sealer was observed on two oil export risers and one gas export riser operating in the splash zone. Further lab-based studies that were conducted to identify possible reasons for the TSA failure on the Heindrun risers revealed that the tendency of blistering increases with increase of coating thickness and the rise of pipe temperature. It was also observed that blistering can be mitigated by using a silicone sealer [72].

A very good performance of sealed TSA coatings that were applied on risers connected to sacrificial anodes was reported on the Jolliet tension leg platform operating in the Gulf of Mexico for 13 years [72].

TSA with organic topcoats was also used for the protection of bridges, such as Nidelv bridge in Trondheim, where the duplex system provided protection to the bridge for 30 years. However, when applied to Tromsø bridge, duplex coating failed after a year or less [133]. Some of the suggested possible factors that might have promoted the development of many blisters in the splash zone region included the insufficient quality of blast-cleaning and insufficient coating thickness [136].

Recently, TSA has been tested for the protection of offshore wind turbines as a part of the Cost Reduction for Offshore Wind Now *(*Crown) project [137]. TSA with epoxy paint as a sealant is also being used for the protection of offshore wind turbines operating in the Baltic Sea as a part of the Arkona project [138].

2.9 Summary

The literature review revealed that TSA has proven its capability to successfully protect steel from corrosion in harsh marine environments when applied properly. The main conclusions that can be drawn from the substantial amount of work that has been devoted to understanding mechanisms and parameters controlling the performance of TSA are as follows:

1. It appears that the most economical spraying technique that is capable of producing coatings with low level of porosity and good adhesion is the electric arc spraying method.

2. Coating thickness is an important parameter that influences performance. The optimal thickness has been reported to be between 150–375 μm. A lower thickness can result in an insufficient amount of aluminium to provide long-term protection to the substrate. An excessive coating thickness may lead to high residual coating stress leading to its premature failure.

3. The application of sealants can prolong the lifetime of the coating. Moreover, it has been suggested that sealing can prevent blistering. However, a low viscosity sealant that flows easily inside the pores without staying on top of the TSA should be used. The application of a thick organic layer on TSA may lead to an accelerated dissolution of the coating. The suggested failure mechanisms include the development of an acidic environment underneath the organic layer, the development of voluminous corrosion products rising the organic coating, anodic undermining, and cathodic disbondment.

4. It is important to differentiate between the self-corrosion of the coatings and how protective they are for steel when the coating is damaged or connected to bare steel. If large area of steel is exposed, the corrosion of TSA can be significantly higher due to the anodic nature of the coating.

5. TSA has mostly been used in offshore structures with some form of CP system in place. Recently, TSA has been applied on offshore wind turbines as a stand-alone corrosion control method. However, no standards that cover the suitability of using TSA as a primary CP system exist.

Chapter 3 Methodology

3.1 Materials

S355 J2G3 carbon steel plates (Parker Steel - Table 3-1) - cut into 40x40x6 mm squares - and glass slides (75x26x1 mm) were used as substrate materials. Glass slides were chosen (based on their poor electrical conductivity) to study the influence of the substrate on the corrosion performance of the coatings. Before spraying, steel and glass slides were degreased with industrial methylated spirit (IMS) and prepared by blasting with 36 mesh alumina abrasive blasting grit to obtain a rough surface to which molten particles can attach onto. After grit blasting, samples were rinsed with IMS and dried using compressed air. The surface treatment processes followed the same procedures as adopted by the industry.

The substrates were then sprayed with AA1050, AA1100, Al-5%Mg and Zn-15%Al (Metallisation Ltd. - Table 3-2) using twin wire arc spraying method (ARC 140 pistol Metallisation Ltd.) to a thickness of approximately 350 μm. The desirable thickness was achieved in multi-pass spraying. Spraying parameters are provided in Table 3-3.

Table 3-1 Chemical composition of steel substrate.

Grade	**Element wt % (mill sheet data)**							
	C	**Si**	**Mn**	**P**	**S**	**V**	**N**	**Fe**
EN10025 S355 J2G3	**0.12**	**0.390**	**1.39**	**0.14**	**0.019**	**0.065**	**0.003**	**balance**

Table 3-2 Chemical composition of wires used for spraying and electrochemical tests

Element wt% Material	Si	Fe	Cu	Mn	Mg	Zn	Ti	Ni	Cr	Pb	Sn	Zr	Al
1050 Al wire	0.07	0.21	<0.01	<0.01	0.000	0.000	0.000	<0.01	-	<0.01	<0.01	-	Bal.
1100 Al wire	0.06	0.18	0.19	<0.01	<0.01	<0.01	0.01	0.01	-	<0.01	<0.01		
Al-5%Mg wire	0.11	0.13	<0.01	0.12	4.94	0.16	0.08	<0.01	0.11	0.01	0.02	<0.01	Bal.
Zn-15%Al wire	0.10	0.01	<0.01	<0.01	<0.01	Bal.	<0.01	<0.01	<0.01	0.02	0.01	<0.01	13.2

Table 3-3 Spraying parameters.

	Wire size [mm]	Air pressure [bar]	Stand-off [mm]	Increment step [mm]	Horizontal traverse [mm/s]	Current [Amps]	Spraying Angle [°]
TSA on steel	2.3	5	125	10	400	200	90
TSA on glass	2.3	5	300	10	500	200	90
TSZ on steel	2.3	5.5	125	8	400	160	90
TSZ on glass	2.3	5.5	130	8	400	160	90

3.2 Experimental procedure

3.2.1 Full immersion experiments

3.2.1.1 Samples preparation

a) Al wires and bare steel

Before electrochemical testing, S355 steel coupons (Parker Steel - Table 3-1) and 1050 Al wires (Metallisation Ltd - Table 3-2) were ground with 1200P SiC paper, washed with IMS, and allowed to passivate in air for 1 h.

b) TSA-coated steel

An electrical connection between the steel samples and the potentiostat was obtained via a threaded rod (insulated with heat-shrink tubing) and between glass samples via copper tape. The rods, copper tape and the back and sides of the samples were

covered with 3 layers of stop-off lacquer Type 45 (MacDermid plc, Birmingham, UK) as shown in Figure 3-1.

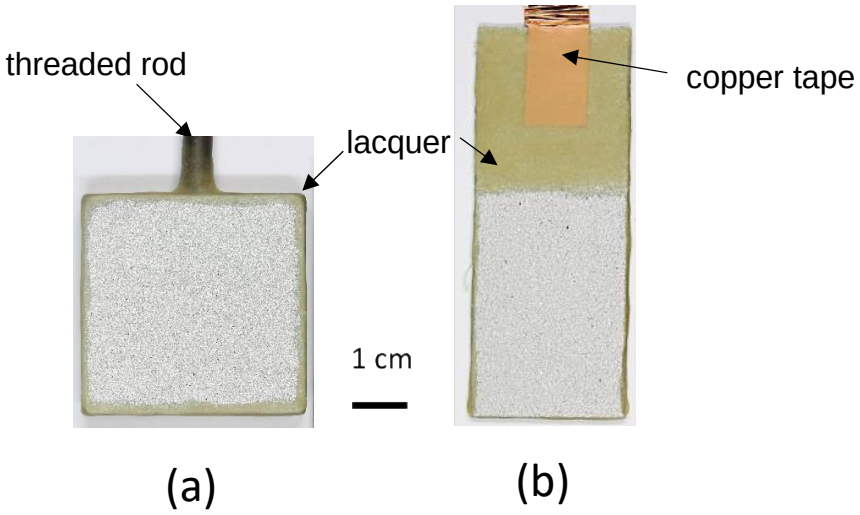

Figure 3-1 Images of samples prepared for immersion tests: (a) TSA on steel, (b) TSA on glass.

To simulate a defect in the coating, circular holidays (defects) were made in the middle of several samples using a flat drill bit (ø 10 mm). Approximately 5% of the coating area was removed to simulate a defect which could have occurred during the transportation or assembly of an offshore wind turbine.

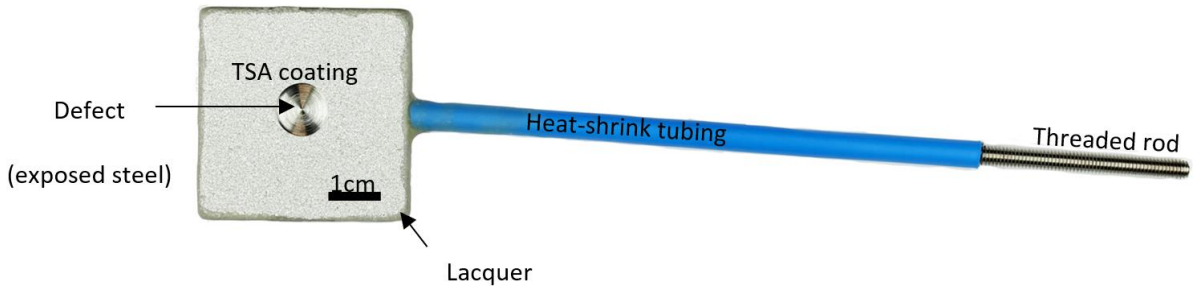

Figure 3-2 TSA-coated steel sample with 5% of the coating area removed to simulate a defect in the coating.

For tests with sealed TSA (1050 AA), 6 sealant systems were selected and evaluated:

1) Epoxy resin
2) Epoxy resin containing 0.5% low density (0.06 g/cm^3) graphene (GNP10)
3) Epoxy resin contaning 0.1% ultra low desnity (0.004 g/cm^3) graphene (GNP35)
4) Epoxy paint
5) Epoxy based paint containing 0.5% low density (0.06 g/cm^3) graphene (GNP10)
6) Epoxy based paint containg 0.1% ultra low desnity graphene (0.004 g/cm^3) (GNP35)

The GNP 35 graphene in the sealant is in the form of very thin crumpled sheets with high surface area. The GNP10 graphene is of moderate surface area. Both epoxies and paints were provided by Applied Graphene Materials company in the form of two-pack components with curing agent. The exact composition of the sealants is confidential property of the company. The sealants were selected based on the NORSOK M- 501standard [89] which states that for low-temperature operations (below 120°C) two-component epoxy should be used.

Each sealant was applied on a separate sample using a brush. To avoid too thick a layer of the sealant, the excess of the material was removed using a plastic plate. Care was taken to leave small amount of TSA exposed to ensure the sacrificial properties of the coating remain intact. All sealants were applied within several hours after the deposition of the coating and they were left to dry under a fume cupboard for 7 days. After 7 days, threaded connections were preapared and 3 layers of stop-off lacquer Type 45 (MacDermid plc, Birmingham, UK) were applied on the back and sides of the samples to avoid exposure of the bare steel to seawater, as shown in Figure 3-3. Circular holidays were made in the middle of several samples using a flat drill bit (ø 10 mm).

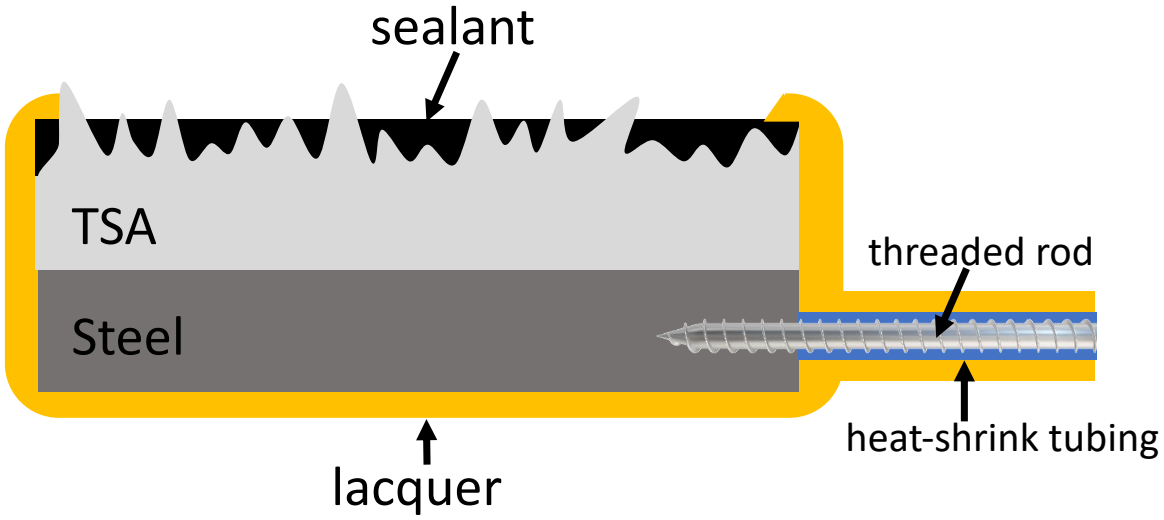

Figure 3-3 Schematic showing location of lacquer on TSA-coated steel.

For examination of cross-sections, samples were sectioned using an abrasive cutter (Buehler abrasimet 2) and cold mounted with EpoFix resin (Struers). Mounted specimens were ground down to P2500 using SiC papers and polished using 3 and 1 µm diamond paste. SEM and EDX analysis was conducted using EVO LS15 SEM (Zeiss).

3.2.1.2 Experimental methods

For electrochemical measurements, a typical 3 electrode system consisting of Ag/AgCl (KCl sat.) reference electrode, Pt/Ti counter electrode, and a sample as a working electrode was used, as shown in Figure 3-4. Surface area of counter electrode was significantly bigger than the surface area of the working electrode.

Measurements of the OCP and linear polarisation resistance (LPR) scans were performed using a Biologic VMP-300 potentiostat. Polarisation curves were generated using an IVIUM potentiostat (IVIUM Technologies). All the experiments were

performed in artificial seawater ASTM D1141-98 [139] (ReAgent) of pH 8.2 (at 20°C). The temperature of the electrolyte inside beakers was controlled with the use of a water bath of constant temperature, as shown schematically in Figure 3-5. Evaporation of water from the test solution was monitored daily. The electrolyte was replenished with deionised (DI) water to maintain the original level of the solution.

The temperature of the water bath was maintained with the use of a heat exchanger with temperature controller and a pump for temperature homogeneity inside the bath. Temperature was monitored using a thermocouple connected to the computer.

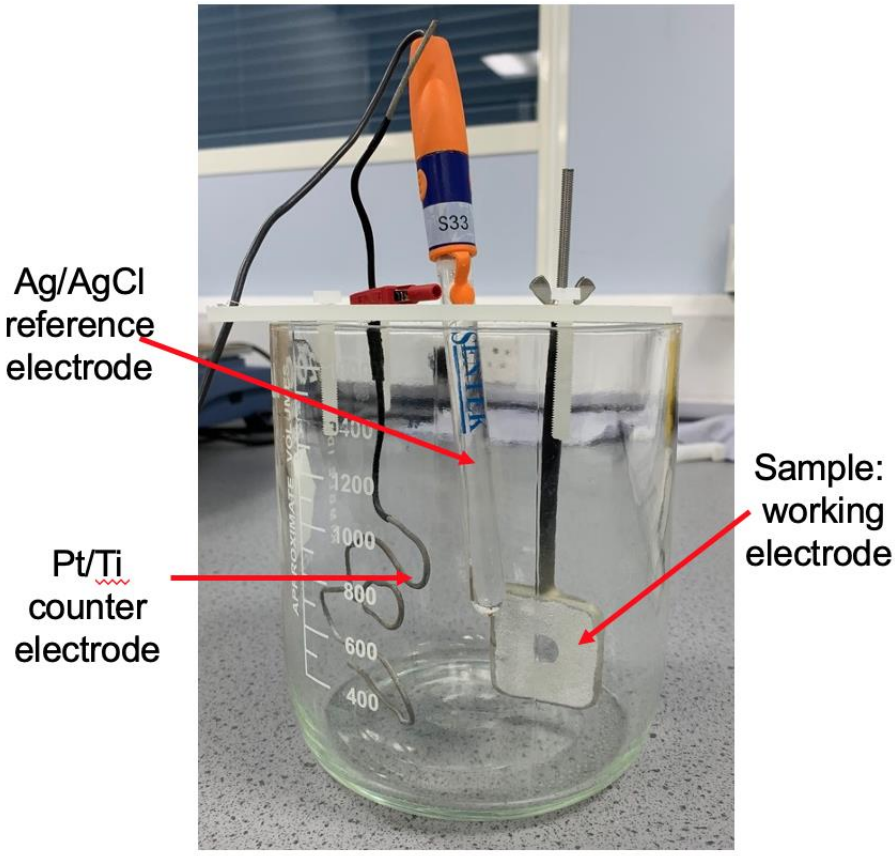

Figure 3-4 **Electrochemical cell**

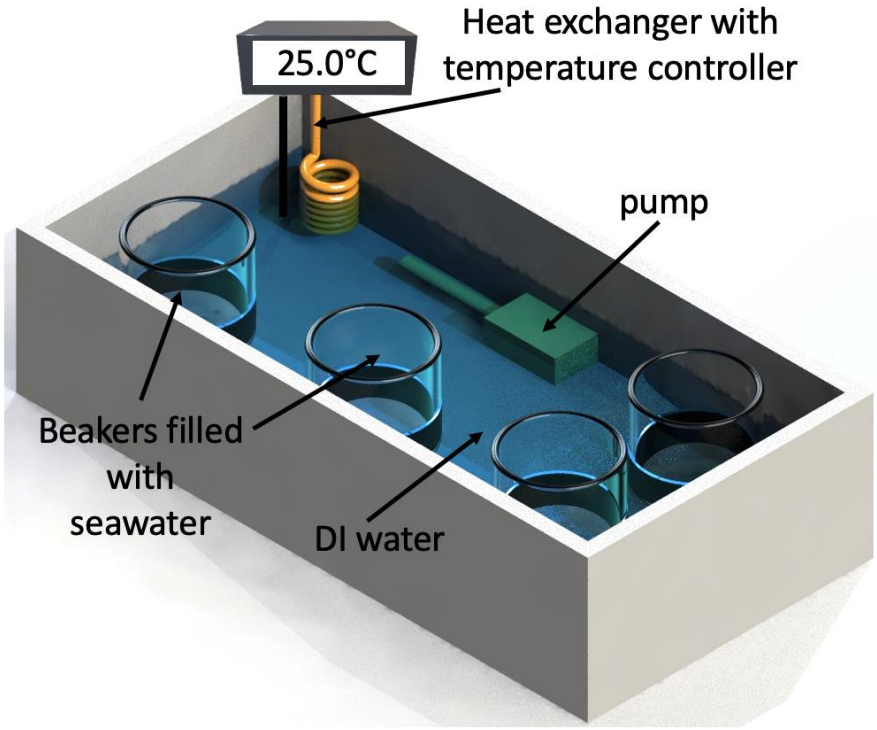

Figure 3-5 Schematic of a set-up for controlling temperature of test solution during corrosion testing.

The electrochemical tests involved:

- measurement of the OCP of the samples,
- LPR scans performed (±10 mV vs OCP) every 6 h, to determine polarisation resistance (Rp),
- anodic and cathodic polarisation scans (performed on separate samples) with the scan rate 1 mV/s. The anodic polarization curves were generated by sweeping the potential from −10 mV from the OCP to positive potentials and the cathodic polarization curves were measured starting at +10 mV from the OCP and sweeping negative.

3.2.2 Experiments under droplets

3.2.2.1 Silver wire experiments

Measurements of the OCP under droplets of artificial sea water were performed using a silver wire as a reference electrode and TSA-coated steel as a working electrode. Both electrodes were connected to a potentiostat (Biologic VMP-300) by copper tape, copper wires and a threaded rod. Potential was measured every 1 s. The experimental set-up is depicted in Figure 3-6. The silver wire pseudo-reference electrode was calibrated against an Ag/AgCl KCl sat.

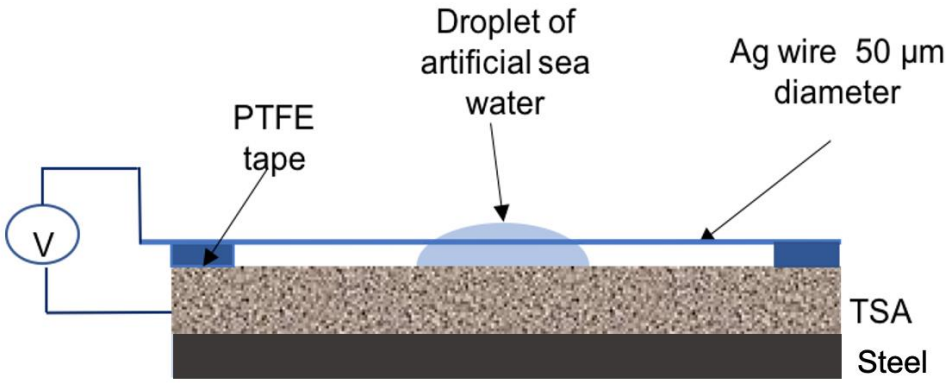

Figure 3-6 Schematic view of a silver wire cell.

For generation of anodic and cathodic polarisation curves, a three-electrode set-up was used, as shown in Figure 3-7. Anodic polarisation curves were generated by sweeping the potential from -25 mV relative the OCP, with the sweep rate of 1 mV/s. Cathodic polarisation curves were produced by sweeping the potential from +25 mV relative to the OCP, with the same sweep rate. The surface area under the droplets was estimated based on pictures taken during the measurements with the use of ImageJ software.

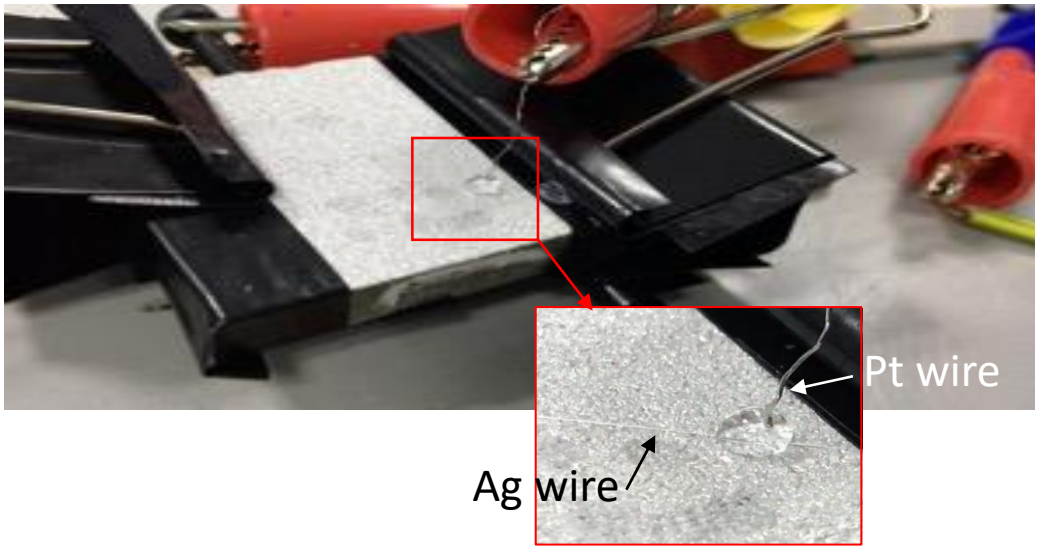

Figure 3-7 Set-up for electrochemical measurements under a droplet of ASW, where Ag wire works as a reference electrode, Pt wire as a counter electrode and TSA as a working electrode.

3.2.2.2 Luggin probe experiments

Electrochemical measurements under 10 μL droplets of artificial seawater were conducted in a 3-electrode configuration (Figure 3-8). A tailor-made Luggin probe was prepared as a reference electrode by placing an Ag/AgCl (KCl saturated) electrode into a syringe filled with synthetic seawater. Pt wire was used as a counter electrode and the sample was connected as a working electrode.

Immediately after the deposition of the droplets, the OCP was monitored for 2 minutes and then anodic polarization curves were generated by sweeping the potential from −10 mV from the OCP to positive potentials, with the sweep rate equal to 1 mV/s. Cathodic polarization curves were measured in separate droplets, beginning at +10 mV from the OCP and sweeping negative, with the same magnitude sweep rate of 1 mV/s. Experiments were conducted at room temperature with no environmental controls.

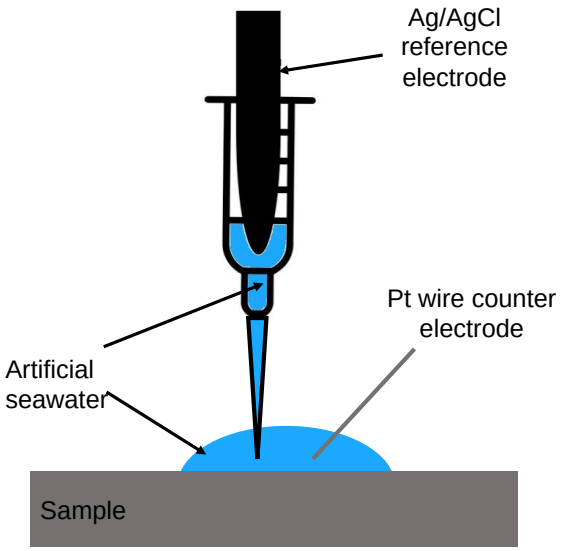

Figure 3-8 Schematic representation of the electrochemical measurements conducted in a droplet of artificial seawater using a Luggin probe as a reference electrode.

3.2.2.3 Calibration of Ag wire electrode vs Ag/AgCl electrode

To determine the potential difference between the two reference electrodes (Ag wire and Ag/AgCl electrode) a potential measurement was performed on Al under 15 µL droplet of ASW. In this experiment the potential of aluminium was alternately measured using the two reference electrodes. Higher values of potential were recorded for Ag wire (potential oscillated around -650 mV), than for Ag/AgCl KCl sat. electrode (around -750 mV). Based on the results of this experiment it was assumed that the potential difference between Ag wire and Ag/AgCl electrode is 100 mV. Exemplar calibration data are shown in Appendix 1.

3.2.2.3 Atmospheric corrosion tests

Three types of samples were used for the experiments, namely AA 1050- H14 sheet (Smiths Metal Centres Ltd.), TSA deposited on glass slides, and TSA deposited on

carbon steel plates. Chemical composition of Al-sheet, Al wire used for spraying and steel substrate are shown in Table 3-4.

Prior to the tests, samples were ultrasonically washed with methanol and left to dry in a desiccator.

Table 3-4 Chemical composition of aluminium and steel used for atmospheric corrosion tests

Element wt% / Material	Si	Fe	Cu	Mn	Mg	Zn	Ti	Al	C	P	S	V	N
AA 1050-H14 sheet	0.04	0.36	0.001	0.003	0.000	0.001	0.009	Bal.	-	-	-	-	-
S355JR Steel	0.390	Bal.	-	1.39	-	-	-	-	0.12	0.14	0.019	0.065	0.003

Before testing, two desiccators with saturated aqueous salt solutions of KCl and K_2SO_4 were prepared to obtain the relative humidity (RH) of 84% and 97%, respectively, in accordance with ASTM E104-02 standard [140].

Arrays of artificial seawater (ASW) ASTM D1141–98 [139] droplets of volumes 1.5 and 2.5 µL were deposited onto samples using a micropipette. Samples were then put inside the sealed desiccators (as schematically shown in Figure 3-9), which were kept at constant temperature of 30°C inside an atmospheric chamber for 2 weeks. After the completion of the tests, samples were taken out from the desiccators and rinsed with deionised water and methanol.

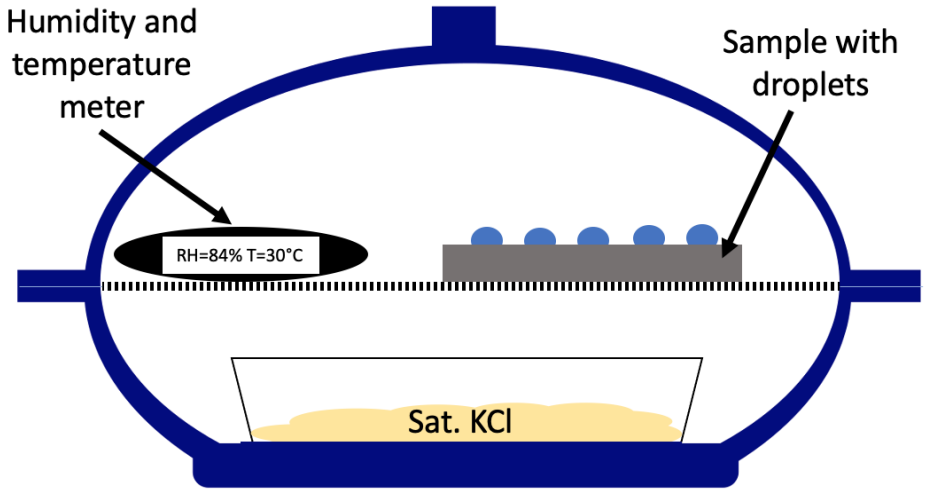

Figure 3-9 Schematic representation of the set-up for atmospheric corrosion testing.

3.2.3 Characterisation of corrosion products

Identification of corrosion products on “typical” droplets was performed using Raman spectroscopy (Renishaw InVia spectrometer with confocal microscope) using an excitation wavelength of 488nm with ~ 1 mW focused through a 20x working distance

objective. All measurements were performed with 100% laser power during 10 s exposure time and 2 accumulations. The range of collected Raman shift was between 200 cm^{-1} and 1600 cm^{-1}. The data were baseline subtracted and cosmic ray signals were removed. Principal component analysis (PCA) was performed using the WiRE™ software (Renishaw) to identify the main constituents present. Then, maps were created via direct classical least square analysis (DCLS) performed with the use of control standards taken from RRUFF database. BMP images were created which were then used to generate the plots of Raman shifts versus intensity using Matlab. The data used for generation of plots was averaged. Corrosion products were also analysed with the use of SEM/EDX Joel 6060LV and optical microscope (Leica DFC420).

3.2.4 Roughness measurements

Roughness of TSA was determined using an Alicona InfiniteFocus SL 3D surface profilometer and associated IF Measure Suite software in compliance with BS EN ISO 4288:1998: “Geometric product specification (GPS). Surface texture. Profile method: Rules and procedures for the assessment of surface texture”. The vertical resolution of the measurements was 0.5 μm.

Chapter 4 Electrochemical Behaviour of Aluminium and Steel in Simulated Seawater Environments

4.1 Introduction

Temperature affects corrosion of metals in aqueous environments in several ways. It influences rates of electrochemical reactions, the solubility and diffusivity of dissolved gasses, the solubility of oxide layers, and the type of corrosion products.

The aim of this chapter is to investigate the effect of temperature on corrosion performance of aluminium and steel in synthetic seawater (under full immersion conditions) and to get an insight into the influence of temperature on cathodic and anodic reactions occurring on those metals. The ultimate goal is to get an understanding of the suitability of using aluminium as a sacrificial anode for corrosion protection of steel operating in seawater at different temperatures. Gave and Shirkhanzadeh [141] observed that temperature has an important impact on the performance of the Al-Fe couple in water containing low concentration of chloride ions in the temperature range 20 - 90°C. However, little attention was dedicated to the performance of the Al-Fe couple in cold seawater environments.

4.2 Results and discussion

4.2.1 Effect of temperature on corrosion of steel in artificial seawater

Figure 4-1 (a) shows the results of the OCP measurements of steel immersed in artificial seawater at 0, 4 ,25 and 32°C for 32 days. The vertical lines correspond to the LPR measurements during which the potential was swept from -10 to 10 mV versus the OCP to obtain the Rp values, which are presented in Figure 4-2. It can be noticed from the magnified view in Figure 4-1 (b), that during the first 12 h of immersion, the potential of steel at 0°C was the highest, followed by 4, 25 and 32°C. At all temperatures, the potential initially exhibited a rapid decrease, associated with the dissolution of air- formed oxide layers. At warmer temperatures (25 and 32°C), after approximately 5 days of immersion (Figure 4-1 (a)), the potential started to rise, likely due to the formation of corrosion products, which were observed on the samples after the immersion. Depending on the nature and amount of the corrosion deposits, they can provide better or worse barrier to the diffusion of oxygen to the metal's surface. Shen et al. [18] who studied corrosion performance of high strength steel in 3.5% NaCl at 0 and 25°C reported loose corrosion products (consisting mainly of $Fe(Cl_xO_y)$ and Fe_3O_4) on the sample exposed to the cold electrolyte, and a compact iron oxide film (Fe_3O_4) on the sample corroding at warm temperature. Less protective corrosion products resulted in the higher corrosion rate and lower corrosion potential (50 mV) at 0°C than at 25°C after 56 days in NaCl.

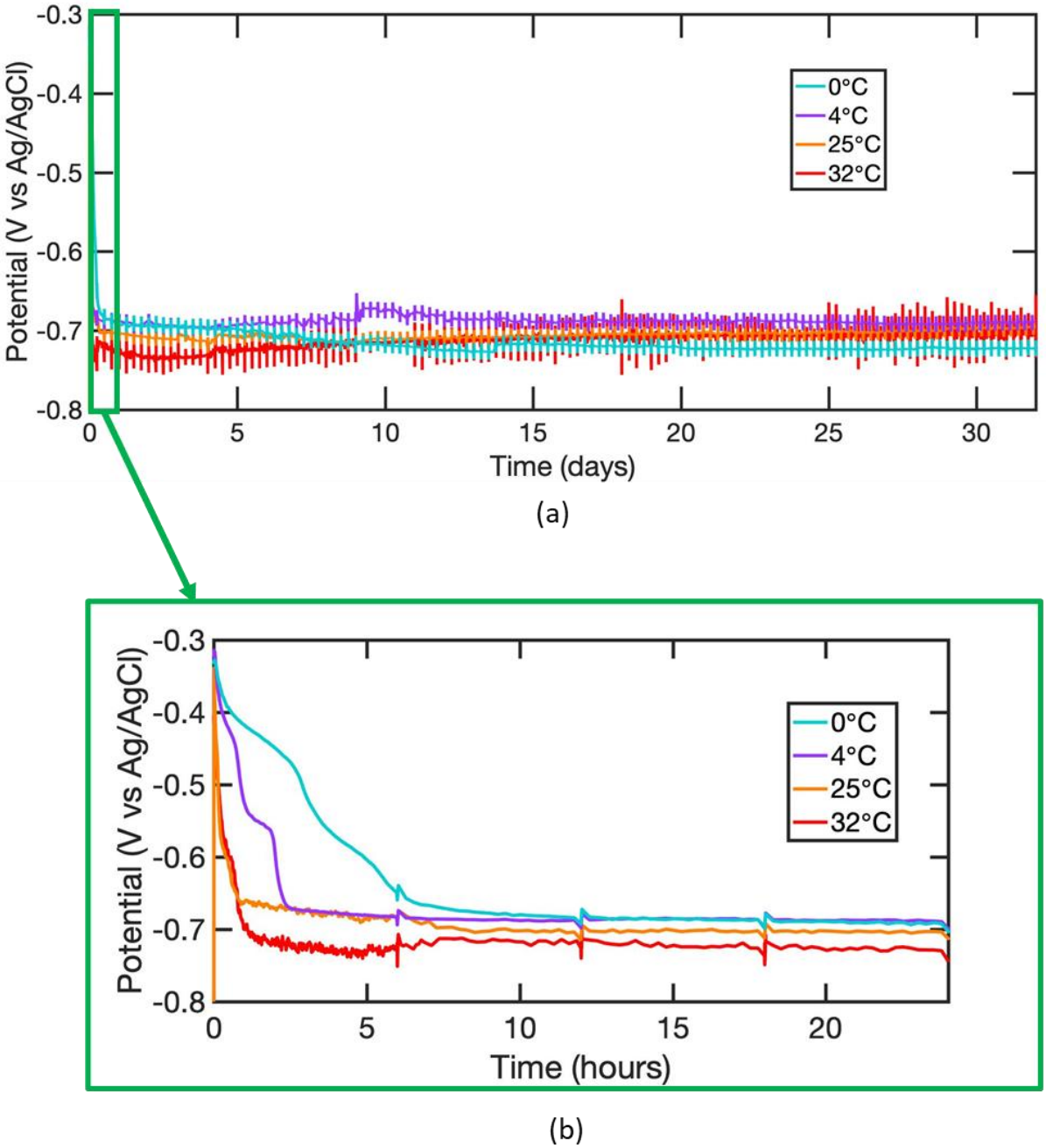

Figure 4-1: OCP of S355 steel in artificial seawater for 32 days as a function of temperature (a) and a magnified view of the first 24 h of immersion (b).

It can be noticed from Figure 4-1 (a), that at the end of the experiment the potential difference between the samples exposed to different temperatures was quite small: - 0.72 V at 0°C, -0.70 V at 4°C, -0.69 V at 25°C and -0.70 V at 32°C. Mercer and Lumbard [16], who studied corrosion of mild steel in artificial and real seawater, observed that there is no clear effect of temperature between 5 and 40°C on the mass loss of mild steel. The corrosion rate of steel in seawater is closely related to the solubility and diffusivity of oxygen since the main cathodic reaction is the reduction of this gas. When temperature increases the solubility of oxygen decreases but its diffusivity increases. It has been observed [142] that up to 80°C, the temperature rise causes an increase in the corrosion rate of steel.

Figure 4-2 presents the results of the LPR measurements of carbon steel immersed in artificial seawater at different temperatures, which were conducted by sweeping the potential from -10 to +10 mV from the OCP and calculating the slope of the obtained line. The Rp values obtained in this technique allow to estimate the corrosion rate of the metal (Rp is inversely proportional to the corrosion current density). From data presented in Figure 4-2 the highest Rp (and therefore the lowest corrosion rate) was recorded at 0°C (20 000 $\Omega \cdot cm^2$ after 32 days). Moreover, the Rp values were increasing with the immersion time, indicating that the corrosion rate was decreasing. At higher temperatures (4 and 25°C) the Rp values were lower and stabilised very quickly at around 5000 and 2000 $\Omega \cdot cm^2$.

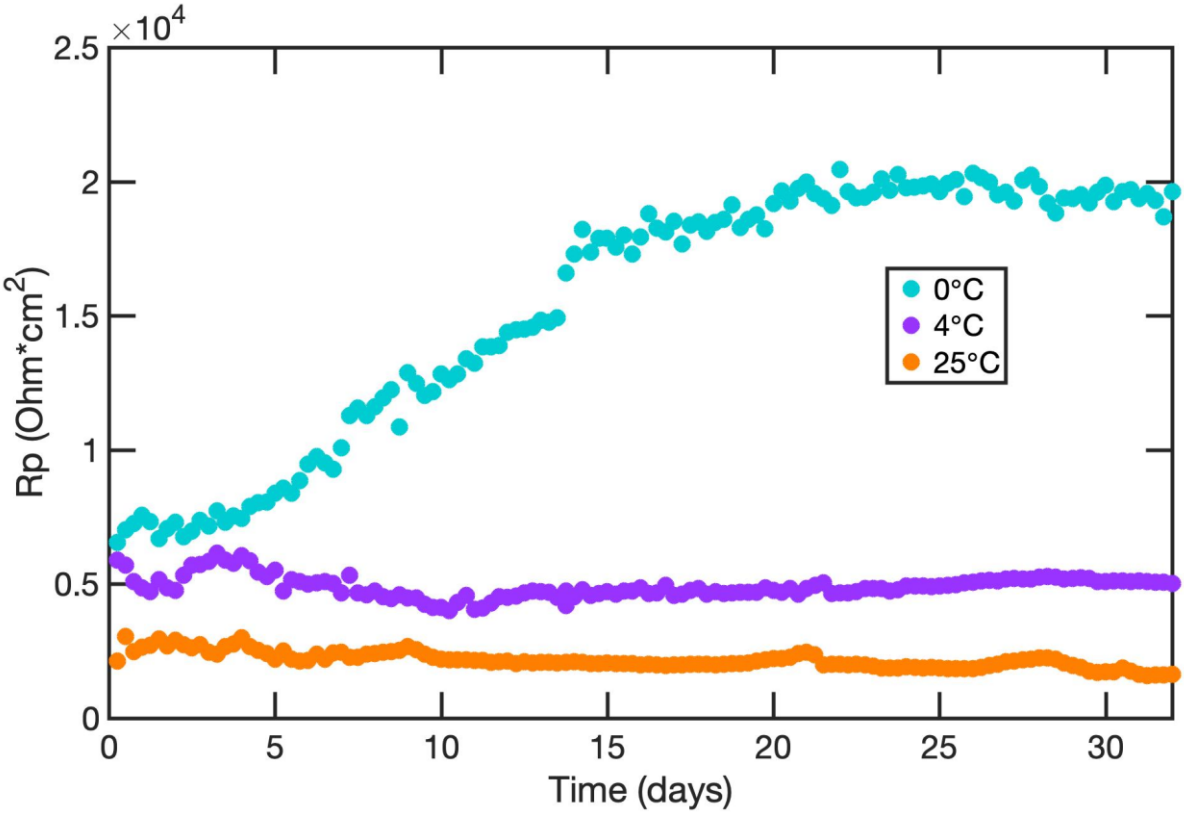

Figure 4-2 Evolution of polarisation resistance of S355 steel immersed in artificial seawater at 0, 4, and 25℃. Rp values obtain from the LPR measurements (±10 mV vs OCP).

Figure 4-3 shows cathodic and anodic polarisation curves measured on separate steel samples after a 3 - h immersion in artificial seawater at different temperatures. From the anodic branches, it is evident that the anodic current density increases with temperature. Cathodic reactions are also affected by the temperature change, and they increase with temperature. However, the increasing trend is slightly more difficult to observe. A visual inspection of the samples performed after the measurements revealed the presence of rust and white deposits (most likely calcareous: $CaCO_3$ and $Mg(OH)_2$) on the surfaces of the samples. It is likely that those products affected the diffusion of oxygen from the bulk solution towards the electrode. To avoid the presence of the deposits, another set of polarisation curves was generated after 5 min of immersion in ASW. The results are presented in Figure 4-4.

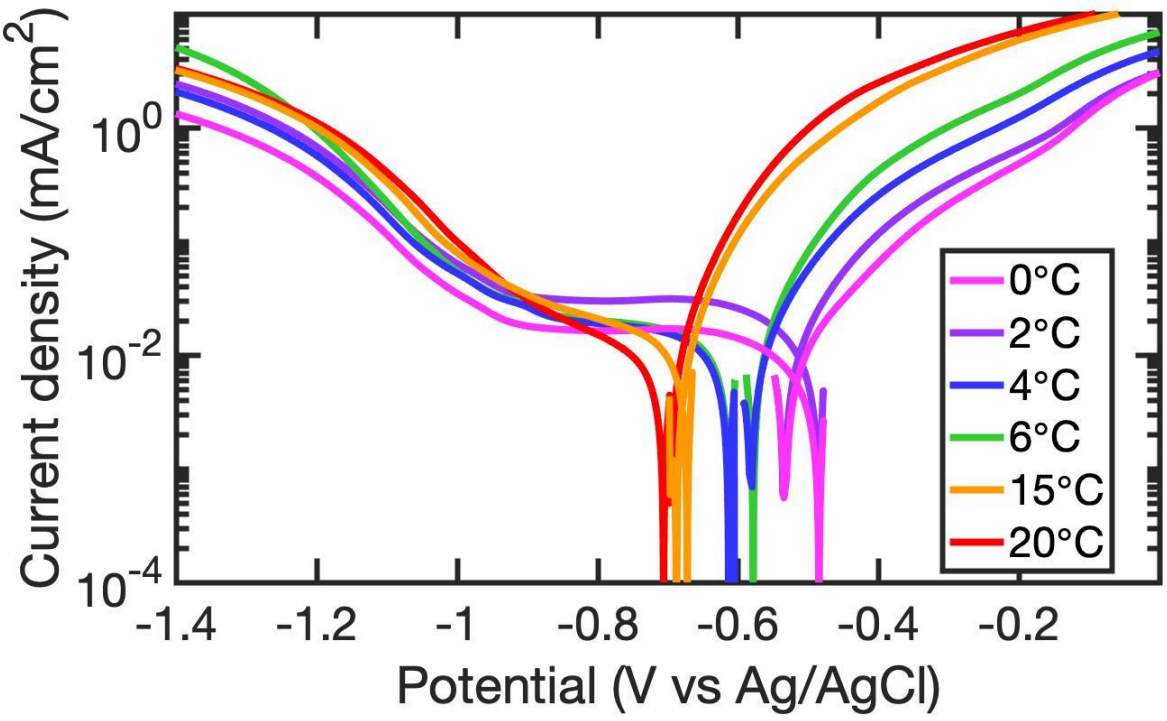

Figure 4-3: Cathodic and anodic polarisation scans performed on S355 steel after 3 - h immersion in artificial seawater at different temperatures. Scans started from ±10 mV from the OCP with the scan rate of 1 mV/s.

From Figure 4-4 it is clear that the cathodic reactions are enhanced at higher temperatures. Furthermore, Figure 4-5 revealed the influence of the immersion time on the mass transfer limited current density. Longer immersion time (3 h) resulted in lower current density, due to the presence of corrosion products and calcareous deposits.

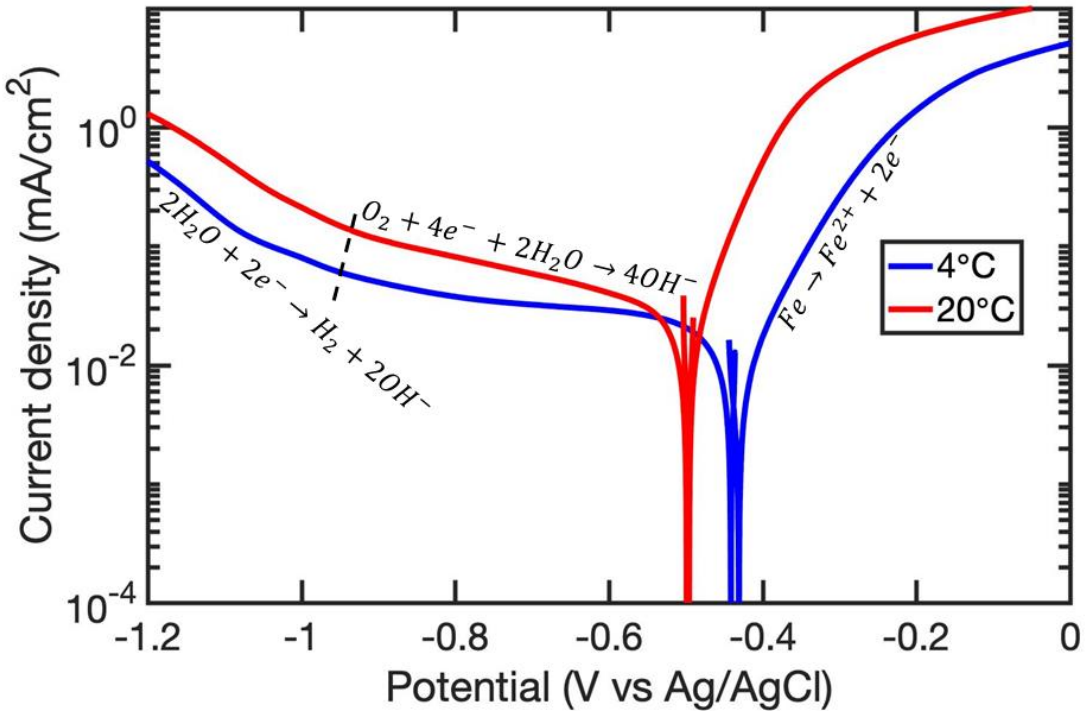

Figure 4-4 Cathodic and anodic polarisation scans performed on S355 steel after 5 - min immersion in artificial seawater at different temperatures. Scans started from ±10 mV from the OCP with the scan rate of 1 mV/s.

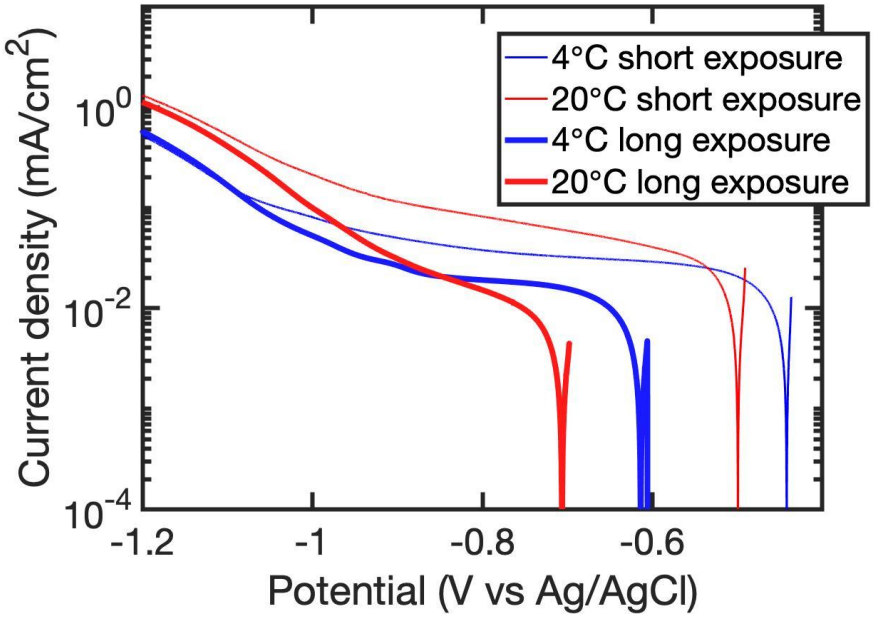

Figure 4-5 Cathodic polarisation curves performed on S355 steel after 5 min (thin lines) and 3 h (thick lines) immersion in ASW. Scans started from 10 mV from the OCP with the scan rate of 1 mV/s.

Both anodic and cathodic reaction rates increase with temperature leading to little change in the corrosion potential. Figure 4-3 clearly shows the decrease of the corrosion potential with temperature (after 3 hours of immersion). This indicates the predominance of anodic activity during the initial hours of immersion which, in case of iron, follows Equation 2-1.

The two main cathodic reactions occurring in neutral and alkaline solutions (pH of seawater is approximately 8.2) are reduction of oxygen and reduction of water.

4.2.2 Effect of temperature on aluminium in artificial seawater

4.2.2.1 Long exposures

Figure 4-6 presents the results of the measurements of the OCP of AA 1050 wires immersed in ASW at different temperatures. It can be observed that the potential of samples immersed at 4, 15 and 20°C stabilised quickly (within 2 days) at around - 0.7 V. At 25 and 30°C, however, the potential exhibited a very different behaviour. During the first 3 days of the immersion, the potential decreased significantly from approximately - 0.75 V to -1.30 V, and then started to rise gradually until it reached - 1 V after 32 days.

The initial decrease of the potential was probably due to the dissolution of air-formed oxide film, and the subsequent increase with the precipitation of new oxides/hydroxides. It was previously observed that the temperature influences the nature of the corrosion deposits forming on aluminium immersed in water. Below 40°C, a single layer of bayerite forms, whereas above this temperature (up to 100°C) an inner layer of pseudo-boehmite and an outer layer of bayerite precipitates [33] .

More noble potential values of aluminium alloy (AA 5052) immersed in seawater at 4°C than at 25°C were also observed by Dexter [37] and Rowland [38]. They linked the potential ennoblement (of approximately 200 mV) with different behaviour of CO_2 at different temperatures. They proposed that at 4°C H_2CO_4 is formed, which works as a cathodic depolariser which causes the ennoblement of the potential, whereas at 25°C CO_3^{2-} is being incorporated into the film which causes more active potentials.

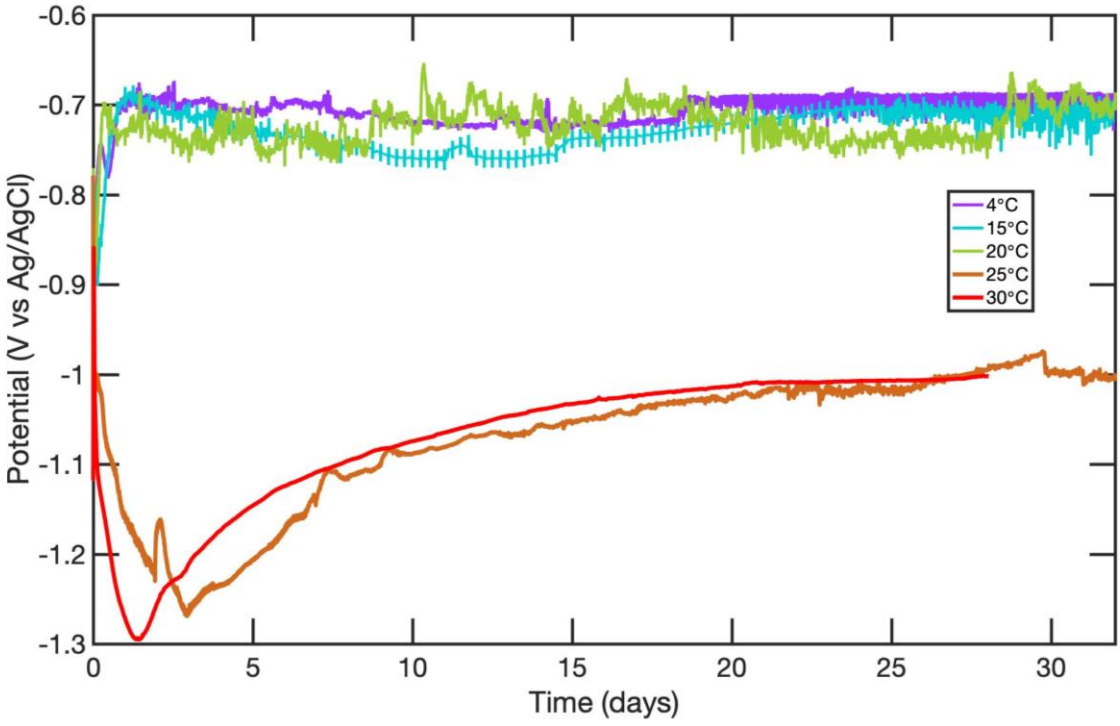

Figure 4-6: OCP of Al AA1050 wires immersed in artificial seawater at different temperatures for 32 days.

The effect of temperature on the potential of Al exposed to seawater was also confirmed during an experiment in which the temperature of ASW was increased from 4°C to 23°C after 4 days of immersion. The results are shown in Figure 4-7. It can be seen that, in agreement with the data from Figure 4-6, the potential of Al exposed at 4°C was around -0.7 V. When the temperature of the solution increased to 23°C, the potential decreased to approximately -0.88 V and started to rise gradually. The

potential decrease could be due to two reasons: either enhanced anodic activity associated with dissolution of the oxide film or inhibited cathodic activity due to lower solubility of oxygen in seawater at higher temperatures (Figure 2-2 (b)).

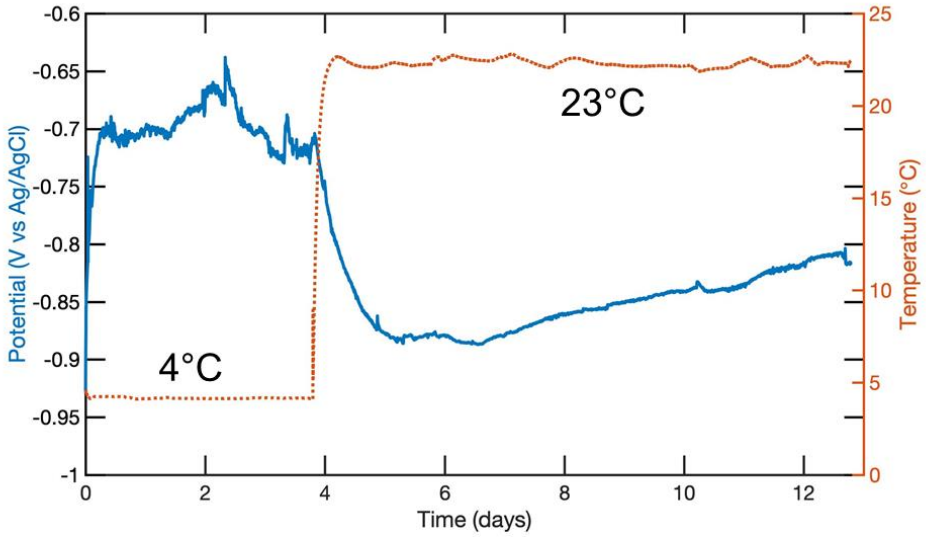

Figure 4-7: OCP of AA 1050 wire immersed in artificial seawater as a function of time and temperature.

4.2.2.2 Shorter exposures

Figure: 4-8 shows results of the 2.7-day (65 h) measurements of the OCP of AA 1050 wires immersed in ASW at different temperatures. It can be clearly seen that wires exposed to colder seawater (0-20°C) exhibited higher (less negative) potential values and stabilised quickly at approximately -0.7 V. Wires exposed to warmer solutions (above 20°C), however, showed a decrease of the potential with temperature. The magnified view of the first 5 hours of immersion shows that at all temperatures, the potential initially increases and then starts to decrease. At higher temperatures (25 and 32°C), the decreasing trend of the potential is then maintained for several hours. At lower temperatures (0-20°C), on the other hand, the initial potential increase and decrease is followed by another potential rise.

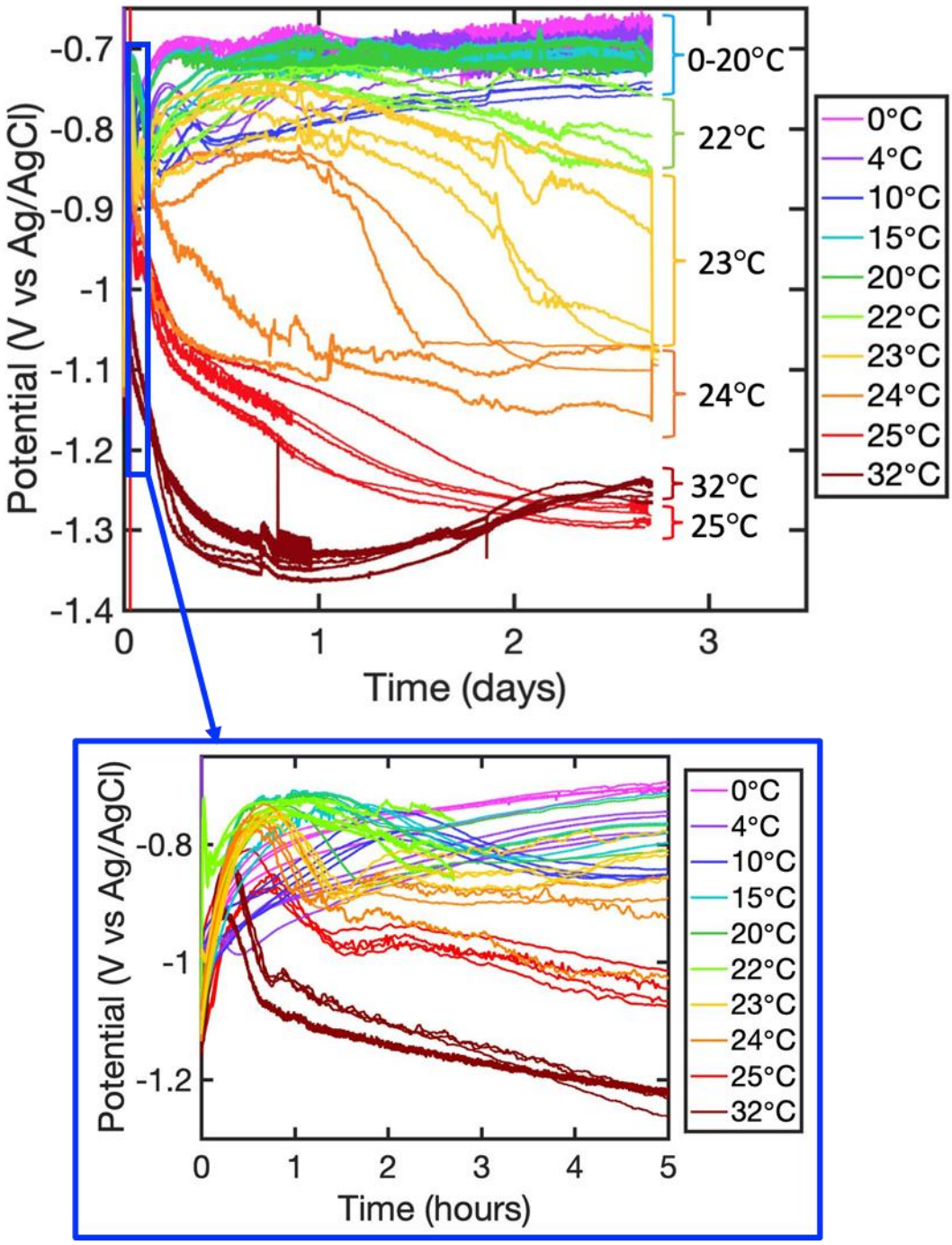

Figure: 4-8 OCP of AA 1050 wires immersed in artificial seawater for 2.7 days as a function of temperature.

To get a better insight into the corrosion mechanisms, anodic polarisation curves were conducted after the completion of the 2.7-day immersion test. The results are shown in Figure 4-9. It can be clearly seen that the passive region is much wider at higher temperatures. Moreover, the passive current density increases with temperature, which indicates a faster dissolution of the oxide film at higher temperatures. The magnified view of the region where the sudden increase of current density was observed shows an increase in noise, most probably due to pitting. However, a clear pitting potential cannot be distinguished. In order to explore the influence of temperature on pitting susceptibility, shorter immersion tests (3 h) were performed to ensure that the OCP does not reach the pitting potential before the anodic polarisation is performed. The results of the 3-h OCP measurements can be seen in Figure 4-10. It can be seen that the pitting potential was not reached during this timeframe. Moreover, at higher temperatures the potential increases faster than at lower temperature, as can be seen from the magnified view in Figure 4-10. After 30 min of immersion, the potential at 25°C is the highest and then starts to decrease and after 3h it exhibits the lowest potential value in comparison with other temperatures.

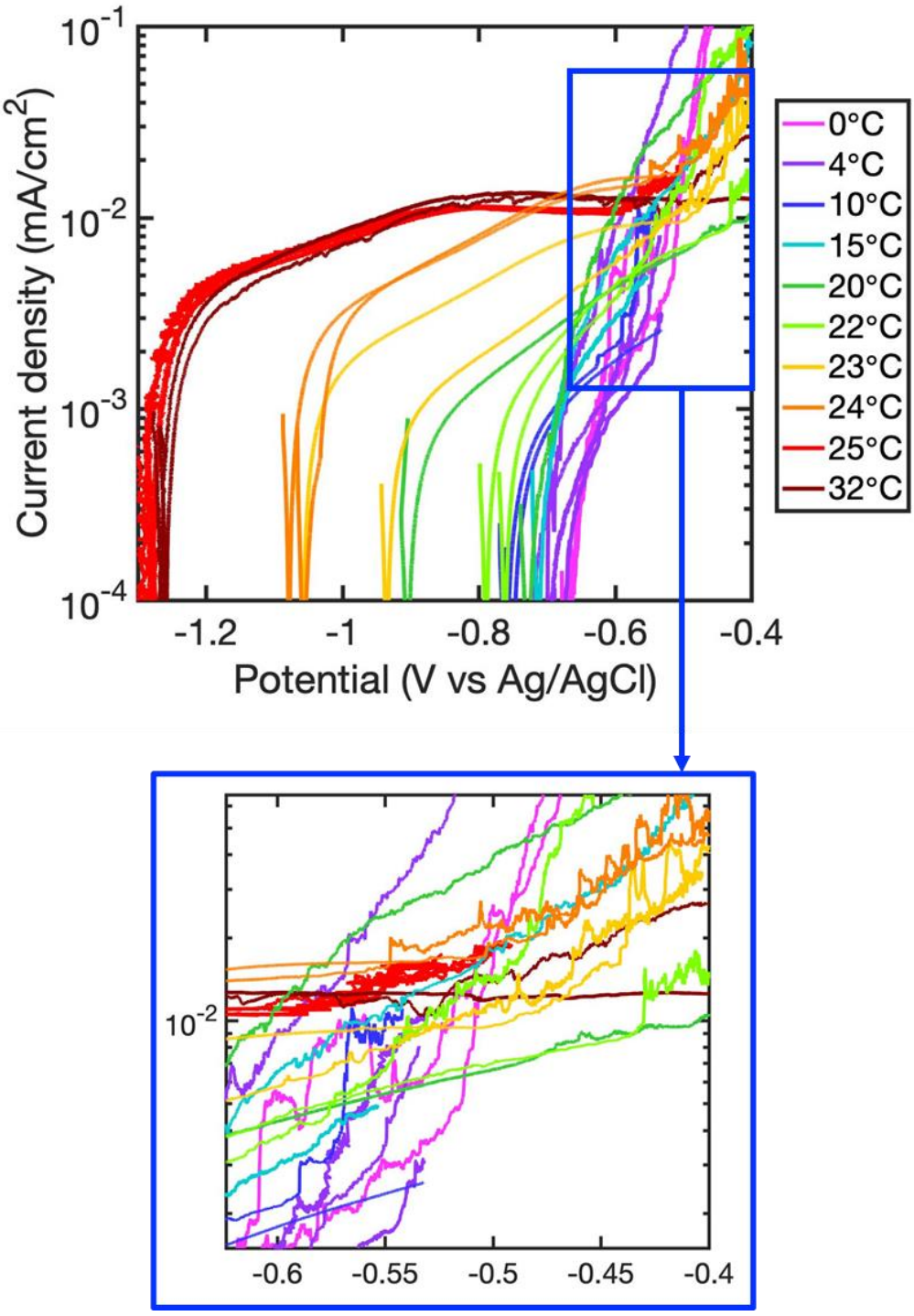

Figure 4-9: Anodic polarisation scans performed on AA 1050 wires after 2.7 days immersion in artificial seawater at different temperatures. Scans started from ±10 mV from the OCP with the scan rate of 1 mV/s.

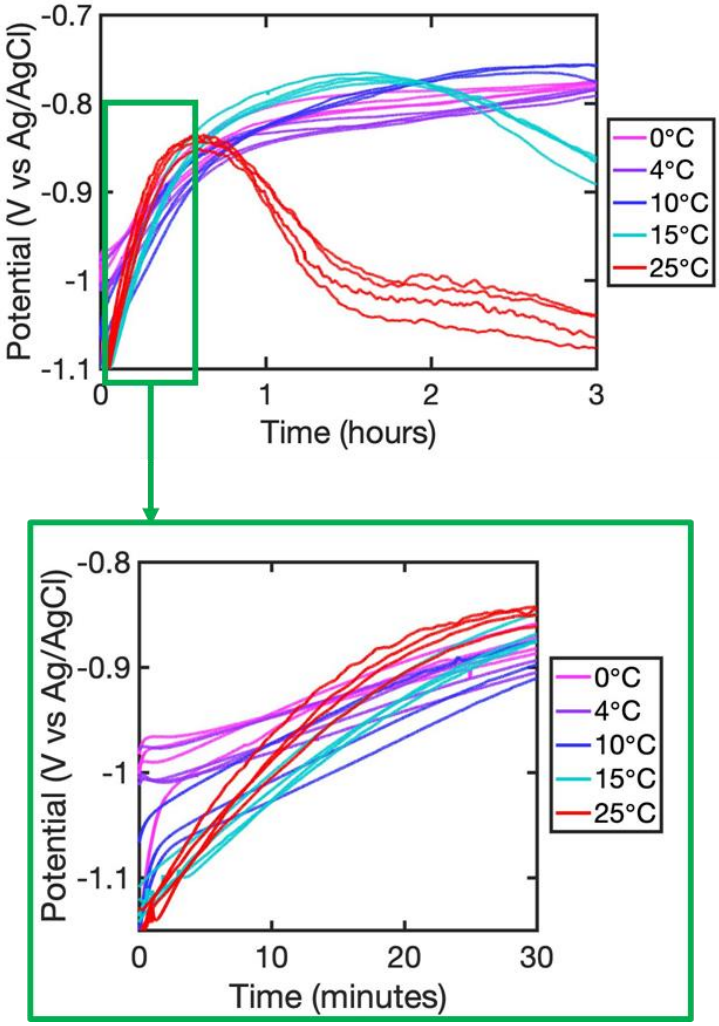

Figure 4-10: OCP of AA 1050 wires immersed in artificial seawater for 3 h as a function of temperature.

Cathodic and anodic polarisation curves performed on AA 1050 wires after 3 h of immersion in ASW can be found in Figure 4-11 (a) and (b), respectively. It can be seen that cathodic current density increases with temperature, which can be also seen from Figure 4-12, which shows cathodic current density at -1.3 V. Moreover, the change of the slope of the cathodic branch (at more cathodic potentials), associated with the hydrogen evolution reaction also changes its location with temperature. At 0 and 4°C it occurred at approximately -1.40 V, at 10 and 15°C around -1.45 V and at 25°C at approximately -1.48 V.

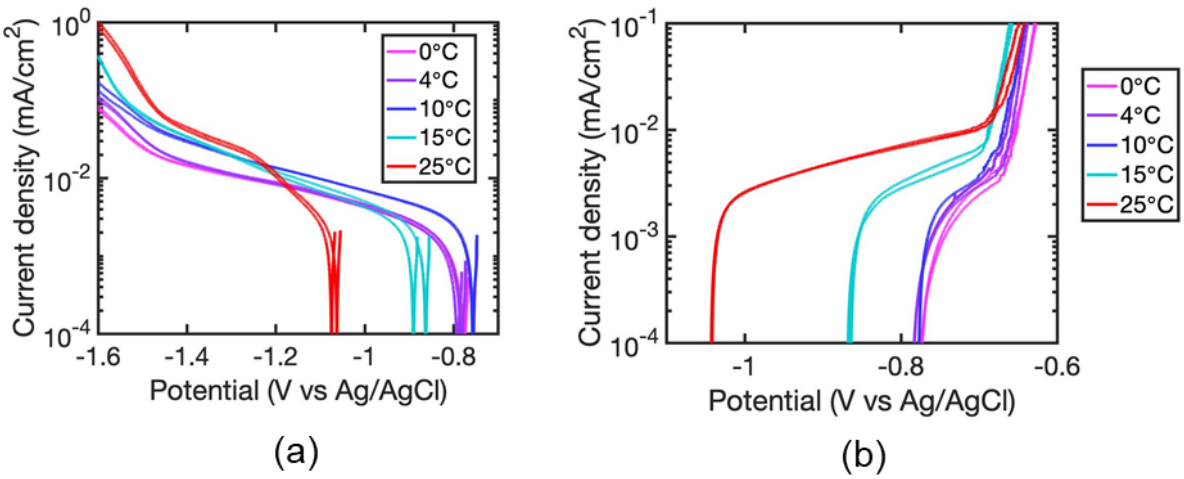

Figure 4-11: Cathodic (a) and anodic (b) polarisation curves performed on AA 1050 wires after immersion in artificial seawater for 3 h at different temperatures.

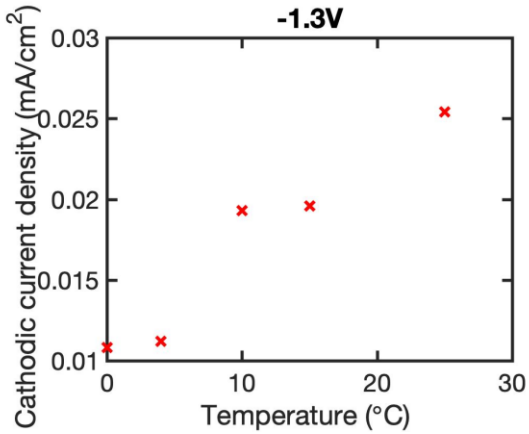

Figure 4-12: Cathodic current density at -1.3 V (vs Ag/AgCl electrode) after three hours of immersion in artificial seawater.

From anodic polarisation curves (Figure 4-11 (b)) one can notice that in the temperature range 0-25°C, the pitting potential of AA 1050 in seawater changes very little with temperature, decreasing from -0.67 V (at 0°C) to -0.70 V (at 25°C). Similar observation was made by Soltis et al. who studied the influence of temperature on the pitting potential of high purity aluminium (99.99%) in NaCl solutions [33]. They observed a slow decrease of the pitting potential with temperature between 1 and 30°C, as can be observed in Figure 4-13. To compare the results obtained in this work with data generated by Soltis et al., pitting potentials were extracted from Figure 4-11,

converted to SCE scale and added to the figure made by Soltis et al (Figure 4-13). It can be noticed that a similar decreasing trend was obtained in both cases. However, the values of pitting potentials measured in NaCl solution are higher than in seawater. The reason for that could be different concentration of the solution (salinity of seawater is 0.6 M) and different level of purity of the aluminium (99.99% used by Soltis et al. and 99.5% in this project).

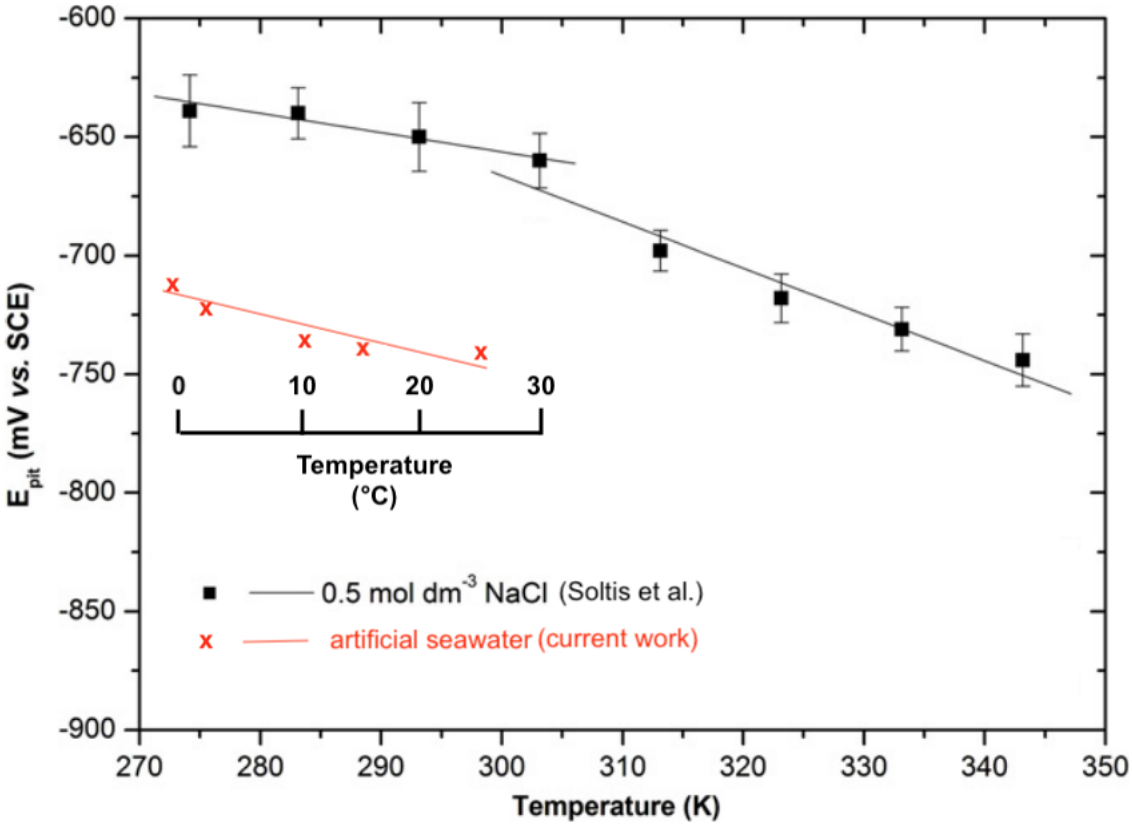

Figure 4-13 Pitting potential of aluminium as a function of temperature. Data obtained using AA 1050 in artificial seawater compared with work conducted using high purity aluminium in NaCl by Soltis et al. Original figure taken from [33]***, modified with data generated in this project.***

Figure 4-14 shows results of potentiostatic polarisation in passive region (-0.76 V applied) of AA 1050 wire in ASW at 4 and 21°C. One can clearly see a higher number and intensity of metastable pitting events as temperature and current density increase

(due to closer proximity to the pitting potential). The increase of the current density with temperature was also observed by Soltis et al. [33].

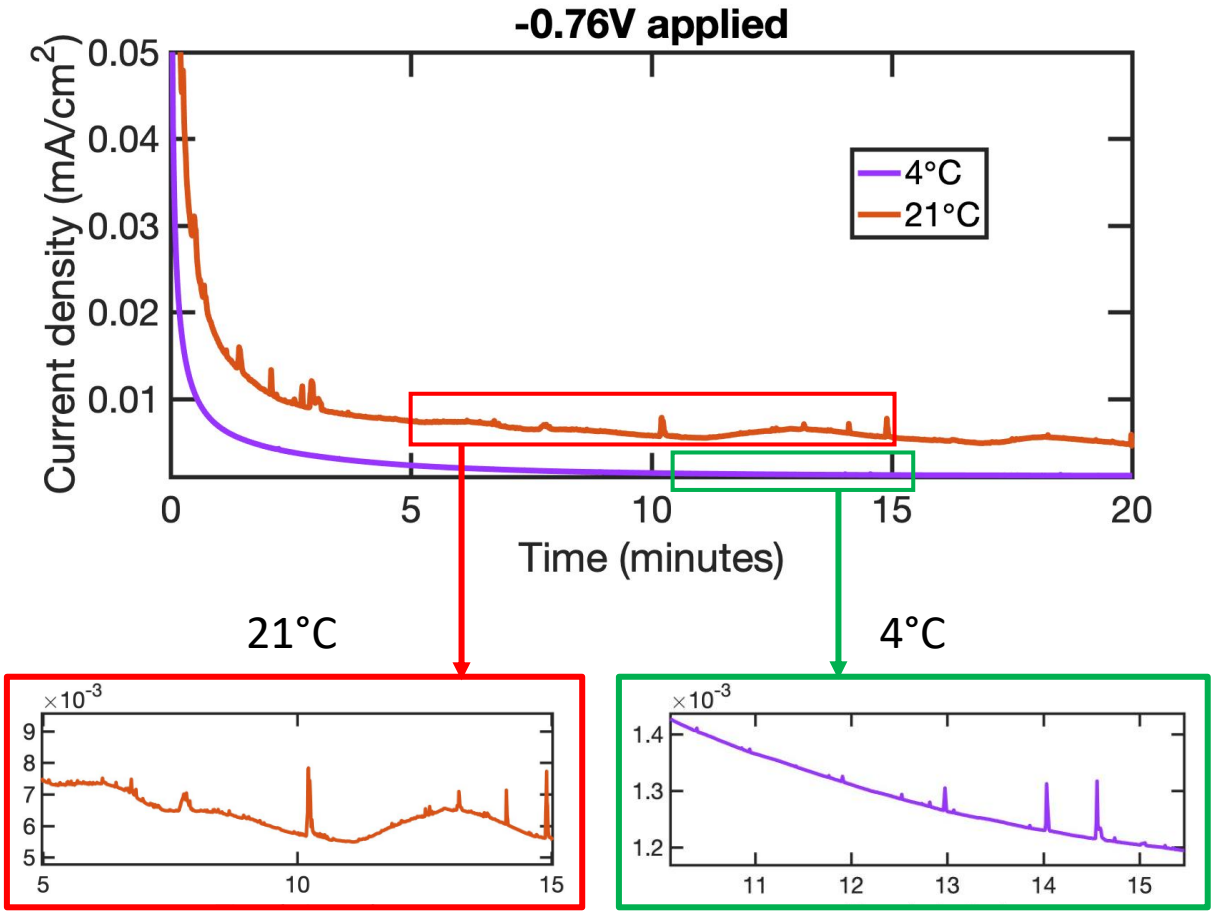

Figure 4-14: Potentiostatic polarisation (-0.76 V) performed on AA 1050 wires immersed in artificial seawater at different temperatures; Wires ground using 1200 SiC paper and alcohol and allowed to passivate in air for 15 min.

Higher values of current density at higher temperatures indicate lower thickness of the oxide layer, due to the faster dissolution rate. Feng et al. [143] who studied the effects of low temperature on aluminium hydrolysis generated solubility data of Al at 25°C and 4°C in solution of $AlCl_3$. The results are shown in Figure 4-15. It can be observed that

at pH 8 (pH of seawater) the solubility of Al is an order of magnitude greater at 25°C than at 4°C.

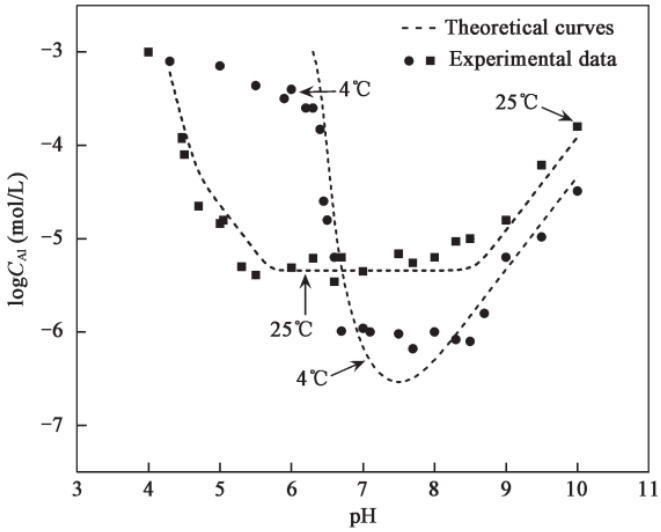

Figure 4-15 Solubility of aluminium in $AlCl_3$ solution at 4 and 25℃. Graph taken from [143]***.***

4.2.2.3 Long and short exposures - comparison

Figure 4-16 presents cathodic and anodic polarisation curves performed on AA 1050 wires after 30 min (thin lines) and 65 h (thick lines) immersion in ASW at 4 and 25°C. One can notice that polarisation curves performed after different immersion times look different. After 30 min immersion, cathodic current density is significantly higher at higher temperature (thin red line) and the passive current density is also slightly higher (thin red line). After longer immersion time (65 h), however, cathodic current density values at 25 and 4°C are of the same order of magnitude, whereas there is a significant difference between the passive current density at those two temperatures (1.0 log unit higher at 25°C). Moreover, the corrosion potential changes significantly with the immersion time. After 30 min, the corrosion potential at both temperatures was located very close to each other (between -0.8 and -0.9 V), whereas after 65 h, corrosion

potential at 25°C shifted towards more cathodic potentials (between - 1.2 and -1.3 V), whereas at 4°C towards more anodic (around -0.7 V).

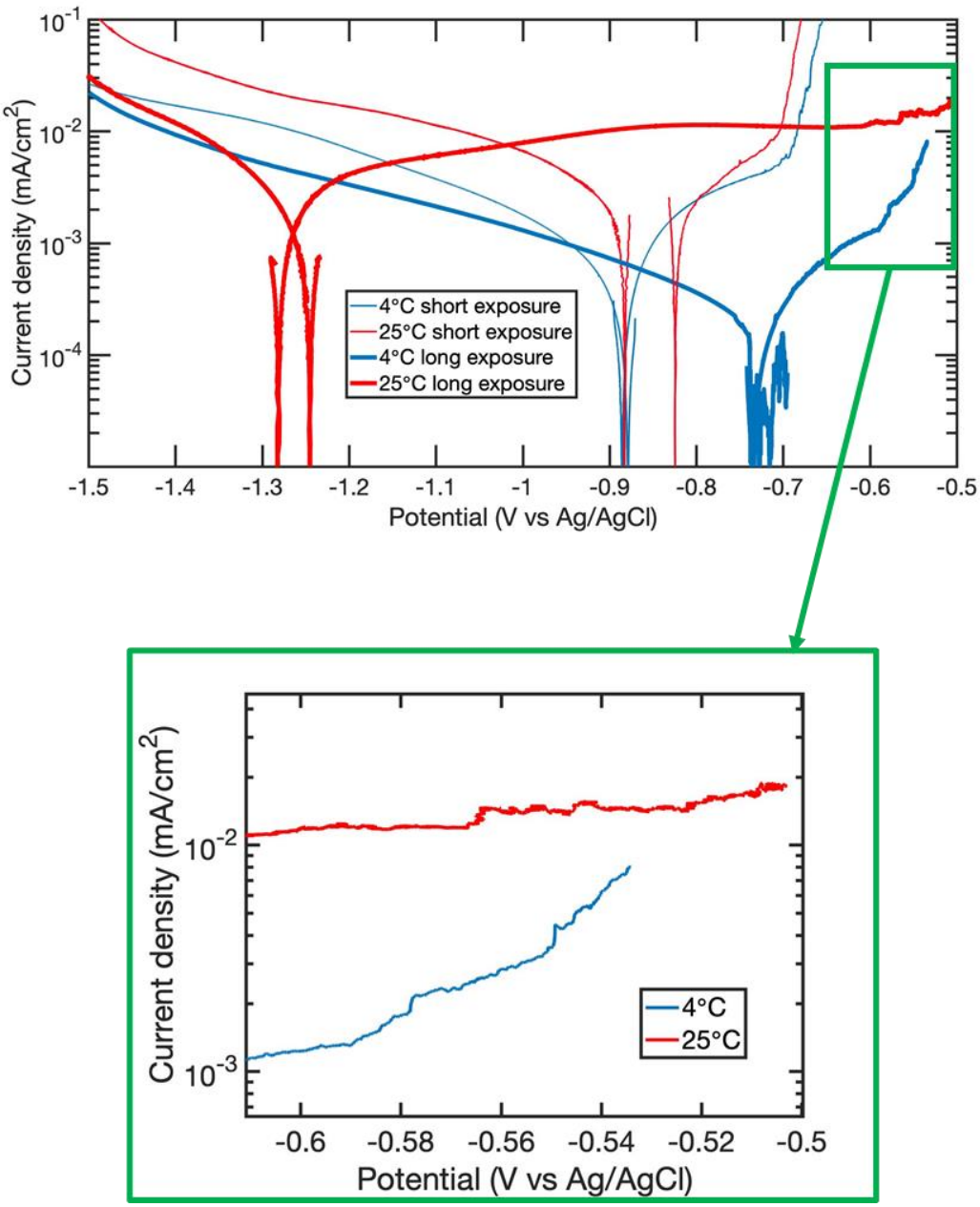

Figure 4-16: Polarisation curves generated on AA 1050 wires after 30 min (thin line) and 65 h of immersion (thick line) with the scan rate 1 mV/s.

A significantly higher cathodic activity at warmer temperature after short immersion time is most probably related to higher diffusivity of oxygen at higher temperatures (Figure 2-2). After a longer immersion time (65 h), the passive current density starts to dominate and shifts the corrosion potential, which can be illustrated using Evan's diagram Figure 4-17. It can be noticed that after short immersion times, pitting potential is well-defined at around (-0.68 V), whereas after longer immersion time it is not. This could be related to the depletion of available pitting initiation sites after longer immersion.

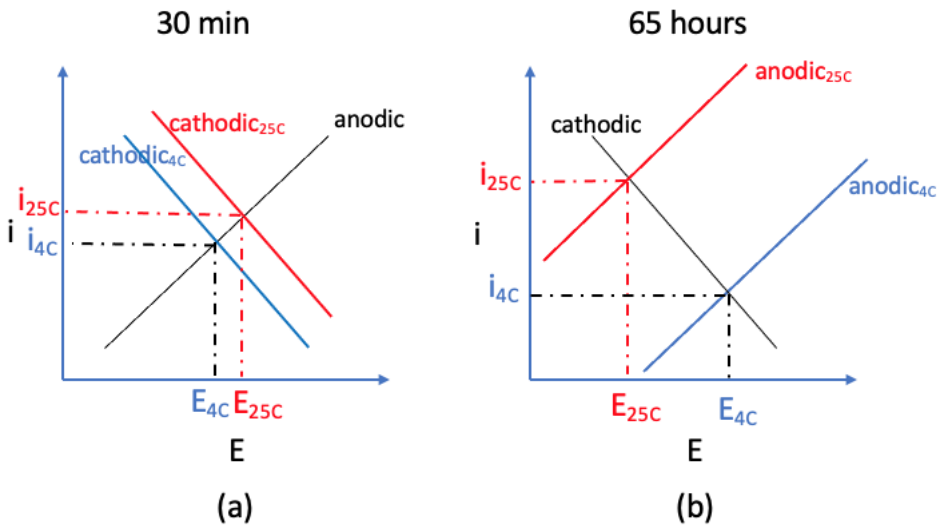

Figure 4-17 Evan's diagram explaining the effect of the immersion time and temperature on cathodic and anodic activity of aluminium in seawater. At short immersion time cathodic reaction dominates, at longer immersion time passive current density dominates.

4.2.3 Performance of aluminium as a sacrificial anode

Figure 4-18 shows corrosion potential of steel (red dots) and aluminium (blue crosses) in artificial seawater after different immersion times in ASW as a function of temperature. It can be seen that after short immersion times (3 h) there is a potential difference between Al and steel at all temperature tested. However, after longer

immersion times (65 h), the potential of Al and steel reach almost identical values in the temperature range 0 - 20°C. At higher temperatures the potential of Al becomes lower, whereas the potential of steel remains at the same value of approximately - 0.7 V. Limited amount of data gathered after significantly longer immersion time (30 days) suggests that the potential of steel remains stable at approximately -0.7 V. The potential of Al seems to exhibit similar values in the temperature range 0 – 20°C. At 25°C, the potential is much lower (approximately -1 V), therefore it is possible that after 30 days, a similar temperature – potential relationship exists above 20°C.

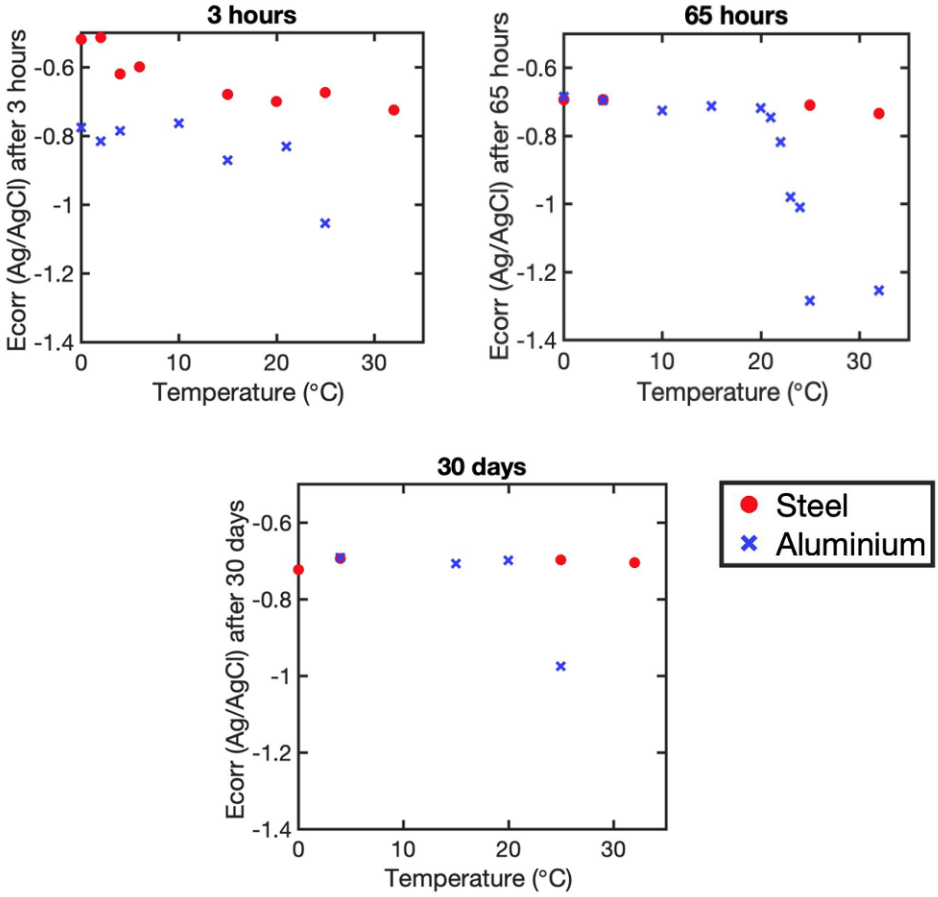

Figure 4-18: Corrosion potential of aluminium and steel in artificial seawater after different immersion times in artificial seawater as a function of temperature.

It is widely accepted (e.g. [39]) that for successful cathodic protection, the desired protective potential for carbon and low-alloy steel should be in the range of - 0.8 to - 1.1 V (Ag/AgCl/seawater). A structure polarised to less negative potentials is considered “under-protected”, whilst polarised to more negative potentials “over - protected”. When steel is connected to aluminium, a mixed potential is established between those two metals. Figure 4-18 shows that above 20°C, the potential of aluminium is sufficiently low to provide the required level of protection to steel.

Results gathered during the short-term testing revealed important information regarding the performance of Al-steel couples operating in seawater. It has been shown that temperature has little effect on the potential of steel (Figure 4-1), and therefore the potential of the couple is controlled by the sensitivity of aluminium to the temperature level (Figure: 4-8).

Furthermore, it was noticed that the mechanisms controlling the potential of aluminium are time-dependent (Figure 4-16). During short exposures to seawater (minutes), the potential of Al is controlled by the cathodic reactions, whilst during longer immersions (days) passive current density dominates. Lower passive current density recorded at colder temperatures (Figure 4-11) indicates thicker oxide layers, due to slower dissolution rates. This is likely related to the lower solubility of aluminium in cold seawater, which explains the worse performance of aluminium (as a sacrificial metal) at colder temperatures (Figure 4-18).

4.3 Conclusions

1. Temperature appears to have a very little effect on the corrosion potential of steel immersed in ASW over the range 0-32°C. The potential stabilises within 10 h of immersion.
2. Evolution of the corrosion potential of aluminium in seawater is strongly time-dependent and steady-state is not reached before approximately 30 days at warm temperatures (above 20°C).
3. During short immersion times (minutes), the potential of aluminium is controlled by the cathodic reactions. After longer immersion times (days), the potential is controlled by the passive current density.
4. The passive current density of aluminium increases significantly with temperature. This correlates with higher solubility of aluminium.
5. Temperature has a small effect on pitting potential of aluminium in seawater after short exposures. After longer exposures (days), there is no well-defined pitting potential.
6. In cold seawater (below 20°C), the potential of aluminium is very close to the potential of steel (around -0.7 V) and therefore it is very likely that aluminium may provide less effective sacrificial protection to steel at lower temperature.

Chapter 5 Performance of Thermally Sprayed Coatings Under Submerged Conditions

5.1 Introduction

Application of sacrificial metallic coatings, such as thermally sprayed aluminium (TSA), zinc and their alloys, is a promising corrosion mitigation method for steel operating in marine environments. Such coatings are not only capable of providing protection to the steel when they are intact, but they work well also when the coating is partially damaged, and the steel is directly exposed to corrosive seawater. Due to their greater activity in the galvanic series with respect to steel, Al and Zn coatings provide cathodic protection to steel, working as an evenly distributed sacrificial anode. The most commonly studied alloys for the preparation of thermally-sprayed Al coatings for the corrosion protection of steel included AA 1050 (99.5% Al) and Al–5%Mg.

The temperature of surface seawater varies from approximately -2°C (the Arctic Ocean) to 32°C (the Persian Gulf). The level of protection provided by the coatings may differ in cold arctic water from the one observed in warm water close to the equator, especially if there is damage in the coating. To date the majority of the testing of TSA coatings has been performed at either room or elevated temperature, for example: [6–12,74]. Limited studies have been conducted at cold temperatures: [81,144]. No studies focusing on the performance of TSA operating at temperatures below 5°C have been found.

Since one of the characteristic features of thermally sprayed coatings is their porous nature, the application of an appropriate sealant can be beneficial to prolong the service life of the sacrificial coating. A good sealant should be able to fill out the pores

and prevent the penetration of the electrolyte through the coating. In accordance with the NORSOK M-501 standard [89], for operations below 120°C, two-component epoxy should be used. However, it is known that polymers tend to suffer from permeability problems, and they degrade with time. A promising candidate to improve the performance of standard epoxy sealants is the addition of graphene nanoplatelets. Due to its high surface area and impermeability to gases, graphene addition can potentially improve barrier properties of conventional sealants.

In this chapter, the influence of several parameters, such as coating composition, substrate as well as temperature and the addition of graphene-containing sealants on the corrosion performance of arc-sprayed coatings immersed in synthetic seawater, is investigated and discussed.

5.2 Results and discussion

5.2.1 The effect of alloy coating composition and substrate.

Figure 5-1 shows the results of the LPR measurements of several thermally sprayed coatings of different compositions applied onto glass and steel substrates during the immersion in artificial seawater at 25°C. The following coatings compositions were tested: two commercially pure aluminium alloys from 1000 series (AA 1100 and AA 1050), AlMg5% and ZnAl15%.

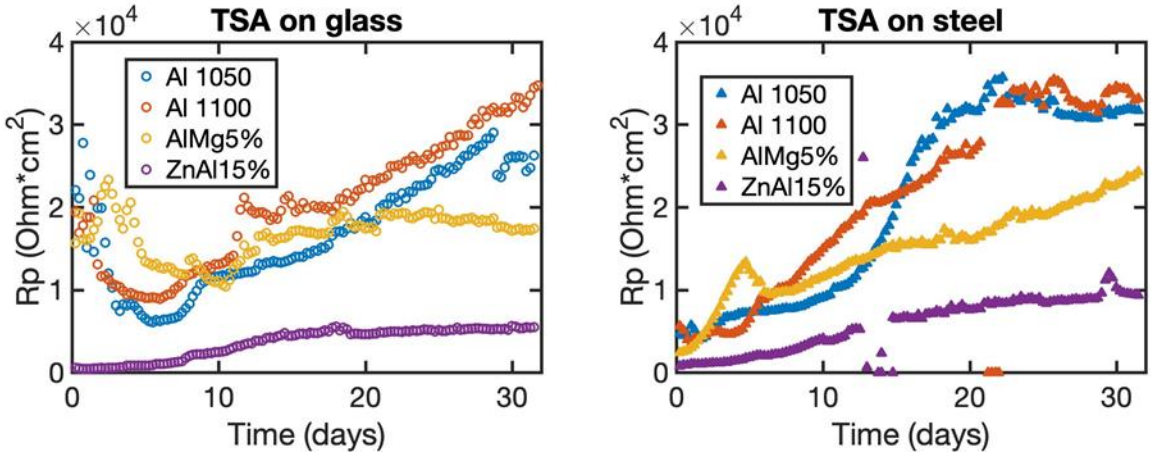

Figure 5-1 Polarisation resistance of thermally sprayed coatings deposited on glass (o) and steel (Δ) as a function of time during immersion in artificial seawater at 25℃.

It can be noticed from Figure 5-1 that the initial Rp values obtained from the coatings deposited on glass are higher than the one sprayed on steel. This can be related to the existence of a thicker oxide film on the coatings, which dissolves during the initial days of the immersion (Rp values decrease). Aluminium is a reactive metal, so it oxidises rapidly when the molten droplets come in contact with air and moisture. Since glass is significantly less conductive than steel, when molten droplets land on the substrate, they cool down at a slower rate on glass, which leads to the development of a thicker oxide layer. The oxide films which can be found on aluminium include amorphous or poorly crystalline alumina as well as crystalline γ-Al_2O_3, η- Al_2O_3 and α - Al_2O_3 [145]. Upon immersion in aerated seawater, the air-formed layer breaks down [146] and starts to dissolve, which explains the decreasing polarisation resistance. It should be noted that after approximately 10 days of the immersion, when the air-formed film was fully dissolved, the Rp values of the coatings on both substrates exhibited similar values and, in both cases, showed increasing trend until the end of

the immersion. The increase of the polarisation resistance can be explained by the build-up of corrosion deposits on the surface of the coatings.

Figure 5-1 demonstrates that AA 1050 and AA 1100 coatings exhibited a very similar evolution of the Rp values, which implies a similar rate of corrosion. Moreover, it can be observed that coatings with 5% magnesium (both on steel and glass) showed lower polarisation resistance at the end of the immersion test in comparison with pure aluminium coatings. This indicates that AlMg5% coating corroded faster. However, the fastest dissolution (and therefore the lowest Rp) was observed on the ZnAl15% coatings during the whole duration of the test.

Figure 5-2 presents the results of the potential monitoring of the coatings in artificial seawater. It can be noticed that the potential of ZnAl15% coatings sprayed on glass and steel was very stable and exhibited a very similar slightly increasing trend around -1 V. The potential of aluminium coatings, however, varied over time. For Al coatings, in almost all cases there was a significant decrease of the potential during several initial days of the immersion, followed by the potential rise. The initial decline of the potential is most probably associated with the dissolution of air-formed oxide layers and the gradual increase with the formation of new oxide/hydroxide films in the aqueous media.

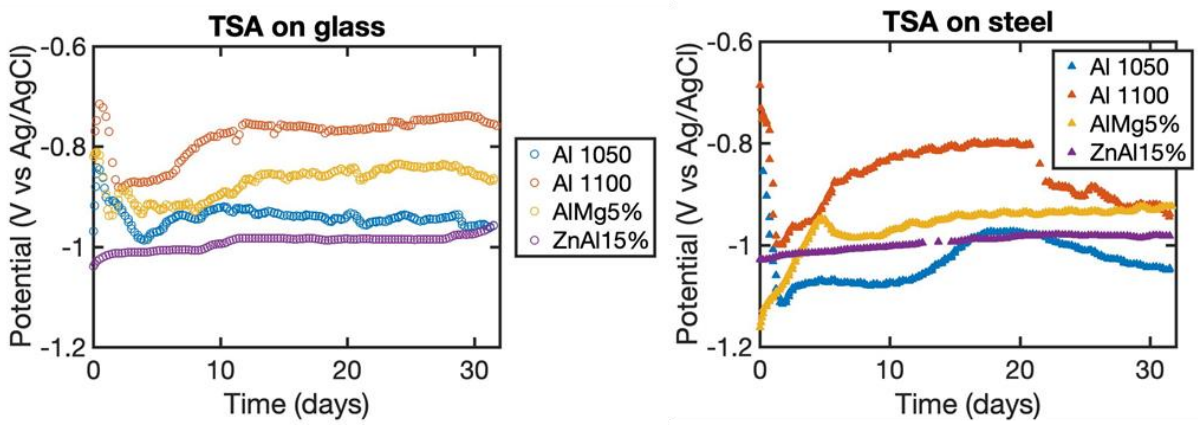

Figure 5-2 Evolution of the OCP of various thermally sprayed coatings deposited on glass (o) and steel (Δ) as a function of time during the immersion in artificial seawater at 25℃.

Different potentials among aluminium coatings can be attributed to the different contents of alloying elements. AA 1100 has higher content of Cu than AA 1050, which shifts the potential higher (potential of Cu in seawater is between −0.4 V_{SCE} to −0.3 V_{SCE} [147]). In the case of AlMg5%, one would expect the potential to be lower than AA 1100 and AA 1050, due to the presence of Mg (-1.63 to -1.6 V_{SCE} in flowing seawater [148]). It can be noticed that AlMg5% coating on steel exhibited a very low potential of approximately - 1.15 V upon the immersion in seawater, which then started to rise to approximately - 0.95 V after 5 days. The potential then fluctuated and finally stabilised at around -0.95 V. Higher potentials of arc-sprayed AlMg5% and AlMg3% coatings on steel, in comparison to pure Al coating, were also observed by Park and Kim during immersion test in natural seawater [85].

The initial potential of the AlMg5% coating is probably related to the formation of mixed oxides of Al_2O_3 and MgO during spraying. It has been previously observed on AlMg10% that the thickness and the composition of the oxides depend on the temperature of formation [149]. The oxides formed at room temperature on AlMg10% consisted mainly of aluminium oxide, while at 430°C mainly of magnesium oxide.

However, it should be noted that only one sample of each kind has been tested, therefore the differences between the OCP of the alloys give only some indications of which of them could be the most effective for the sacrificial protection of steel. For instance, the AA 1100 alloy exhibited the highest potential values and therefore would be less effective in reducing the potential of steel into the protective region (below - 0.8 V). The most promising alloys, on the other hand, seem to be AA 1050 and ZnAl15% due to low potential values. However, it can be seen from the LPR measurements (Figure 5-1), that the Rp values of ZnAl15% alloy are significantly lower than the one of AA 1050, which indicates higher self-corrosion rate. Since an ideal sacrificial coating should be able to lower the potential of steel into the region where steel is immune to corrosion, and at the same time should corrode slowly to provide protection for the required service life of the structure (which in case of offshore structures is at least 20 years), AA 1050 seems to perform best among all the alloys tested.

5.2.2 The effect of temperature and damage

5.2.2.1 Undamaged TSA coatings

Figure 5-3 shows the results of the potential measurements of TSA-coated steel immersed in artificial seawater at different temperatures. As one can see, the samples immersed in colder seawater (between 0 and 15°C) exhibited higher potential values than the samples operating in warmer electrolyte (25 and 32°C). Moreover, the potential of the samples exposed to colder seawater exhibited an increasing trend during the initial days of the immersion, followed by the significant potential drop and its subsequent gradual increase, whereas the samples exposed to the warmer solutions, did not exhibit the initial potential increase. The potential increase is most

probably associated with the growth of oxide/hydroxides layers on TSA. At warm temperatures, the solubility of the aluminium oxide is higher [150,151], and therefore - when the samples are placed in the warm solution - the dissolution of the air-formed oxide layers starts immediately after the immersion in the seawater. At colder temperatures, the kinetics of the reactions is slower, hence the dissolution starts after couple of days of the immersion.

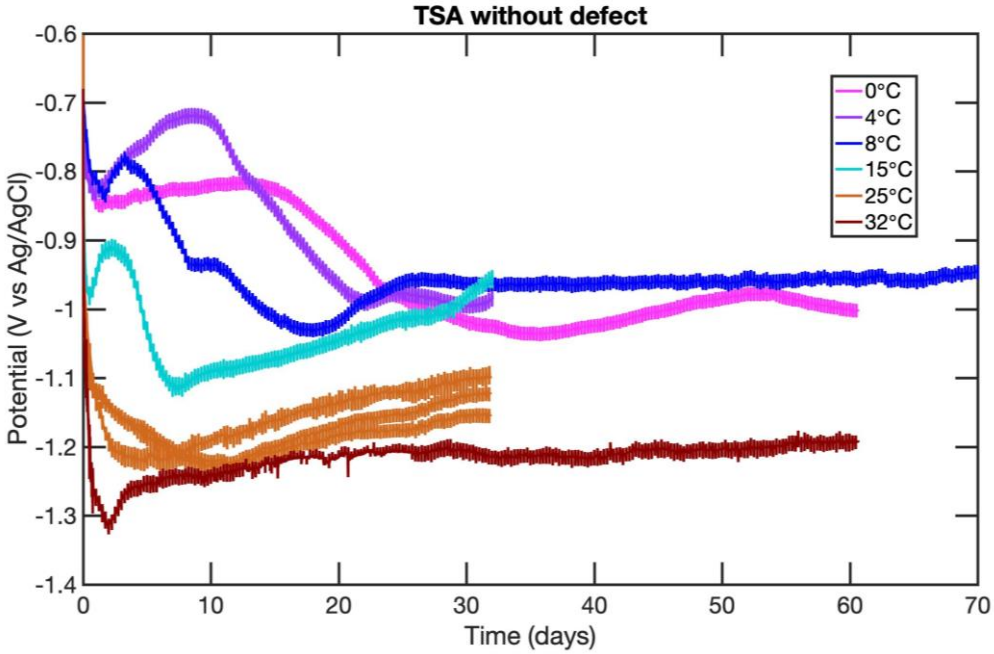

Figure 5-3 OCP of TSA-coated steel without defects at different temperatures.

Similar potential evolution at warm temperature of TSA-coated steel was observed by Lee at al. [11], who studied the behaviour of TSA in 3.5% NaCl solution at 26-28°C. Based on the potential measurements coupled with EIS analysis, they attributed the initial potential decrease to the active dissolution of the aluminium coating and the subsequent potential increase to the formation and accumulation of corrosion products, which blocked the pores inside the coating.

The higher potential values of TSA coatings at colder temperatures are consistent with the measurements performed on the solid Al wires (Chapter 4). However, it should be

noted that the potential measured on the TSA coatings is lower than the one measured on the wires. The possible explanation could be the porous nature of the thermally sprayed coatings. In case of the wires, the whole surface area of the samples is exposed at the same time. In case of the TSA coatings, most probably this is not the case and it takes time for the solution to penetrate the coatings through the pores and defects. When the seawater penetrates the coating, “new” surfaces of the coating are successively being exposed to the electrolyte and therefore the potential of the coating remains lower for a longer period of time.

5.2.2.2 Damaged TSA coatings

The images of the TSA-coated steel with 5% of the coating removed to simulate a defect, after the immersion in artificial seawater at different temperatures are shown in Figure 5-4. It can be observed that apart from the samples exposed at 4°C, all the artificially made defects in the coatings are covered with white deposits. The samples which were exposed at 4°C look different. They have significantly fewer deposits in the defects and the sample immersed for 70 days contains noticeable amount of rust on the exposed steel. It is known from the literature that those deposits are calcareous in nature and their precipitation on the exposed steel can be attributed to the increased pH near the surface of the electrode (as a result of the cathodic reactions). High concentration of OH^- ions triggers the precipitation of $Mg(OH)_2$ and $CaCO_3$.

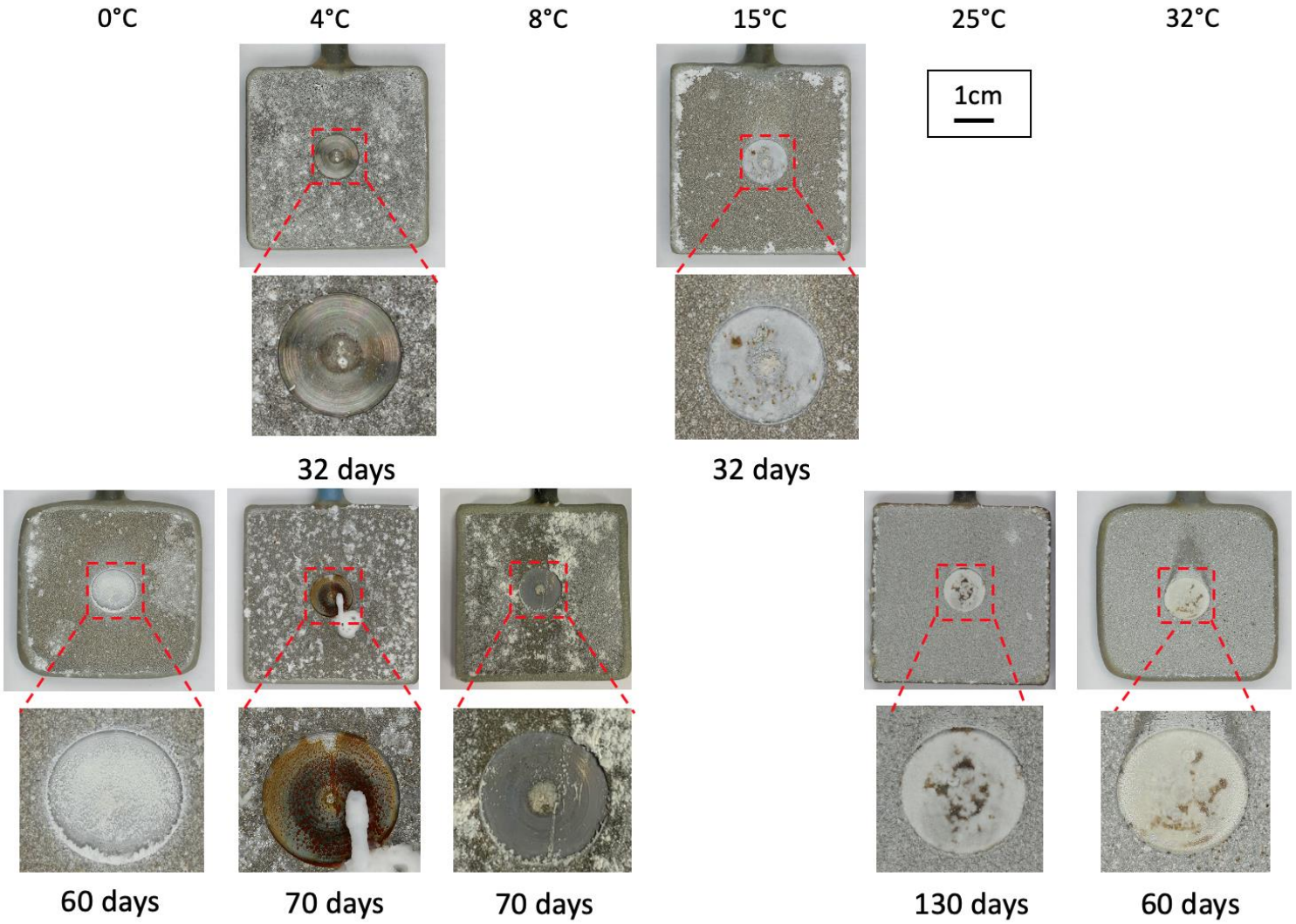

Figure 5-4 Images of TSA-coated steel with defects after the completion of the immersion tests.

The potential measurements of the samples shown in Figure 5-4 are presented in Figure 5-5. It can be observed that - apart from the samples immersed at 4°C – the potential of all samples stabilised at around -0.9 V. The two samples immersed at 4°C (in separate experiments) showed a different behaviour, with the potential stabilising at around -0.75 V. Higher potential correlates well with the lack of calcareous deposits. When steel is covered by the deposits, cathodic reactions are inhibited, which results in the decrease of the potential. At 4°C, calcareous deposits did not form, and the potential was significantly higher. The reason for the lack of deposits at 4°C is not clear and requires further investigation.

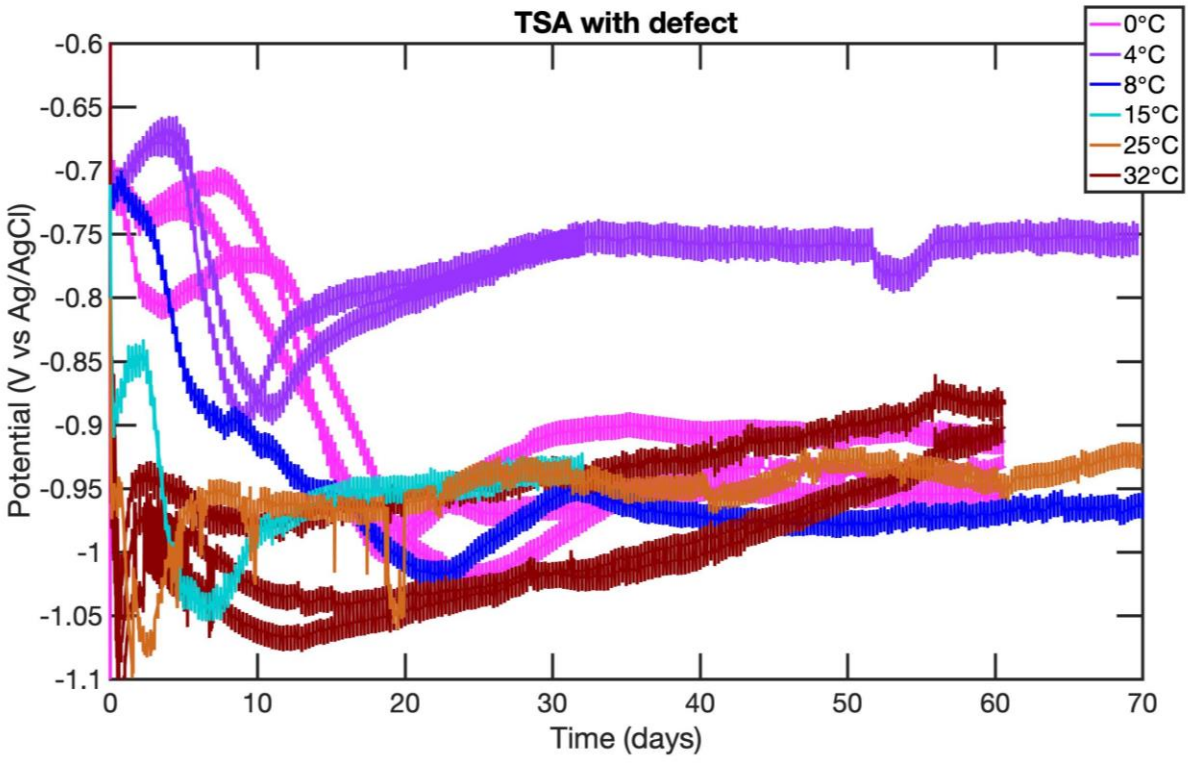

Figure 5-5 OCP of TSA-coated steel with defects immersed in artificial seawater at different temperatures.

Comparing Figure 5-3 and Figure 5-5, one can notice that the potential of the samples with defects is higher compared with samples without damage. When some part of the coating is removed, a mixed potential is established between the Al coating and the steel substrate, therefore the potential of the damaged samples is higher. In case of samples without defects, it is possible that there is some limited amount of interconnected porosity in the coating. However, once the coating starts to corrode, corrosion products are forming on the coating, blocking the pores and preventing the contact between the electrolyte and the substrate.

To verify the effect of temperature on the potential of TSA-coated steel with defects another immersion test was conducted. In this experiment, three TSA-coated steel samples (with 5% defects) as well as a bare steel sample were immersed in seawater at 0°C. Unfortunately, after 52 days the temperature control was lost (due to a power cut) and the temperature of the solution has risen to room temperature (RT). This rather unfortunate event revealed some interesting information regarding the influence of temperature on the OCP and Rp of the samples and gave an opportunity to explore the subject further. After the power cut, the samples remained immersed at RT for 13 days. Subsequently, the temperature of the test solution was cooled down back to 0°C. The results are shown in Figure 5-6 (a) and (b). It can be noticed that when the temperature of the seawater changed from 0°C to RT and stabilised, the potential of the TSA-coated samples was 40 mV lower, and the potential of bare steel was 20 mV lower than at colder temperature. The decrease of the temperature resulted also in the decrease of the Rp values indicating higher corrosion rate at RT. It should be noted that the Rp of bare steel remained stable at RT, while the Rp of TSA-coated samples started to rise, most probably due to the formation of calcareous deposits. Once the

temperature was cooled down back to 0°C, Rp of bare steel sample went back up to the previous level (approximately 1.5 x 10^4 Ω•cm^2). Rp of TSA-coated samples, however, increased significantly from 2 x 10^4 to 7 x 10^4 Ω•cm^2. The rise of the Rp was accompanied by the potential increase from -0.97 to -0.84 V, which indicates that the decrease of the temperature resulted in inhibition of anodic reactions (dissolution of the TSA coating) due to lower solubility of aluminium, as discussed in Chapter 4.

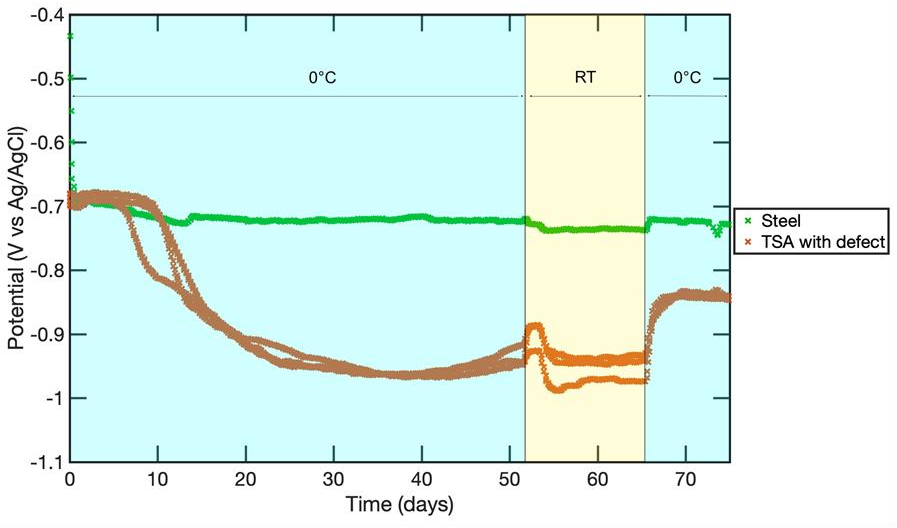

(a)

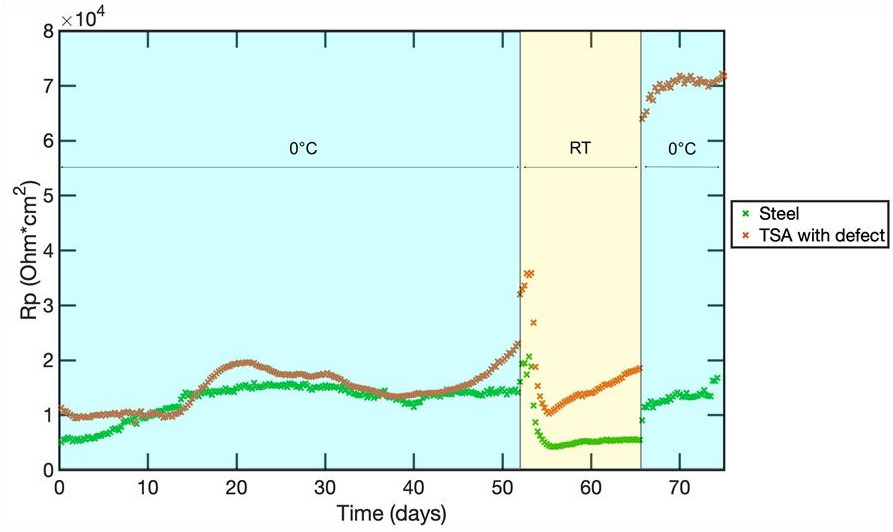

(b)

Figure 5-6 Evolution of the OCP (a) and Rp (b) of TSA-coated steel with a defect as well as bare steel immersed in artificial seawater as a function of temperature.

Another possible explanation of the potential rise at colder temperature could be the dissolution of deposits which have formed in the defect at RT, when the temperature was changed back to 0°C. This explanation was proposed by Lin and Dexter [116] who observed an increase of the current density on cathodically polarised steel when temperature of seawater was decreased from 25 to 3°C (Figure 2-16). They attributed the increase of the current to the dissolution of aragonite ($CaCO_3$). However, very high

Rp values and presence of white deposits in the defects after the completion of the experiment, points towards a strong influence of the anodic activity of the aluminium coating.

Other studies focusing on the effect of temperature on the precipitation of calcareous minerals during cathodic protection of steel revealed that fewer deposits are formed at low temperatures (below 10°C) [116] and they are less protective in nature [115]. However, the results gathered in this project do not fully follow the above statements. It can be observed from Figure 5-7 that small amounts of deposits have formed at 4 and 8°C inside the defects on TSA-coated steel. Milling marks can be easily noticed, which indicates poor coverage of the steel by the deposits. Moreover, noticeable signs of rust are evident on the sample exposed at 4°C from Figure 5-4. Those results agree with the previous observations. However, significant amounts of white deposits can be seen inside the defect on the sample exposed at 0°C and no signs of corrosion of steel can be seen on the sample. Scanning electron microscopy (SEM) combined with energy dispersive X-Ray (EDX) analysis revealed that deposits formed at 0°C are predominantly Mg-rich. This can be seen from Figure 5-8, which depicts the distribution of elements within the artificially made defects (in TSA coatings) after the immersion in seawater at different temperatures.

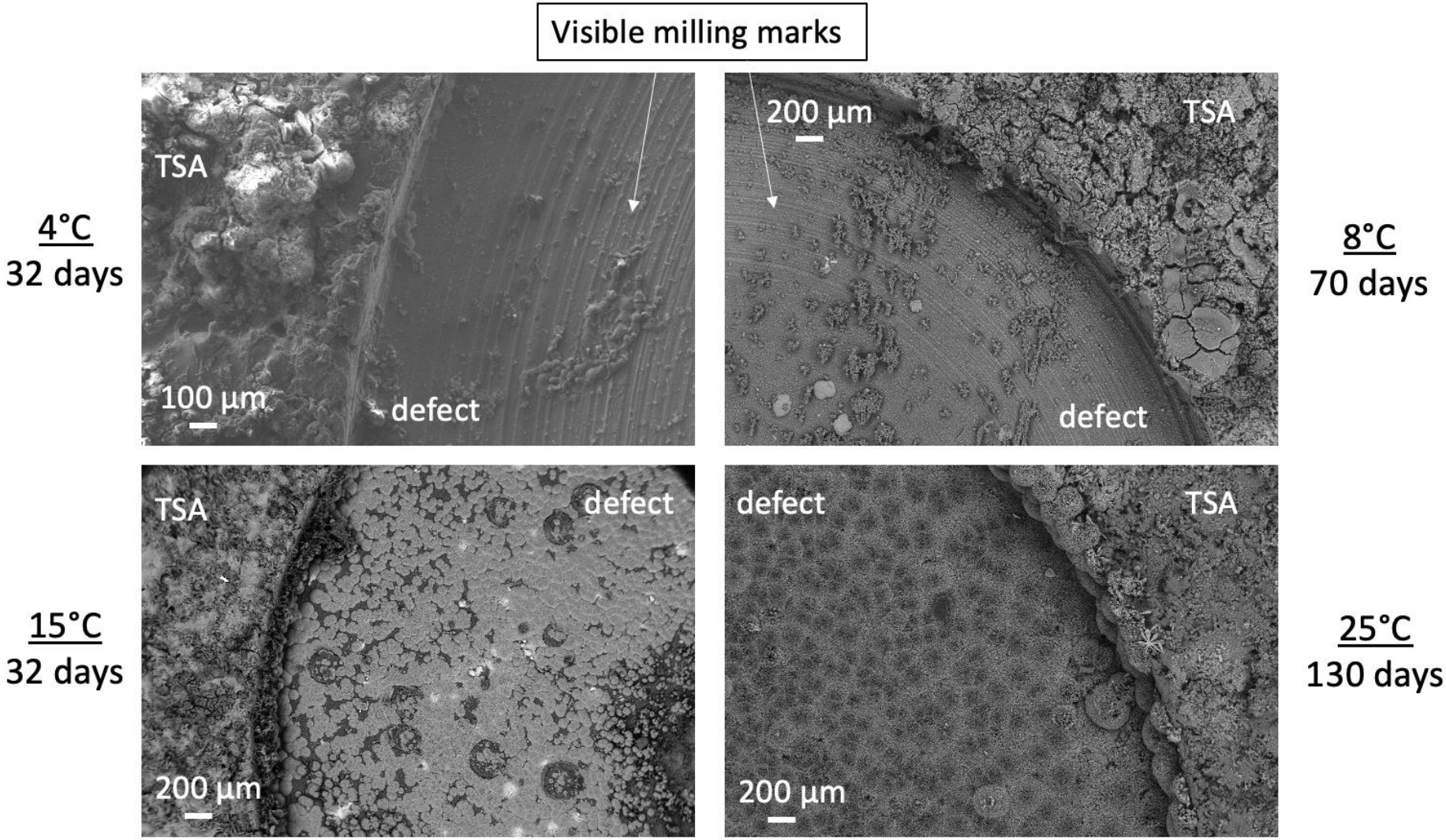

Figure 5-7 SEM images showing defects in TSA coating covered, or partially covered, with calcareous deposits, which formed during the immersion in artificial seawater at different temperature.

It is likely that greater amount of deposits formed at 0°C is associated with very low solubility of $Mg(OH)_2$ and the significant potential drop during the immersion (to approximately -1 V). At this potential, both oxygen reduction and hydrogen evolution occur on the steel surface, which results in higher production rate of OH^- ions and, consequently, more alkaline pH. Calculated pH values required for the precipitation of calcareous deposits found in the literature [152]: 7.3-8.7 for $CaCO_3$ and 9.3-11.25 for $Mg(OH)_2$ explain enhanced precipitation of $Mg(OH)_2$ at 0°C in comparison with 4°C, where the potential did not decrease below -0.9 V, and therefore the dominant cathodic reaction was the reduction of oxygen.

SEM analysis also revealed that Ca-rich deposits have formed at all temperatures tested, however, in different amounts. This can be seen from Figure 5-8 and Figure 5-9 which shows the EDX maps collected from the defect region of the sample corroded at 4°C - under higher magnification. It can be noticed that during the immersion at 0, 4 and 8°C, small Ca-rich deposits formed in localised spots of the defects. At 15°C, however, even though the duration of the test was shorter than the one at 0 and 8°C (only 32 days), Ca-rich minerals precipitated in larger quantities and in the form of big agglomerates, which can be seen in Figure 5-10.

Mg-rich deposits were detected at all temperatures except 25°C, however, it is possible that they precipitated underneath the dense and uniform $CaCO_3$ layer, which can be seen in Figure 5-10 and Figure 5-7. The presence of Mg-rich deposits, identified as brucite $(MgOH)_2$, located underneath Ca-rich layer (of aragonite) was previously reported by Echaniz et al. [10], who studied artificially damaged TSA coating on steel during a 90-day immersion in simulated seawater environments at 26°C.

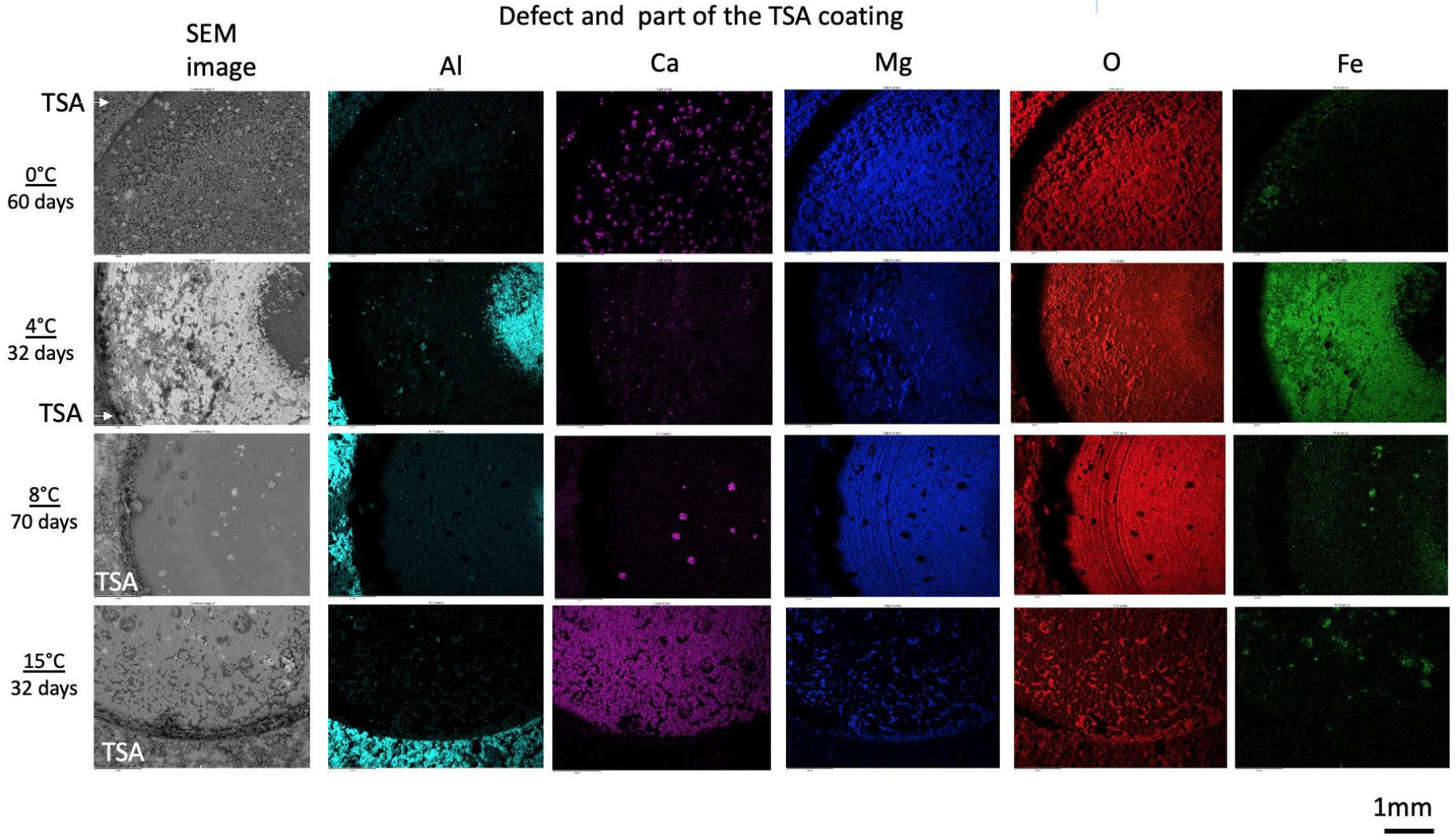

Figure 5-8 EDX maps of several TSA-coated samples with defects after immersion in artificial seawater at different temperatures. Maps show distribution of elements inside the defects.

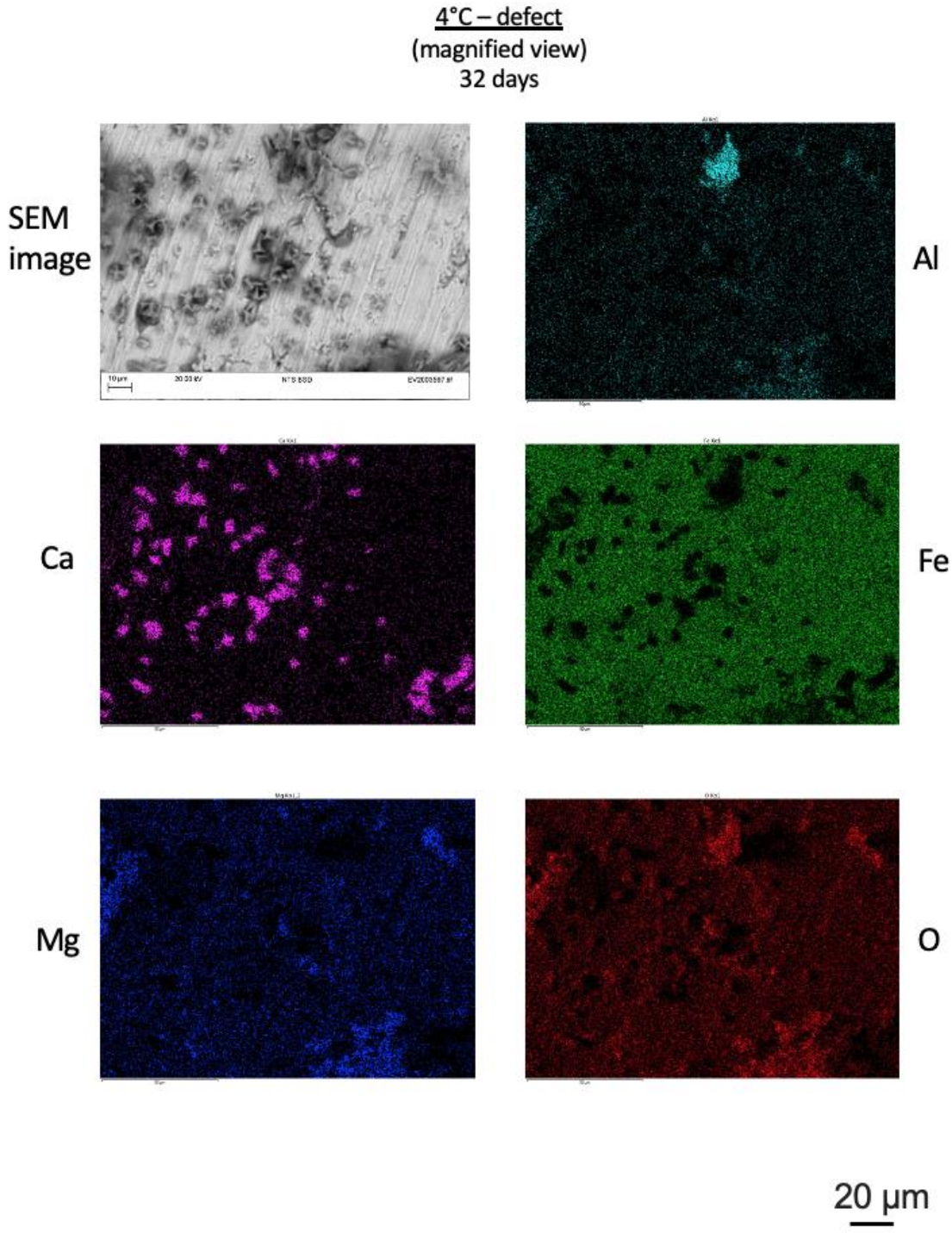

Figure 5-9 EDX maps of deposits formed during the immersion in artificial seawater at 4℃, under higher magnification. Maps show distribution of elements inside the defects. Presence of small Ca-rich deposits is clearly seen.

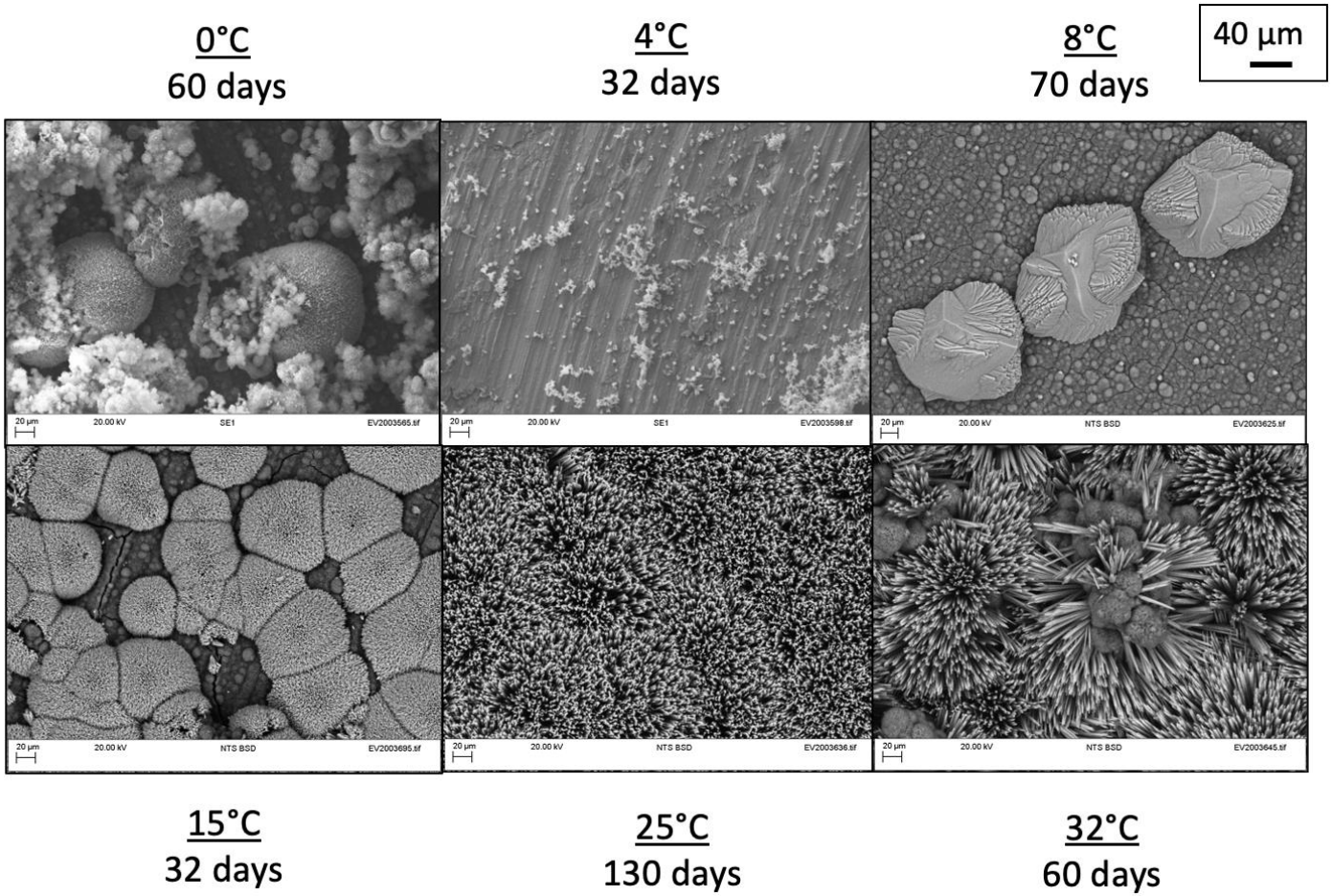

Figure 5-10 SEM images of deposits formed on the exposed steel on the TSA-coated samples with defects after the immersion in artificial seawater at different temperatures.

Raman spectroscopy was used to identify the minerals which have formed on the surface of exposed steel. The results are presented in Figure 5-11. Point measurements which were conducted on different samples are shown in colours, whereas the reference spectra in black. It can be noticed that aragonite ($CaCO_3$), with characteristic peaks of approximately 1085, 705, 203 and 155 cm^{-1} [153], was detected on all the tested samples. This is in line with the detection of Ca using EDX analysis (Figure 5-8). Moreover, according to the literature [154], aragonite can be identified by its orthorhombic structure and needle-like appearance. This morphology was observed on the surfaces of the samples exposed at 0,15, 25 and 32°C (Figure 5-10). Ca-rich deposits which formed at 8°C, looked different though, and it was most probably a different $CaCO_3$ polymorph, such as calcite, which is known to have a rhombohedral structure and cubic appearance [154].

Raman spectroscopy confirmed the presence of aragonite and brucite but also detected another mineral which matches the reference spectrum of Quintinite ($MgAl_2(OH)_{12}(CO)_3 \bullet 3H_2O$), with characteristic peaks of 1062, 973 and 559 cm^{-1} [155]. Quintinite is a one of the hydrotalcite group minerals. EDX mapping (shown in Figure 5-12) confirmed the presence of Al and Mg in the middle of the defects.

Raman spectroscopy of the deposits formed on the coatings detected felsobanyaite ($Al_4(SO_4)(OH)_{10} \bullet 4H_2O$) with the strong peak at 979 cm^{-1} [156], at all temperatures tested. Hydrotalcite ($Mg_6Al_2CO_3(OH)_{16}(H_2O)$, on the other hand, was only detected at warm temperatures (25 and 32°C). Dawsonite ($NaAl(CO_3)(OH)_2$), with its strong peak at 1506 cm^{-1} [156], was only detected at 0°C. A reference spectrum matching the 1150 cm^{-1} peak could not be found using available reference libraries, however this peak could be corresponding to chloraluminite ($AlCl_3 \bullet 6H_2O$) [156].

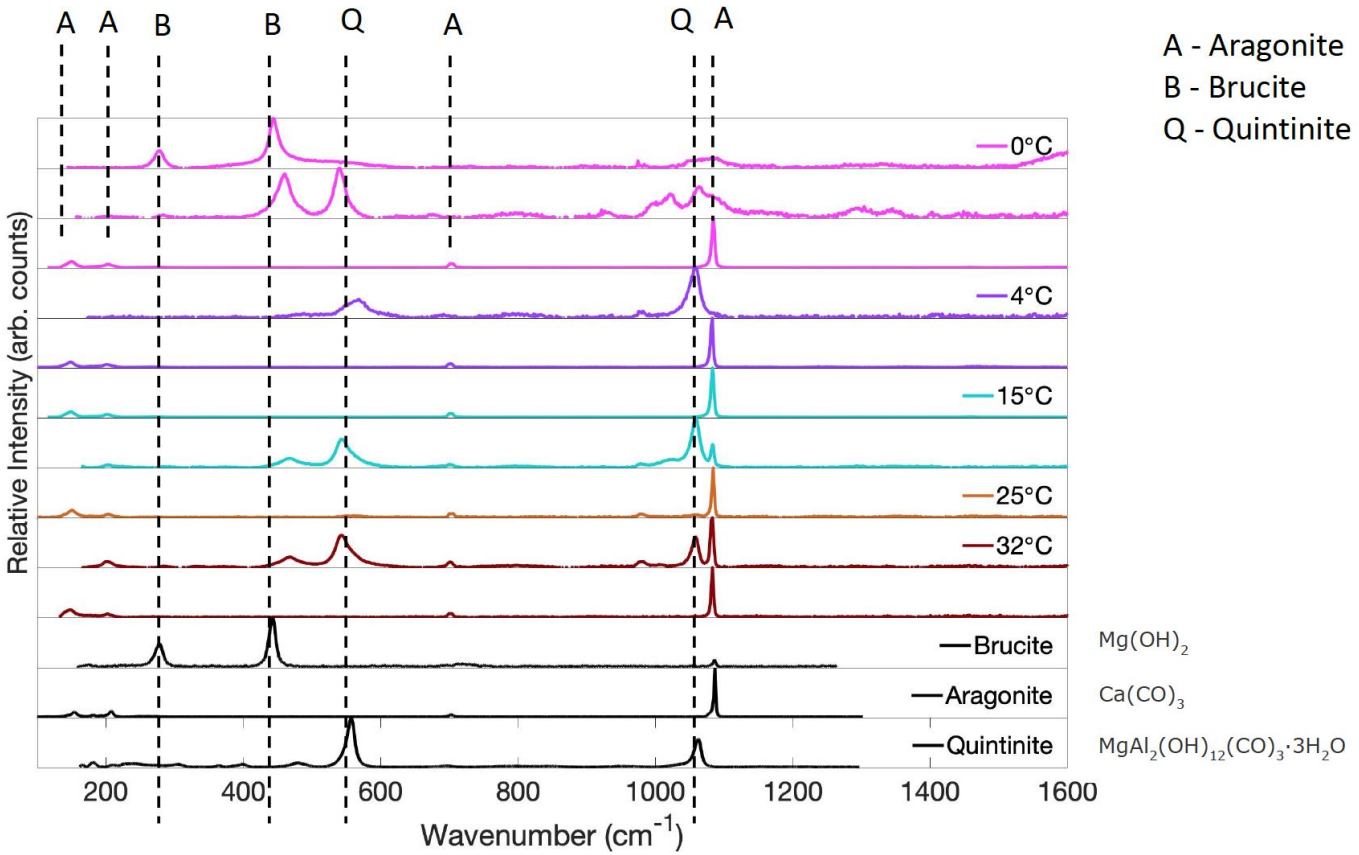

Figure 5-11 Raman spectroscopy analysis performed on deposits which formed on the exposed steel on the TSA-coated samples with defects during the immersion in artificial seawater at different temperatures. Different colours correspond to spectra collected from samples immersed at different temperatures. Black spectra were taken from RRUFF database and correspond to the reference minerals.

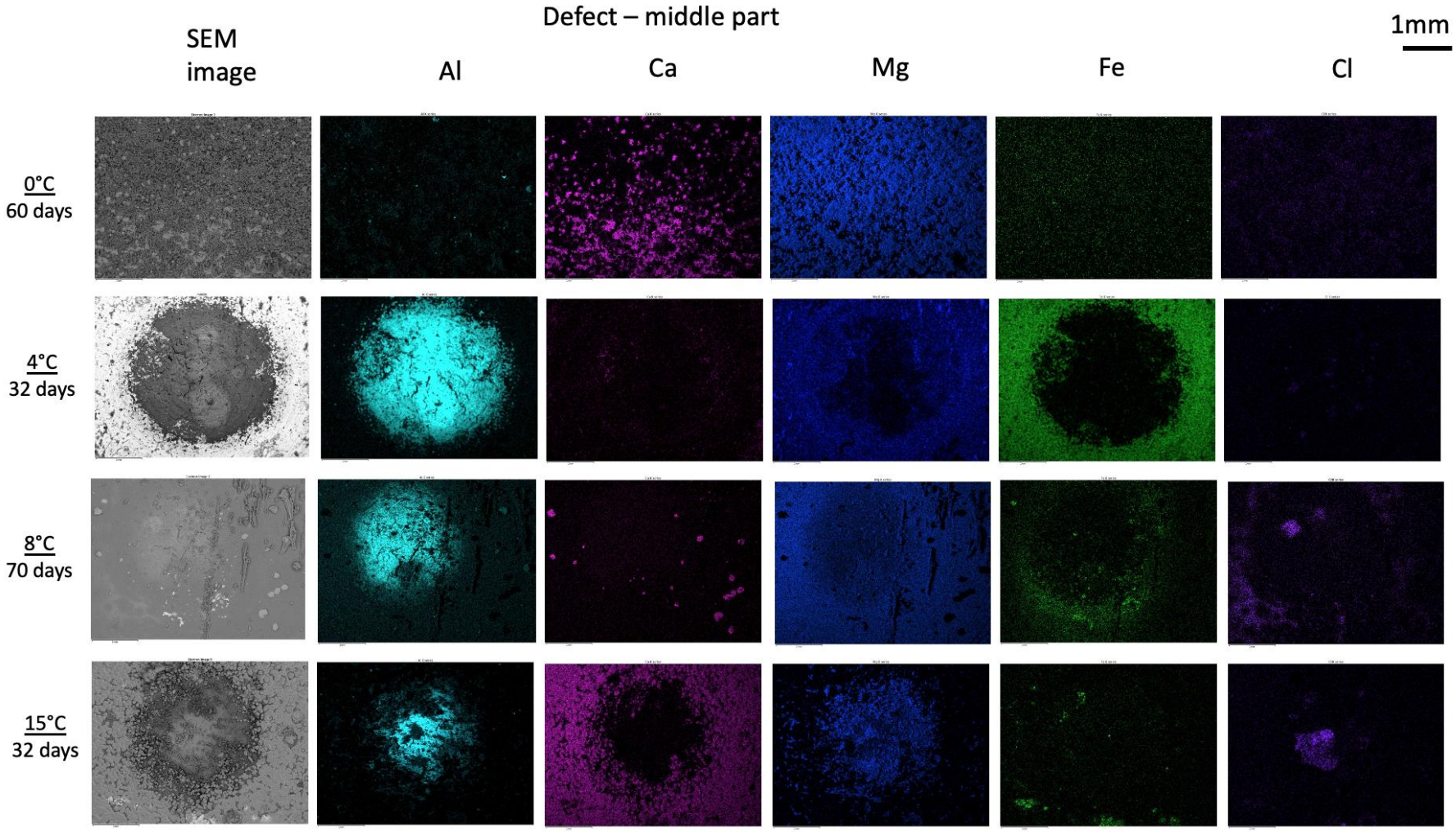

Figure 5-12 EDX maps of several TSA-coated samples with defects after immersion in artificial seawater at different temperatures. Maps show distribution of elements inside the defects.

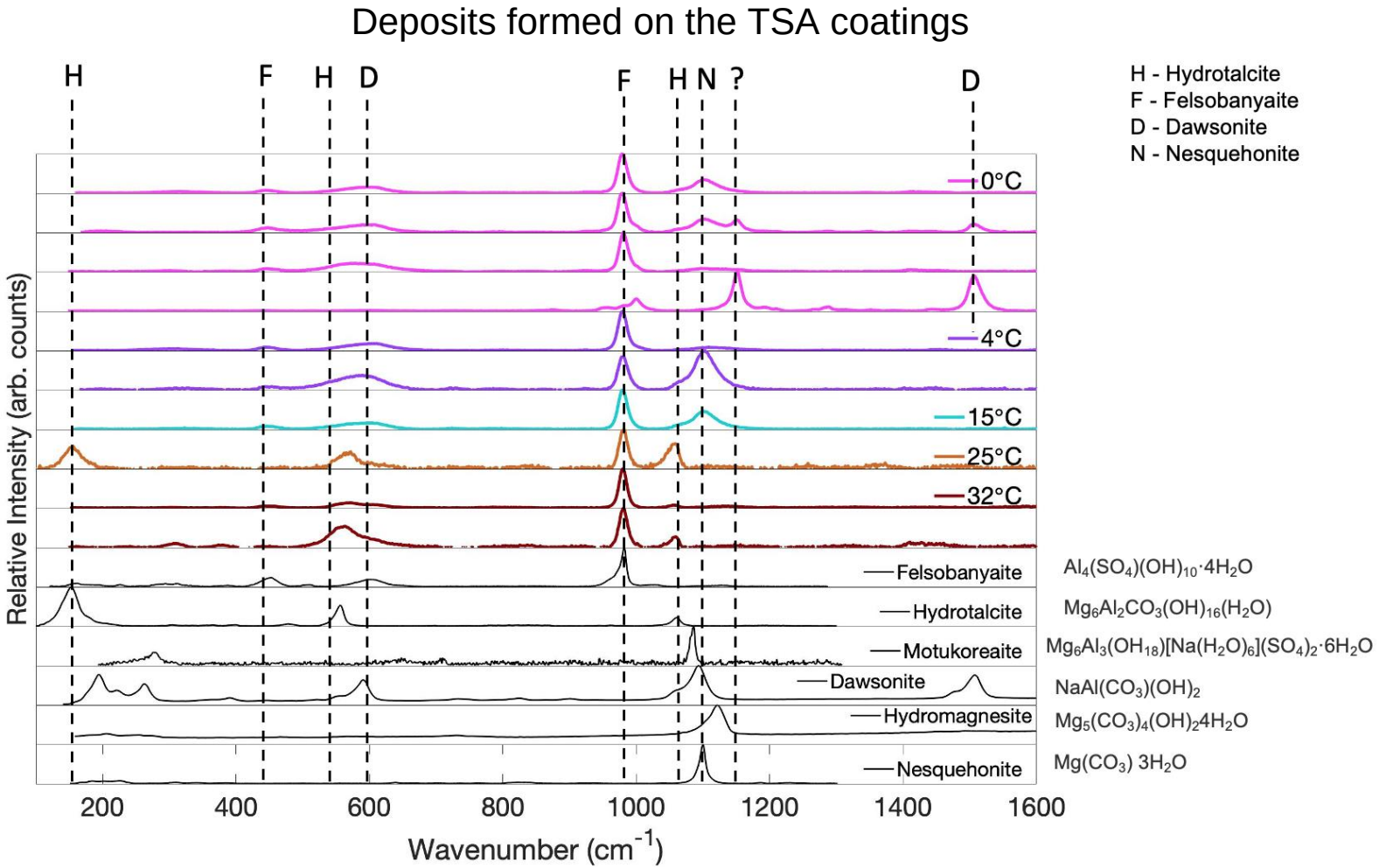

Figure 5-13 Results of Raman spectroscopy analysis performed on deposits which formed on the exposed steel on the TSA - coated samples with defects during the immersion in artificial seawater at different temperatures. Different colours correspond to spectra collected from samples immersed at different temperatures. Black spectra were taken from RRUFF database and correspond to the reference minerals.

5.2.3 The effect of sealing

5.2.3.1 Samples without defects 25°C – full immersion

Figure 5-14 shows the results of the potential measurements of TSA-coated steel with epoxy-based sealants and paints with and without addition of graphene nanoplatelets (GNP) as well as unsealed TSA-coated steel during the immersion in artificial seawater at 25°C.

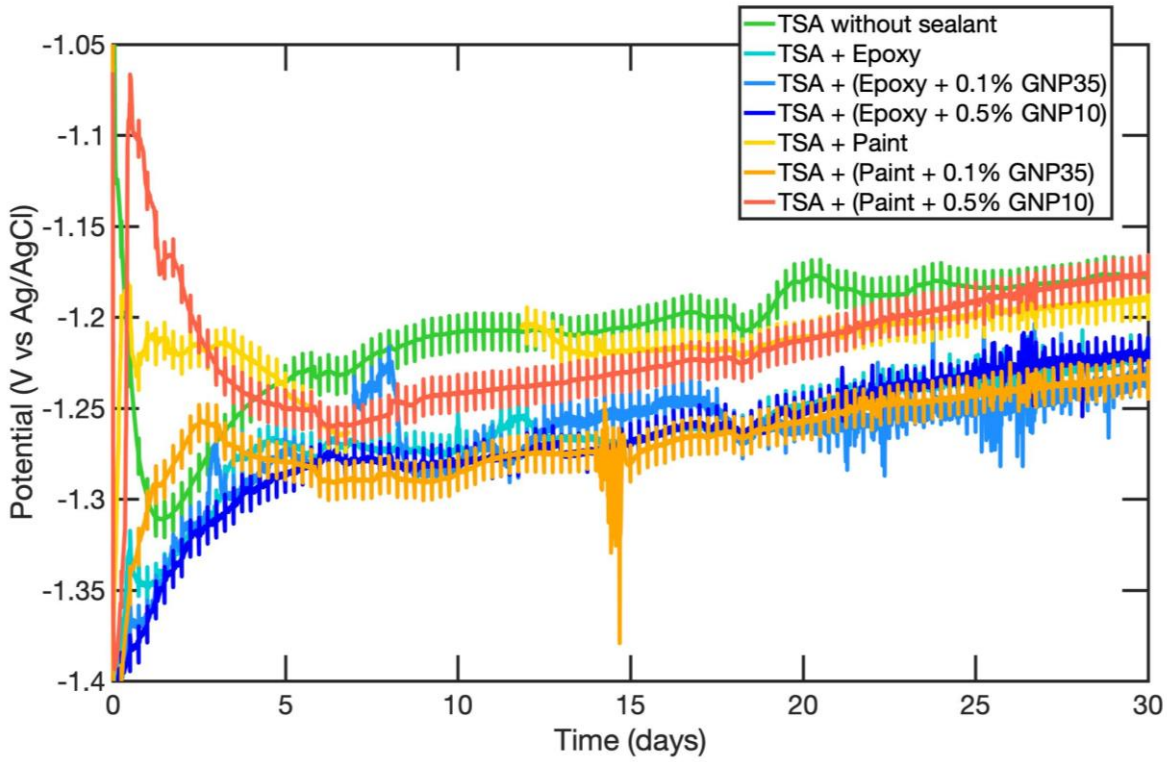

Figure 5-14 Evolution of the OCP of TSA-coated steel with several sealant systems with and without addition of graphene nanoplatelets (GNP) as a function of time during immersion in artificial seawater at 25℃. Vertical lines represents the potential sweep during the LPR measurements.

It can be noticed that during the first 4 days of immersion, the potential of samples sealed with paints was higher than those sealed with epoxy. However, after 4 days the potential of all the samples reached similar values between -1.3 V and -1.2 V and started to increase gradually until the end of the experiment. The potential of all epoxy - sealed samples and the sample sealed with paint +0.1% graphene stabilised

at - 1.25 V after 30 days of immersion, whereas all other samples stabilised at -1.2 V. It can be observed that between the 5th and 25th day of immersion, the potential of the TSA-coated steel without any sealant was the highest. Since during the application of sealants, the excess of the material was scraped off and small amounts of the coatings were left exposed, it is possible that during the immersion the sealed samples suffered from localised corrosion which resulted in more active potential values. The unsealed sample, on the other hand, had all the coating exposed and passivated at a faster rate.

The results of the LPR measurements of sealed and unsealed TSA samples on steel are presented in Figure 5-15. It can be noticed that the lower Rp values were recorded on the TSA-coated samples without any sealant. This indicates that this sample corroded at a faster rate than the sealed samples. However, it should be pointed out, that Rp values presented in the Figure 5-15 are expressed as a function of projected surface area of the TSA coating. In the case of the sealed samples, the true surface area of the coating contacting the electrolyte was probably much smaller.

It can be also seen from Figure 5-15 that the Rp values of the samples sealed with epoxy-based sealants are significantly higher than other samples and the highest values were recorded on the samples sealed with the addition of 0.1% graphene to the epoxy. Interestingly, the addition of 0.5% of graphene did not result in the increase of the Rp values compared with the sample sealed with epoxy without any graphene. It is possible that the addition of more graphene leads to its aggregation inside the epoxy and its uneven distribution within the epoxy layer. Since the role of the graphene nanoplatelets is to increase the barrier properties of the sealant (by increasing the pathway length of corrosive species diffusivity through the epoxy), it is important to

obtain an even distribution of the nanoplatelets. Most probably that was achieved when 0.1% graphene was added into the epoxy.

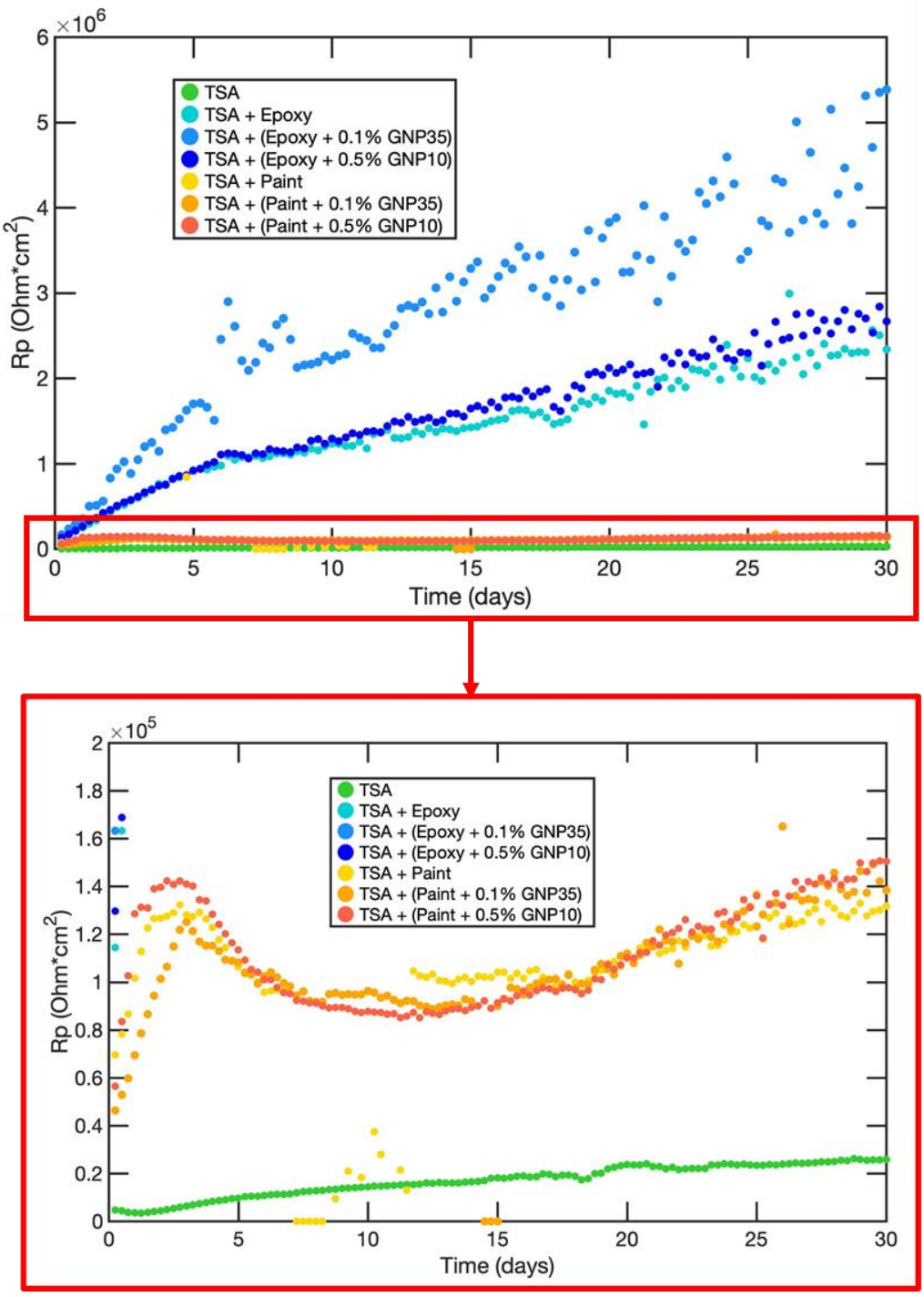

Figure 5-15 Evolution of Rp of TSA-coated steel sealed with various sealers with and without graphene nanoplatelets (GNP) and unsealed TSA-coated steel as a function of time during immersion in artificial seawater at 25℃. Rp expressed as a function of projected surface area of the TSA coating.

Work conducted by other researchers on epoxy/graphene composite showed that the best mechanical properties, resulting from the best dispersion within the epoxy matrix, were obtained with 0.3% graphene loading. Higher graphene content of 0.5% resulted in nonuniform dispersion and aggregates formation [106]. Moreover, other studies focusing on the corrosion performance on graphene/epoxy coatings confirmed that the addition of too much graphene into the epoxy might have detrimental effect on the corrosion performance of the coating [105,107,108]. A greater amount of graphene, and therefore large surface area, leads to stronger van der Waals forces and π- π interactions [109] which cause agglomeration of the nanoplatelets. It is possible that graphene dispersed better in epoxy than in paint and therefore it increased the barrier properties of the epoxy. In the paints, however, most probably the GNP agglomerated and caused formation of small defects.

The paint, although epoxy-based, also contains some additives, such as titanium dioxide, barium sulphate and the solvent (xylene). It is possible that those substances adversely impact graphene dispersion within the polymer matrix. This hypothesis was also provided by other authors who studied an epoxy paint reinforced with 0.5% reduced graphene oxide and graphite applied on steel [157]. Their work revealed a reduced corrosion performance of the paint with the fillers, in comparison with the neat coat, during the immersion and cycling fog tests in saline environment.

In the current study, a worse performance of graphene-reinforced paint was not detected by the visual inspection of the samples after the test. None of the samples showed any signs of the deterioration of the coatings. All the samples were visually very similar before and after the immersion, as illustrated by Figure 5-16. However, it should be highlighted that in the current study paints were applied onto the aluminium coating, not directly onto the steel substrate.

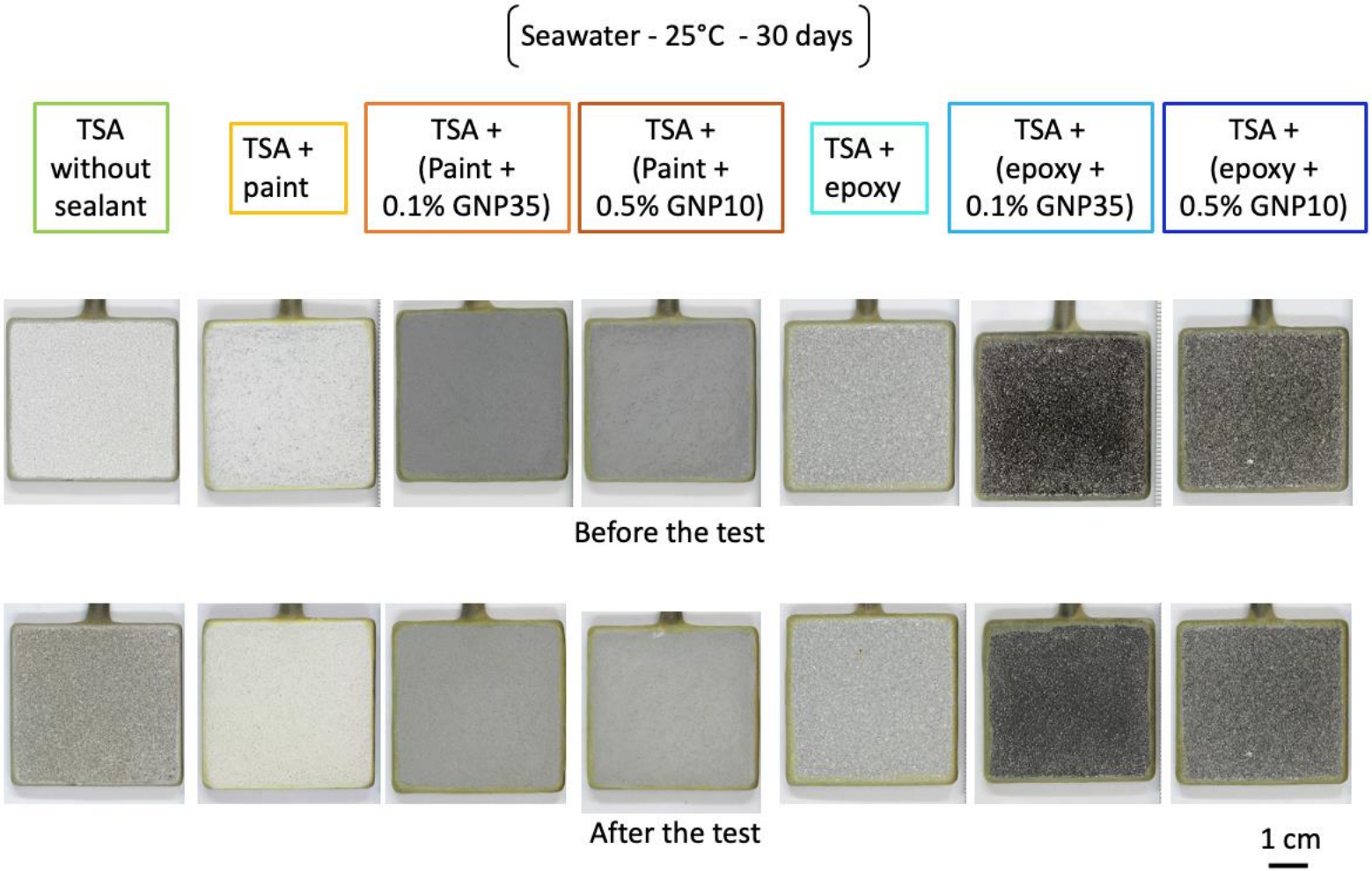

Figure 5-16 TSA-coated steel samples with sealants and a reference sample without a sealant before and after the immersion in artificial seawater for 30 days at 25 ℃.

5.2.3.2 Samples with defects at 25°C – full immersion

Figure 5-17 shows the results of the potential measurements of TSA-coated steel with epoxy-based sealants and paint sealants with and without the addition of GNP as well as unsealed TSA-coated steel and bare steel during the immersion in artificial seawater at 25°C. All the TSA-coated samples had 5% of the coating removed to simulate its defect.

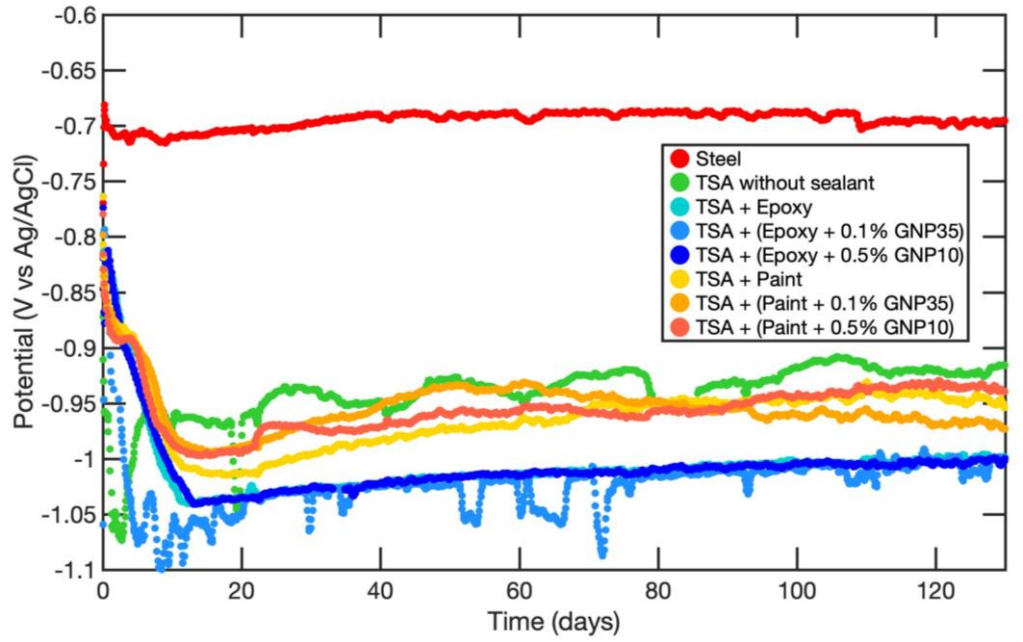

Figure 5-17 Evolution of the OCP of TSA-coated steel with 5% coating removed to simulate a defect, sealed with various sealants (with and without addition of graphene) and bare steel as a function of time during immersion in artificial seawater at 25℃.

It can be observed that the potential of the bare steel stabilised quickly at around - 0.7 V, whereas the values of the potential of the TSA-coated steel samples were significantly lower during the whole duration of the experiment. Moreover, it can be noted that the potentials of the samples sealed with epoxy reached the lowest and very similar values after approximately 20 days of the immersion. The potential of the samples sealed with paint exhibited potentials close to the potential of the unsealed sample. The results of the LPR measurements (Figure 5-18) revealed that the samples

protected with the epoxy exhibited higher Rp values than the samples sealed with paints. Higher Rp values combined with lower potential values indicate inhibition of the cathodic reactions. Since the size of the cathode (exposed steel) of all the samples was initially the same, the inhibited cathodic reactions could be related to the thicker or more protective calcareous deposits forming on the steel.

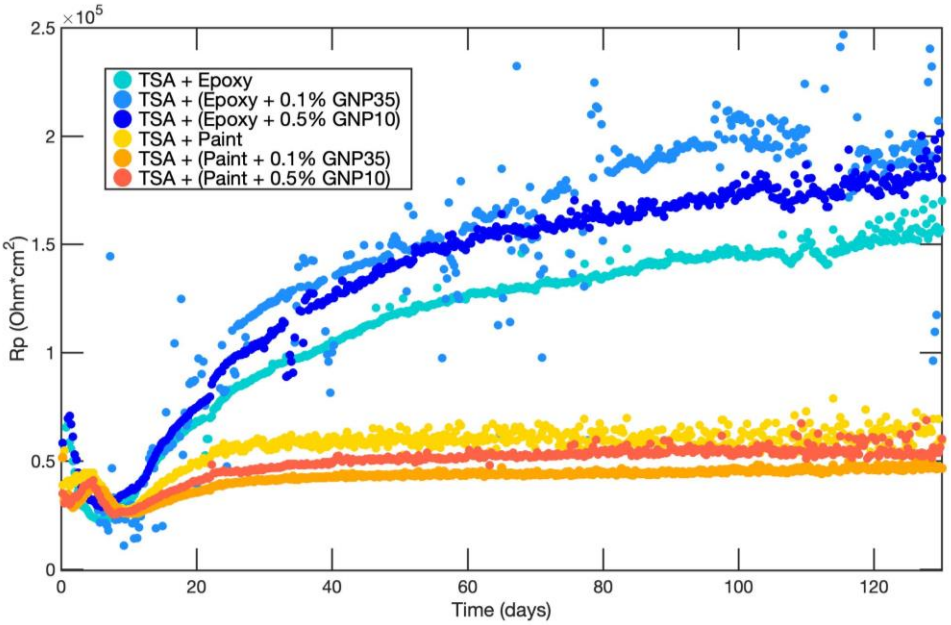

Figure 5-18 Evolution of Rp of TSA-coated steel with 5% coating removed to simulate a defect, sealed with various sealants (with and without addition of graphene) as a function of time during immersion in artificial seawater at 25℃.

The results of the LPR measurements (Figure 5-18) also confirm the effects of the graphene addition to the sealants. It can be observed that the samples sealed with the graphene-loaded epoxy exhibited higher Rp values which indicate lower corrosion rates. Samples sealed with the graphene-loaded paints, however, showed slightly lower Rp values than the neat paint.

The highest Rp values were recorded on the sample sealed with 0.1% ultra-low-density (0.004 g/cm^3) graphene GNP35. Graphene in this sealant is in the form of very thin crumpled sheets with high surface area. The GNP10 graphene is of moderate density (0.06 g/cm^3) and surface area. It seems that lower amount of GNP35 in epoxy

provides better corrosion resistance properties than GNP10. This is probably related to its better dispersion within the matrix and better blocking characteristics towards electrolyte and oxygen diffusion, as discussed in the previous section.

The appearance of the TSA samples with sealants is shown in Figure 5-19 and Figure 5-20. It can be noticed that all the defects are fully covered with calcareous deposits and the epoxy-sealed samples seem to have more deposits coming out of the defects and starting to expand on the coatings. This is in line with the inhibition of cathodic reactions and therefore lower potential and higher Rp values. Moreover, Figure 5-20 revealed that the corrosion products forming on the epoxy sealed coatings are quite small and uniformly distributed across the coating. Corrosion deposits on the paint-sealed TSA formed in a few big agglomerations.

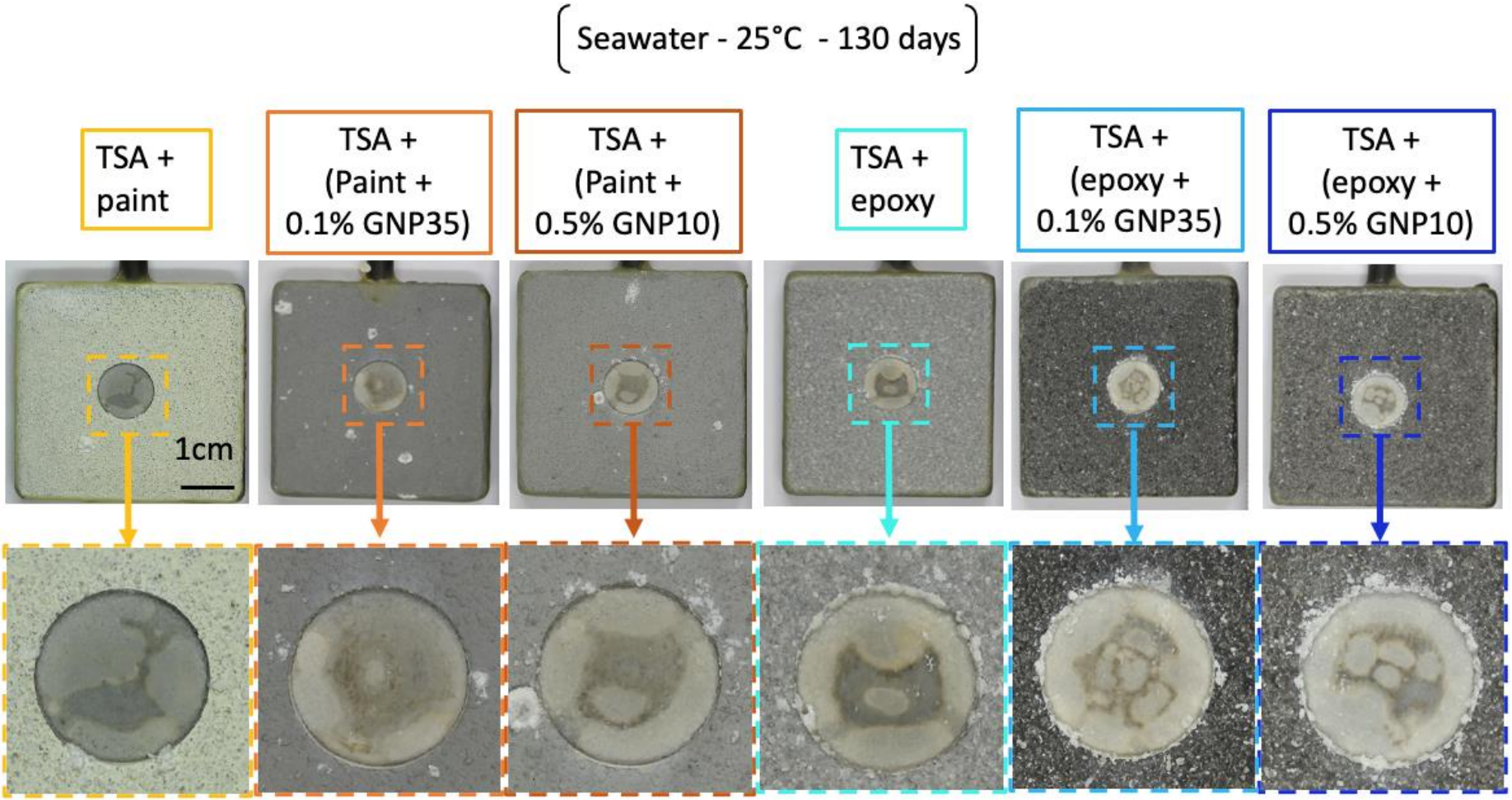

Figure 5-19 TSA-coated steel samples with defects and sealants after the immersion in seawater at 25℃ for 130 days. Magnified views present defects in the TSA coatings (made before the immersion in the seawater) fully covered with calcareous deposits.

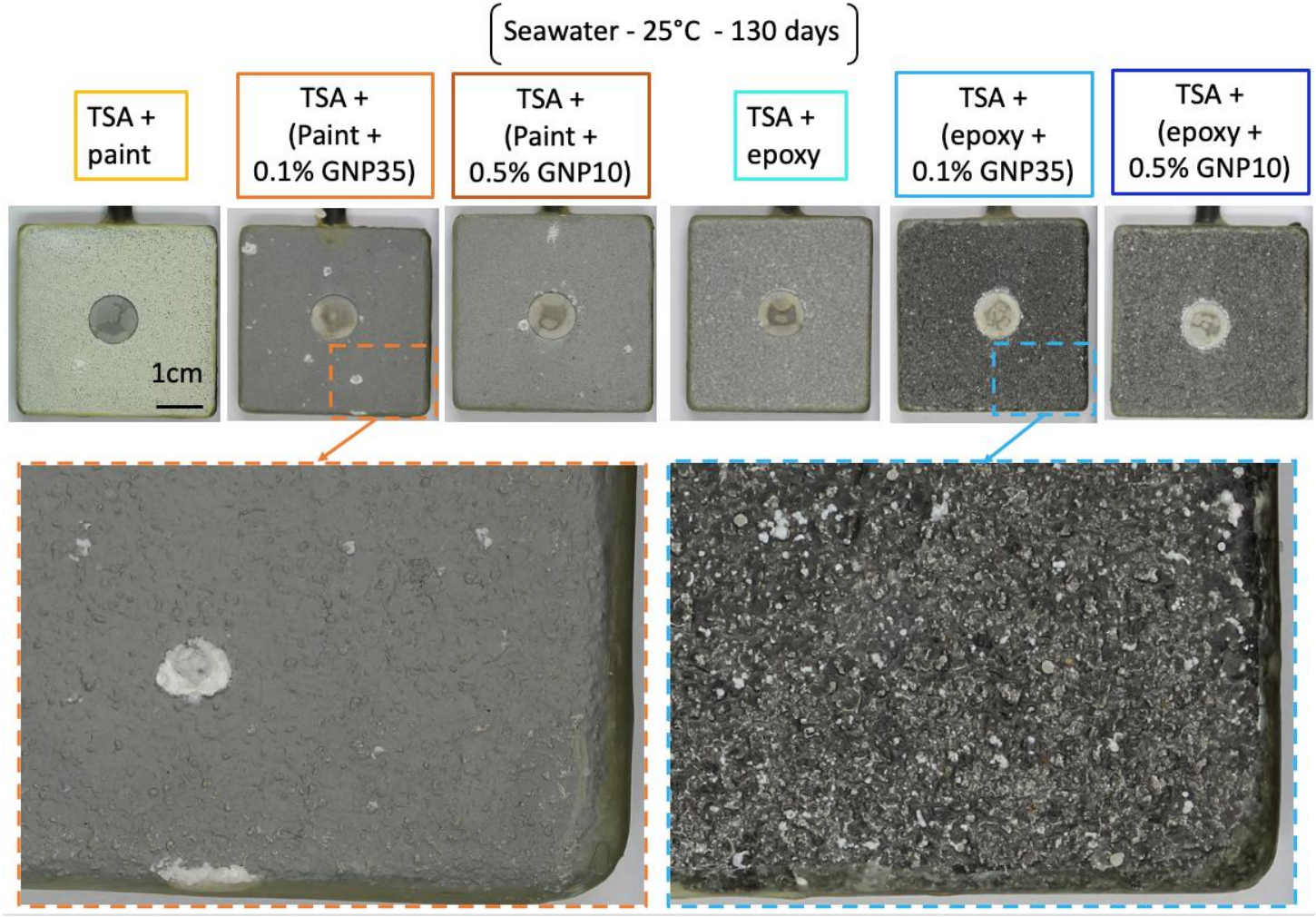

Figure 5-20 TSA-coated steel samples with defects and sealants after the immersion in seawater at 25℃ for 130 days. Magnified views show sealed coatings with corrosion products formed during the immersion. Deposits on paints formed in bigger agglomerations in several spots, whereas on epoxy they were distributed uniformly across the whole coating as small granules.

To verify the presence of larger amounts of calcareous deposits formed on the samples sealed with epoxy, cross-sections of the samples were prepared as schematically shown in Figure 5-21. It can be observed that the samples were cut vertically to examine the upper and bottom part of the defects.

SEM images of cross-sections of defects are shown in Figure 5-22. One can observe a thicker layer of deposits on the epoxy-sealed sample. This can be even better seen from Figure 5-23 and Figure 5-24, where the distribution of Ca and Mg is shown in the form of layered EDX maps. It is clearly visible that the Ca layer is thicker on the epoxy-sealed sample. Moreover, Mg-rich layer precipitated underneath the Ca-rich layer. This was related to the local pH in the vicinity of the cathode. Upon the immersion in seawater, a galvanic couple is established between the aluminium layer and the exposed steel, where Al becomes a net anode and steel a net cathode. Due to its lower potential, Al starts to dissolve preferentially (which can be seen by the significant potential drop in Figure 5-17) and this action is accompanied by cathodic activity at the exposed steel. This leads to a local increase of pH, due to the production of OH^- ions during reduction of oxygen and water on steel. This increased pH triggers precipitation of brucite, which is known to form at pH range 9.3-11.25 [152]. Once it is formed, pH lowers and aragonite starts to precipitate at pH range 7.3-8.7 [152].

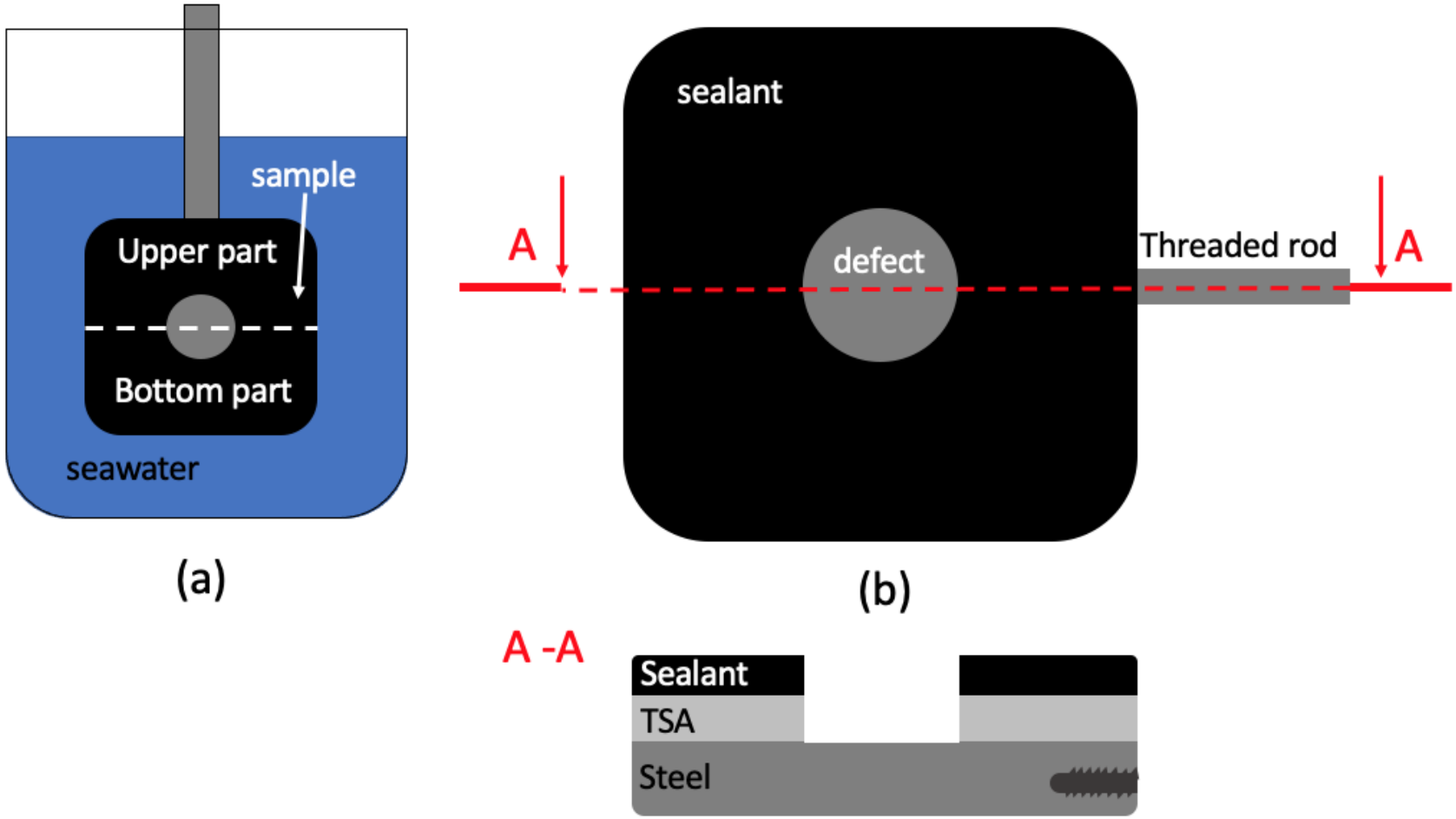

Figure 5-21 Schematic representation of the orientation of the samples during immersion tests (a) and direction of cutting for metallographic preparation (b).

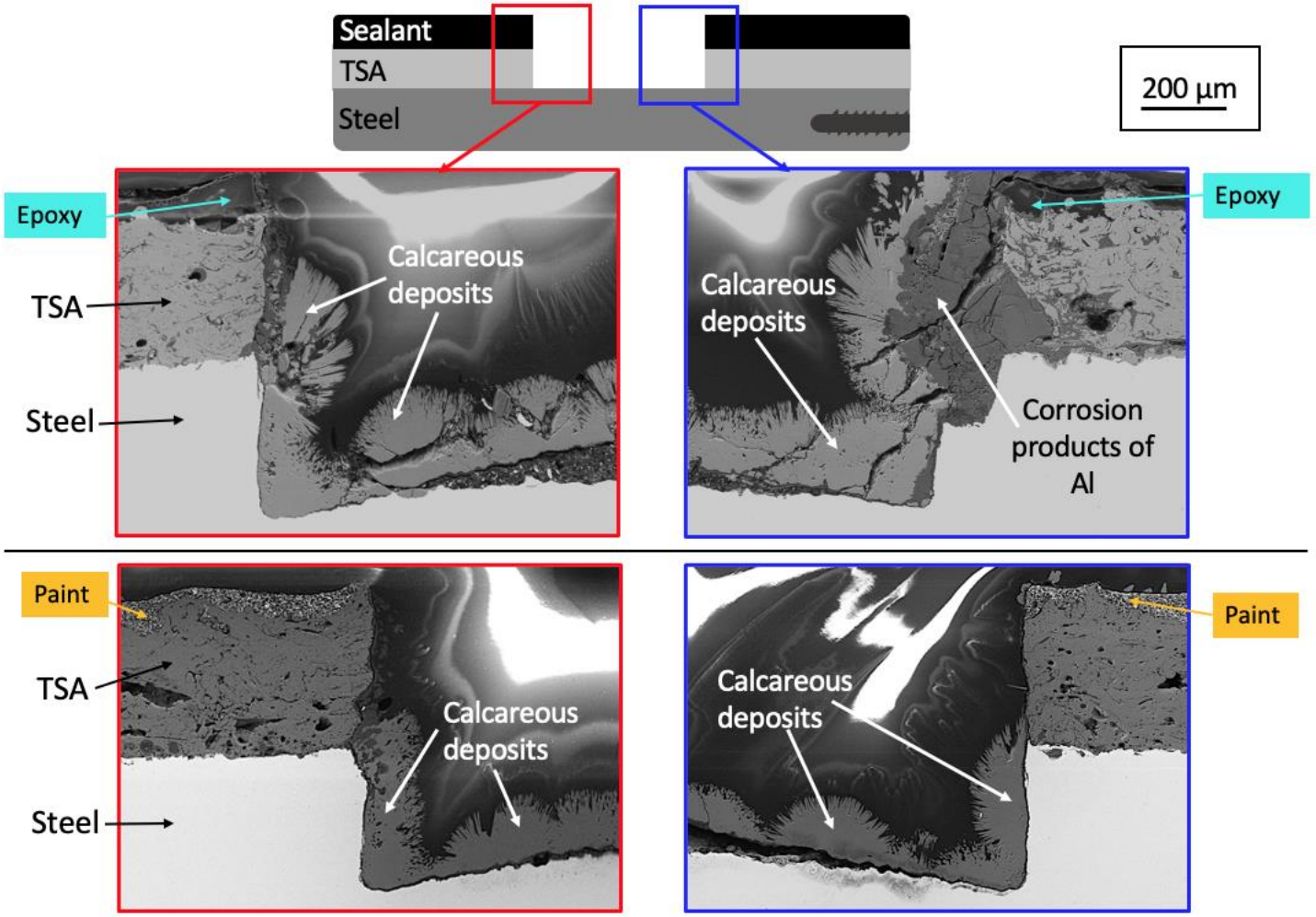

Figure 5-22 SEM images of the cross-sections of TSA-coated steel sealed with epoxy and paint after the immersion in seawater at 25℃ for 130 days. The images show the bottom and upper part of the defects.

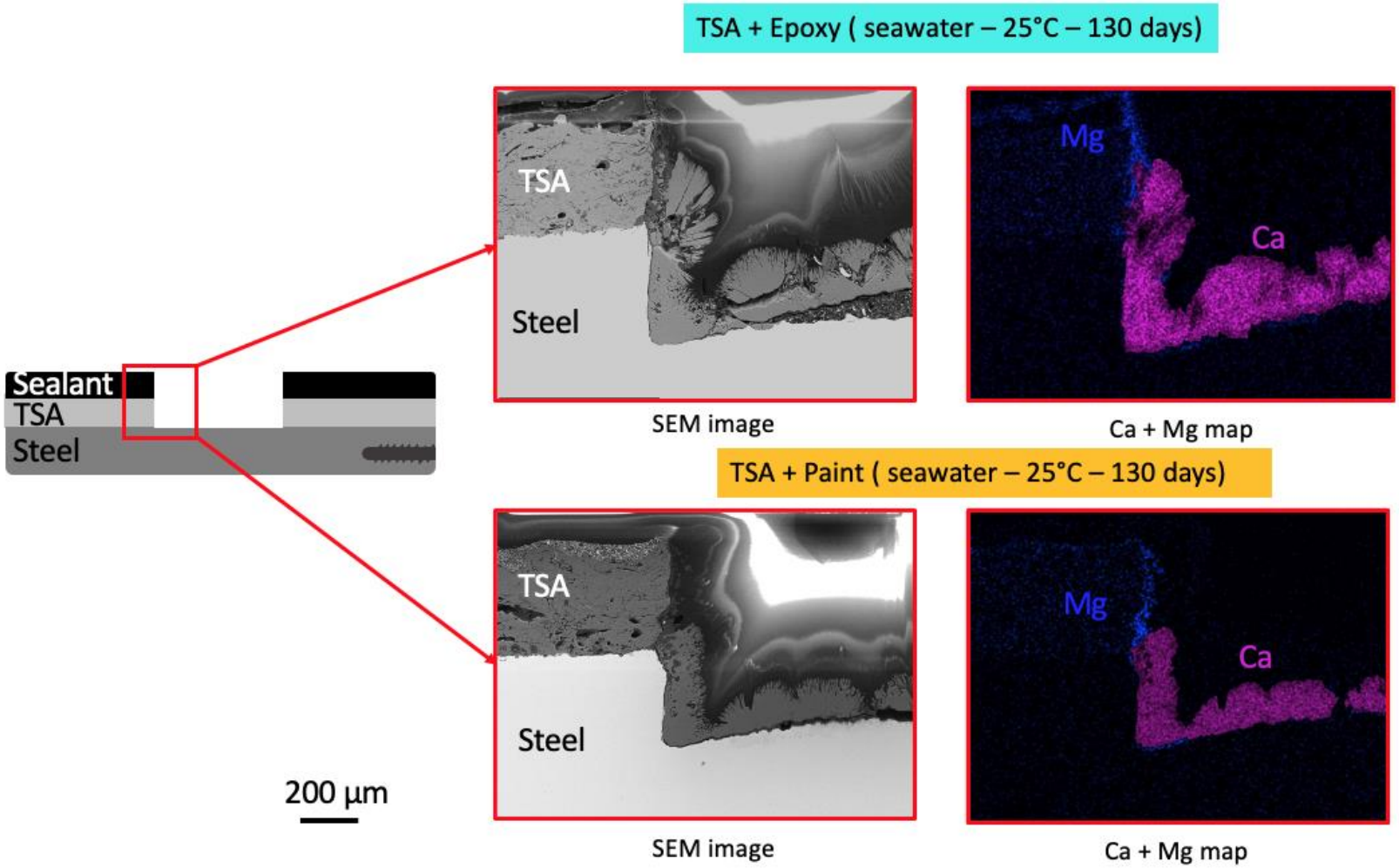

Figure 5-23 SEM images and EDX maps showing distribution of Mg and Ca in the bottom part of the defect inside TSA-coated steel after the immersion in seawater at 25℃ for 130 days.

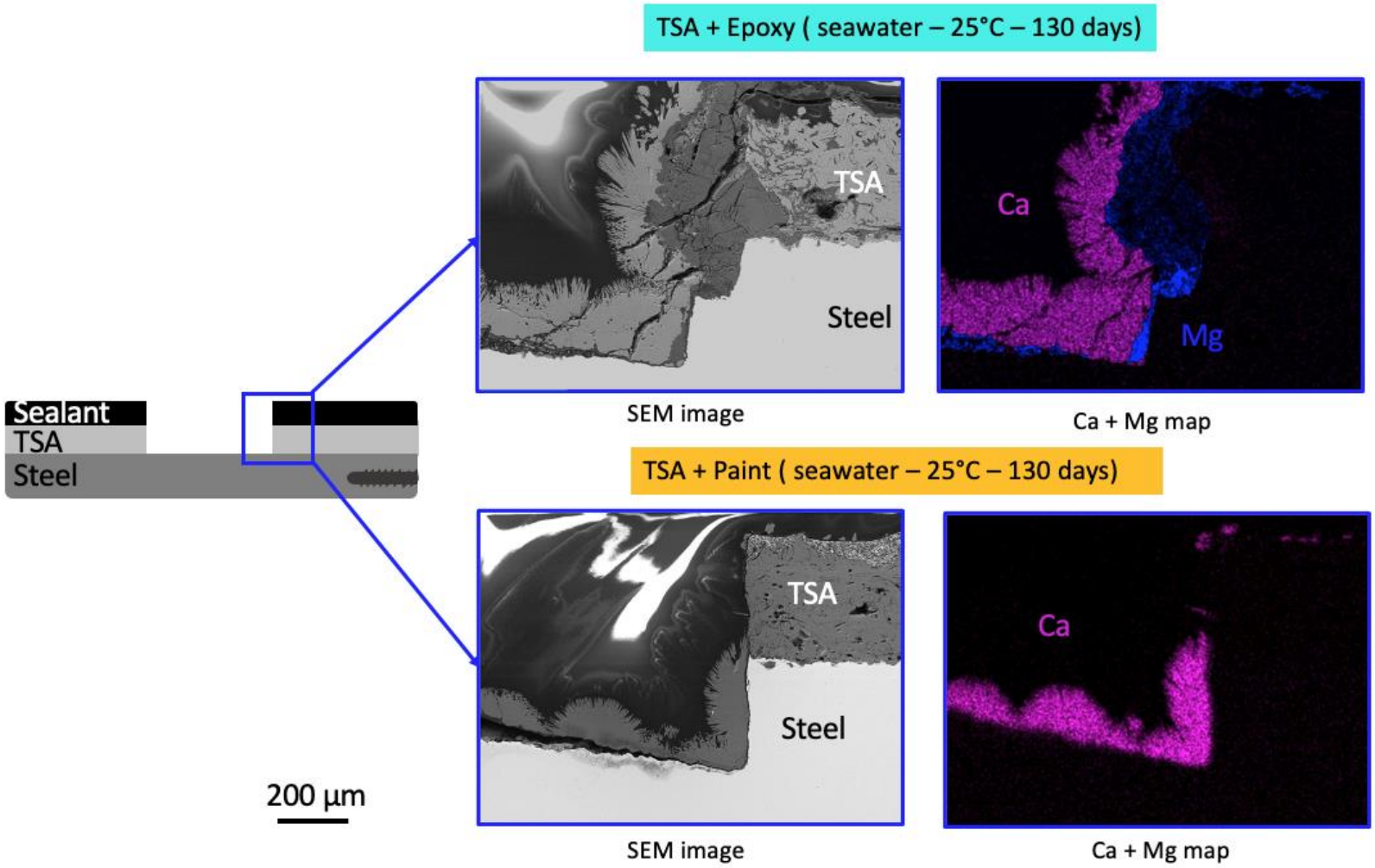

Figure 5-24 SEM images and EDX maps showing distribution of Mg and Ca in the upper part of the defect inside TSA-coated steel after the immersion in seawater at 25℃ for 130 days.

It should also be noted that Mg was not only detected as $Mg(OH)_2$, but it was also found together with Al - in the vicinity of the TSA coating (Figure 5-25). Most probably Mg and Al co-precipitated in the form of hydrotalcite-like mineral. This is in line with Raman spectroscopy analysis, which revealed the presence of $Mg_6Al_2CO_3(OH)_{16}(H_2O)$ on the sample corroding at 25°C (Figure 5-13).

EDX analysis of the cross-section of the TSA-coated steel sealed with paint (Figure 5-26) revealed similar distribution of elements to the epoxy-sealed sample, but it is clear that the amount of deposits is much smaller. It is also evident that less amount of the aluminium coating has dissolved during the immersion, which resulted in lower cathodic activity.

Higher dissolution rate of the aluminium coating under the epoxy was also demonstrated by the electrochemical measurements. It can be seen that the potential of epoxy-covered samples was more active (lower) and at the same time the Rp values were higher. Since in case of the sealed samples most of the TSA was covered by the organic layer, the Rp response was dominated by the steel. Therefore, higher Rp values indicate lower corrosion rate of steel, which can be explained by thicker layer of calcareous deposits.

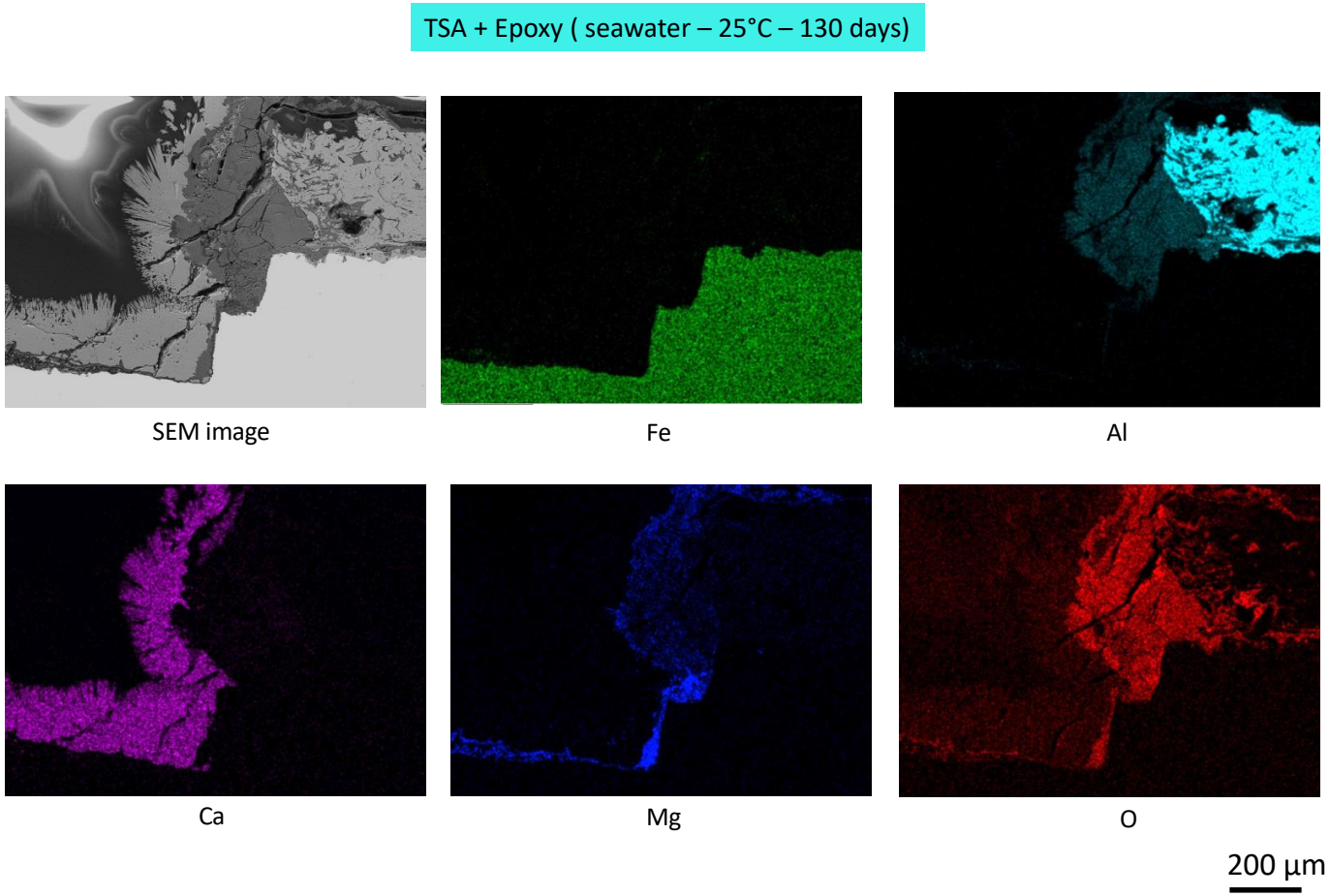

Figure 5-25 EDX maps of the upper part of the defect of the TSA-coated steel sealed with epoxy, after the immersion in seawater at 25℃ for 130 days.

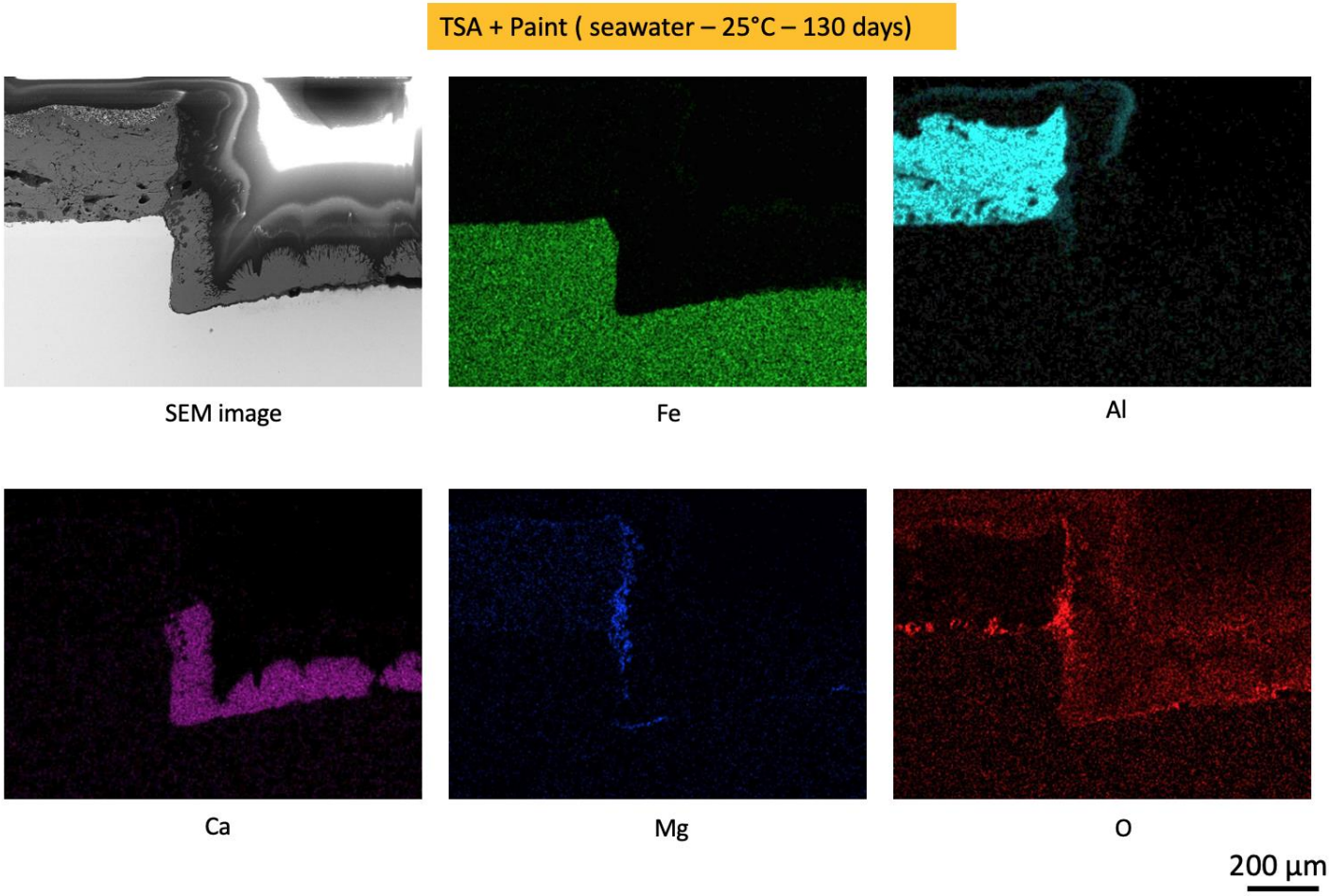

Figure 5-26 EDX maps of the bottom part of the defect of the TSA-coated steel sealed with paint, after the immersion in seawater at 25℃ for 130 days.

The evidence that TSA corroded more under the epoxy than under the paint can be seen from the SEM analysis of the cross-sections of the coatings. Multiple sides full of deposits, above the sealant, but also gathering underneath it, were observed on the TSA-coated steel with epoxy (Figure 5-27). EDX analysis revealed that those deposits consisted mainly of Al and O, and therefore were corrosion products of aluminium. However, small amounts of other elements, such as S, Mg, Ca, Cl and Na were also detected by the EDX analysis, suggesting that seawater gained entry to the TSA layer. Significantly smaller amount of corrosion products was detected underneath the paint (Figure 5-28). The majority of the coating looked intact, but several corrosion deposits were found underneath the paint.

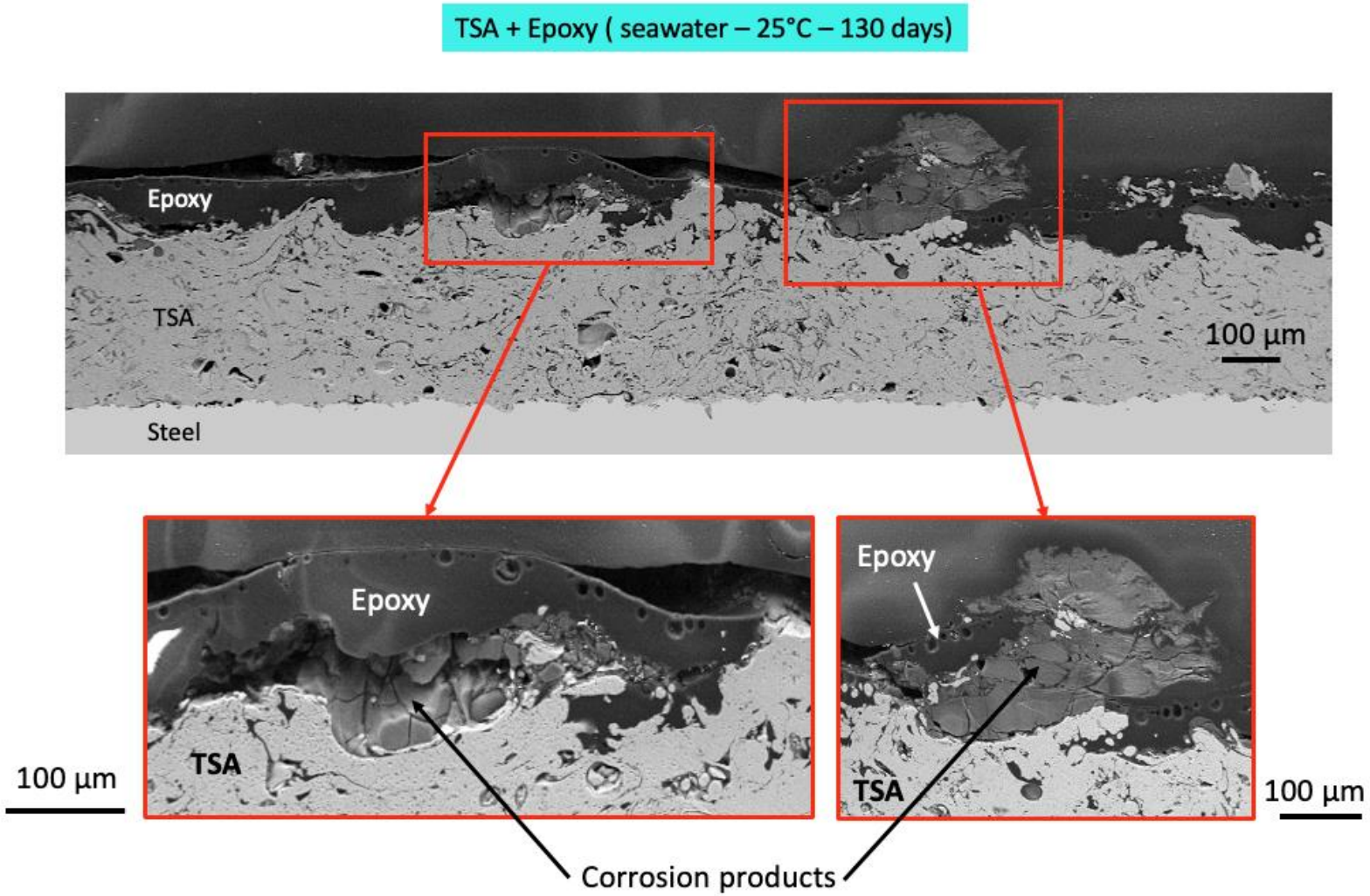

Figure 5-27 SEM images of the cross-section of the TSA-coated steel with epoxy after the immersion in seawater at 25℃ for 130 days.

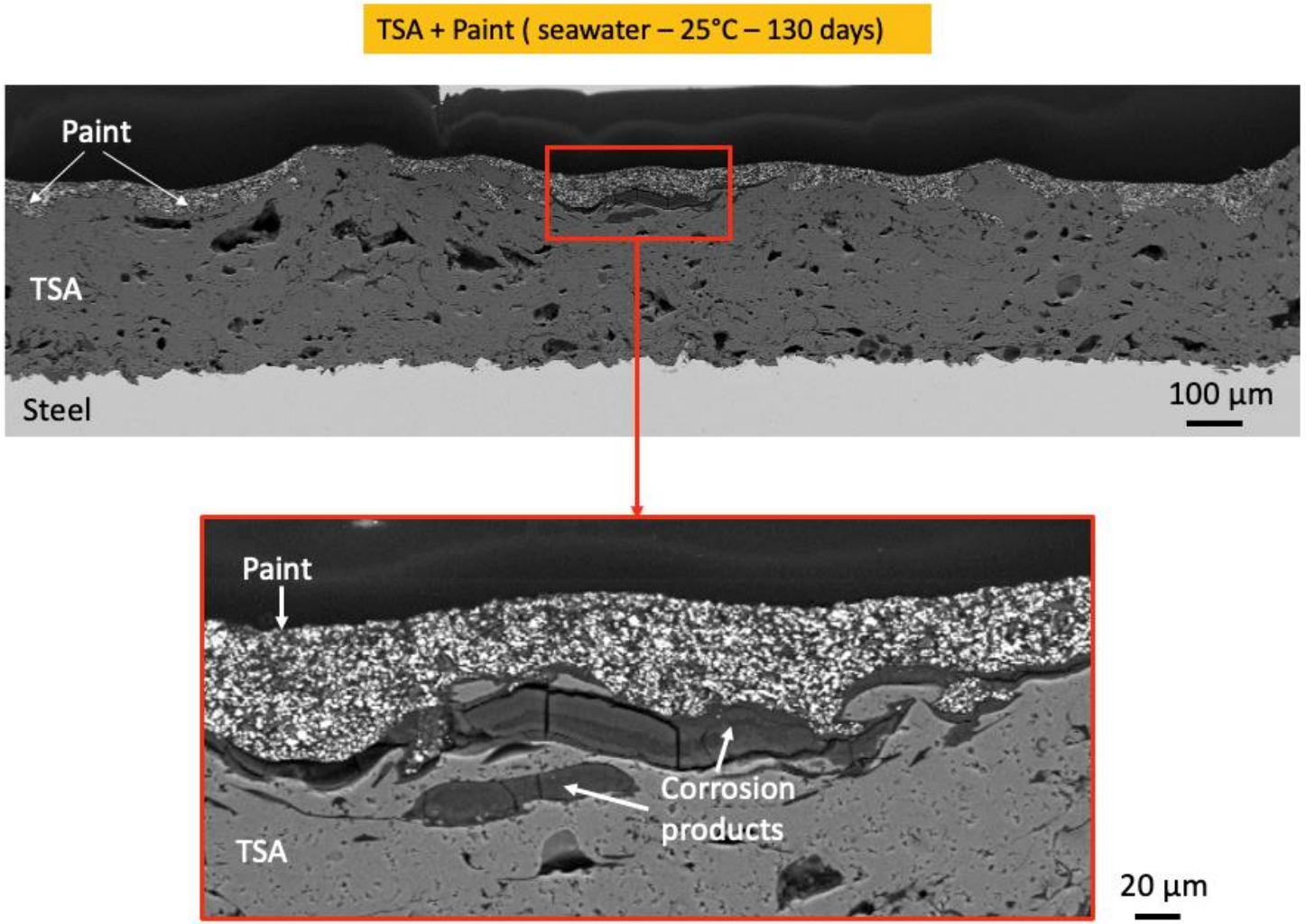

Figure 5-28 SEM images of the cross-section of the TSA-coated steel with paint after the immersion in seawater at 25℃ for 130 days.

A good sealant should not block the sacrificial actions of the coating towards the steel. The purpose of the sealant is to seal the pores in the coating to make it impervious and prevent penetration of the electrolyte towards the steel substrate which would enhance the self-corrosion of the coating. To ensure that the TSA layer is not fully covered, the method of application of both epoxy and paint was exactly the same and involved application and spreading the sealants using a brush, then scraping off the material excess to leave small pieces of the coating exposed. However, even though the application method was the same, the outcome was different.

SEM analysis of the cross-sections of the sample (Figure 5-28) revealed that paint covered the majority of the TSA coating. It can also be seen from Figure 5-20 that the paint was in a very good condition after the immersion, and there were only a few corrosion deposits in several spots present on top of it. Epoxy, however, was uniformly covered with small deposits. Those deposits probably formed in the areas where TSA was initially exposed to the electrolyte. It is possible that - due to its worse fluidity and higher viscosity - epoxy was easier to scrape off, and therefore more TSA was left exposed. In the case of paint, a very thin layer covered the majority of the coating.

Previous research focusing on painting and sealing the TSA coatings suggested that covering TSA with organic coatings would result in blistering and accelerated degradation of the aluminium layer. Knudsen [103] who simulated a TSA/organic system where TSA was either in electrical contact with bare steel or contained a defect observed severe degradation of the coating after 37.5 days of salt spray testing using seawater. Similarly, Sumon et al. [104] who tested several organic coatings on TSA (with and without a scribe) using salt spray exposure (62.5 days), observed organic coating delamination on TSA-coated samples both on scribed and on intact ones. In this study, no delamination or blistering was observed on any of the samples after 130

days immersion in seawater. Even samples sealed with paint, which probably covered most of the aluminium layer, did not develop any blisters. According to Knudsen [103], deterioration of the aluminium coating occurs when the organic coating is thick and capable of holding aggressive chloride ions at the coating surface, which leads to the development of hydrochloric acid (and hence accelerated corrosion of Al).

In this work no blistering or extensive corrosion of the aluminium coating was detected. This could be due to appropriate thickness of the sealants, which could not hold the acidic environment, and also good blocking properties of the paint.

Overall, judging by the condition of the TSA-coatings and electrochemical data, samples which were sealed with paints performed better than epoxies. Less TSA was consumed under the paints and less corrosion products were found on the coatings. Addition of graphene did not seem to affect the performance of those sealants.

5.2.3.1 Samples with defects at 4°C – full immersion

Figure 5-29 Evolution of the OCP of TSA-coated steel with 5% defect and epoxy sealants with and without graphene as a function of time during immersion in artificial seawater at 4°C.

shows the results of measurements of the OCP of TSA-coated steel with 5% defect and epoxy sealants with and without graphene as well as TSA-coated steel without a sealant and bare steel during the immersion in artificial seawater at 4°C. It can be noticed that the potential of bare steel stabilised very quickly at around -0.69 V and remained stable during the whole exposure to seawater.

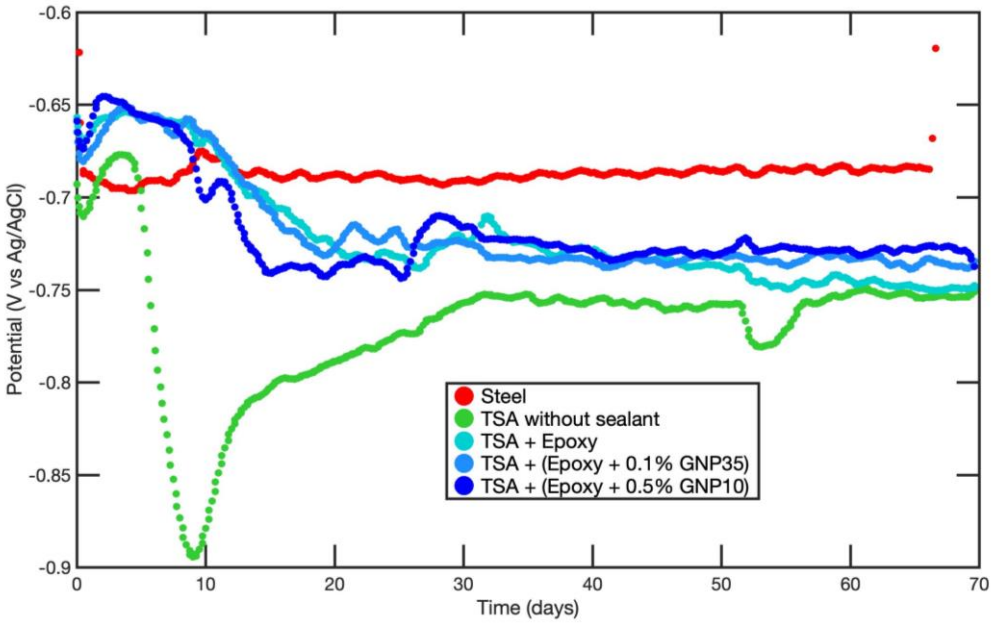

Figure 5-29 Evolution of the OCP of TSA-coated steel with 5% defect and epoxy sealants with and without graphene as a function of time during immersion in artificial seawater at 4 ℃.

During approximately the first 10 days of immersion, the potential of all the sealed TSA samples with defects was higher than the potential of steel, which indicates that the exposed steel (defect) was not protected by the TSA coating. After 10 days, the potentials decreased below the potential of steel and stabilised at around -0.73 V. The unsealed TSA sample also exhibited a short period of time (during the first week of immersion) during which the potential was above the potential of bare steel. However, it should be noted that the potential of the unsealed sample dropped significantly lower (from approximately -0.68 V to -0.90 V) than the potential of the sealed samples. The potential of the unsealed sample then started to gradually increase and reached approximately -0.75 V after 32 days. The more significant drop of the potential was likely associated with the dissolution of the aluminium coating. The unsealed sample had more aluminium exposed, therefore more aluminium could dissolve during the immersion.

The application of sealants resulted in a very poor performance of the TSA samples in cold seawater, which is clearly visible in Figure 5-30 - presenting the images of the samples after the completion of the immersion tests. It can be observed that the defects in the coatings are full of rust. The defect in the unsealed TSA coating has also some noticeable amount of rust, but significantly less than the sealed samples. The poor performance of the TSA samples in cold seawater is most likely associated with low solubility of aluminium oxide at cold temperatures. The application of sealants resulted in covering significant amounts of the coating, which resulted in very little aluminium available to dissolve with very slow dissolution rate, due to the low solubility.

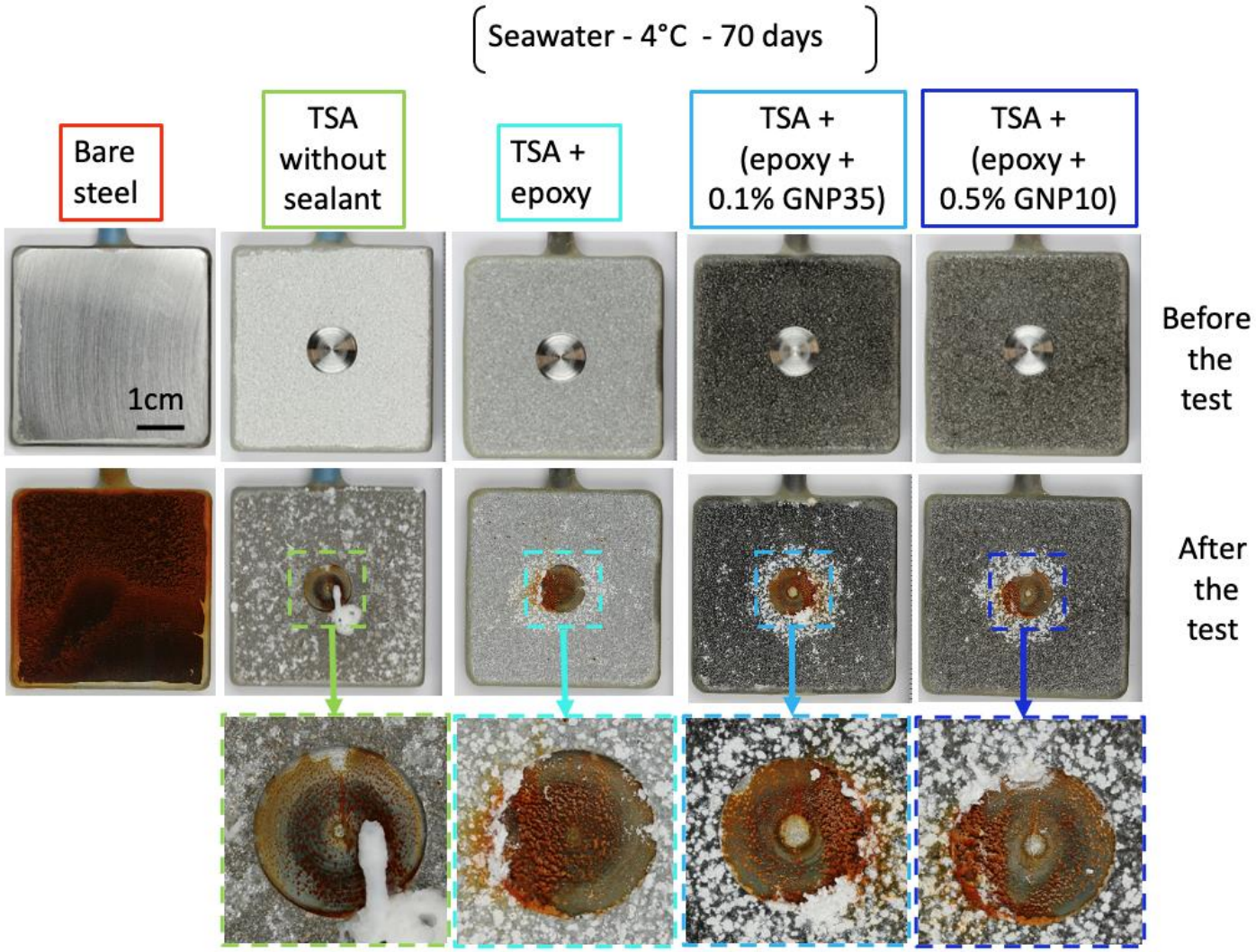

Figure 5-30 TSA-coated steel samples with defects and sealants after the immersion in seawater at 4℃ for 70 days. Magnified views show defects in the TSA coatings (made before the immersion in the seawater) covered with rust.

SEM analysis of cross-sections of the samples revealed a significant difference in amount and morphology of the deposits formed in the defect region. It can be noticed from Figure 5-31 that the deposits formed at 4°C are less dense and they do not fully cover the steel substrate. Moreover, they do not resemble the structure of brucite and aragonite which was observed at 25°C. EDX analysis of the deposits confirmed the lack of the thin Mg-rich layer underneath the Ca-rich layer. Moreover, EDX mapping of the TSA-coated steel with epoxy+0.5% GNP revealed that at 4°C Ca precipitated together with Al and Mg, in the vicinity of the TSA coating (Figure 5-32). At 25°C, Al was found together with Mg only, most probably in the form of hydrotalcite ($Mg_6Al_2CO_3(OH)_{16}(H_2O)$ – which was detected by Raman spectroscopy. At lower temperature aluminium possibly precipitates also in the form of different mineral, for example alumohydrocalcite ($CaAl_2(CO_3)_2(OH)_4 4H_2O$). This is yet to be confirmed.

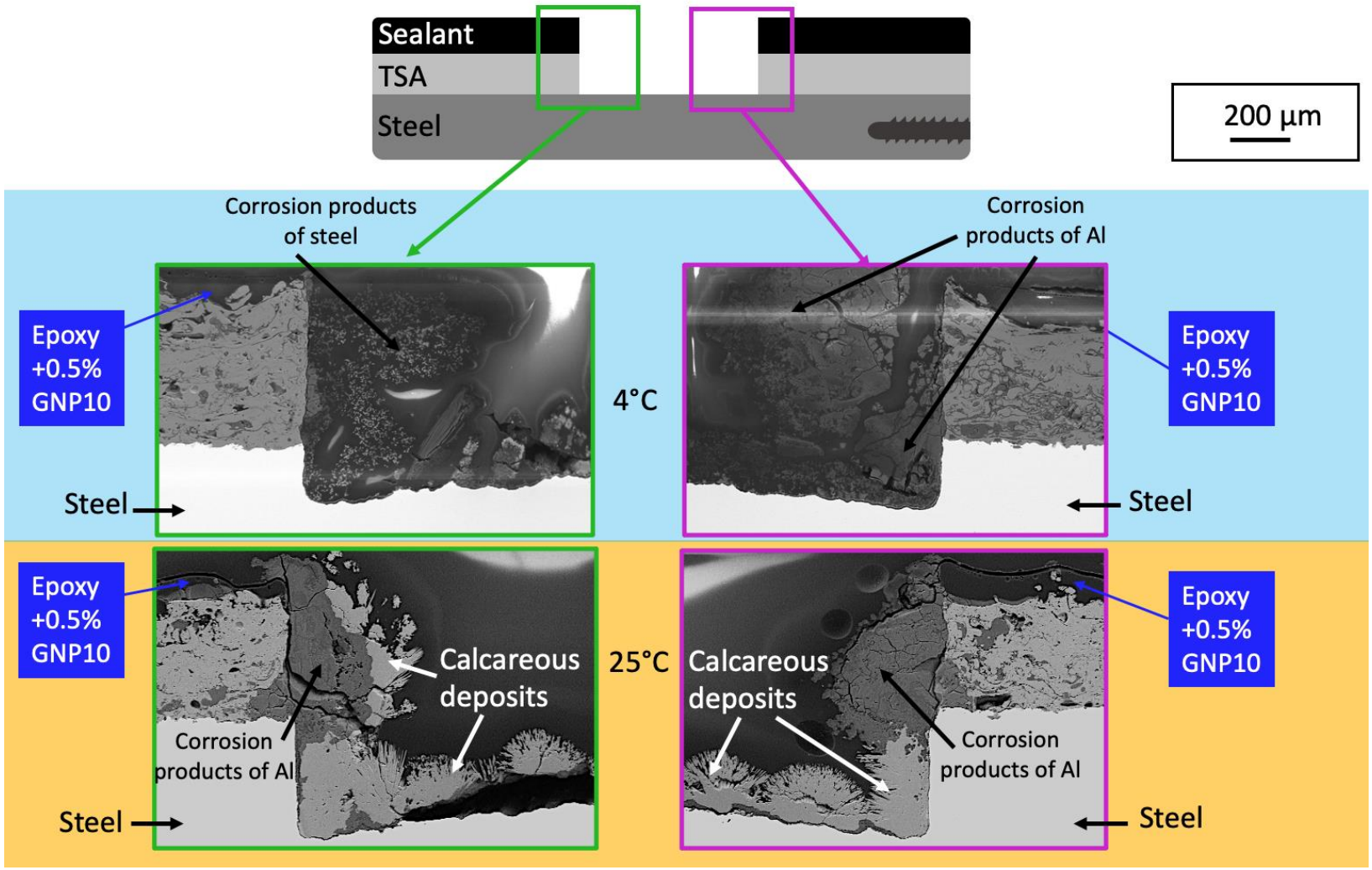

Figure 5-31 Comparison of the cross-sections of TSA-coated steel sealed with epoxy+ 0.5% GNP10 after the immersion in seawater at 4℃ and 25℃. The SEM images show the bottom (green) and upper (pink) part of the defect.

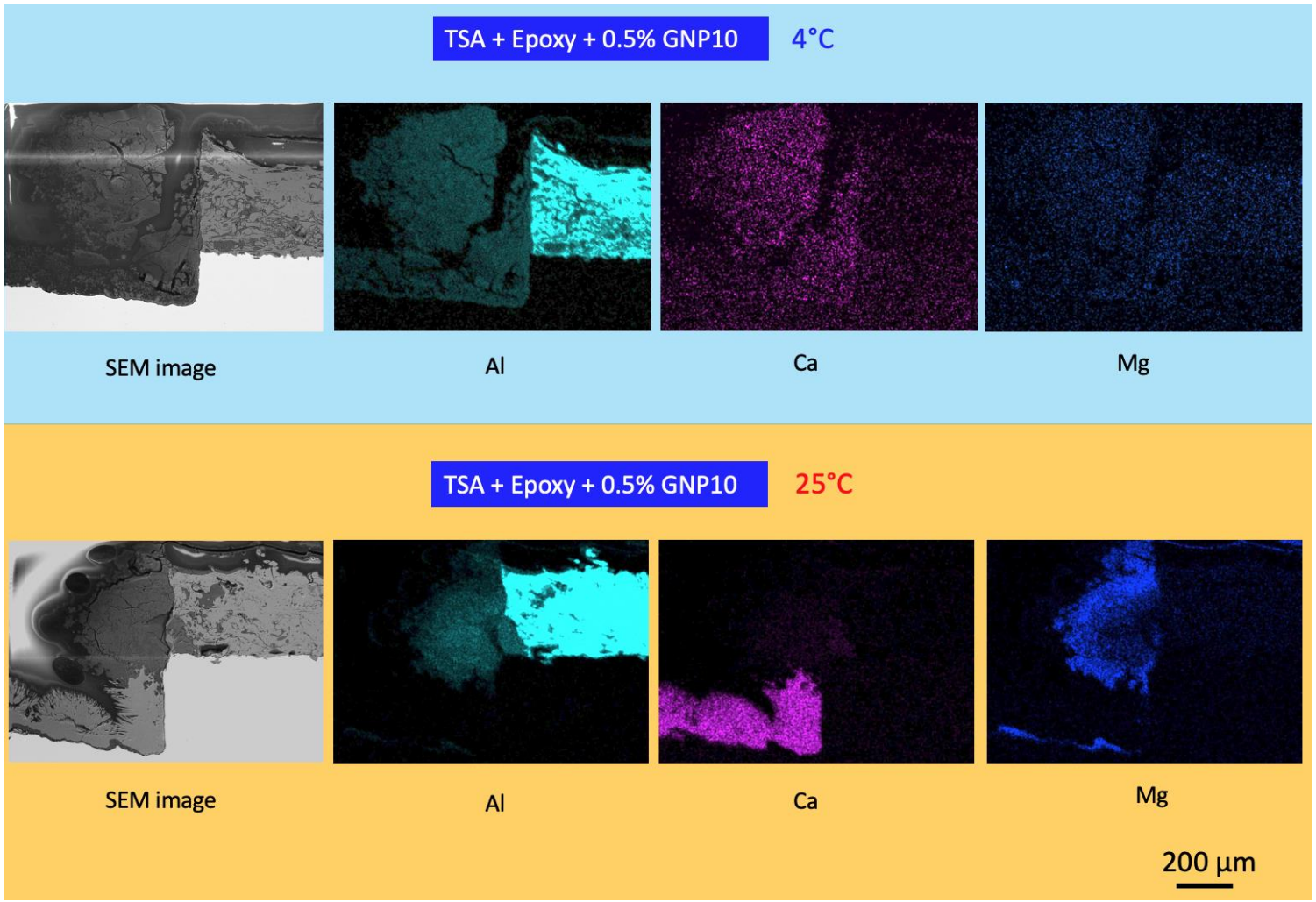

Figure 5-32 Comparison of deposits formed during the immersion in seawater at 4℃ and 25℃ inside the defects of TSA-coated steel with epoxy sealant containing 0.5% GNP.

From EDX maps, showed in Figure 5-33, it can be observed that Mg was found together with Fe. This indicates that instead of precipitating as brucite ($Mg(OH)_2$), Mg reacted with ferrous ions and perhaps precipitated as coalingite ($Mg_{10}Fe^{3+}_2(CO_3)(OH)_{24}•2H_2O$) or iowaite ($Mg_6Fe^{3+}_2(OH)_{16}Cl_2•4H_2O$).

Analysis of the middle part of the defects revealed small regions containing Ca-rich deposits, likely $CaCO_3$. Those deposits were surrounded by Fe- and Mg-rich deposits. This can be seen in Figure 5-34.

The lack of $Mg(OH)_2$ and very low amount of $CaCO_3$ was most probably caused by unfavourable pH in the vicinity of the cathode. Since Al did not manage to polarise the steel below the required -0.8 V (Figure 5-29) insufficient amount of OH^- was produced to trigger the precipitation of brucite.

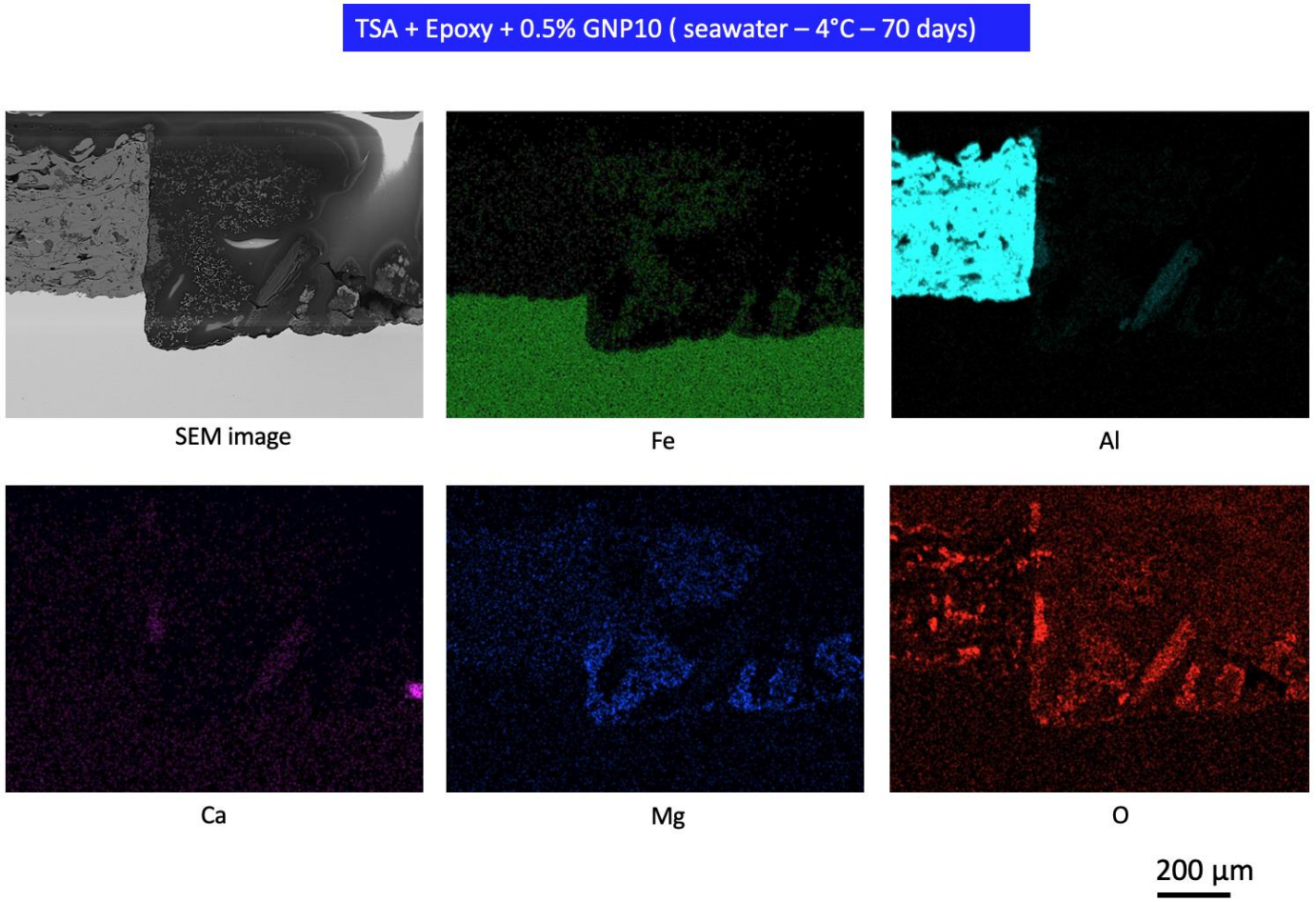

Figure 5-33 EDX maps of the bottom part of the defect of the TSA-coated steel sealed with epoxy+ 0.5% GNP10, after the immersion in seawater at 4℃ for 70 days.

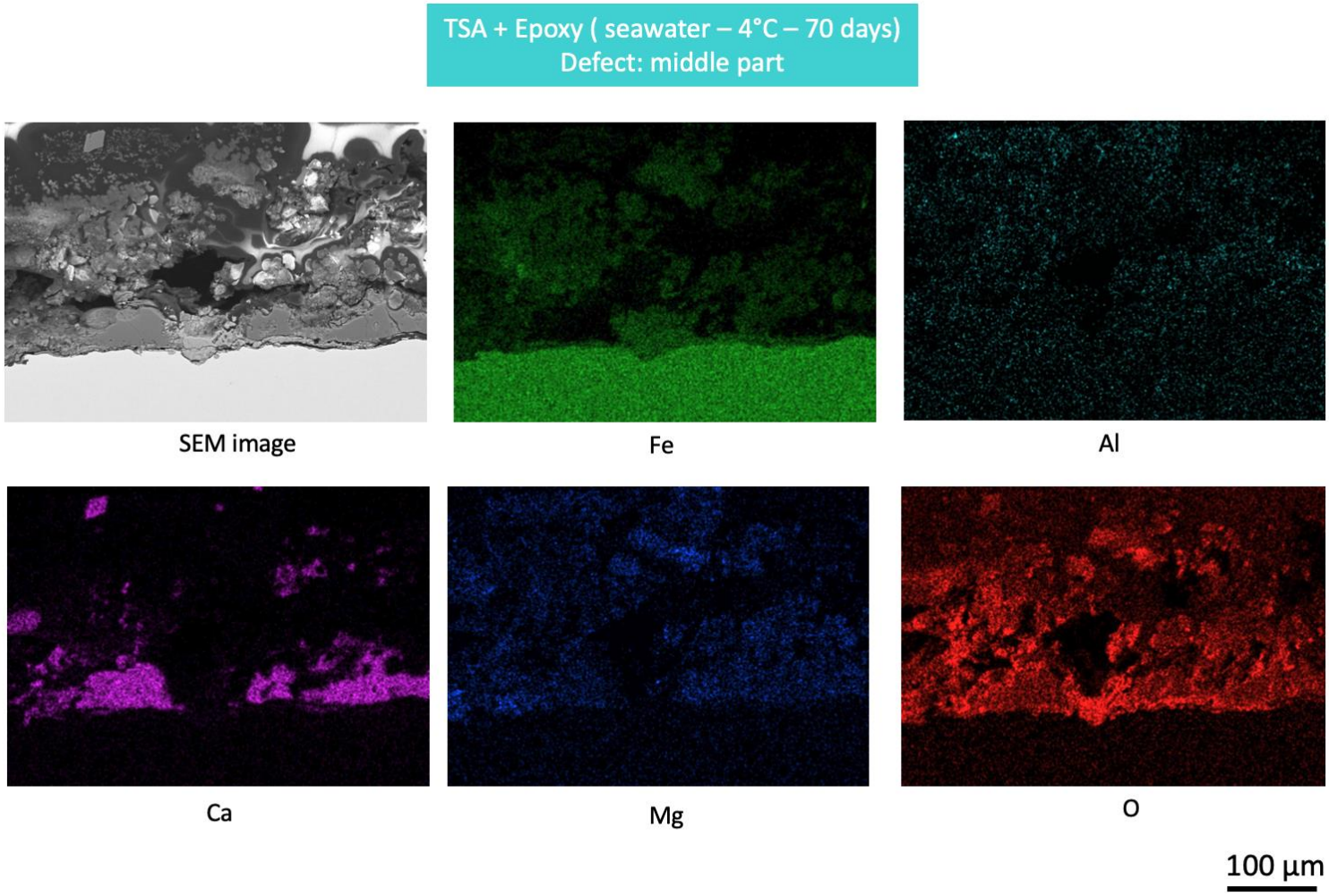

Figure 5-34 EDX maps of the middle part of the defect of the TSA-coated steel sealed with epoxy, after the immersion in seawater at 4℃ for 70 days.

The addition of graphene to the epoxy did not seem to significantly improve the performance of the epoxy sealant at low temperature. All the sealed samples performed worse than the sample without any sealant, regardless of whether GNP was added to the epoxy or not.

However, SEM analysis of the cross-sections of the coatings after the immersion in seawater showed some indications that graphene might have improved barrier properties of the epoxy. It can be noticed from the Figure 5-35, that gaps were found between the graphene-loaded epoxy and TSA. It is possible that due to improved blocking properties of epoxy with graphene, seawater could not easily penetrate the organic layer, and once the corrosion initiated, it continued to actively progress. Perhaps in the case of the neat epoxy, seawater could penetrate the polymer and neutralise the acidic environment, which could have resulted in precipitation of corrosion products between the TSA – epoxy interface. Several cavities filled with corrosion products were found on the cross-section of the sample, as can be observed in Figure 5-35.

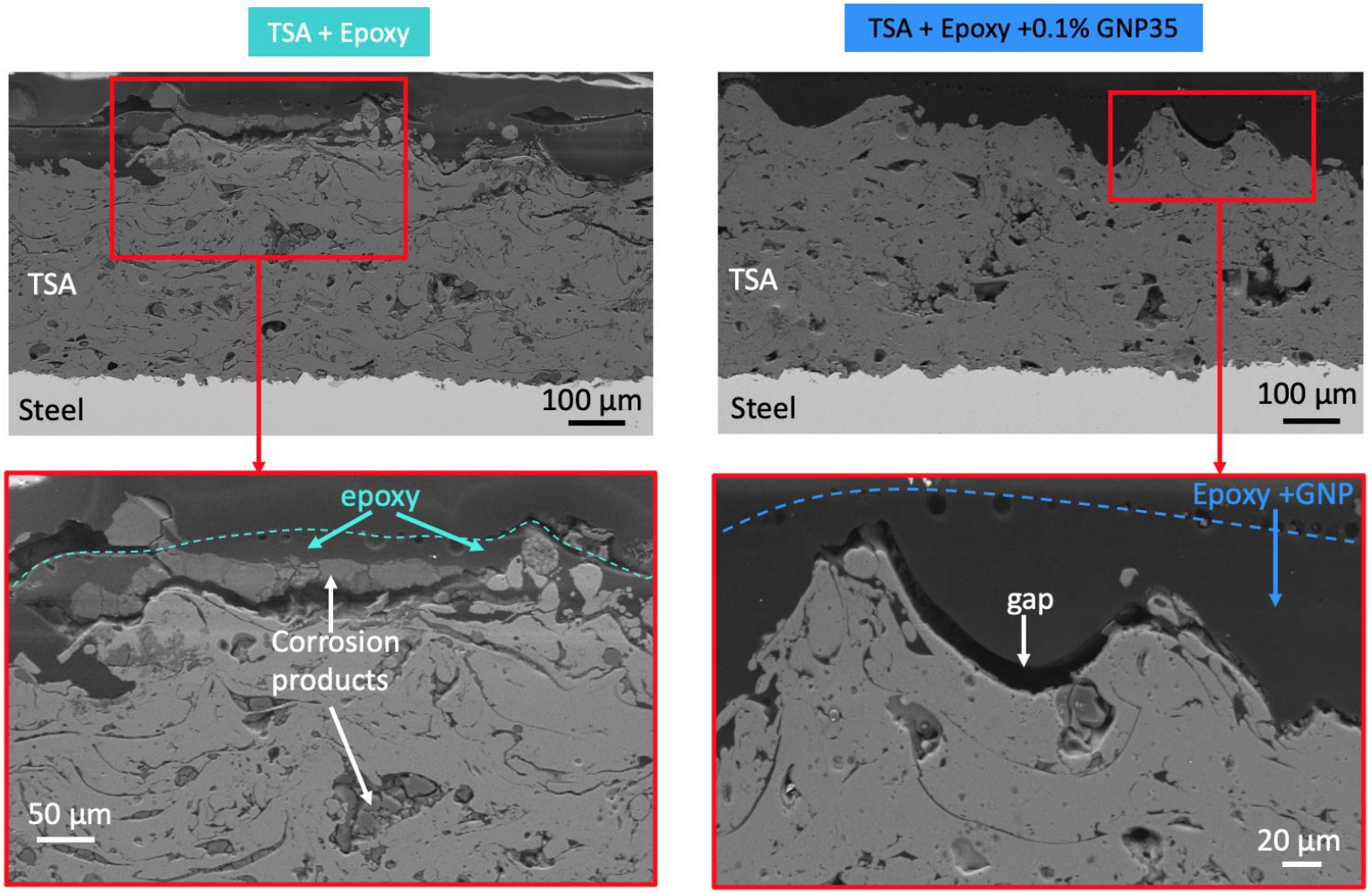

Figure 5-35 SEM images of the cross-sections of the TSA-coated steel with epoxy sealants after the immersion in seawater at 4℃ for 70 days.

5.2.3.2 Samples with defects at 25°C - alternating immersion

Figure 5-36 and Figure 5-37 display the results of the OCP and Rp monitoring of 4 samples: bare steel, TSA-coated steel with 5% defect, TSA-coated steel with epoxy sealant and 5% defect, and TSA-coated steel with epoxy sealant containing 0.1% graphene nanoplatelets. The 350-day alternating immersion test involved 10 min immersion in seawater at 25°C followed by 50 min drying in air, repeated every hour.

The data from Figure 5-36 show that the potential of bare steel sample exhibited a sharp rise from approximately -0.65 V to -0.4 V during first 7 days of the experiment, followed by a gradual increase to -0.35 V at 35 days. From day 35, the potential was gradually decreasing to approximately -0.55 V after 350 days. It can be noticed that all of the TSA-coated samples exhibited significantly lower potentials. The lowest potential, between -1 V and -0.7 V was recorded on the TSA-coated samples without any sealant. The potential of both of the sealed TSA samples stabilised very quickly between -0.8 V and -0.7 V, which is slightly above the desired protection potential of - 0.8 V.

The results of the LPR measurements (Figure 5-37) revealed the effect of graphene on the performance on the epoxy sealant under alternating immersion situation. It can be noticed that up to approximately 130 days the TSA-coated steel protected with graphene-containing sealant exhibited the highest polarisation resistance. This indicates that the corrosion rate of this sample was the lowest. Moreover, the Rp values were increasing with the immersion time, due to the build-up of corrosion products. After 130 days, the Rp values started to decrease from approximately 15000 to 1150 $\Omega \cdot cm^2$. The Rp values of the TSA-coated sample with neat epoxy were increasing until approximately 250 days to 7000 $\Omega \cdot cm^2$ and then started to decrease to approximately 2300 $\Omega \cdot cm^2$ at the end of the experiment.

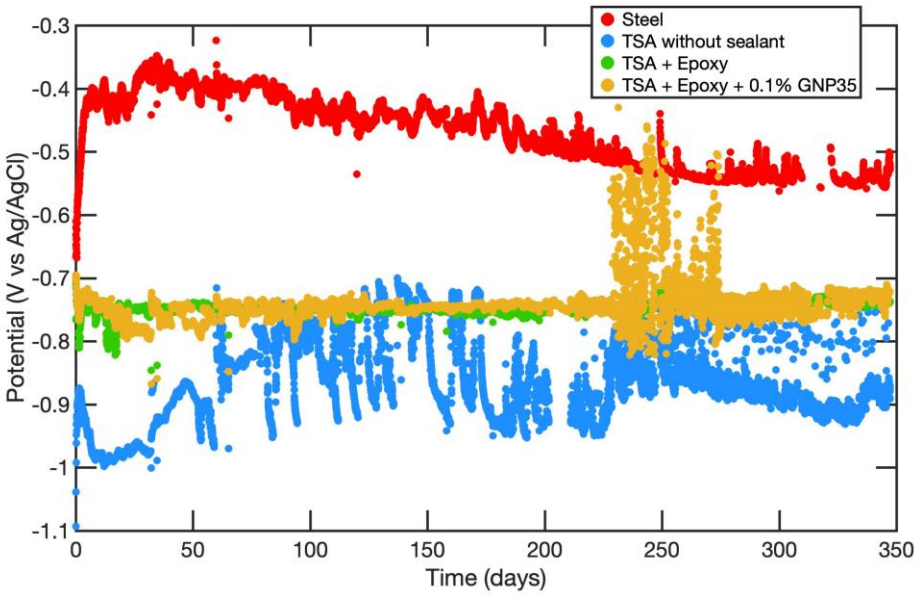

Figure 5-36 Evolution of the OCP of TSA-coated steel with 5% defect and epoxy sealants with and without graphene and bare steel as a function of time during alternating immersion (10 min immersed and 50 min in air) in artificial seawater at 25℃.

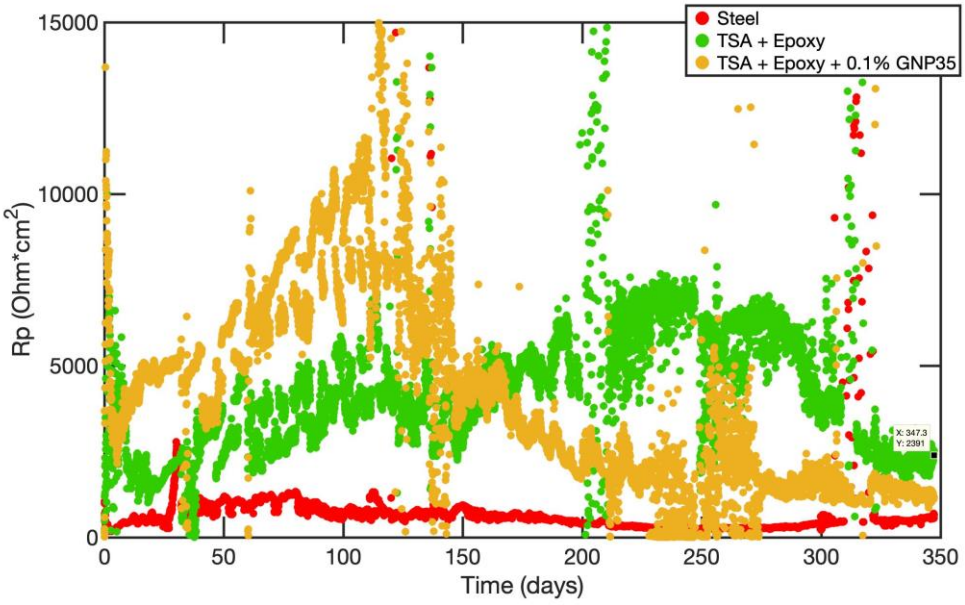

Figure 5-37 Evolution of the Rp (calculated from the LPR method) of TSA-coated steel with 5% defect and epoxy sealants with and without graphene and bare steel as a function of time during alternating immersion (10 min immersed and 50 min in air) in artificial seawater at 25℃.

The decrease of the Rp values of the TSA-coated samples with sealants was most probably associated with the failure of the epoxy layer. It is possible that up to 130 days of immersion, the addition of graphene was beneficial, and it resulted in improved blocking properties of the epoxy. However, once the corrosive species managed to penetrate the polymer, the accelerated corrosion of TSA initiated. Images of the samples taken during the test, shown in Figure 5-38, clearly demonstrate that after 9 months the graphene-containing epoxy was covered with white deposits, most probably corrosion products of aluminium. Epoxy without graphene had some deposits too, but significantly less than the graphene-containing sample. Figure 5-38 also shows that the TSA sample without any sealant performed best, not much corrosion deposited on the coating, and the defect was fully covered with white calcareous deposits. It should be also noted that the sealed samples developed rust in the defects from the first day of the immersion, whereas the unsealed TSA sample did not. It seems that the application of sealant under alternating immersion conditions is not needed and can be even detrimental to the TSA coating, as it inhibits its sacrificial actions. The addition of graphene provided a short-term improvement to the epoxy (up to 130 days), but it seems to have a detrimental effect under long-term testing.

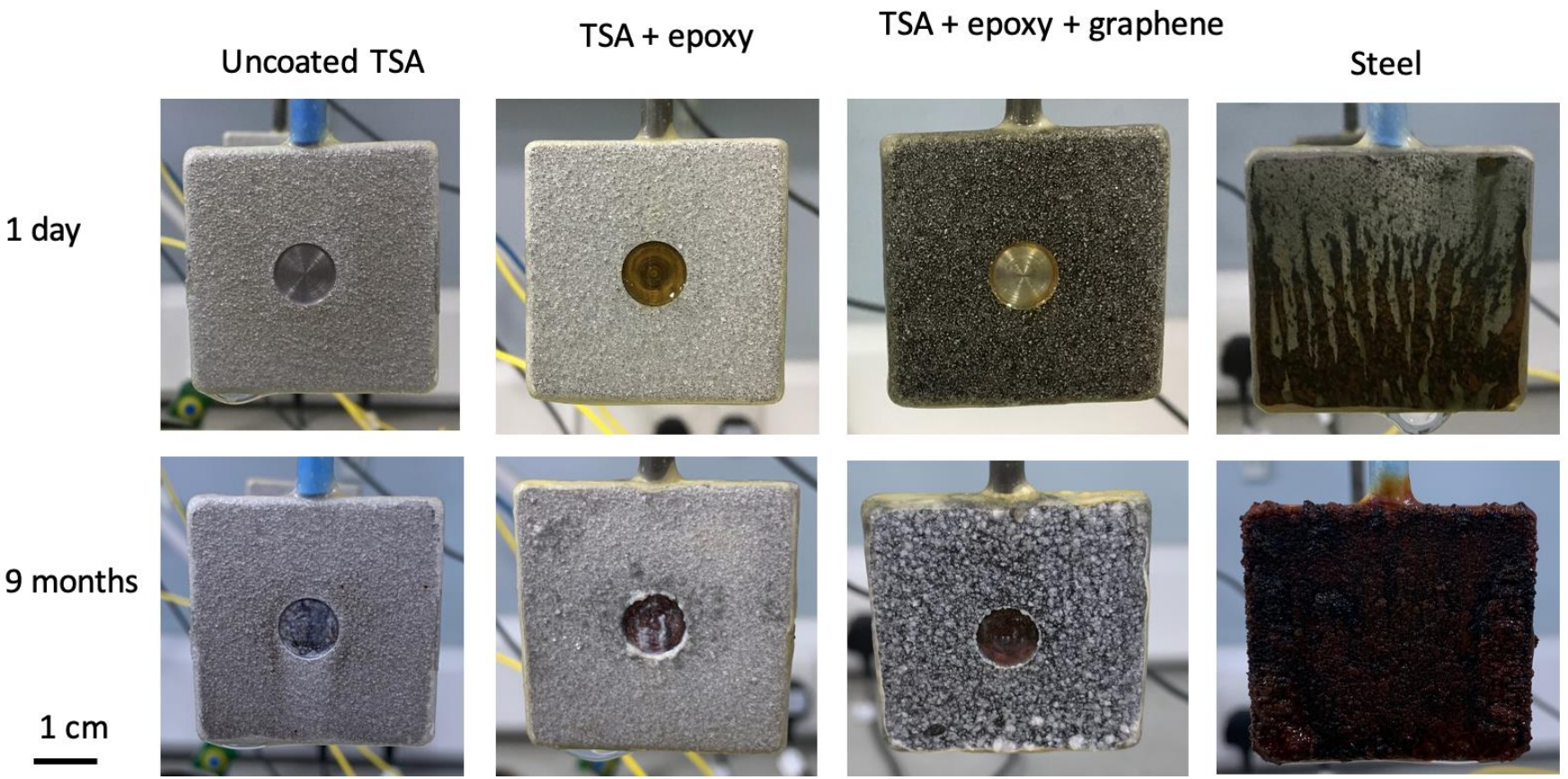

Figure 5-38 TSA-coated steel with 5% defect and epoxy sealants with and without graphene as well as bare steel during the alternating immersion test (10 min immersed and 50 min in air) in artificial seawater at 25℃.

5.3 Conclusions

1. Several alloys were used to deposit thermally sprayed coatings onto carbon steel and glass substrates to assess their performance as sacrificial coatings. During a 32-day immersion test in artificial seawater at 25°C, AA 1050 showed lower corrosion potential compared with AlMg5% and AA 1100 and therefore it was the most effective in moving the potential of steel into the protective region (below -0.8 V).
2. ZnAl15% alloy, exhibited significantly lower Rp values (indicating higher corrosion rate) compared with Al coatings, and therefore this coating would have a shorter lifetime in-service.
3. TSA (AA 1050) coatings with defects exposed to seawater at 0,15, 25 and 32°C provided sacrificial protection to carbon steel for at least 60 days. The exposed steel was covered with calcareous deposits and no visible steel corrosion products were observed on the samples.
4. TSA coatings (AA 1050) exposed to 4°C did not provide adequate protection to carbon steel substrates. A significant amount of rust was observed in the defect region after the 70-day immersion in seawater.
5. The application of sealants onto TSA operating at 25°C can be beneficial in preventing the contact between the electrolyte and the steel substrate.
6. Sealants should not be applied onto TSA operating at 4°C, as they impair the performance of the coating. At this temperature, the kinetics of the sacrificial dissolution of the aluminium layer is very slow and the application of sealants slows it down even more. Sealed samples exhibited higher corrosion potential

values than the unsealed sample and more rust deposits were found inside the defects.

7. Paints perform better than epoxy sealants. Less TSA was consumed under the paints and less corrosion products were found on the coatings. Addition of graphene did not seem to affect the performance of those sealants.
8. For alternating drying and wetting exposures, sealing of TSA might be ineffective or even detrimental, as it inhibits its sacrificial actions. TSA without sealant performed better under alternating drying and wetting conditions. Less corrosion products were observed on the coating and the defect was fully covered with white calcareous deposits.

Chapter 6 Performance of Thermally Sprayed Coatings under Splash Zone and Atmospheric Conditions.

The last section of this chapter has been published in the following paper:

Syrek-Gerstenkorn, Berenika, Paul Shiladitya, and Davenport Alison J: " Use of thermally sprayed aluminium (TSA) coatings to protect offshore structures in submerged and splash zones*."* Surface and Coatings Technology *374 (2019): 124- 133.*

6.1 Introduction

TSA offers long-term, maintenance-free protection to steel operating under full seawater immersion, by working as a barrier to the corrosive environment when intact and acting as an evenly distributed anode which sacrificially protects steel when damaged.

However, offshore constructions operate not only in constant seawater immersion but also in alternating wetting and drying conditions in the so called “splash zone”. This zone is particularly corrosive due to constant splashing of highly aerated seawater. Confined volumes of electrolyte, easy access to oxygen and atmospheric pollutants deposited on the surface lead to more severe corrosion in this region than in the submerged zone.

To date, the majority of laboratory testing has focused on the performance of TSA under full immersion conditions (for example [10,11,76,78,81,128]). A limited study under simulated splash zone conditions concentrated mainly on the change of weight of the samples during the exposures [158,159]. In this chapter, electrochemical methods have been employed to study the behaviour of thermally-sprayed coatings

under a droplet of artificial seawater. This approach provides an insight into electrochemical reactions that determine the corrosion performance of the coatings. In addition, corrosion products which formed on the coatings were examined using Raman spectroscopy. They were compared with corrosion products on solid aluminium.

6.2 Electrochemistry under droplets

6.2.1 Effect of the droplet volume

The effect of the initial droplet size on the OCP of TSA-coated steel was investigated using several seawater droplets of different volumes: 2.5, 5 and 10 µL. The potential was recorded against Ag wire without controlling the environmental conditions. The results are shown in Figure 6-1.

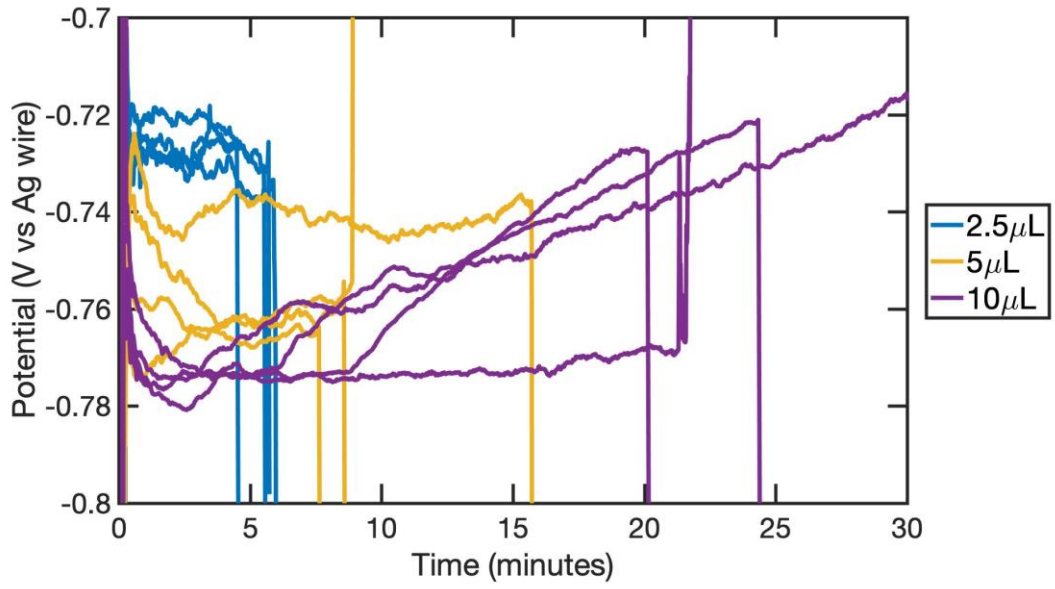

Figure 6-1 Evolution of the OCP of TSA (AA 1050) coating on steel measured under droplets of artificial seawater against a silver wire as a reference electrode without controlling the environmental conditions (RH=42%, T=20ºC measured during the experiments).

One can observe that the highest potential of approximately -0.73 V was recorded under the smallest droplets (2.5 µL). Larger droplets of 5 and 10 µL exhibited significantly lower potential values between -0.78 V and -0.74 V during the first 6 min of the measurements. The potential of 10 µL displayed an increasing trend from approximately -0.78 to -0.72 V during the tests. Since the relative humidity (RH) measured during the experiments was 42%, the droplets were evaporating during the measurement. Therefore, the measurements under larger droplets lasted longer.

More active potential under larger droplets could be related to the larger surface area under the droplet. Since TSA is quite porous, it is possible that the pores act as small cavities which enable initiation and propagation of localised corrosion. It is possible that more pores were present under larger droplets, which resulted in higher corrosion activity.

The effect of NaCl droplet size on the OCP of carbon steel was studied by Li and Hihara [160]. They also reported lower potential values under large droplets (i.e., D > ~100 µm) associated with active corrosion. Higher potential under smaller droplets were explained by passivation of the substrate and lack of corrosion attack.

Increasing potential values in case of the large droplets could be related to the precipitation of salts during evaporation of water from the droplet. Once the droplet starts to lose water, the concentration of ions starts to increase, and when the saturation level of a given salt is achieved, it starts to precipitate out of the droplet.

6.2.2 Effect of RH

The effect of RH on the potential of TSA-coated steel was investigated under 10 µL droplets of artificial seawater. Different RH levels were tested: 98, 90, 42 and 30%. The results are displayed in Figure 6-2.

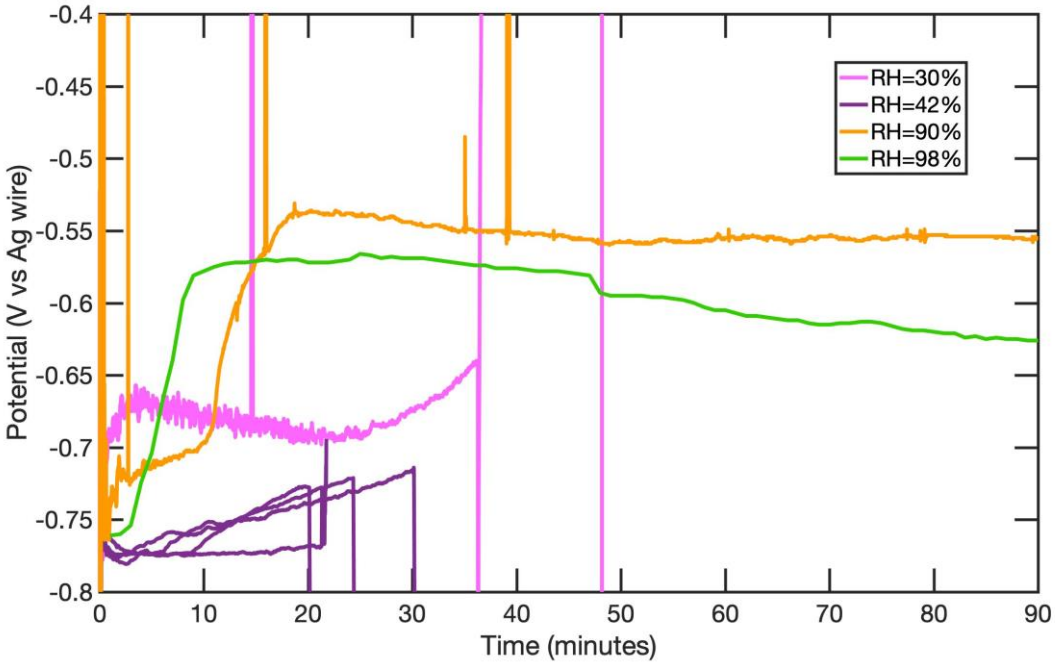

Figure 6-2 Evolution of the OCP of TSA (AA 1050) coating on carbon steel measured under 10 µL droplets of artificial seawater against a silver wire as a reference electrode under constant RH and temperature (20.5ºC) conditions.

It can be noticed that the lowest potential was recorded at 42% RH. Higher potential, fluctuating between -0.70 and -0.65 V, was recorded at 30% RH. At 90% RH, the potential stabilised at approximately -0.55 V after 20 minutes from the deposition of the droplet. At 98% RH, the potential reached approximately -0.57 V within 10 min after the deposition of the droplet, and then started to decrease gradually to -0.63 V after 90 min.

RH affects the properties of seawater droplets in several ways. It controls the equilibrium water activity of the solution, which in turn affects the concentration of ionic species and precipitation of salts. The presence of precipitates within the droplet changes the density and hence the conductivity of the solution. It also lowers the available cathodic area. Since RH dictates the bulk liquid-solid phase transition known as deliquescence (absorption of water vapour by a solid salt to form a liquid electrolyte)

and efflorescence (crystallisation of salts from a liquid electrolyte), one can predict the sequence of precipitation of seawater constituents from the droplet upon drying. Table 6-1 presents efflorescence relative humidity (ERH) and deliquescence relative humidity (DRH) of major seawater compounds. The information from the table can be used to explain the results of OCP measurements presented in Figure 6-2.

Table 6-1 Efflorescence relative humidity (ERH) and deliquescence relative humidity (DRH) of major constituents of evaporated seawater at RT. Reproduced from [161]***.***

Constituent	ERH (%)	DRH (%)
NaCl	40-55	76
$MgCl_2 \cdot 6H_2O$	-	33
$MgSO_4 \cdot H_2O$	-	85
$KMgCl_3 \cdot 6H_2O$	40-55	59
$CaSO_4$	80-90	-

It can be noticed that the potential measured at 30% RH was the noisiest. Since after the deposition the droplet was exposed to significantly lower RH than the equilibrium RH with unevaporated seawater (RH 98%), the droplet started to lose water and shrink. It can be noticed from Table 6-1 that this was accompanied by the precipitation of salts, starting from precipitation of $CaSO_4$ and finishing with $MgCl_2$. This indicates that the electrolyte reached very high chloride concentration which explain more active potential.

At 90% RH, most probably $CaSO_4$ precipitated which explains the higher potential in comparison with 98% RH – where the activity of water inside the droplet is in equilibrium with the activity of water in the atmosphere.

6.2.3 Comparison between splash zone and full immersion conditions

6.2.3.1 Preliminary measurements under droplets

To get an insight into anodic and cathodic activity under seawater droplets two methods were employed to produce polarisation curves. The first one involved the insertion of a silver and platinum wire into the body of the droplet, which worked as a pseudo-reference electrode and counter electrode, respectively. The results using this set-up are shown in Figure 6-3.

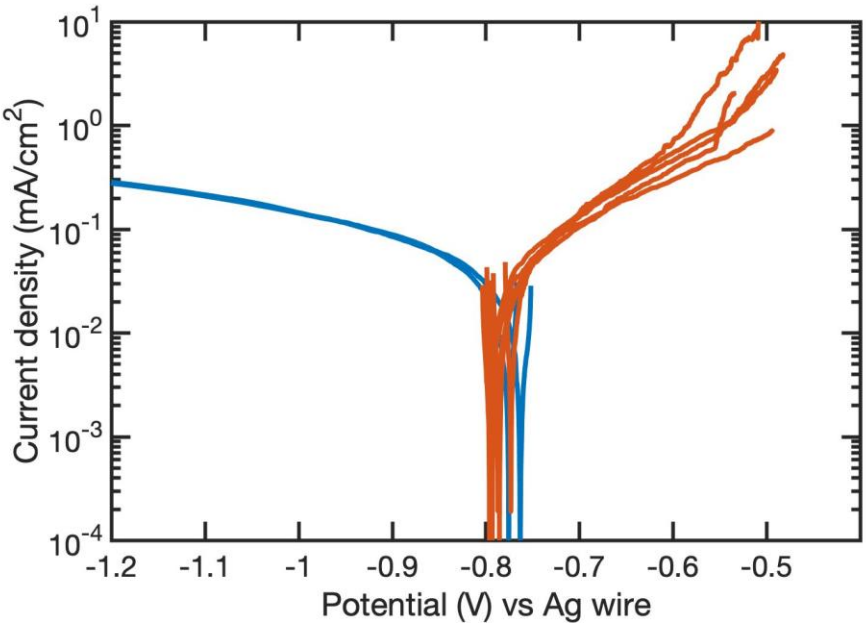

Figure 6-3 Cathodic and anodic polarisation curves measured under 10 µL droplets of artificial seawater on TSA-coated steel using a silver wire as a reference electrode and a platinum wire as a counter electrode without controlling the environmental conditions (RH=37%, T=20.2ºC measured during the experiments). Measurements conducted immediately after the deposition of the droplets.

It can be seen that the good reproducibility was achieved using this method, however the potential sweeps were recorded in reference to the silver wire. Another set up was also tried. A tailor-made Luggin probe was prepared as a reference electrode by placing an Ag/AgCl electrode (electrode that was used for the full immersion experiments) into a syringe filled with synthetic seawater. Pt wire was used as a counter electrode and the sample was connected as a working electrode. The results are shown in Figure 6-4 together with the results generated using the Ag wire method (converted into the Ag/AgCl scale by subtracting 100 mV, as described in section 3.2.2.3 in the methodology chapter).

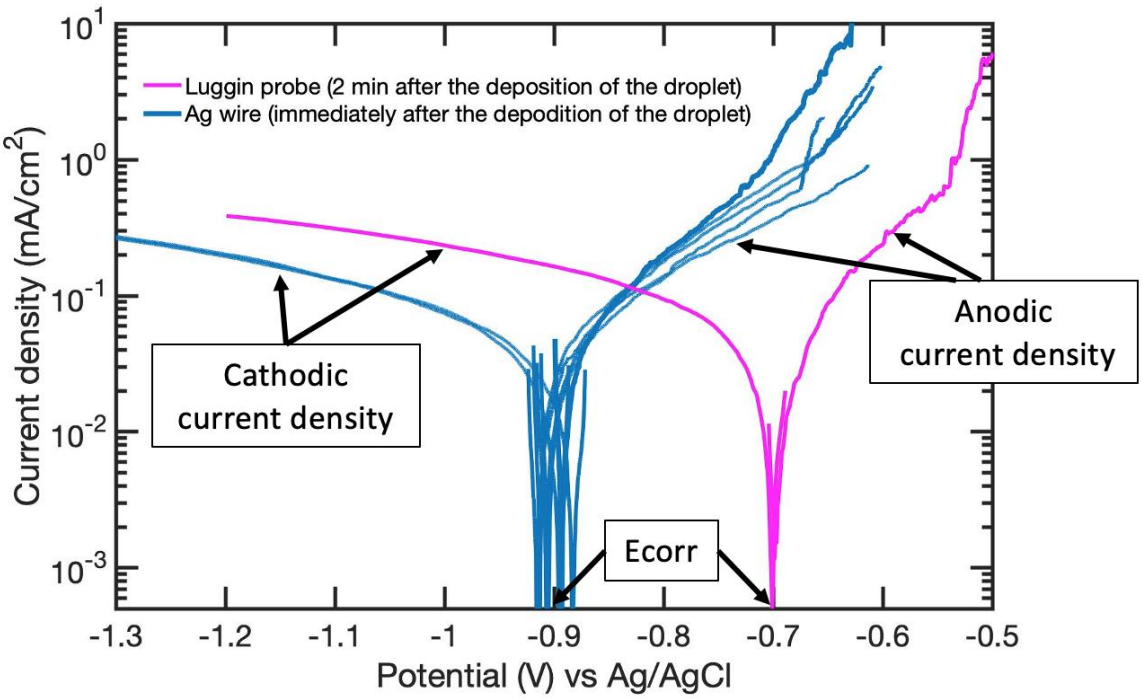

Figure 6-4 Comparison of the polarisation curves generated under 10 µL droplets of ASW on Al-coated steel using a Ag wire and Luggin probe; Scan rate: 1 mV/s; (RH=37%, T=20.2ºC measured during the experiments using a Ag wire, RH=53%, T=21.3ºC measured during the experiments using a Luggin probe).

It can be noticed that the results seem to vary significantly. For example, there is 200 mV difference between the corrosion potential (Ecorr) measured using the Luggin

probe and the Ag wire. There is also noticeable difference between anodic and cathodic current density.

However, it should be pointed out, that in case of Ag-wire method, the measurement was initiated immediately after the deposition of the droplet, whereas in case of the Luggin probe, 2 min after the deposition. It can be clearly seen from Figure 6-5, that the potential recorded under the droplet changed from approximately -0.9 V to -0.7 V during the first 2 min of the measurement, which explains discrepancy between the data presented in Figure 6-4.

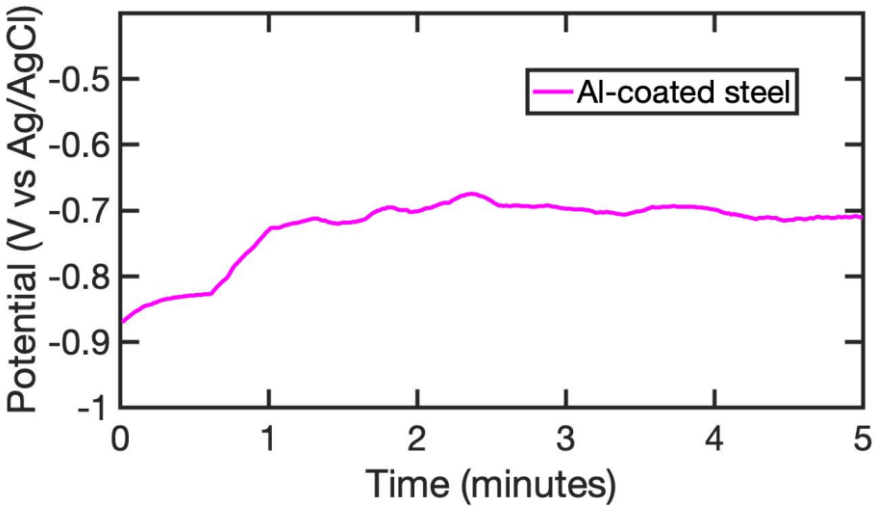

Figure 6-5 OCP of Al-coated steel under a 10 µL droplets of ASW measured using a Luggin probe; (RH=53%, T=21.3ºC measured during the experiments).

Since the Luggin probe method does not require conversion of the potential from Ag wire to Ag/AgCl scale, it was chosen for further measurements.

6.2.3.2 Performance of coated and uncoated steel samples

Figure 6-6 shows a comparison between the OCP measured under droplets and full seawater immersion on Al-coated steel, ZnAl15% - coated steel and bare steel. One can observe a very similar potential evolution under both conditions. In both cases, the potential of bare steel was the highest (between -0.6 and -0.3 V), followed by Al-coated

steel (between -0.9 and -0.5 V) and ZnAl-coated steel (approximately -1 V). The measured potentials under the droplet are consistent with the Ecorr values measured during potentiodynamic polarisation scans (Figure 6-7). Polarisation scans also revealed that ZnAl coating shows higher anodic activity and similar cathodic activity to Al coating under a droplet of artificial seawater, therefore it performs better as a sacrificial coating.

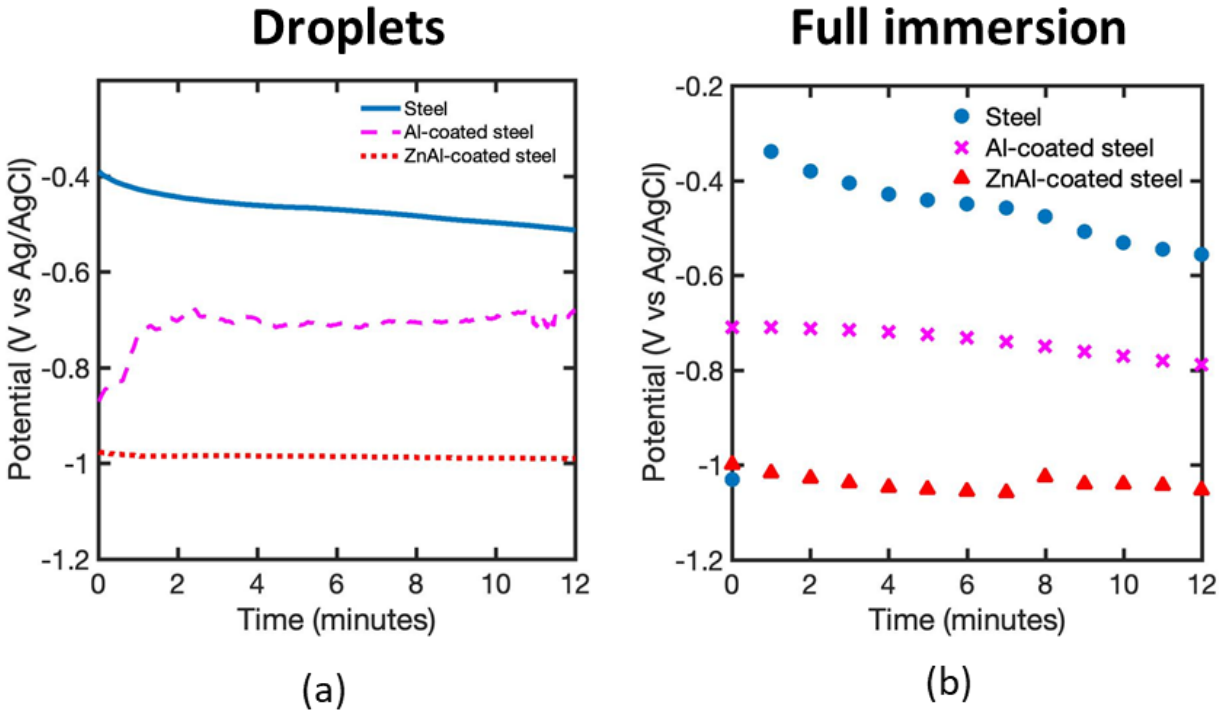

Figure 6-6 Results of the measurements of the OCP of Al-coated steel, ZnAl-coated steel and bare steel under 10 µL droplet of ASW (a) and under full immersion conditions (b); (RH=53%, T=21.3ºC measured during the experiments).

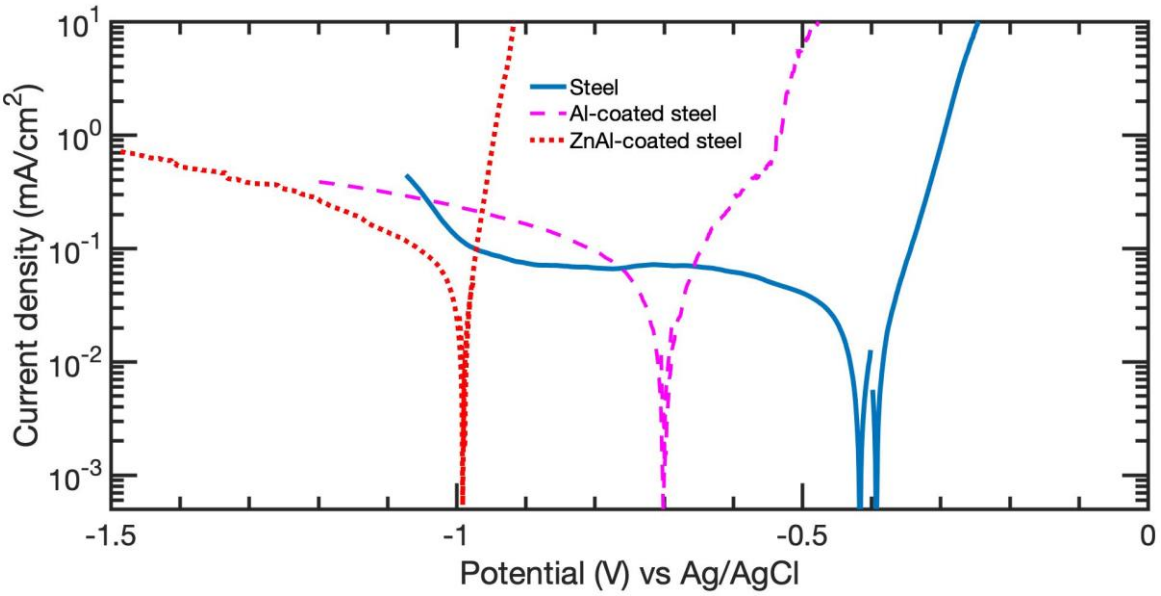

Figure 6-7 Polarization curves generated under 10 µL droplets of ASW on ZnAl-coated steel, Al-coated steel, and bare steel, 2 min after the deposition of the droplet. Scan rate: 1 mV/s; (RH=53%, T=21.3ºC measured during the experiments).

A comparison of polarisation curves measured under a seawater droplet and full seawater immersion on Al-coated steel is shown in Figure 6-8. The results revealed higher cathodic activity under the droplet. This is most likely associated with quick diffusion of oxygen to the cathodic site.

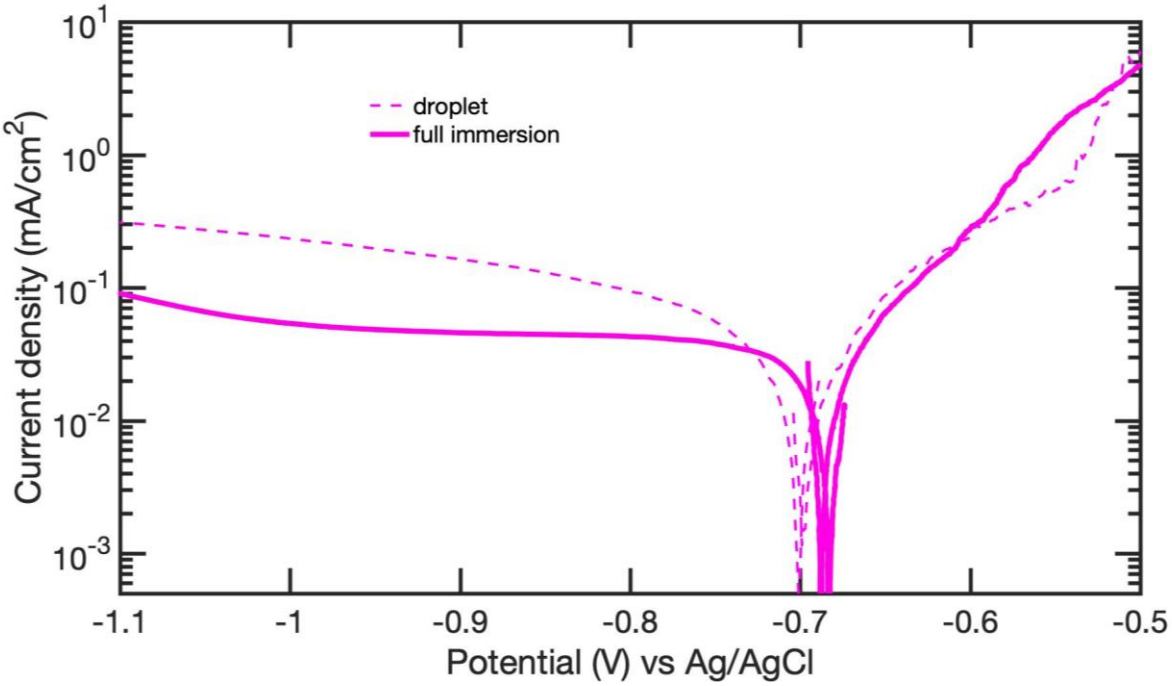

Figure 6-8 Comparison of cathodic and anodic polarisation curves performed on TSA-coated steel under 10 µL droplet of ASW and full immersion in ASW.

6.3 Atmospheric corrosion experiments

6.3.1 Solid aluminium

Figure 6-9 presents secondary electron SEM images of the corroded surface of AA 1050 sheet sample after a 2-week exposure to ASW at RH=84±4% and T=30±1ºC, after the removal of the droplet. One can notice several morphologies of corrosion products formed on the surface of the metal. Very thin corrosion products can be observed under the main body of the droplet, but several agglomerations of dense, mound-like corrosion products are also visible outside the droplet.

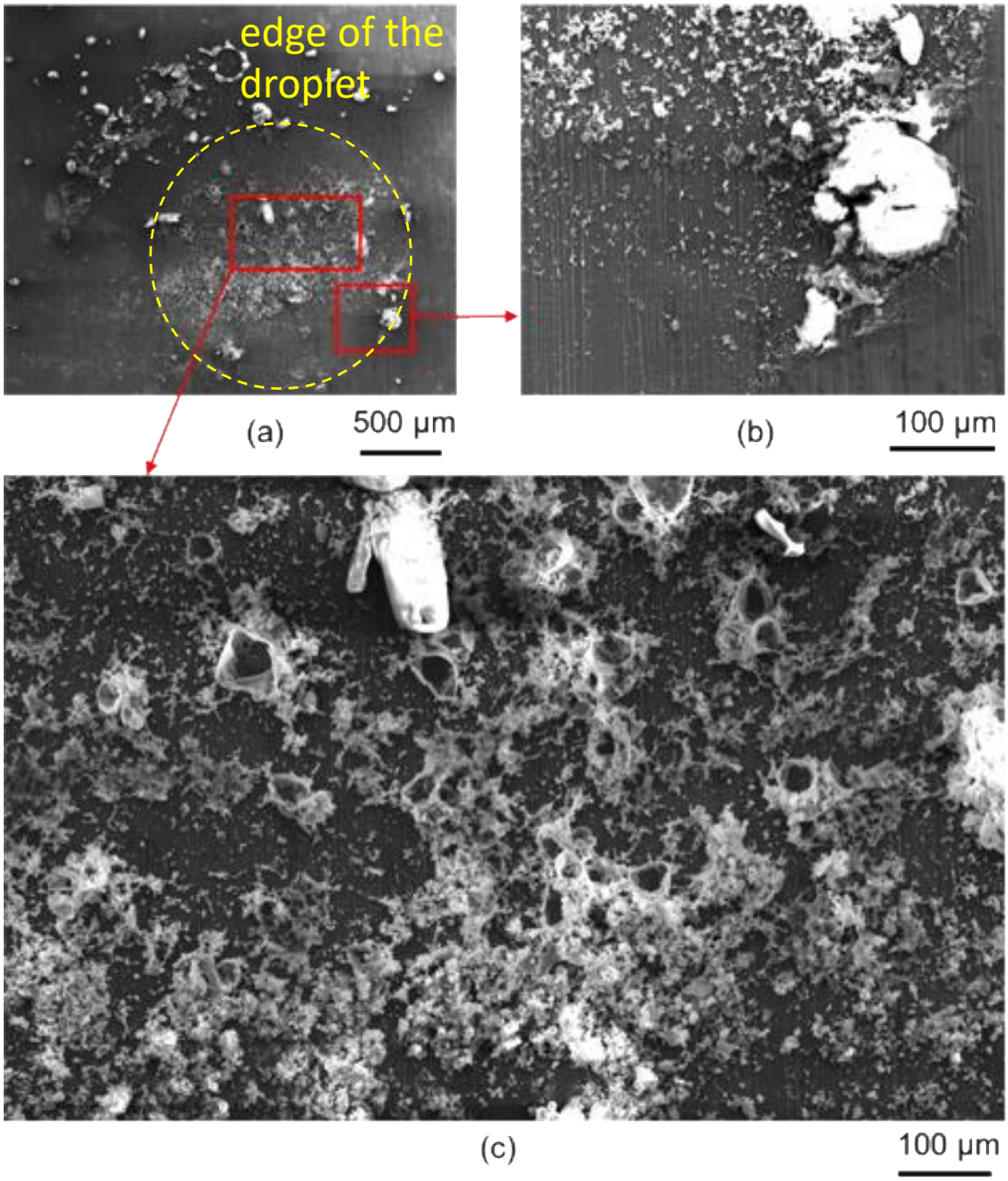

Figure 6-9 Secondary electron SEM images of AA 1050 sheet after 2-week exposure to 1.5 µL droplet of ASW and RH=84 ± 4% and T=30 ºC ± 1; (a) view of the whole droplet, (b) and (c) magnified images of the boxed areas from (a) showing morphology of the corrosion products.

To identify the corrosion products formed under the droplet EDX mapping was performed. The results of the analysis are shown in Figure 6-10. One can notice that chlorine as well as sodium were detected outside the main body of the droplet. However, chlorine was only found in places where the dense corrosion products were

formed, whereas sodium was uniformly distributed around the edge of the droplet. Sulphur, on the other hand, was only detected under the droplet.

Analysis performed using Raman spectroscopy revealed the presence of felsobanyaite ($Al_4(SO_4)(OH)_{10}\cdot 4H_2O$) in the main body of the droplet, and dawsonite ($NaAlCO_3(OH)_2$) outside the droplet, which can be seen in Figure 6-10. The collected and reference Raman spectra are presented in Figure 6-11 and Figure 6-12. EDX analysis confirmed the presence of sulphur in felsobanyaite and sodium in dawsonite. Aluminium sulphate hydrates are common corrosion products on aluminium exposed to marine atmosphere [162–164]. Sulphates present in the solution are adsorbed on aluminium oxide layer [165] and converted into corrosion products.

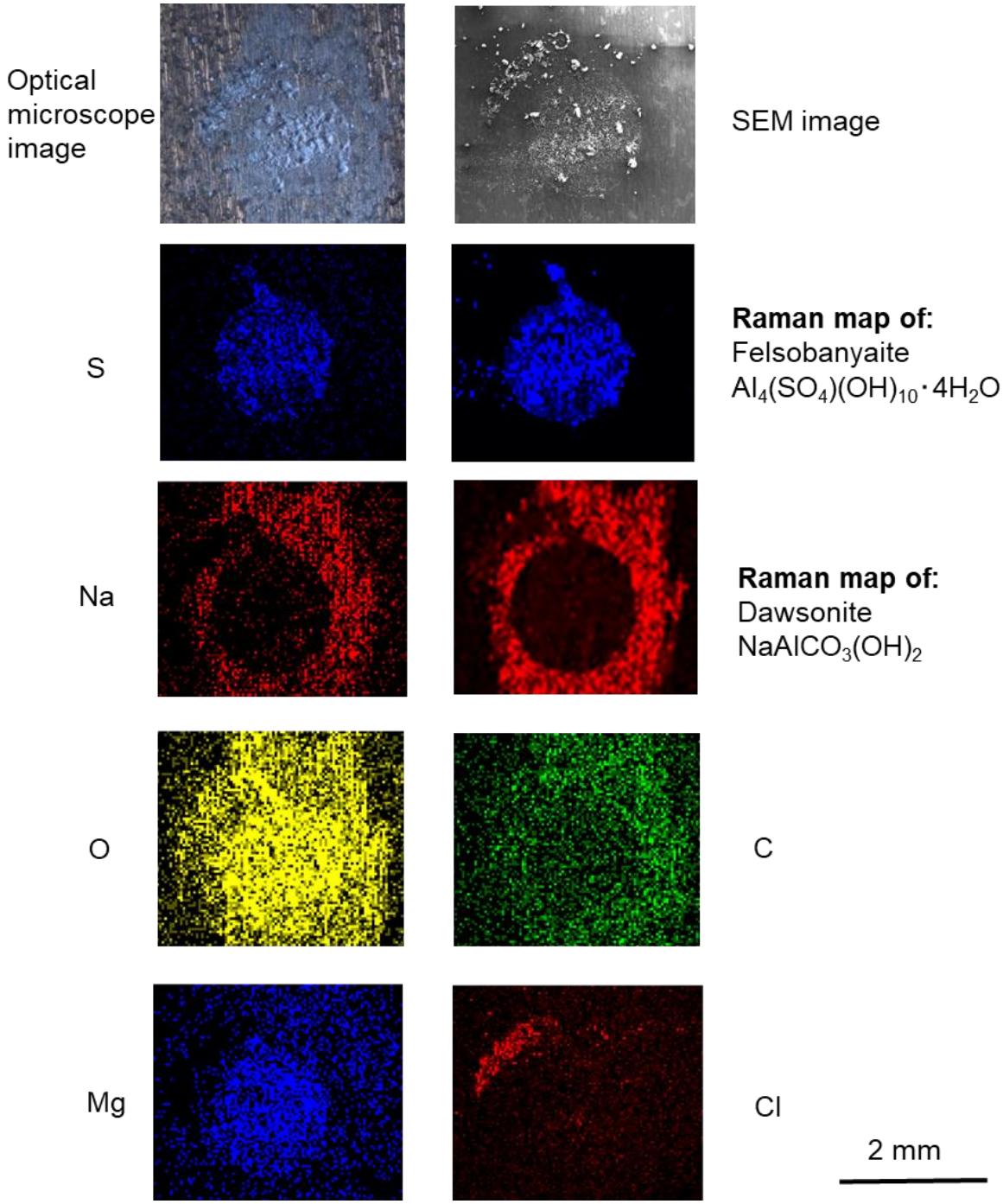

Figure 6-10 Image of corroded AA 1050 sheet sample after 2-week exposure to 1.5 µL droplet of ASW and RH=84±4% and T=30±1 °C; EDX maps of sulphur, oxygen, sodium, magnesium, chlorine and carbon; Raman maps of felsobanyaite and dawsonite; SEM and optical microscope images of the corroded region under the droplet.

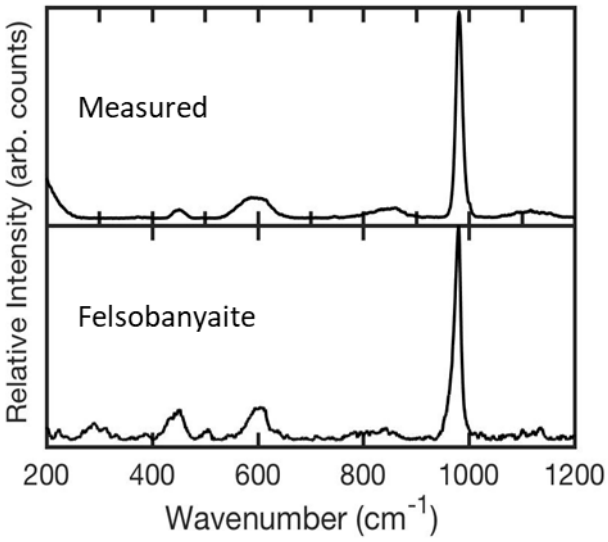

Figure 6-11 Comparison of the measured Raman spectrum (averaged and baseline corrected) formed on the 1050 Al sheet sample after 2-week exposure to 1.5 μL droplet of ASW and RH=84±4% and T=30±1 °C and standard spectrum of felsobanyaite taken from RRUFF database (RUFF ID: R060239).

Felsobanyaite (also known as basaluminite), has been previously detected by Glanvill on aluminium under a droplet of artificial seawater [166]. It precipitates at pH>4.5-5.0 [167] in accordance to the following equation [168]:

$$4Al^{3+} + SO_4^{2-} + 14H_2O \rightarrow Al_4(SO_4)(OH)_{10} \cdot 4H_2O + 10H^+ \quad \text{Equation 6-1}$$

Spreading of droplets at high humidity has been reported by others, mainly on zinc [44–47], copper [48–50] and steel [46,51]. The presence of dawsonite in the spreading region is associated with the development of cathodic regions near the droplet edge, where the water layer thickness is the lowest, and hence the diffusion of oxygen is facilitated. When cathodic reactions proceed, OH^- ions are being produced. Aluminium oxides are soluble in alkaline solutions, which leads to dissolution of the passive film and a change in the interfacial energy. As a result, a pH gradient is established within the droplet, leading to a change in the interfacial energy between the metal and the electrolyte, resulting in the droplet spreading [48]. To balance the negative charge,

cations present in the solution (for example Na^+) are attracted to the spreading region, which has easy access to carbon dioxide. Since precipitation of dawsonite requires alkaline conditions [169], with pH 10.3 being the most favourable [170], it could be assumed, that alkaline conditions were present in the spreading region which facilitated precipitation of dawsonite :

$$Al^{3+} + 2OH^- + Na^+ + HCO_3^- \rightarrow NaAlCO_3(OH)_2 + H^+ \qquad \text{Equation 6-2}$$

Dawsonite was also detected by Schaller et al. [171] on aluminium after exposure to an NaCl droplet and 80% RH. Moreover, carbonate deposits were also observed on aluminium after exposure to NaCl, by Blucher at al. [172] and [173].

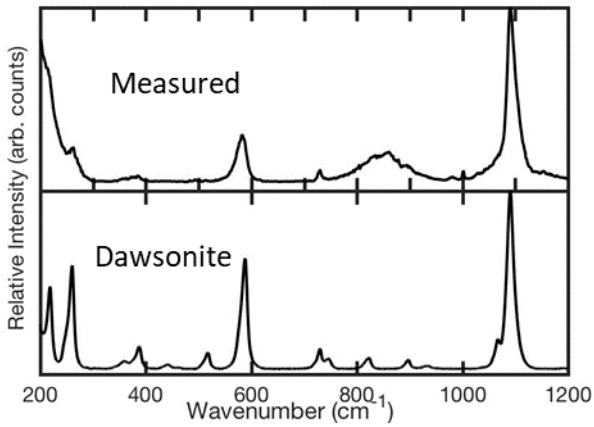

Figure 6-12 Comparison of the measured Raman spectrum (averaged and baseline corrected) formed on the 1050 Al sample after 2-week exposure to 1.5 μL droplet of ASW and RH=84±4% and T=30±1 °C and standard spectrum of dawsonite taken from RRUFF database (RUUFF ID: R120093).

6.3.2 TSA

EDX analysis of corrosion products (Figure 6-13) formed under the 1.5 μL droplet of ASW on TSA deposited on a glass slide during a 2-week exposure to RH=84±4% and T=30±1 °C revealed the presence of chlorine, sulphur, and oxygen. Corrosion products were dense and formed under the main body of the droplet.

Raman spectroscopic analysis (Figure 6-14) indicated the presence of felsobanyaite, however the additional peak at 1002 cm^{-1} suggests the possibility of the formation of some other sulphate product like for example aluminite ($Al_2(SO_4)(OH)_4 \cdot 7H_2O$) or alunogen ($Al_2(SO_4)_3 \cdot 17H_2O$).

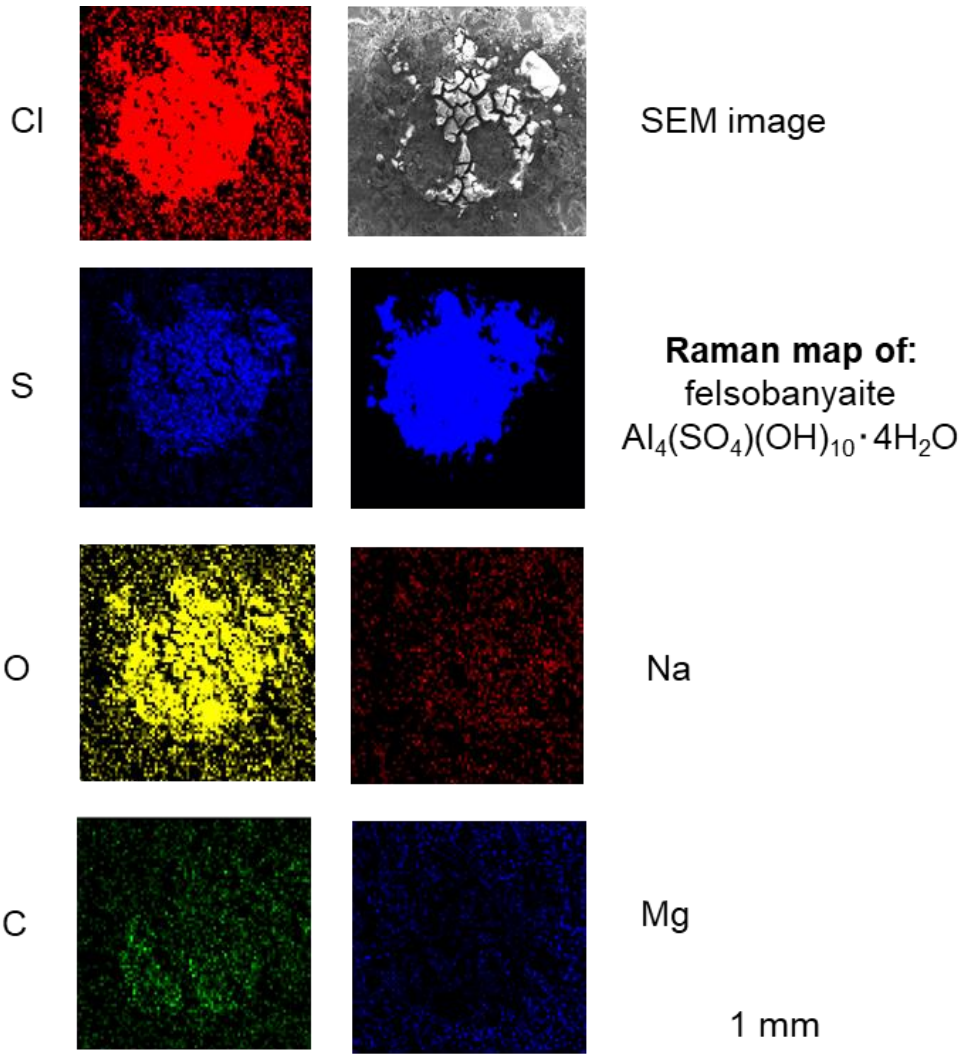

Figure 6-13 Image of corroded TSA on glass sample after 2-week exposure to 1.5 µL droplet of ASW and RH=84±4% and T=30±1 °C; EDX maps of chlorine, sulphur, oxygen, sodium, magnesium, and carbon; Raman maps of felsobanyaite; SEM image of the corroded region under the droplet.

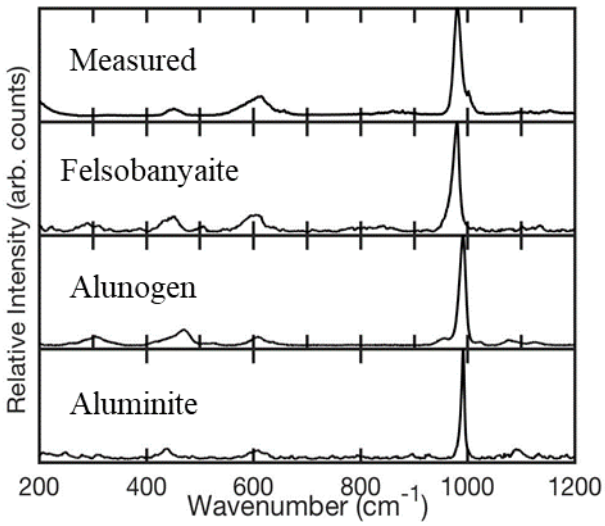

Figure 6-14 Comparison of the measured Raman spectrum (averaged and baseline corrected) formed on the TSA on glass sample after 2-week exposure to 1.5 μL droplet of ASW and RH=84±4% and T=30±1 °C and standard spectrum of felsobanyaite (RUFF ID: R060239), alunogen (RUFF ID: R070601) and aluminite (RUFF ID: R060691) taken from RRUFF database.

Tests performed on the TSA coating deposited on steel showed the same corrosion product (felsobanyaite) located under the main body of the droplet.

One can notice the lack of dawsonite or any similar carbonates on TSA. The possible reason for this could be that the droplets did not spread (as shown in Figure 6-15) on TSA samples because of the very rough surface.

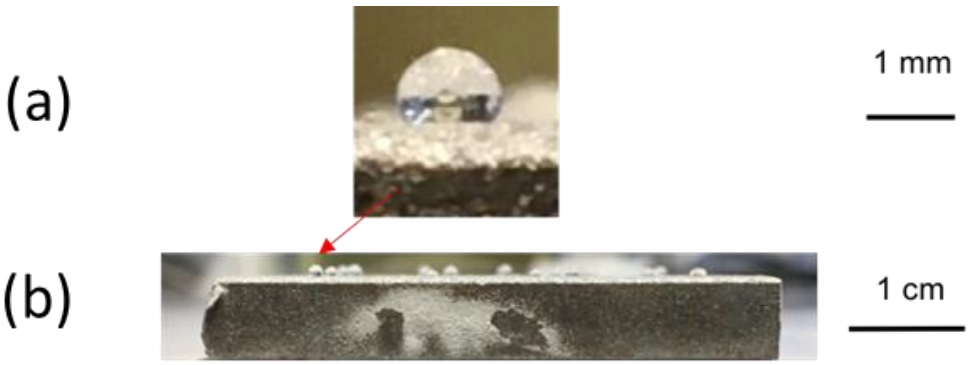

Figure 6-15 Arrays of droplets of ASW on TSA on steel sample, immediately after the completion of 2-week exposure; (a) magnified image of the first droplet from a side view showing its spherical shape, (b) side view of the sample.

Since the spreading of the droplet on smooth solid metal surface is associated with the development of separate anodic and cathodic regions, it can be assumed that anodic and cathodic reactions were not so clearly separated on TSA coatings. The roughness of the coating (TSA on steel (Figure 6-16, Figure 6-17) is as follows: Ra=26.5μm, TSA on glass: Ra=24.0 μm), influences the wettability of the droplet [174,175]. Moreover, the lack of spreading could also be associated with the presence of porosity within the coating or the presence of a thicker oxide layer.

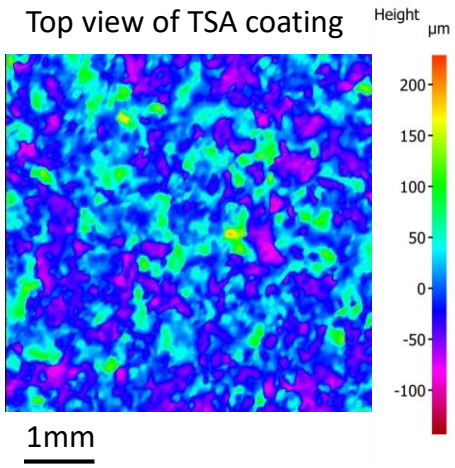

Figure 6-16 Surface roughness of uncorroded TSA coating.

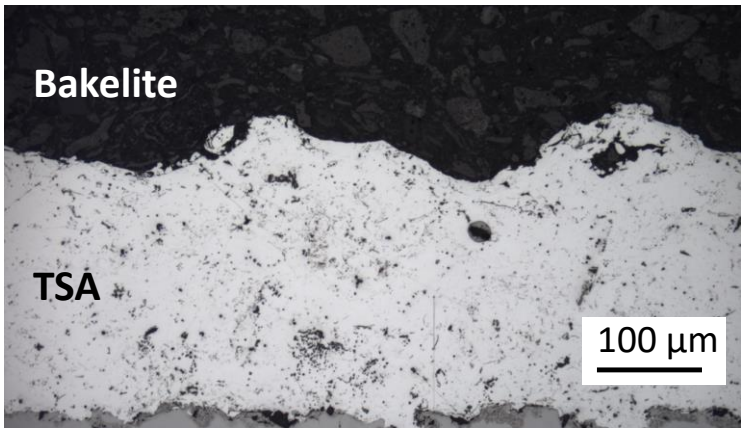

Figure 6-17 Optical micrograph of a cross-section of uncorroded TSA coating showing surface morphology.

6.4 Conclusions

1. Electrochemical measurements performed under droplets of artificial seawater on TSA-coated steel revealed higher cathodic activity under droplets in comparison with full immersion conditions.

2. ZnAl coating shows higher anodic activity and similar cathodic activity to Al coating under a droplet of artificial seawater, therefore it performs better as a sacrificial coating.

3. Examination of corrosion products formed on 1050 aluminium sheet and TSA (AA 1050) under a droplet of artificial seawater revealed the presence of sulphur containing products such as felsobanyaite and /or aluminite in the main body of the droplet. On 1050 Al sheet, dawsonite has formed in well-defined spreading region, where the cathodic reactions take place, whereas on TSA anodic and cathodic reactions are not clearly separated.

4. Sulphur (from the sulphates in seawater) plays an important role in corrosion processes, therefore the use of aqueous solutions of NaCl as a substitute for seawater for the evaluation of corrosion performance of TSA coatings in marine environments should be avoided, as it could lead to results not representative of seawater exposure.

5. The distribution of cathodic and anodic regions on thermally sprayed coatings is significantly different than on solid metal, probably due to the difference in surface morphology. On solid metal, carbonate-containing product was detected in the well - defined spreading region, whereas on TSA mostly sulphur-containing corrosion products were found in the main body of the droplet.

Chapter 7 General discussion, conclusions and future work

7.1 General discussion

The application of TSA coatings is one of corrosion mitigation methods which can be used to protect steel structures operating in harsh marine environments. Due to its sacrificial actions when coupled to steel, TSA is not only capable of providing barrier properties towards the substrate from seawater when the coating is intact, but it also provides sacrificial protection when the coating is damaged. However, the effectiveness of the sacrificial properties of the coating depends on the operating conditions during the exposure.

The results obtained in this research revealed new information regarding the performance of TSA, solid aluminium and steel at cold temperatures - under full immersion conditions. Moreover, the results of atmospheric corrosion tests provided an insight into the corrosion behaviour of TSA under droplets of seawater. This has not been addressed in the available literature before.

This project focused also on exploring and identifying the key parameters which must be taken into account to successfully predict the corrosion performance of sacrificial coatings in real marine environments. The findings are discussed and summarised below.

7.1.1 Temperature

Tests performed on TSA-coated steel samples with defects revealed significantly better performance of the coatings in warm (25 and 32°C) than in cold (4°C) seawater.

This was attributed to higher activity of the coating and higher deposition rate of calcareous deposits.

The effect of temperature was even more pronounced when TSA was sealed. Sealed samples which were exposed to warm seawater (25°C) performed well. Calcareous deposits were found in the areas were steel was in direct contact with the seawater. They were dense and protective towards the substrate. Samples immersed in cold seawater (4°C), on the other hand, performed poorly and sealed TSA did not provide sufficient polarisation to the steel. This resulted in visible rust in the defects.

Literature review revealed that TSA has been mainly used to protect offshore structures operating in the North Sea. The temperature of surface seawater of this particular environment varies between 4 and 16°C [176]. Currently, TSA is also being used for the protection of offshore wind turbines operating in the Baltic Sea [138] which temperature can drop to 0°C in winter time and rise above 20°C in summer [176]. The results obtained in this research indicate that the level of corrosion protection provided by TSA, towards an offshore structure operating in those regions, depends strongly on the time of installation. If the offshore structure is assembled during a cold winter season and the coating gets damaged during transportation or installation, it is likely that TSA will not provide cathodic protection towards the underlying steel. However, if the structure is installed during summer season, TSA will provide full corrosion protection towards the substrate, even if the coating contains a discontinuity.

7.1.2 Time

Experiments conducted on damaged and intact TSA coatings on steel revealed that the evolution of the potential during the immersion in seawater is strongly time and temperature dependent. At low temperatures, longer time is required for the potential

to stabilise, due to slower kinetics of the reactions. At all temperatures tested, the potential exhibited significant variations during initial 30 days of immersion. Therefore, in order to correctly assess the corrosion behaviour of the coatings, seawater exposures of at least 30 days are needed. Shorter exposures (often adopted by other researchers - Table 2-4) might lead to misleading results.

7.1.3 Seawater vs NaCl for testing TSA

One of the most common corrosion testing methods is salt spray test (ASTM B117 [177]) during which 5wt% NaCl solutions is sprayed on the samples exposed to warm temperature (35°C). This approach is widely used because NaCl is the most abundant seawater constituent and Cl^- ions are known to be responsible for breaking up passive layers on metals and triggering localised corrosion attack. However, the results of the atmospheric corrosion tests performed on TSA coatings revealed the presence of sulphur-containing corrosion products of aluminium after the corrosion testing. This indicates that SO_4^{2-} ions plays an important role in corrosion processes. Moreover, the immersion tests performed on damaged TSA coatings on steel revealed the formation of calcareous deposits: $Mg(OH)_2$ and $CaCO_3$ - on the cathode and Mg- and Ca-containing aluminium products in the vicinity of the anode. This clearly shows that NaCl cannot be used as a substitute for natural seawater, as Mg^{2+} and Ca^{2+} play not only an extremely important part in the cathodic protection mechanisms (precipitation of calcareous deposits decrease the area of the steel to be protected and therefore decrease the current demand from the coating), but also in corrosion of aluminium.

7.1.4 Exposure type

Tests performed on sealed TSA coatings on steel - under alternating wetting and drying conditions, showed how important it is to appropriately design the experiments to mimic the condition that the real structure is exposed to. Alternating immersion conditions resulted in different behaviour of the samples in comparison with full immersion conditions. Under full seawater immersion at 25°C, sealed TSA performed well. It provided sufficient polarisation of the substrate which resulted in suppression of corrosion attack on steel and development of calcareous deposits on the exposed substrate, whereas under alternating seawater immersion at the same temperature, significant corrosion of the exposed steel was observed. This indicates that application of sealants might be beneficial for TSA operating under full immersion but detrimental under alternating immersion, for example in the tidal zone.

7.1.5 Summary

To successfully predict the corrosion performance of sacrificial coatings in real marine environments, one should test the coatings under representative conditions and for sufficient amount of time. This project revealed that temperature, chemistry of the solution, application of sealants and operating conditions have great influence on the behaviour of the coatings. Those parameters should be included in the design of experiments to appropriately assess the efficiency and lifetime of the coatings to protect steel from corrosion in seawater.

The knowledge obtained during the course of this project and described in this thesis is novel and can be used by industrial organisations to develop more resilient coatings for protection of critical elements of the offshore infrastructures. Better corrosion

protection systems will not only have a positive economic impact, but it will also increase safety by decreasing chances of corrosion-provoked catastrophic failures.

7.2 General conclusions

Based on various tests performed on thermally sprayed coatings for corrosion protection of steel operating in seawater environments the following conclusions can be drawn:

1. Al 1050 showed lower corrosion potential compared with AlMg5% and Al 1100, therefore it was the most efficient in moving the potential of steel into the protective region (below -0.8V) under full immersion conditions. ZnAl15% alloy, exhibited significantly lower Rp values (indicating higher corrosion current density) compared with Al coatings, and therefore this coating would have a shorter lifetime in-service.
2. Temperature affects corrosion performance of TSA (AA 1050) coatings on steel in several ways. First of all, it affects the potential of aluminium, which is initially controlled by the cathodic reactions and later by the passive current density. Second of all, it influences the precipitation of calcareous deposits ($Mg(OH)_2$ and $CaCO_3$) on exposed steel. At low temperatures (below 20°C) the potential of Al is closer to the potential of steel and less calcareous deposits precipitate. Therefore, the protection efficiency provided by the TSA is lower.
3. Before conducting electrochemical testing on TSA coatings in seawater, pre-exposures of at least 30 days are needed to obtain a stable corrosion potential. Shorter exposures might lead to misleading results.
4. Sealants can be used to prolong the lifetime of TSA coatings operating under full seawater immersion at warm temperatures (25°C). However, they should

not be used for cold (4°C) seawater applications or alternating drying and wetting exposures, because they impair the sacrificial actions of the TSA under those conditions.

5. Examination of corrosion products formed on TSA (AA 1050) under a droplet of artificial seawater revealed the presence of sulphur containing products such as felsobanyaite in the main body of the droplet.
6. Examination of corrosion products formed on TSA (AA 1050) after full seawater immersion revealed that not only sulphur but also magnesium and calcium can be incorporated into corrosion products of aluminium. Moreover, ions present in seawater play important roles in the precipitation of calcareous deposits on cathodically polarised steel. Calcareous minerals are capable of impeding the diffusion of oxygen to the steel surface and reducing the dissolution rate of aluminium. Therefore, the use of aqueous solutions of NaCl as a substitute for seawater for the evaluation of corrosion performance of TSA coatings in marine environments should be avoided, as it could lead to results not representative of seawater exposure.
7. The distribution of cathodic and anodic regions on thermally sprayed coatings is different than on solid metal, probably due to the difference in surface morphology. On solid metal, carbonate-containing product was detected in the well - defined spreading region, whereas on TSA mostly sulphur-containing corrosion products were found in the main body of the droplet.

7.3 Recommendations for future work

The findings described in this thesis contributed to answer several gaps in knowledge about the fundamental mechanisms of corrosion of TSA. However, to further increase the confidence in this technology and accelerate its adoption by the industry, further work remains to be completed. Suggested areas of further research include:

1. Further research on the corrosion performance of damaged TSA at 4°C

Results of the experiments described in chapter 5 revealed different behaviour of TSA - coated steel immersed in seawater at 4°C. The effectiveness of coating at this temperature was significantly worse than at any other temperature tested. Required polarisation was not provided by the TSA and precipitation of calcareous deposits was inhibited. The reason of the different behaviour was not identified and requires further investigation.

2. Research on effectiveness of TSA when there is a damage after the coating has been in service for a few months

The corrosion tests described in this thesis (in chapter 5) where designed to simulate a situation when TSA gets damaged during transportation or installation of an offshore structure. However, TSA can also get damaged in service (ice drift, floating objects etc.). It is not known if the coating which has been corroding for a few months/years, and has been covered with corrosion products, is able to provide cathodic protection towards the steel.

3. The performance of damaged TSA coatings working in conjunction with external CP in cold seawater.

The outcome of the testing described in chapter 5 revealed that the corrosion protection of steel provided by TSA in cold seawater is less efficient than in warm

electrolyte. This was attributed to lower solubility of the aluminium layer and slower deposition rate of calcareous deposits. This could potentially be improved by the addition of external CP which could trigger precipitation of the calcareous minerals. However, external CP would also influence the dissolution rate of the TSA layer and therefore could potentially significantly decrease the lifetime of the coating.

4. The determination of minimal salinity of water needed for the TSA to work effectively, especially if TSA contains defects and operates in cold environment.

In this project all the tests were conducted with the use of standard ASTM 1141 seawater of fixed composition. However, it should be pointed out that sometimes the salinity of the water could be lower than usual 3.5%, for example close to an estuary. It is likely that the effectiveness of TSA is worse in the water containing lower amount of Cl^- ions, which are responsible for breaking the passive layer of aluminium.

References

1. The Crown Estate *Offshore Wind - Operational report 2017*;
2. Jensen, B.B. Specifying corrosion protection for the offshore wind turbine industry. *Corros. 2017* **2017**, 1–10.
3. Kaiser, M.J.; Snyder, B.F. *Offshore Wind Energy Cost Modeling: Installation and Decommissioning*; Springer Science & Business Media, 2012; ISBN 978-1-4471-2487-0.
4. López-Ortega, A.; Bayón, R.; Arana, J.L. Evaluation of protective coatings for high-corrosivity category atmospheres in offshore applications. *Materials (Basel).* **2019**, *12*, 1325.
5. Veritas, D.N. Recommended practice DNVGL-RP-0416 Corrosion protection for wind turbines. **2016**.
6. Han, M.S.; Woo, Y. Bin; Ko, S.C.; Jeong, Y.J.; Jang, S.K.; Kim, S.J. Effects of thickness of Al thermal spray coating for STS 304. *Trans. Nonferrous Met. Soc. China (English Ed.* **2009**, *19*, 925–929.
7. Paul, S.; Lee, C.M.; Harvey, M.. D.F. Improved coatings for extended design life of 22%Cr duplex stainless steel in marine environments. In Proceedings of the Thermal Spray 2012: Proceedings from the International Thermal Spray Conference and Exposition; ASM International: Houston, Texas, USA, 2012; pp. 544–549.
8. Knudsen, O.Ø.; Van Bokhorst, J.; Clapp, G.; Duncan, G. Technical note: Corrosion of cathodically polarized thermally sprayed aluminum in subsea mud at high temperature. *Corrosion* **2016**.
9. Syrek-Gerstenkorn, B.; Paul, S.; Davenport, A.J. Use of thermally sprayed aluminium (TSA) coatings to protect offshore structures in submerged and splash zones. *Surf. Coatings Technol.* **2019**, *374*, 124–133.
10. Echaniz, R.G.; Paul, S.; Thornton, R. Effect of seawater constituents on the performance of thermal spray aluminum in marine environments. *Mater. Corros.* **2019**, *70*, 996–1004.
11. Lee, H.S.; Singh, J.K.; Park, J.H. Pore blocking characteristics of corrosion products formed on Aluminum coating produced by arc thermal metal spray process in 3.5 wt.% NaCl solution. *Constr. Build. Mater.* **2016**, *113*, 905–916.
12. Abedi Esfahani, E.; Salimijazi, H.; Golozar, M.A.; Mostaghimi, J.; Pershin, L. Study of corrosion behavior of Arc sprayed aluminum coating on mild steel. *J. Therm. Spray Technol.* **2012**, *21*, 1195–1202.
13. Malik, A.U.; Ahmad, S.; Andijani, I.; Al-Fouzan, S. Corrosion behavior of steels in Gulf seawater environment. *Desalination* **1999**, *123*, 205–213.
14. Li, S.; Zeng, Z.; Harris, M.A.; Sánchez, L.J.; Cong, H. CO 2 corrosion of low carbon steel under the joint effects of time-temperature-salt concentration. *Front. Mater.* **2019**, *6*, 1–17.
15. Liu, Y.; Gao, Z.; Lu, X.; Wang, L. Effect of temperature on corrosion and cathodic protection of X65 pipeline steel in 3.5% NaCl solution. *Int. J. Electrochem. Sci.* **2019**, *14*, 150–160.
16. Mercer, A.D.; Lumbard, E.A. Corrosion of mild steel in water. *Br. Corros. J.* **1995**, *30*, 43–55.
17. Xing, W.; Yin, M.; Lv, Q.; Hu, Y.; Liu, C.; Zhang, J. Oxygen Solubility, Diffusion

Coefficient, and Solution Viscosity. In *Rotating Electrode Methods and Oxygen Reduction Electrocatalysts*; Xing, W., Ed.; Elsevier B.V.: Vancouver, 2014; pp. 1–31 ISBN 9780444632784.
18. Shen, Y.; Dong, Y.; Li, H.; Chang, X.; Wang, D.; Li, Q.; Yin, Y. The Influence of Low Temperature on the Corrosion of EH40 Steel in a NaCl Solution. *Int. J. Electrochem. Sci.* **2018**, *13*, 6310–6326.
19. Garrigues, L.; Pebere, N.; Dabosi, F. An investigation of the corrosion inhibition of pure aluminum in neutral and acidic chloride solutions. *Electrochim. Acta* **1996**, *41*, 1209–1215.
20. Davis, J.R. *Corrosion of aluminium and aluminium alloys*; ASM International, 1999; ISBN 0-87170-641-5.
21. Reboul, M.C.; Baroux, B. Metallurgical aspects of corrosion resistance of aluminium alloys. *Mater. Corros.* **2011**, *62*, 215–233.
22. MacDonald, D.D.; Butler, P. The thermodynamics of the aluminium-water system at elevated temperatures. *Corros. Sci.* **1973**, *13*, 259–274.
23. Thomas, J.K.; Ondrejcin, R.S. An evaluation of the thickness and emittance of aluminum oxide films formed in low-temperature water. *J. Nucl. Mater.* **1993**, *199*, 192–213.
24. Alwitt, R.S. The Growth of Hydrous Oxide Films on Aluminum. *J. Electrochem. Soc.* **1974**, *121*, 1322–1328.
25. Hart, R.K. The formation of films on aluminium immersed in water. *Trans. Faraday Soc.* **1957**, *53*, 1020–1027.
26. Feng, X.; Baojie, Z.; Chery, L. Effects of low temperature on aluminum(III) hydrolysis: Theoretical and experimental studies. *J. Environ. Sci.* **2008**, *20*, 907–914.
27. Uhlig, H.H. *Uhlig's Corrosion Handbook*; Third.; John Wiley & Sons, 2011;
28. Johnson, W.K. Recent Developments in Pitting Corrosion of Aluminium. *Br. Corros. J.* **1971**, *6*, 200–204.
29. Ambat, R.; Davenport, A.J.; Scamans, G.M.; Afseth, A. Effect of iron-containing intermetallic particles on the corrosion behaviour of aluminium. **2006**, *48*, 3455–3471.
30. Szklarska-Smialowska, Z. Pitting corrosion of aluminum. *Corros. Sci.* **1998**, *41*, 1743–1767.
31. Frankel, G.S. Pitting corrosion of metals. A review of the critical factors. *J. Electrochem. Soc.* **1998**, *145*, 2186–2198.
32. Soltis, J. Passivity breakdown , pit initiation and propagation of pits in metallic materials – Review. *Corros. Sci.* **2015**, *90*, 5–22.
33. Soltis, J.; Laycock, N.J.; Krouse, D. Temperature dependence of the pitting potential of high purity aluminium in chloride containing solutions. *Corros. Sci.* **2011**, *53*, 7–10.
34. Ezuber, H.; El-Houd, A.; El-Shawesh, F. A study on the corrosion behavior of aluminum alloys in seawater. *Mater. Des.* **2008**, *29*, 801–805.
35. Broli, A.; Holtan, H. Determination of characteristic pitting potentials for aluminium by use of the potentiostatic methods. *Corros. Sci.* **1977**.
36. Al-Moubaraki, A.H.; Al-Rushud, H.H. The Red Sea as a Corrosive Environment: Corrosion Rates and Corrosion Mechanism of Aluminum Alloys 7075, 2024, and 6061. *Int. J. Corros.* **2018**, 1–15.
37. Dexter, S.C. Effect of variations in sea water upon the corrosion of aluminum.

Corrosion **1980**, *36*, 423–432.
38. Rowland, H.T.H.T.; Dexter, S.C. Effects of the sea water carbon dioxide system on the corrosion of aluminum. *Corrosion* **1980**, *36*, 458–467.
39. Veritas, D.N. *Recommended practice DNVGL-RP-B401 Cathodic protection design*; 2017;
40. Hackerman, N. Effect of Temperature on Corrosion of Metals by Water. *Ind. Eng. Chem.* **1952**, *44*, 1752–1755.
41. Hao, L.; Zheng, F.; Chen, X.; Li, J.; Wang, S.; Fan, Y. Erosion corrosion behavior of aluminum in flowing deionizedwater at various temperatures. *Materials (Basel).* **2020**, *13*, 1–14.
42. Huang, I.-W.; Hurley, B.L.; Yang, F.; Buchheit, R.G. Dependence on Temperature, pH, and Cl − in the Uniform Corrosion of Aluminum Alloys 2024-T3, 6061-T6, and 7075-T6. *Electrochim. Acta* **2016**.
43. Melchers, R.E. Influence of temperature on sea water immersion corrosion of aluminium (UNS A95086). *Br. Corros. J.* **2001**, *36*, 201–204.
44. Cole, I.S.; Muster, T.H.; Furman, S.A.; Wright, N.; Bradbury, A. Products Formed during the Interaction of Seawater Droplets with Zinc Surfaces: I. Results from 1- and 2.5-Day Exposures. *J. Electrochem. Soc.* **2008**, *155*, C244–C255.
45. Chen, Z.Y.; Persson, D.; Leygraf, C. Initial NaCl-particle induced atmospheric corrosion of zinc - Effect of CO2 and SO2. *Corros. Sci.* **2008**, *50*, 111–123.
46. Nazarov, A.; Thierry, D. Rate-determining reactions of atmospheric corrosion. In Proceedings of the Electrochimica Acta; 2004; pp. 2717–2724.
47. Neufeld, A.K.; Cole, I.S.; Bond, A.M.; Furman, S.A. The initiation mechanism of corrosion of zinc by sodium chloride particle deposition. *Corros. Sci.* **2002**, *44*, 555–572.
48. Schindelholz, E.J.; Cong, H.; Jove-Colon, C.F.; Li, S.; Ohlhausen, J.A.; Moffat, H.K. Electrochemical aspects of copper atmospheric corrosion in the presence of sodium chloride. *Electrochim. Acta* **2018**, *276*, 194–206.
49. Chen, Z.Y.; Persson, D.; Nazarov, A.; Zakipour, S.; Thierry, D.; Leygraf, C. In Situ Studies of the Effect of CO2 on the Initial NaCl-Induced Atmospheric Corrosion of Copper. *J. Electrochem. Soc.* **2005**, *152*, B342–B351.
50. Chen, Z.Y.; Persson, D.; Samie, F.; Zakipour, S.; Leygraf, C. Effect of Carbon Dioxide on Sodium Chloride-Induced Atmospheric Corrosion of Copper. *J. Electrochem. Soc.* **2005**, *152*, B502–B511.
51. Tsuru, T.; Tamiya, K.I.; Nishikata, A. Formation and growth of micro-droplets during the initial stage of atmoshperic corrosion. *Electrochim. Acta* **2004**, *49*, 2709–2715.
52. Morton, S.C.; Frankel, G.S. Atmospheric pitting corrosion of AA7075-T6 under evaporating droplets with and without inhibitors. *Mater. Corros.* **2014**, *65*, 351–361.
53. Glanvill, S. Atmospheric corrosion of AA2024 in ocean water environments. *PhD thesis, Univ. Birmingham* **2018**.
54. S.W. Dean, W.H.A. Atmospheric corrosion of wrought aluminum alloys during a ten-year period. *Degrad. Met. Atmos.* **1988**, *ASTM Inter*, 191–205.
55. de la Fuente, D.; Otero-Huerta, E.; Morcillo, M. Studies of long-term weathering of aluminium in the atmosphere. *Corros. Sci.* **2007**, *49*, 3134–3148.
56. Lyon, S.B.; Thompson, G.E.; Johnson, J.B.; Wood, G.C.; Ferguson, J.M. Accelerated atmospheric corrosion testing using a cyclic wet/dry exposure test:

aluminum, galvanized steel, and steel. *Corrosion* **1987**, *43*, 719–726.
57. King, P.C.; Cole, I.S.; Corrigan, P.A.; Hughes, A.E.; Muster, T.H. FIB/SEM study of AA2024 corrosion under a seawater drop, part I. *Corros. Sci.* **2011**, *53*, 1086–1096.
58. Dan, Z.; Takigawa, S.; Muto, I.; Hara, N. Applicability of constant dew point corrosion tests for evaluating atmospheric corrosion of aluminium alloys. *Corros. Sci.* **2011**, *53*, 2006–2014.
59. Dan, Z.; Muto, I.; Hara, N. Effects of environmental factors on atmospheric corrosion of aluminium and its alloys under constant dew point conditions. *Corros. Sci.* **2012**, *57*, 22–29.
60. Leygraf, C.; Wallinder, I.O.; Graedel, T. *Atmospheric Corrosion*; Second Edi.; John Wiley & Sons: New Jersey, 2016;
61. Cunningham, T.; Avery, R. Sealer coatings for thermal-sprayed aluminum in the offshore industry. *Mater. Perform.* **2000**, *39*, 46–48.
62. Tejero-Martin, D.; Rezvani Rad, M.; McDonald, A.; Hussain, T. Beyond traditional coatings: a review on thermal-sprayed functional and smart coatings. *J. Therm. Spray Technol.* **2019**, *28*, 598–644.
63. Fournier, J.; Miousse, D.; Legoux, J.-G. Wire-arc sprayed nickel based coatings for hydrogen evolution reaction in alkaline solutions. *Int. J. Hydrogen Energy* **1995**, *24*, 519–528.
64. Malek, M.H.A.; Saad, N.H.; Abas, S.K.; Shah, N.M. Thermal arc spray overview. *IOP Conf. Ser. Mater. Sci. Eng.* **2013**, *46*, 012028.
65. Davis, J.R. Introduction to thermal spray processing. In *Handbook of Thermal Spray Technology*; ASM International, 2004.
66. Amin, S.; Panchal, H. A review on thermal spray coating processes. *Int. J. Curr. Trends Eng. Res.* **2016**, *2*, 556–563.
67. Pombo Rodriguez, R.M.H.; Paredes, R.S.C.; Wido, S.H.; Calixto, A. Comparison of aluminum coatings deposited by flame spray and by electric arc spray. *Surf. Coatings Technol.* **2007**, *202*, 172–179.
68. Gartland, P.O.; Eggen, T.G. Cathodic and anodic properties of thermally sprayed Al and Zn-based coatings in seawater Paper No. 367. In Proceedings of the Corrosion 90; NACE International: Houston, TX, 1990.
69. Bardal, E. The effect of surface preparation on the adhesion of arc and flame-sprayed aluminum and zinc coatings to mild steel. In Proceedings of the 7th International metal spraying conference; London, 1973.
70. Lieberman, E.S.; Clayton, C.R.; Herman, H. *Thermally sprayed active metal coatings for corrosion protection in marine environments*; Report, Defense Technical Information Center, USA, 1984;
71. Malek, M.H.A.; Saad, N.H.; Abas, S.K.; Roselina, N.R.N.; Shah, N.M. Performance and microstructure analysis of 99.5% aluminium coating by thermal arc spray technique. *Procedia Eng.* **2013**, *68*, 558–565.
72. Thomason, W.H.; Olsen, S.; Haugen, T.; Fischer, K. Deterioration of Thermal Sprayed Aluminum Coatings on Hot Risers Due to Thermal Cycling. *Corros. 2004* **2004**, 1–37.
73. Bland, J. Corrosion Testing of Flame-Sprayed Coated Steel - 19 Year Report. *Am. Weld. Soc.* **1974**.
74. Paul, S.; Harvey, M.D.F.; Ho, Q.Y.; Yunus, K.; Fisher, A.C. Corrosion testing of thermally sprayed aluminum. In Proceedings of the Thermal Spray 2015:

Proceedings from the International Thermal Spray Conference; ASM International: Long Beach, California, USA, 2015; pp. 964–970.
75. Quale, G.; Årtun, L.; Iannuzzi, M.; Johnsen, R. Cathodic protection by distributed sacrificial anodes – A new cost- effective solution to prevent corrosion of subsea structures Paper No. 8941. In Proceedings of the Corrosion 2017; NACE International: New Orleans, Louisiana, USA, 2017.
76. Abedi Esfahani, E.; Salimijazi, H.; Golozar, M.A.; Mostaghimi, J.; Pershin, L. Study of corrosion behavior of arc sprayed aluminum coating on mild steel. *J. Therm. Spray Technol.* **2012**, *21*, 1195–1202.
77. Knudsen, O.Ø.; Van Bokhorst, J.; Clapp, G.; Duncan, G. Technical note: Corrosion of cathodically polarized thermally sprayed aluminum in subsea mud at high temperature. *Corrosion* **2016**, *72*, 560–568.
78. Abdoli, L.; Huang, J.; Li, H. Electrochemical corrosion behaviors of aluminum-based marine coatings in the presence of Escherichia coli bacterial biofilm. *Mater. Chem. Phys.* **2016**, *173*, 62–69.
79. Li, N.; Li, W.Y.; Yang, X.W.; Alexopoulos, N.D.; Niu, P.L. Effect of powder size on the long-term corrosion performance of pure aluminium coatings on mild steel by cold spraying. *Mater. Corros.* **2017**, *68*, 546–551.
80. Bai, X.; Tang, J.; Gong, J.; Lü, X. Corrosion performance of Al–Al 2 O 3 cold sprayed coatings on mild carbon steel pipe under thermal insulation. *Chinese J. Chem. Eng.* **2017**, *25*, 533–539.
81. Paul, S. Corrosion performance of damaged thermally sprayed aluminiun in synthetic seawater at different temperatures. *Therm. Spray Bull.* **2015**, *67*, 139–146.
82. Yung, T.Y.; Chen, T.C.; Tsai, K.C.; Lu, W.F.; Huang, J.Y.; Liu, T.Y. Thermal spray coatings of Al, ZnAl and Inconel 625 alloys on SS304L for anti-saline corrosion. *Coatings* **2019**, *9*, 32.
83. Ghali, E. *Corrosion Resistance of Aluminum and Magnesium Alloys: Understadning, Performance and Testing*; John Wiley & Sons, 2010;
84. Morakul, S.; Otsuka, Y.; Miyashita, Y.; Mutoh, Y. Effect of Mg concentration on interfacial strength and corrosion fatigue behavior of thermal-sprayed Al-Mg coating layers. *Eng. Fail. Anal.* **2018**, *88*, 13–24.
85. Park, I.C.; Kim, S.J. Electrochemical characteristics in seawater for cold thermal spray-coated Al-Mg alloy layer. *Acta Metall. Sin. (English Lett.* **2016**, *29*, 727–734.
86. Wilson, H.; Johnsen, R.; Rodriguez, C.T.; Hesjevik, S.M. Properties of TSA in natural seawater at ambient and elevated temperature. *Mater. Corros.* **2019**, *7*, 293–306.
87. Adamiak, M.; Czupr Nski, A.; Kopy, A.; Monica, Z.; Olender, M.; Gwiazda, A. The properties of arc-sprayed aluminum coatings on armor-grade steel. *Metals (Basel).* **2018**, *8*, 142.
88. Fauchais, P.; Vardelle, A. Thermal sprayed coatings used against corrosion and corrosive wear. In *Advanced Spray Applications*; Jazi, H.S., Ed.; IntechOpen, 2012; pp. 3–39 ISBN 978-953-51-0349-3.
89. NORSOK standard M-501 Surface preparation and protective coating 2004.
90. López-Ortega, A.; Bayón, R.; Arana, J.L. Evaluation of protective coatings for offshore applications. Corrosion and tribocorrosion behavior in synthetic seawater. *Surf. Coatings Technol.* **2018**, *349*, 1083–1097.

91. López-Ortega, A.; Areitioaurtena, O.; Alves, S.A.; Goitandia, A.M.; Elexpe, I.; Arana, J.L.; Bayón, R. Development of a superhydrophobic and bactericide organic topcoat to be applied on thermally sprayed aluminum coatings in offshore submerged components. *Prog. Org. Coatings* **2019**, *137*, 105376.
92. Gu, W.; Shen, D.; Wang, Y.; Chen, G.; Feng, W.; Zhang, G.; Fan, S.; Liu, C.; Yang, S. Deposition of duplex Al2O3 /aluminum coatings on steel using a combined technique of arc spraying and plasma electrolytic oxidation. *Appl. Surf. Sci.* **2006**, *252*, 2927–2932.
93. López-Ortega, A.; Arana, J.L.; Rodríguez, E.; Bayón, R. Corrosion, wear and tribocorrosion performance of a thermally sprayed aluminum coating modified by plasma electrolytic oxidation technique for offshore submerged components protection. *Corros. Sci.* **2018**, *143*, 258–280.
94. Pang, X.; Wang, R.; Wei, Q.; Zhou, J. Effect of epoxy resin sealing on corrosion resistance of arc spraying aluminium coating using cathode electrophoresis method. *Mater. Res. Express* **2018**, *5*, 016527.
95. Wang, Y.; Zhang, T.; Zhao, W.; Tang, X. Sealing Treatment of Aluminum Coating on S235 Steel with Thermal Diffusion of Zinc. *J. Therm. Spray Technol.* **2015**, *24*, 1052–1059.
96. Lee, H.-S.; Singh, J.K.; Ismail, M.A. An effective and novel pore sealing agent to enhance the corrosion resistance performance of Al coating in artificial ocean water. *Sci. Rep.* **2017**, *7*, 41935.
97. Lee, H.; Kumar, A.; Mandal, S.; Singh, J.K.; Aslam, F.; Alyousef, R.; Albduljabbar, H. Effect of sodium phosphate and calcium nitrate sealing treatment on microstructure and corrosion resistance of wire arc sprayed aluminum coatings. *Coatings* **2020**, *10*, 33.
98. Liu, L.M.; Wang, Z.; Song, G. Study on corrosion resistance properties of hydrothermal sealed arc sprayed aluminium coating. *Surf. Eng.* **2010**, *26*, 399–406.
99. Armada, S.; Tilset, B.G.; Pilz, M.; Liltvedt, R.; Bratland, H.; Espallargas, N. Sealing HVOF thermally sprayed WC-CoCr coatings by sol-gel methods. *J. Therm. Spray Technol.* **2011**, *20*, 918–926.
100. Wang, R.; Zhou, J. Effect of glass powder sealings on the corrosion resistance of arc sprayed Al coating. *Mater. Res. Express* **2019**, *6*, 086566.
101. Wenming, L.; Tianyuan, S.; Dejun, K. Effects of laser remelting on surface-interface morphologies, bonding modes and corrosion performances of arc-sprayed Al coating. *Anti-Corrosion Methods Mater.* **2017**, *64*, 43–51.
102. Fischer, K.P.; Thomason, W.H.; Rosbrook, T.; Murali, J. Performance history of thermal-sprayed aluminum coatings in offshore service. *Mater. Perform.* **1995**, *34*, 27–35.
103. Knudsen, O.Ø.; Rogne, T.; Røssland, T. Rapid degradation of painted TSA Paper No. 04023. In Proceedings of the Corrosion 2004; NACE International: New Orleans, Louisiana, USA, 2004.
104. Sumon, T.A.; Lyon, S.B.; Scantlebury, J.D. Failure of aluminium metal spray/organic duplex coating systems on structural steel. *Corros. Eng. Sci. Technol.* **2013**, *48*, 552–557.
105. Wang, X.; Qi, X.; Lin, Z.; Battocchi, D. Graphene reinforced composites as protective coatings for oil and gas pipelines. *Nanomaterials* **2018**, *8*.
106. Wei, J.; Atif, R.; Vo, T.; Inam, F. Graphene Nanoplatelets in Epoxy System:

Dispersion, Reaggregation, and Mechanical Properties of Nanocomposites. *J. Nanomater.* **2015**, *2015*.
107. Wang, X.; Tang, F.; Qi, X.; Lin, Z. Mechanical, electrochemical, and durability behavior of graphene nano-platelet loaded epoxy-resin composite coatings. *Compos. Part B Eng.* **2019**, *176*, 107103.
108. Sun, W.; Wu, T.; Wang, L.; Yang, Z.; Zhu, T.; Dong, C.; Liu, G. The role of graphene loading on the corrosion-promotion activity of graphene/epoxy nanocomposite coatings. *Compos. Part B Eng.* **2019**, *173*, 106916.
109. Anwar, Z.; Kausar, A.; Rafique, I.; Muhammad, B. Advances in Epoxy/Graphene Nanoplatelet Composite with Enhanced Physical Properties: A Review. *Polym. - Plast. Technol. Eng.* **2016**, *55*, 643–662.
110. Abakah, R.R.; Huang, F.; Hu, Q.; Wang, Y.; Jing, L. Comparative study of corrosion properties of different graphene nanoplate/epoxy composite coatings for enhanced surface barrier protection. *Coatings* **2021**, *11*, 1–18.
111. Ce, N.; Paul, S. The effect of temperature and local pH on calcareous deposit formation in damaged thermal spray aluminum (TSA) coatings and its implication on corrosion mitigation of offshore steel structures. *Coatings* **2017**, *7*, 52.
112. Li, C.; Du, M.; Qiu, J.; Zhang, J.; Gao, C. Influence of temperature on the protectiveness and morphological characteristics of calcareous deposits polarized by galvanostatic mode. *Acta Metall. Sin. (English Lett.* **2014**, *27*, 131–139.
113. Yan, J.-F.; White, R.E.; Griffin, R.B. Parametric studies of the formation of calcareous deposits on cathodically protected steel in aeawater. *J. Electrochem. Soc.* **1993**, *140*, 1275–1280.
114. Hartt, W.H.; Culberson, C.H.; Smith, S.W. CALCAREOUS DEPOSITS ON METAL SURFACES IN SEAWATER - A CRITICAL REVIEW. *Corrosion* **1984**.
115. Kunjapur, M.M.; Hartt, W.H.; Smith, S.W. Influence of temperature and exposure time upon calcareous deposits. *Corrosion* **1987**, *43*, 674–679.
116. Lin, S.-H.; Dexter, S.C. Effects of temperature and magnesium ions on calcareous deposition. *Corrosion* **1988**, *44*, 615–622.
117. Barchiche, C.; Deslouis, C.; Gil, O.; Refait, P.; Tribollet, B. Characterisation of calcareous deposits by electrochemical methods: Role of sulphates, calcium concentration and temperature. *Electrochim. Acta* **2004**, *49*, 2833–2839.
118. Paul, S. Behavior of damaged thermally sprayed aluminum (TSA) in aerated and dearated seawater Paper No. 12766. In Proceedings of the Corrosion 2019; NACE International: Nashville, Tennessee, USA, 2019.
119. Ce, N.A.; Paul, S. Protection of hot subsea risers by using thermally sprayed aluminium. *Anti-Corrosion Methods Mater.* **2017**, *64*, 299–305.
120. Pryor, M.J.; Keir, D.. Galvanic corrosion I. Current flow and polarization characteristics of teh aluminum-steel and zinc-steel couples in sodium chloride solution. *J. Electrochem. Soc.* **1957**, *104*, 269–275.
121. Kuroda, S.; Kawakita, J.; Takemoto, M. An 18-year exposure test of thermal-sprayed Zn, Al, and Zn-Al coatings in marine environment. *Corrosion* **2006**, *62*, 635–647.
122. Mansford, R.E. Sprayed aluminium and zinc. *Corros. Technol.* **1956**, 314–316.
123. Hoar, T.P.; Radovici, O. Zinc-aluminium sprayed coatings. *Trans. IMF* **1964**, *42*, 211–222.
124. Panossian, Z.; Mariaca, L.; Morcillo, M.; Flores, S.; Rocha, J.; Peña, J.J.;

Herrera, F.; Corvo, F.; Sanchez, M.; Rincon, O.T.; et al. Steel cathodic protection afforded by zinc, aluminium and zinc/aluminium alloy coatings in the atmosphere. *Surf. Coatings Technol.* **2005**, *190*, 244–248.
125. Watkins, K.O. Painting of metal-sprayed structural steelwork: report on the condition of specimens after 10 years' exposure. *Br. Corros. J.* **1974**, *9*, 204–210.
126. Kumar, A.; Van Blaricum, V.; Beitelman, A.; Boy, J. Twenty year field study of the performance of coatings in seawater. In *Corrosion Testing in Natural Waters*; Young, W., Kain, R., Eds.; ASTM International, 1997; Vol. Second vol, pp. 74–90.
127. Bukowski, J.; Kumar, A. Coatings and cathodic protection of piling on seawater: results of 10-year exposure at LaCosta Island, Fl. *Tech. Rep. M-321, Constr. Eng. Lab, US Army.* **1982**.
128. Zhu, Q.J.; Wang, K.; Wang, X.H.; Hou, B.R. Electrochemical impedance spectroscopy analysis of cold sprayed and arc sprayed aluminium coatings serviced in marine environment. *Surf. Eng.* **2012**, *28*, 300–305.
129. Jiang, Q.; Miao, Q.; Liang, W.; Ying, F.; Tong, F.; Xu, Y.; Ren, B.; Yao, Z.; Zhang, P. Corrosion behavior of arc sprayed Al–Zn–Si–RE coatings on mild steel in 3.5wt% NaCl solution. *Electrochim. Acta* **2013**, *115*, 644–656.
130. Lee, H.S.; Kwon, S.J.; Singh, J.K.; Ismail, M.A. Influence of Zn and Mg alloying on the corrosion resistance properties of Al coating applied by arc thermal spray process in simulated weather solution. *Acta Metall. Sin. (English Lett.* **2018**, *31*, 591–603.
131. Lee, H.S.; Singh, J.K.; Ismail, M.A.; Bhattacharya, C.; Seikh, A.H.; Alharthi, N.; Hussain, R.R. Corrosion mechanism and kinetics of Al-Zn coating deposited by arc thermal spraying process in saline solution at prolong exposure periods. *Sci. Rep.* **2019**, *9*, 1–17.
132. Tiong, D.K.-K.; Pit, H. Experiences on "theramal spray aluminum (TSA)" coating on offshore structures Conference paper No. 04022. In Proceedings of the Corrosion 2004; NACE International: New Orleans, Louisiana, USA, 2004.
133. Doble, O.; Pryde, G.; Oil, K. Use of thermally sprayed aluminum in the Norwegian Offshore Industry. *Prot. Coatings Eur.* **1997**, *2*, 1–10.
134. Knudsen, O.Ø. *Coating systems for long lifetime: thermally sprayed duplex systems SINTEF report A14189*; 2010;
135. Mandeno, W.L. Thermal metal spray: Successes, failures and lessons learned. In Proceedings of the Proceedings of Australasian Corrosion Association Corrosion & Prevention Conference; 2012.
136. Klinge, R. Altered specifications for the protection of Norwegian steel bridges and offshore structures against corrosion. *Steel Constr.* **2009**, *2*, 109–118.
137. Ltd., T. CROWN project commended for offshore win corrosion work Available online: https://www.twi-global.com/media-and-events/press-releases/2018-02-collaborative-crown-project-commended-for-offshore-wind-corrosion-work (accessed on Jan 7, 2020).
138. Matthiesen, H. Arkona Offshore wind project Available online: ttps://www.norwep.com/content/download/32957/239720/version/1/file/Mathiesen+2017-12-04_Norwegian+Offshore+Delegation_Arkona+Offshore+Wind+Project.pdf. (accessed on Jan 7, 2020).

139. International, A. ASTM D1141-98, Standard Practice for the Preparation of Substitute Ocean Water 2013.
140. ASTM ASTM E104 Standard Practice for Maintaining Constant Relative Humidity by Means of Aqueous Solutions. **2012**, 1–5.
141. Gabe, D.R.; Shirkhanzadeh, M. Polarity Reversal of the AI-Fe Galvanic Couple. *Br. Corros. J.* **1980**, *15*.
142. Porte, H.A. The effect of environment on the corrosion of metals in sea water - a literature survey. *Tech. Note N-907, Nav. Civ. Eng. labolatory* **1967**.
143. Feng, X.; Baojie, Z.; Chery, L. Effects of low temperature on aluminum(III) hydrolysis: Theoretical and experimental studies. *J. Environ. Sci.* **2008**, *20*, 907–914.
144. Gartland, P.O.; Eggen, T.G. *Cathodic and anodic properties of thermally sprayed Al and Zn - based coatings in seawater*; NACE international: Houston, 1990;
145. Gopalan, R.; Prabhu, N.K. Oxide bifilms in aluminium alloy castings - A review. *Mater. Sci. Technol.* **2011**, *27*, 1757–1769.
146. Lorking, K.F.; Mayne, J.E.O. The corrosion of aluminium. *J. Appl. Chem.* **2007**, *11*, 170–180.
147. Thierry, D.; Leballeur, C.; Larche, N. Galvanic series in seawater as a function of temperature, oxygen content and chlorination. *NACE - Int. Corros. Conf. Ser.* **2016**, *1*, 214–224.
148. Ganesan, P.; Renteria, C.M.; Crum, J.R. Versatile Corrosion Resistance of INCONEL Alloy 625 in Various Aqueous and Chemical Processing Environments. *Miner. Met. Soc.* **1991**, 663–680.
149. Wakefield, G.R.; Sharp, R.M. The composition of oxides formed on Al-Mg alloys. *Appl. Surf. Sci.* **1991**, *51*, 95–102.
150. Hakim, S.H.; Shanks, B.H. Manipulation of mesoporous structure and crystallinity in spontaneously self-assembled hierarchical metal oxides. *Microporous Mesoporous Mater.* **2010**, *135*, 105–115.
151. López Valdivieso, A.; Reyes Bahena, J.L.; Song, S.; Herrera Urbina, R. Temperature effect on the zeta potential and fluoride adsorption at the α-Al2O3/aqueous solution interface. *J. Colloid Interface Sci.* **2006**, *298*, 1–5.
152. Smith, W.R.; Paul, S. Natural deposit coatings on steel during cathodic protection and hydrogen ingress. *Coatings* **2015**, *5*, 816–829.
153. Nehrke, G.; Poigner, H.; Wilhelms-Dick, D.; Brey, T.; Abele, D. Coexistence of three calcium carbonate polymorphs in the shell of the Antarctic clam Laternula elliptica. *Geochemistry, Geophys. Geosystems* **2012**, *13*.
154. Flaten, E.M.; Seiersten, M.; Andreassen, J.P. Polymorphism and morphology of calcium carbonate precipitated in mixed solvents of ethylene glycol and water. *J. Cryst. Growth* **2009**, *311*, 3533–3538.
155. Theiss, F.; López, A.; Frost, R.L.; Scholz, R. Molecular and Biomolecular Spectroscopy Spectroscopic characterisation of the LDH mineral quintinite Mg4Al2(OH)12CO33H2O. *Spectrochim. Acta Part A Mol. Biomol. Spectrosc.* **2015**, *150*, 758–764.
156. Chukanov, N. V; Vigasina, M.F. *Vibrational (Infrared and Raman) Spectra of Minerals and Related Compounds*; 2020; ISBN 9783030268022.
157. do Nascimento Silva, M.; Kassab, E.; Ginoble Pandoli, O.; Leite de Oliveira, J.; Pereira Quintela, J.; Bott, I.S. Corrosion behaviour of an epoxy paint reinforced with carbon nanoparticles. *Corros. Eng. Sci. Technol.* **2020**, *0*, 1–6.

158. Hou, B.-R.; Zhang, J.; Duan, J.-Z.; Li, Y.; Zhang, J.-L. Corrosion of thermally sprayed zinc and aluminium coatings in simulated splash and tidal zone conditions. *Corros. Eng. Sci. Technol.* **2003**.
159. Zhao, W.M.; Wang, Y.; Liu, C.; Dong, L.X.; Yu, H.H.; Ai, H. Erosion-corrosion of thermally sprayed coatings in simulated splash zone. *Surf. Coatings Technol.* **2010**.
160. Li, S.; Hihara, L.H. Atmospheric-Corrosion Electrochemistry of NaCl Droplets on Carbon Steel. *J. Electrochem. Soc.* **2012**, *159*, C461-C468 (2012).
161. Schindelholz, E.; Risteen, B.E.; Kelly, R.G. Effect of Relative Humidity on Corrosion of Steel under Sea Salt Aerosol Proxies: II. MgCl2, Artificial Seawater. *J. Electrochem. Soc.* **2014**.
162. Lobnig, R.E.; Siconolfi, D.J.; Maisano, J.; Grundmeier, G.; Streckel, H.; Frankenthal, R.P.; Stratmann, M.; Sinclair, J.D. Atmospheric Corrosion of Aluminum in the Presence of Ammonium Sulfate Particles. *J. Electrochem. Soc.* **1996**, *143*, 1175–1182.
163. Graedel, T.E. Corrosion mechanisms for aluminum exposed to the atmosphere. *J. Electrochem. Soc.* **1989**, *136*, 204C-212C.
164. Friel, J.J. Atmospheric corrosion products on aluminium, zinc, and aluminium-zinc metallic coatings. *Corrosion* **1986**, *42*, 422–426.
165. Kolics, A.; Polkinghorne, J.C.; Wieckowski, A. Adsorption of sulfate and chloride ions on aluminum. *Electrochim. Acta* **1998**, *43*, 2605–2618.
166. Glanvill, S. Atmospheric corrosion of AA2024 in ocean water environments. *PhD thesis, Univ. Birmingham* **2018**.
167. España, J.S. The Behavior of Iron and Aluminum in Acid Mine Drainage: Speciation, Mineralogy, and Environmental Significance. In *Thermodynamics, Solubility and Environmental Issues*; Letcher, T.M., Ed.; Elsevier, 2007; pp. 137–149.
168. Falagán, C.; Yusta, I.; Sánchez-España, J.; Johnson, D.B. Biologically-induced precipitation of aluminium in synthetic acid mine water. *Miner. Eng.* **2017**, *106*, 79–85.
169. Chesworth, W. Laboratory Synthesis of Dawsonite and its Natural Occurrences. *Nat. Phys. Sci.* **1971**, *231*, 40–41.
170. Zhang, X.; Wen, Z.; Gu, Z.; Xu, X.; Lin, Z. Hydrothermal synthesis and thermodynamic analysis of dawsonite-type compounds. *J. Solid State Chem.* **2004**, *177*, 849–855.
171. Schaller, R.F.; Jove-Colon, C.F.; Taylor, J.M.; Schindelholz, E.J. The controlling role of sodium and carbonate on the atmospheric corrosion rate of aluminum. *npj Mater. Degrad.* **2017**, *1*.
172. Blücher, D.B.; Svensson, J.-E.; Johansson, L.-G. The NaCl-Induced Atmospheric Corrosion of Aluminum. The influence of Carbon Dioxide and Temperature. *J. Electrochem. Soc.* **2003**, *150*, B93–B98.
173. Blücher, D.B.; Svensson, J.-E.; Johansson, L.-G. The influence of CO2, AlCl3·6H2O, MgCl2·6H2O, Na2SO4 and NaCl on the atmospheric corrosion of aluminum. *Corros. Sci.* **2006**, *48*, 1848–1866.
174. Quéré, D. Wetting and Roughness. *Annu. Rev. Mater. Res.* **2008**, *38*, 71–99.
175. Hong, K.T.; Imadojemu, H.; Webb, R.L. Effects of oxidation and surface roughness on contact angle. *Exp. Therm. Fluid Sci.* **1994**, *8*, 279–285.
176. Siegel, H.; Gerth, M.; Tschersich, G. Sea surface temperature development of

the Baltic Sea in the period 1990-2004. *Oceanologia* **2006**, *48*, 119–131.
177. ASTM *B117-19 Standard Practice for Operating Salt Spray (Fog) Apparatus*; ASTM International: West Conshohocken, PA, 2019;

APPENDICES

Appendix 1

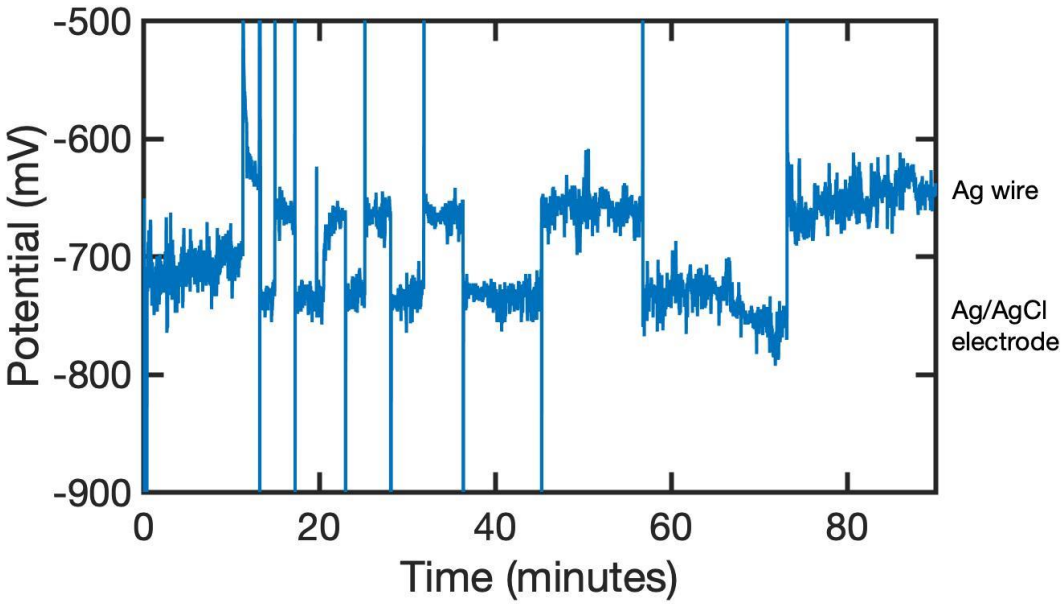

Figure 0-1 OCP of AA 1050 under 15 µL droplet of ASW with the use of two reference electrodes: silver wire and Lugging probe containing Ag/AgCl electrode, which were alternately connected to the potentiostat. Higher potentials were obtained when a Ag wire was used, whereas lower when Ag/AgCl electrode was utilised. Measurement performed at RH=90% and T=25˚C.